Numerical simulation of external and internal flow noise at passenger car components

Von der Fakultät für Maschinenbau
der Technischen Universität Carolo-Wilhemina zu Braunschweig

zur Erlangung der Würde

eines Doktor-ingenieurs (Dr.-Ing.)

genehmigte Dissertation

von Hervé Dechipre

aus Alencon (Frankreich)

eingereicht am: 10. März 2011

mündliche Prüfung am: 26. August 2011

Vorsitzende der Prüfungskommission: Prof. Dr.-Ing. Dragan Kozulovic

Referenten: Prof. Dr.-Ing. Jan Delfs
Prof. Dr.-Ing. Sabine Langer

2012

Abstract

For potential customers, the perception of both quality and comfort can nowadays be a decisive criterion at the moment of buying a vehicle (price apart). The interior noise level participates largely to it. The progress achieved to reduce significantly tire and engine noise have made the contribution of wind noise higher in the overall perception of noise by car passengers and therefore required high attention. In this context and to be able to continually improve acoustic comfort of car passenger, it is essential to develop effective tools to simulate the noise generated by external and internal flows and which could be used in the early phase of the design of a vehicle.

A wide range of numerical methods have been developed in the last years to assess aeroacoustic problems. However most of them require a large amount of computational resources. Therefore this work focuses on the possibility of using stochastic reconstruction of acoustic sources to simulate the noise generated by external and internal flows. The simulations are performed with the aeroacoustic code PIANO developed at the DLR Braunschweig. Two typical automotive applications were chosen to assess the capacity of such methods.

The first application consists in the computation of the acoustic field generated by the flow in two-dimensional duct containing a flat plate at a thickness related Reynolds number of 1300. Two computational aeroacoustic methods have been used. The first method is based on the Linearised Euler Equations (LEE): a single-test vortex is injected in the mean flow to interact with the geometry. The second method is based on the Acoustic Perturbation Equations (APE) and the stochastic sound source modelling introduced by Ewert [42]. It can be shown computationally that even in the absence of the classical Aeolian tone generation resonance type phenomena occur in the duct. This work demonstrates the ability of both methods to predict with accuracy resonance phenomena identified as Parker type modes. The frequency and mode representation computed by both methods are in good agreement with the experiment also presented in this work and the analytical work done by Koch [64].

The second application concerns the broadband noise induced by flow interacting with an automotive rain gutter. Two different profiles of rain gutter have been tested. As both rain gutter's height and oncoming flow's direction vary along the A-pillar on a vehicle, two configurations were designed to investigate experimentally these effects separately. Experimental tests were carried out in the DLR's aeroacoustic wind tunnel in Braunschweig. Acoustic measurements were done by using flush-mounted microphones and far field microphones as well as microphone array to localise the acoustic sources. A difference of more than 10 dB between the two profiles was measured in the far field. The tests showed that the sound level scales almost linearly with the height of the rain gutter and with 6th power of the velocity in the far field.

The numerical work is divided in two parts. The first part focuses on the computation of the structures of the flow and surface pressure level. The topology of the flow was assessed using steady RANS computation. Unsteady SAS-SST and DES models have been used to compute surface pressure fluctuations. Due to the high thickness of the boundary layer the flow computed by the conventional SAS-SST model remained stable therefore stochastic *forcing* terms were used to allow the model to switch into an unsteady mode. A good agreement was then found between the pressure fluctuations and the experiment.

In a second part four different computational methods have been used to predict the the flow-induced noise of an automotive rain gutter. Based on the rain gutter's height, the Reynolds numbers varied between 20 000 and 130 000. The first two methods are based on different wave operators to compute the acoustic field radiated by an unsteady flow field. The first method is the variational formulation of the Lighthill's Equation implemented in the commercial code FFT Actran/LA while the second method is based on the APE system. The two other methods are the same methods as those used for the first application: the injection of a single test-vortex in the flow and the stochastic sound source modelling (RPM). The first two methods produced similar results but remained high sensitivite to the quality of the acoustic sources computed by CFD. A good agreement was found between the RPM modelling and the experiment. The computation of sound in the far field requires a very good representation of the acoustic sources which represents the most challenging part of such simulations.

Zusammenfassung

Abgesehen vom Preis sind Qualität und Komfort heutzutage wichtige Kriterien beim Kauf eines Autos. Entscheidenden Einfluss auf den Komfort hat der Geräuschpegel im Auto. Der Geräuschpegel wird dabei, durch die in den letzten Jahren erzielten Fortschritte bei der Reduzierung von Motor- und Rollgeräuschen, zunehmend von den Windgeräuschen dominiert und benötigt daher besondere Aufmerksamkeit. Um die von Um- und Durchströmung erzeugten Geräusche vorhersagen zu können, und um so zielgerichtete Verbesserungen für den akustischen Komfort der Fahrgäste zu gewährleisten, müssen neue Methoden und Tools entwickelt werden, die eine verlässliche Simulation dieser Geräusche ermöglichen. Die so gewonnenen Erkenntnisse sollen und können dann in die frühe Entwicklungsphase von Fahrzeugen einfließen.

Zahlreiche numerische Methoden wurden in den letzten Jahren entwickelt, um aero- akustische Probleme zugänglich zu machen. Dennoch braucht die Mehrheit dieser Methoden enorm viele Rechnerressourcen. Diese Arbeit fokussiert sich daher auf die Möglichkeit von stochastischen Methoden, um die akustischen Quellen aus gemittelten Strömungsfeldern zu rekonstruieren und das durch Um- und Durchströmung erzeugte Geräusch zu simulieren. Die Simulationen wurden mit der Simulationssoftware PIANO vom DLR Braunschweig durchgeführt. Zwei für die Automobilindustrie typische Anwendungsfälle wurden ausgewählt, um die Möglichkeit der Methode für solche Fälle zu testen.

Im ersten Fall wurde das akustische Feld einer ebenen Platte in einem 2D Kanal mit einer auf die Plattendicke bezogenen Reynoldszahl von 1300 berechnet. Zwei numerische Methoden wurden dafür benutzt. Die erste Methode basiert auf den linearisierten Euler Gleichungen (LEE): Es wird ein Einzel-Testwirbel in die mittlere Strömung injiziert, um mit der Geometrie zu interagieren. Die zweite Methode basiert auf den "Acoustic Pertubation Equations" (APE). Bei diesem von Ewert [42] entwickeltem stochastischen Modell, werden die akustischen Quellen aus mittleren Strömungsgrößen rekonstruiert. Man kann mit den Berechnungen zeigen, dass auch ohne einen klassischen Äolien Ton Resonanz Phänomene im Kanal entstehen können. Diese Arbeit zeigt, dass beide Methoden es ermöglichen, die als Parker Moden identifizierten Resonanz Phänomene mit guter Genauigkeit numerisch vorher zu sagen. Die von beiden Methoden berechnete Frequenz und Moden Darstellung der Parker Resonanzen stimmen gut mit den ebenfalls in der Arbeit gezeigten experimentellen Daten, so wie mit analytischen Arbeiten von Koch [64] überein.

Der zweite Anwendungsfall ist der induzierte Breitbandlärm, der bei der Umströmung automobiler Wasserfangleisten entsteht. Zwei unterschiedliche Wasserfangleistenprofile wurden getestet. Da sowohl die Wasserfangleisten Höhe, als auch die Umströmungsrichtung entlang der A-Säule variiert, wurden zwei Konfigurationen erzeugt, um beide Effekt möglichst unabhängig von einander zu studieren. Die Versuche wurden im aeroakustischem Windkanal des DLR in Braunschweig ausgeführt. Die Versuchsmodelle wurden mit Einbaumikrophone ausgerüstet. Zur Geräuschquellen Lokalisierung wurden Messungen mit

einem Mikrophone Array durchgeführt. Unterschiede von mehr als 10 dB wurden im Fernfeld zwischen beiden Profilen gemessen. Die Messungen zeigen, dass der Geräuschpegel mit der Höhe der Wasserfangleiste fast linear und mit der Anströmgeschwindigkeit zur sechsten Potenz skalieren.

Die numerische Arbeit ist in zwei Teile aufgeteilt. Zunächst werden die Simulation der turbulenten Strukturen sowie die der Messflächendruckpegel gezeigt. Dabei werden stationäre RANS Simulationen genutzt, um die Strömungstopologie abzuschätzen. Transiente SAS-SST und DES Turbulenzmodelle werden für die Berechnung der Flächendruckpegel eingesetzt. Es hat sich gezeigt, dass das SAS-SST Modell vor der Wasserfangleiste auf Grund der vergleichsweise großen Grenzschichtdicke keine turbulenten Strukturen erzeugt hat. Daher wurde zusätzlich ein stochastisches "Forcing" Modell eingesetzt, um den Umschlag in eine turbulente Strömung zu ermöglichen. Danach fanden sich gute Übereinstimmungen zwischen den berechneten und gemessenen Druckschwankungen. Im zweiten Teil der Arbeit werden vier unterschiedliche numerische Methoden benutzt, um die strömungsinduzierten Geräusche der Wasserfangleisten zu berechnen. Basierend auf der Höhe der Wasserfangleisten, lag die Reynoldszahl zwischen 20 000 und 130 000. Die zwei ersten Methoden benutzten unterschiedliche Wellenoperatoren, um das abgestrahlte akustische Feld aus dem transienten Strömungsfeld zu berechnen. Die erste Methode basiert dabei auf einer Variations-Formulierung der Lighthill-Gleichung, so wie sie in der kommerziellen Software FFT Actran/LA implementiert ist. Die zweite Methode basiert auf den APE Gleichungen (Acoustic Perturbation Equations). Die zwei weiteren Methoden sind dieselben, die schon für den ersten Fall (Platte im 2D-Kanal) benutzt wurden: die Injektion eines Einzel Testwirbels in die mittlere Strömung und die von Ewert entwickelte stochastische Turbulenz Modellierung (RPM). Die ersten zwei Methoden liefern ähnliche Ergebnisse, aber zeigen eine hohe Sensitivität zur Qualität der zu Grunde liegenden CFD Simulationen. Sehr gute Übereinstimmung zwischen dem RPM Modell und den Experimenten wurden gefunden. Dafür war eine sehr gute Repräsentation der akustischen Quellen notwendig, was den anspruchsvollsten Teil für solche Berechnungen darstellt.

List of publications

- H. Dechipre, M. Hartmann, J.W. Delfs and R. Ewert, *Aeroacoustic simulation based on linearized Euler equations and stochastic sound source modelling*, Proc. Acoustics'08 Paris, pp.1071-1076, 2008
- H. Dechipre and M. Hartmann, *Aeroacoustic Simulation of an Automotive A-Pillar Rain Gutter*, Proc. 4th EASC Conference, München, 2009
- H. Dechipre, M. Hartmann, R. Ewert and J.W. Delfs, *Investigation of hybrid methods to compute the wind noise generated by an automotive rain gutter*, Proc. EURONOISE 2009, Edinburgh, 2009
- H. Dechipre, M. Hartmann, R. Ewert and J.W. Delfs, *Assessment of numerical methods for computation of automotive rain gutter wind noise*, Proc. 16th AIAA/CEAS Aeroacoustic Conference, Stockholm, 2010

Nomenclature

Abbreviations

APE	Acoustic Perturbation Equations
BL	Boundary layer
CAA	Computational AeroAcoustics
CFD	Computational Fluid Dynamics
CFL	Courant number (Courant-Freidrichs-Lewy)
DES	Detached Eddy Simulation
DLR	Deutsches Zentrum für Luft- und Raumfahrt
DNC	Direct Noise Computation
DNS	Direct Numerical Simulation
DRP	Dispersion Relation Preserving
FFS	Forward Facing Step
FFT	Fast Fourier Transformation
FFM	Far Field Microphone
FMM	Flush-Mounted Microphone
FW-H	Ffowcs-Williams Hawkings
GGI	General Grid Interface
HVAC	Heating, Ventilating and Air Conditioning
LA	Lighthill Analogy
LB	Lattice Boltzmann
LDDRK	Low Dissipation and Dispersion Runge Kutta
LEE	Linearised Euler Equations
LES	Large Eddy Simulation
NS	Navier-Stokes
PIANO	Perturbation Investigation of Aerodynamic NOise
PML	Perfect Matched Layer
POD	Proper Orthogonal Decomposition
RANS	Reynolds-Averaged Navier-Stokes
RFG	Random Fluid Generator
RG	Rain Gutter
RNG	Re-Normalisation Group
RPM	Random Particle Mesh
SAS	Scale Adaptive Simulation
SAS-F	Scale Adaptive Simulation with Forcing Term
SGS	Sub-Grid Scale
SNGR	Stochastic Noise Generation and Radiation
SPL	Sound Pressure Level
SST	Shear Stress Transport
STVI	Single Test Vortex Injection
SVD	Singular Value Decomposition
URANS	Unsteady Reynolds-Averaged Navier-Stokes
VW	Volkswagen

Latin symbols

c	speed of sound
c_p	specific heat capacity at pressure constant $[J/(kg \cdot K)]$
e	specific internal energy $[J/kg] = [m^2/s^2]$
E	energy function of the wavenumber in the turbulence energy spectrum $[m^3/s]$
f,f	frequency $[Hz]$
F_{SST}, F, F_1, F_2	blending functions of the SST turbulence model
$G(.\|.)$	Green function
h	height of the rain gutter $[m]$
k	turbulence kinetic energy $[m^2/s^2]$ or wavenumber $[-]$
k_s	effective wave number $[-]$
L_t	turbulence length scale $[m]$
L_{vK}	von Kármán length scale $[m]$
M	Mach number $[-]$
Nu	Nusselt number: heat-transfer convection against thermal conductivity $[-]$
p	Pressure $[Pa]$
Pr	Prandtl number: characterizes the ratio of velocity boundary layer to thermal boundary layer $[-]$
$\dot{q}$	heat flux $[Pa.m/s]$
q_c, q_m	heat and vortex source terms for the APE $[Pa.s/m^2]$ and $[m/s^2]$
Q	2nd invariant of the velocity gradient tensor $[s^{-2}]$
r	heat losses $[Pa/s]$
$R(.,.)$	two points space-time correlation $[-]$
R_{xy}	cross power spectral density $[-]$
Re	Reynolds number: characterizes the relative importance of inertial and viscous forces in a flow $[-]$
S	invariant of the strain-rate tensor $[s^{-1}]$
S_{ij}	strain-rate tensor - symmetric part of the velocity gradient tensor $[s^{-1}]$
St	Strouhal number describes the oscillating frequency of a flow $[-]$
t	time $[s]$
t_p	plate's thickness $[m]$
T	Temperature $[K]$
T_{ij}	Lighthill tensor $[Pa]$
u_i	i^{th} component of the velocity $[m/s]$
U_0	mean flow velocity $[m/s]$
x_i	i^{th} component of the cartesian coordinate $[m]$
y^+	dimensionless wall distance $[-]$

Greek symbols

δ_{ij}	Kroneker symbol $[-]$
Δt	transient simulation time-step $[s]$
ϵ	turbulence dissipation rate $[J/kg.s]$
γ	isentropic exponent $[-]$
λ	thermal conductivity $[W/(mK)]$ or wavelength $[m]$
μ	molecular dynamic viscosity coefficient $[kg/m.s]$
ν	kinematic viscosity $(= \mu/\rho)$ $[m^2/s]$
ω	turbulence eddy frequency $[s^{-1}]$
Ω_{ij}	rotation tensor - anti-symmetric part of the velocity gradient tensor $[s^{-1}]$
ψ	stream function
ρ	air density $[kg/m^3]$
τ	integral time scale $[s]$
τ_{ij}	viscous stress tensor $[Pa]$

Subscripts, superscripts and other symbols

$\overline{x}$	conventional time average of x
$\langle x \rangle$	ensemble average
x' or x''	fluctuation quantity
x^*	dimensionless quantity
x_t	turbulent quantity

Contents

CHAPTER 1

Introduction

1.1 Problem statement

For potential customers, the perception of both quality and comfort is a decisive criterion at the moment of buying a vehicle (except the price). Amongst the various aspects which determine the comfort inside a vehicle, the interior noise experienced by the passengers is one of them. Historically engine and rolling noises were the most important noise sources. However the recent successes in reducing motor and road/tire noise, have increased the contribution of airflow induced noise (also called 'wind noise'). Over 100 km/h wind noise is generally the dominant noise source [53] and can make it difficult to converse or listen to the radio, but it can also add fatigue on a long highway trip. A potential buyer might even consider high wind noise levels as poor design or built quality which may lead to unsatisfied customers. In addition car manufacturers propose a large choice in infotainment and other embarqued systems which require a low background noise level. A low noise level in the cabin represents a marketing advantage. Therefore car manufacturers have to pay close attention to minimize wind noise.

One could expect that low drag vehicles would also have low wind noise level; however this assumption is not verified in practice. One explanation for this lack of correlation comes from the fact that aerodynamic drag depends largely of the airflow over the rear of the vehicle and its wake while interior wind noise depends largely on details of the exterior airflow around the A-pillar and windscreen[1]. Small openings or gaps around doors, windows or many other components on the outer body such as roof-racks or side-view mirrors may to a large extend contribute to wind noise; on the other hand they will have little or no effect on aerodynamic drag. To this list one can add the air conditioning and the decorative cooling grid as potential source of noise.

The wind noise due to the airflow around the vehicle can be generated in different ways. Firstly, resonance phenomena can be caused by cavities like open roof or spaces around

---

[1] A.R. George in *Aerodynamics of road vehicles* edited by W.H. Hucho, 1998

the door. Further noise can be caused by the flow passing exposed objects such as roof racks, radio antenna or mirrors. This has already been the topic of many experimental and numeric works [53]. Leaks can also be a source of noise. Even by making completely airtight the cabin and suppressing any asperities, a noise due to the overall shape of the vehicle will remain. This noise is due to the pressure fluctuations created over the surface of the vehicle and to the detachments of the flow over the surface of the vehicle. These fluctuations are transmitted inside the cabin by exciting the panels which radiate inside. The lateral front windows are often identified as major noise sources. Three reasons can be advanced to explain it: the flow is detached in this area, the windows are less absorbent than the rest of the structures (like doors) and finally it is close to the driver's ears.

1.2 State of the art in computational aeroacoustics

Aeroacoustics can be defined as a branch of aerodynamics which specially studies the noise generated by flows in the presence of an object. Therefore, it refers to the noise generated by unsteady and irregular flows at contrast to classical acoustics dealing with sound typically generated by the vibration of solids.

The discipline of aeroacoustics is born in 1952, when Lighthill [72] developed his famous analogy to understand the noise generated by the propulsive jets of aircraft. After the Second World War the outstanding advances in aviation technology and the development of jet propeller required a new level of comprehension in flow acoustics. Lighthill's theory was validated by comparing the predicted and measured generated noise from flying large scale commercial jet airplanes. During the next 40 years most of the works in aeroacoustics were based on this analogy between sound generation by flows and the solution of a classical wave equation in a medium at rest, forced by appropriate volume sources. In the last decades the emergence of numerical methods especially developed for computing directly the sound emitted by flows has allowed a rapid evolution of the subject. A special name was even created: Computational Aero-Acoustics (CAA). CAA can be seen as a branch of computational fluid dynamics (CFD), however special treatments (numerical schemes or boundary conditions) had to be developed to allow the propagation of the acoustic waves.

Contribution of aeroacoustics can be observed in many aspects of our daily life: vacuum cleaners, hair dryers, exhausts pipes and ventilation systems are few examples. Aeroacoustic aspects are often important issues for a wide range of engineering applications such as in the transport industry (aerospace, automotive, trains and ships) but also in the energy sector (wind turbines), electronics (i.e. telephones, ventilators) and architecture. In aeronautics noise generated by the turbomachinery [72], trailing edge [75] and slat/flap [43] are generally the most important aspects. Aeroacoustics is nowadays also very important for trains (cavities [91]) and cars [60]. The interaction between the flow and the instabilities at the origin of the sound can even lead to situations with high resonances generating important damages and/or perturbing the comfort and performances of energy installation [70]. Therefore, the reduction of flow induced noise is becoming essential and is often required either for commercial advantages or environmental regulations. Therefore, to continually improve the aeroacoustic performance, effective and accurate numerical methods are required to predict the noise generated by external and internal flows and which could be integrated in the early phase of conception to include aeroacoustic aspects and reduce the tests and development costs.

Two basic phenomena are generally at the origin of aerodynamic noise. Impulsive noise is a result of non-uniformly moving objects. The second one is the result of turbulence, which by its stochastic nature, generates broad band frequency noise. In addition one may consider combustion noise which results from the chemical reactions and the subsequent introduction of entropy in the flows.

During the last decades, many methods have been developed to compute the acoustic field radiated from a turbulent flow, see for example [55]. These methodologies fall into two concepts: direct and hybrid approaches, see figure 1.1.

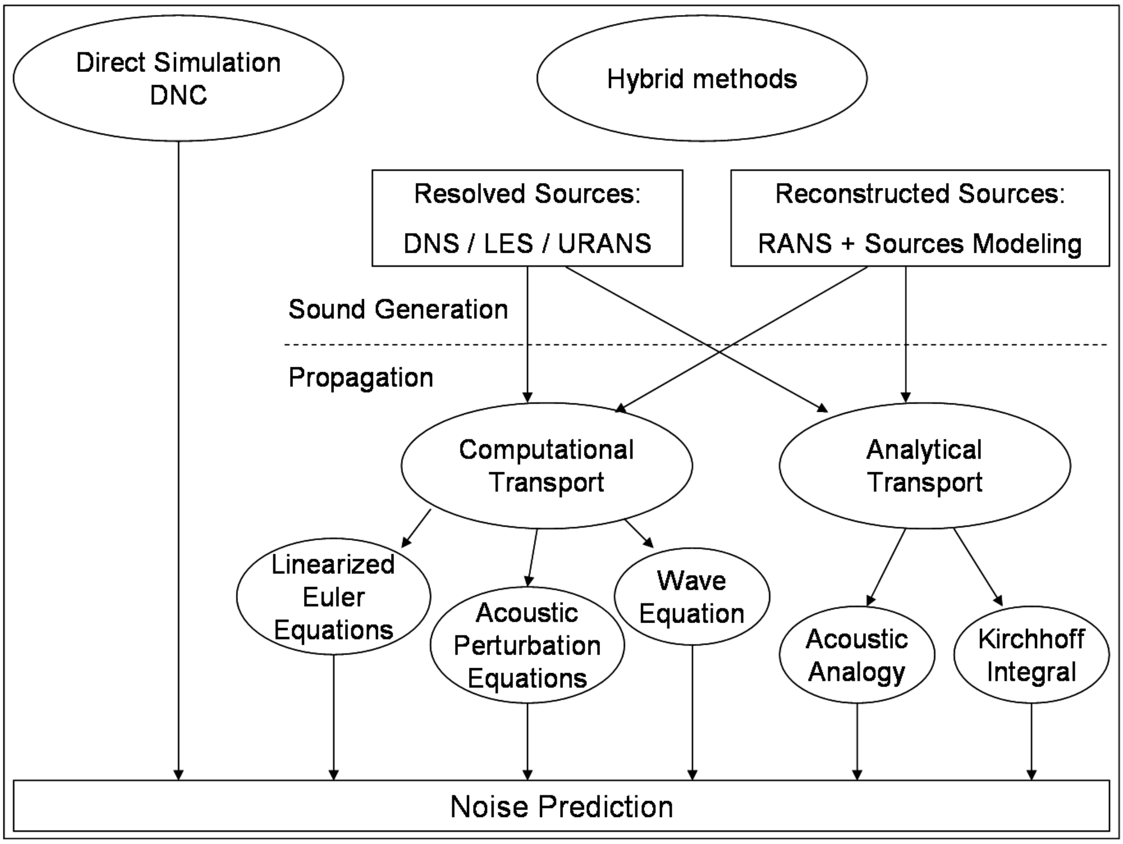

Figure 1.1: Hierarchy of noise prediction methods

The easier concept consists in directly computing the acoustic field in the same time as computing the aerodynamic turbulences at the origin of the noise. The Navier-Stokes equations do not only represent the aerodynamic mechanisms but are also valid in far field to compute the acoustic pressure variations. This approach has the advantage of directly treating the interaction between the aerodynamic sources and the waves. In this approach the simulations should be conducted in a computational domain that includes the noise source region as well as the far field. The mesh must be made such that both the flow and its sound can be well represented. The large disparity between the length scales of the fluctuations of the turbulent velocity and the acoustic quantities (in the order of 10^5) makes however direct methods numerically very expensive and challenging. The acoustic disturbances are also in the order of magnitude of the numerical errors. Therefore, direct methods require specific numerical techniques to propagate waves in the far field. The high computational cost makes its use limited to flows at very low Reynolds number. So far only relatively simple flow configurations have been treated.

Another approach to compute the acoustic field is based on the decoupling of the aerodynamic and acoustic simulations. These methods are generally named *hybrid methods*. The problem is here divided into sound generation and propagation of the generated sound in the far field. In hybrid methods aerodynamic techniques must be used for the evaluation of the flow-field in the near-field. The acoustic sources can either be evaluated by carrying out scale resolving unsteady aerodynamic simulations or by using a model. It is essential that all noise generating mechanisms relevant for the problem to be solved are considered when using hybrid approaches. For most free field applications, the noise generation is purely due to turbulent velocity fluctuations and incompressible source simulation is sufficient. However compressible simulations may be required when the aerodynamic noise is generated by coupling between the flow and the acoustic field (i.e. cavity noise or duct aeroacoustics).

When using unsteady aerodynamic simulations to compute the sources, the displacement of the particles can be assessed by using a microscopic approach like Lattice Boltzmann (LB) or methods based on scale resolving solution of the Navier Stokes equations (direct numerical simulation (DNS), large-eddy simulation (LES) and other derivatives). A direct resolution of the flow (DNS) offers good results but remains generally too expensive for industrial application. Averaged methods are generally preferred to reduce the computational cost; however these methods can only capture fluctuations with large scales and low frequencies. In other words unsteady averaged methods cannot be used for the prediction of broadband noise but might be interesting to qualify tonal phenomena. LES provides nowadays an alternative solution to compute unsteady turbulent flow. In the LES approach, only the large eddies are explicitly resolved while the smaller scales are modelled using a sub grid scale model. However LES remains often still too expensive for high Reynolds number flows.

Motivated by proposing fast methods, few research teams have been working on the possibilities of using a steady flow simulation and a model to represent the fluctuations of the acoustic sources. In cases where the spectrum of generated sound consists of a broadband noise, the unsteady character of the flow at the origin of the acoustic noise which was lost during the averaging process can be reconstructed via a stochastic model. Different models were proposed such as the Stochastic Noise Generation and Radiation (SNGR) model of Bechara et al [14] and its different improvements [21] [19] as well as the Random Particle Mesh (RPM) model introduced by Ewert [42]. The reconstructed term is composed of series of Fourier modes for the SNGR method, whereas a white noise is filtered for the RPM.

Once having computed the turbulent flow, the radiated acoustic field can be either computed by solving a system of equations such as the Linearised Euler Equations (LEE) and derivates or using a propagation operator like for the analogy of Lighthill and other variations (Ffowcs Williams and Hawkings, Curle, Lilley or Phillip). The analogy of Lighthill consists in a clever recombination of the Navier Stokes equations in order to separate the wave operator on the left hand side of the wave equation while the right hand side represents the equivalent sound sources:

$$\frac{\partial^2 \rho}{\partial t^2} - c_0 \nabla^2 \rho = \frac{\partial^2 T_{ij}}{\partial x_i \partial x_j} \tag{1.1}$$

with ρ the density and in which as been introduced the speed of sound c_0 and the Lighthill's tensor T_{ij} defined as:

$$T_{ij} = \rho u_i u_j + \left((p - p_0) - c_0^2(\rho - \rho_0)\right) \delta_{ij} - \tau_{ij} \tag{1.2}$$

with τ_{ij} the viscous stress tensor. The Lighthill equation can be solved by using the Green's function formalism $G(x, t|y, \tau)$. The Green's function characterizes the answer at position x and time t to an impulse at the position y and the time τ.

1.3 Objectives and approaches

1.3.1 Scope of the present work

This short overview shows that many methods have been developed to compute the acoustic field radiated by aerodynamic sources but unfortunately there is not a unique answer to assess all the aeroacoustic problems. For the industry the computational cost and the duration of the simulation are major concerns; therefore in this study, we will focus on the use of methods based on steady flow simulations to compute the aeroacoustic field. This work should allow assessing the following different points:

- Investigate the possibility of using RANS based methods to compute aeroacoustic noise generated by basic configurations at a low Mach number. These methods are considerably less time consuming/costly and more flexible than LES or DNS.
- Assess the possibility of using stochastic models and to apply them to other cases than trailing edge noise or jet noise.
- Compare different methods and define some best practice guidelines for aeroacoustic computations.
- To increase the understanding of the important aspects of performing a noise prediction when using CAA methods both in terms of numerical requirements and in the sound generation process.

The main part of this study consists in the evaluation of the aeroacoustic code developed at the German Aerospace Center (DLR) called PIANO while using different techniques to compute the aeroacoustic field based on a steady flow simulation. The abbreviation PIANO stands for Perturbation Investigation of Aerodynamic NOise. This code was initially developed for the aerospace industry and has demonstrated good results. However the possibility of applying these methods to the automotive industry characterised by lower speed and different types of acoustic sources remains an open question.

1.3.2 Organization of the dissertation

Following this introduction, fundamental principles and methodologies used for CFD and CAA will be are presented in Chapter 2. It outlines the major differences between the requirements of an aerodynamic and an aeroacoustic simulation. It highlights the interest of using specific methods such as hybrid methods in which the simulation of the acoustic sources is separated from the propagation of the noise in the far field. An overview of the DLR's aeroacoustic code PIANO and its specificities used for this work is proposed.

Two different applications are treated in this work. A first application consisting in a simple duct containing a flap is introduced in chapter 3. Numerical simulations as well as tests have been performed. A correlation between the numerical and the experimental results is drawn. In Chapter 4, the noise generated by the flow around a 3D automotive A-pillar rain gutter is investigated. An overview of some works found in the literature is dressed. The results of wind tunnel tests are presented. Steady and unsteady flow simulations have performed to assess the flow structures as well as the acoustic perturbations. Four acoustic numerical methods have then been used to compute the aeroacoustic field. The acoustic sources used in the first two methods result from the unsteady flow simulations while the acoustic far field is computed with different operators. At the opposite the acoustic sources are modelled based on a steady RANS simulation in the other methods. In one case a single-test vortex is used while in the second case a stochastic turbulence field is computed to model the turbulent fluctuations. Finally some conclusions and recommendations for further works complete the last chapter.

CHAPTER 2

Aeroacoustic simulation models

2.1 Introduction

Started in the early twentieth century the development of the Computational Fluid Dynamics (CFD) has since known many successes offering nowadays the possibility of performing with a good accuracy steady or unsteady flow simulations around complex geometries such as a car or an aircraft. This was made possible by the development of complex turbulence models and the optimization of the algorithms but also by the exponential development of the computational facilities during the last decades. However many phenomena remain difficult to simulate and further developments remain to be done. Due to the intrinsic differences in order of magnitude between the acoustic and aerodynamic variables, the computation of the noise generated by the flow around a geometry represents a major issue. In fact the use of the algorithms designed for CFD purpose can be disastrous when one comes to compute noise.

This chapter introduces some fundamental concepts necessary to understand the rest of the dissertation. Some CFD techniques used for this work are firstly presented. The main differences between aerodynamic and aeroacoustic simulations are outlined and an overview of the methods for Computational Aero-Acoustics (CAA) is dressed to make the reader aware of the variety of numerical methods available in aeroacoustics and the technical problems associated. This chapter ends with a brief presentation of DLR's CAA code PIANO used for this work.

2.2 Computational Fluid Dynamics (CFD)

2.2.1 Governing equations

Named after Claude-Louis Navier and Gabriel Stokes, the Navier-Stokes equations represent the basis of fluid dynamics and arise from applying the Newton's second law to fluid motion. By solving these equations, one can compute at each point of a field the value of the main quantities such as the pressure (p), density (ρ) or velocity (u_i). In the case of a Newtonian viscous fluid, the Navier-Stokes equations read:

$$\frac{\partial \rho}{\partial t} + \frac{\partial \rho u_i}{\partial x_i} = 0 \tag{2.1}$$

$$\frac{\partial \rho u_i}{\partial t} + \frac{\partial \rho u_i u_j}{\partial x_j} = -\frac{\partial p}{\partial x_i} + \frac{\partial \tau_{i,j}}{\partial x_j} \tag{2.2}$$

$$\frac{\partial \rho e}{\partial t} + \frac{\partial}{\partial x_i}\left[(\rho e + p)u_i\right] = \frac{\partial \tau_{i,j} u_j}{\partial x_i} - \frac{\partial \dot{q}_i}{\partial x_i} + r \tag{2.3}$$

e, $\tau_{i,j}$, $\dot{q}$ and r represent respectively the specific internal energy, the viscous stress tensor, the heat flux and the heat losses. According to similarity the non dimensional parameters $\mathrm{Re} = \frac{U_0 l}{\nu}$; $M = \frac{U_0}{c_0}$; $Pr = \frac{\mu c_p}{\lambda}$ along with the boundary conditions characterise the flow problem uniquely. Here U_0 is the mean flow velocity, c_0 the speed of sound.

At high Reynolds numbers the flow becomes turbulent, i.e. unsteady, a broad range of spatio-temporal scales and also for large computational domains a large amount of mesh points is required. Then the computation can become quickly too expensive to resolve in time and space and difficult to handle. Therefore, many turbulence models have been developed in the last decades to compute an averaged or partially averaged solution at acceptable cost.

2.2.2 Turbulence quantities

In general, aerodynamic noise is generated by turbulent flows characterised by a velocity field which varies significantly and irregularly in position and time. Although the detailed properties of turbulent velocity are highly disorganised and difficult to predict, its statistical properties are reproducible.

According to the theory developed by Kolmogorov [65] [66], the turbulence is composed of structures which sizes are continuously distributed inside a range of scales bounded by the dimensions of the geometry as the upper limit and by the Kolmogorov scale at the lower limit, where only viscous dissipation occurs. Large eddies have low frequencies and sizes in the order of the flow domain while smaller eddies have high frequencies and are determined by the viscosity of the fluid. Kolmogorov suggested that in every turbulent flow at a sufficiently high Reynolds number, the statistics of the small-scale motions have a universal form that is uniquely determined by the rate of dissipation ϵ and the fluid kinematic viscosity ν. The stretching of the large eddies makes the energy passing down the cascade to smaller and smaller eddies until viscosity causes their dissipation into heat.

A model of the energy spectrum for a quantity like the pressure is represented in figure 2.1, the figure illustrates the five third Kolmogorov's spectrum which means: $E \sim k^{-\frac{5}{3}}$ in the inertial subrange.

Turbulent flows are generally characterised by continuous spectra while a spectrum with discrete frequencies corresponds to unsteady laminar flows. When solving numerically a flow, the resolution of the smallest scales is limited by the mesh which introduces a cut-off limit below which eddies cannot be numerically resolved and are either modelled or ignored.

Various techniques to solve a turbulent flow have been developed from the complete resolution of all scales to the purely statistical approach. An overview of these methods will

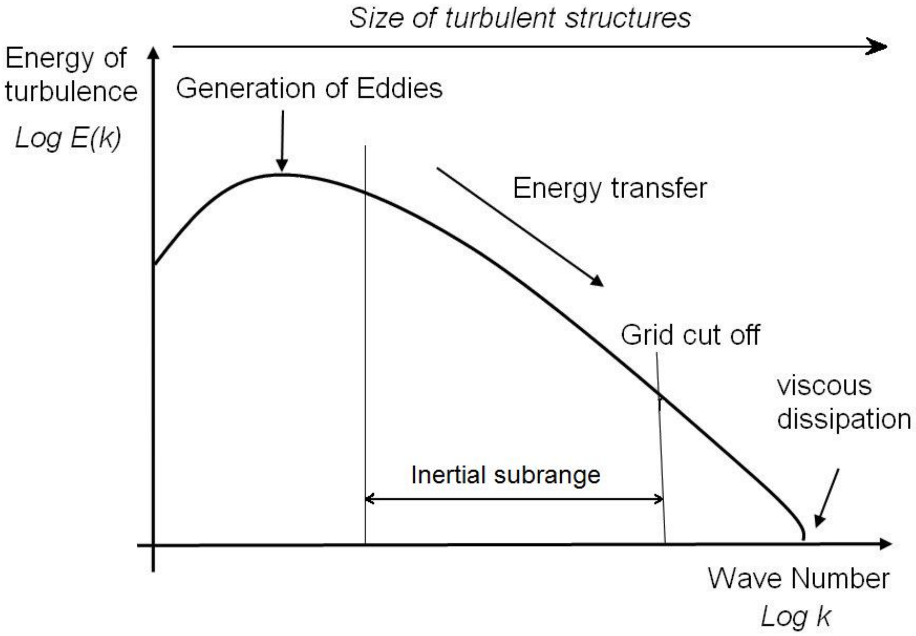

Figure 2.1: Energy spectrum model for homogeneous isotropic turbulence

now be presented. However all methods are not equivalent and do not provide the same amount of information and neither have the same requirements in terms of computation time.

2.2.3 Direct Numerical Simulation (DNS)

The Direct Numerical Simulation (DNS) is probably the simplest conceptual approach and the most accurate one. The method is based on the direct resolution of the full unsteady Navier-Stokes equations without any additional assumptions or models. This means that the whole range of spatial and temporal scales of turbulences must be resolved. In other words, grid spacing and time step must be fine enough to capture the dynamics of the smallest scales of the flow (defined by the Kolmogorov scales) without the need of turbulence model. The domain must also be large enough to represent the largest scales. These criteria make this approach also the most expensive one. Typically for a three dimensional DNS computation, the number of points N^3 must satisfy after [27]:

$$N^3 \geq Re^{9/4} \tag{2.4}$$

The previous spatial requirement goes with a temporal requirement to assure a low courant number, i.e. $u\Delta t/\Delta x$. For an explicit resolution scheme, the courant number must generally be below the unity.

The high spatial and temporal requirements make it difficult if not impossible to use the DNS at industrial relevant Reynolds numbers and for engineering applications with large computational domain. Consequently, even with the rapid progress of computers and massive parallelization, DNS does not yet seem suitable for solving engineering applications in the foreseeable future. The use of this method remains restricted to fundamental research with low Reynolds numbers. DNS stays however a useful tool to get better understanding of fundamental phenomena and to validate numerical turbulence models.

2.2.4 Reynolds Averaged Navier Stokes equations (RANS)

The Reynolds Averaged Navier-Stokes (RANS) method is probably the most applied method to solve engineering flow problems. In contrast to the DNS, the approach is based on the idea of considering the turbulence as a purely statistic process and a modelling of all scales of the turbulence.

Introduced by Osborne Reynolds, this statistical description of the turbulent flow is based on a decomposition of the instantaneous values of the flow quantities (pressure, velocity, temperature and density) into a ensemble averaged part and a fluctuating part:

$$u(x,t) = \overline{u}(x,t) + u'(x,t) \quad \text{with} \quad \overline{u'}(x,t) = 0 \tag{2.5}$$

where the $(\overline{x})$ represents the time average of the quantity x.

The method represents an ensemble average over the entire range of turbulent eddies allowing to greatly reduce the computational cost compared to DNS. The introduction of the Reynolds decomposition leads to the following RANS equations (incompressible flows assumed for clarity of the presentation):

$$\rho\left(\frac{\partial \overline{u}_j}{\partial t} + \overline{u}_i \frac{\partial \overline{u}_j}{\partial x_i}\right) = -\frac{\partial \overline{p}}{\partial x_j} + \frac{\partial}{\partial x_i}\left(\overline{\tau}_{ij} - \rho\overline{u_i' u_j'}\right) \tag{2.6}$$

with τ_{ij} und $\overline{\rho u_i' u_j'}$ representing respectively the viscous stress and the Reynolds stress tensor.

The viscous stress tensor $\tau_{i,j}$ accounts for momentum transfer due to friction. For Newtonian fluids Stokes' postulation (1845) states that the shear stresses are proportional to the velocity gradients, with the molecular viscosity as the proportionality factor:

$$\tau_{ij} = \mu\left(\frac{\partial u_i}{\partial x_j} + \frac{\partial u_j}{\partial x_i}\right) - \underbrace{\delta_{ij}\frac{2}{3}\mu\frac{\partial u_i}{\partial x_i}}_{=0 \text{ for incompressible flow}} \tag{2.7}$$

with δ_{ij} representing the Kronecker symbol.

The Reynolds stress tensor containing the product of fluctuation quantities represents 6 additional unknowns. To close the problem, it is necessary to use additional equations. The number and nature of equations used to close the system define the type of turbulence model. A wide range of turbulence models exist to close the problem. For further details on RANS models, the reader can refer to [125]. The SST model was generally used in this work and will now be presented.

Shear Stress Transport model (SST)

The SST model belongs to the class of eddy viscosity approaches. This model, introduced by Menter [79], was designed to combine the best of two 2-equation models: the k-ϵ model and the Wilcox k-ω model [124]. As depicted in figure 2.2, the boundary layer is divided in 4 parts: the sublayer, the buffer layer, the logarithmic region and the outer region.

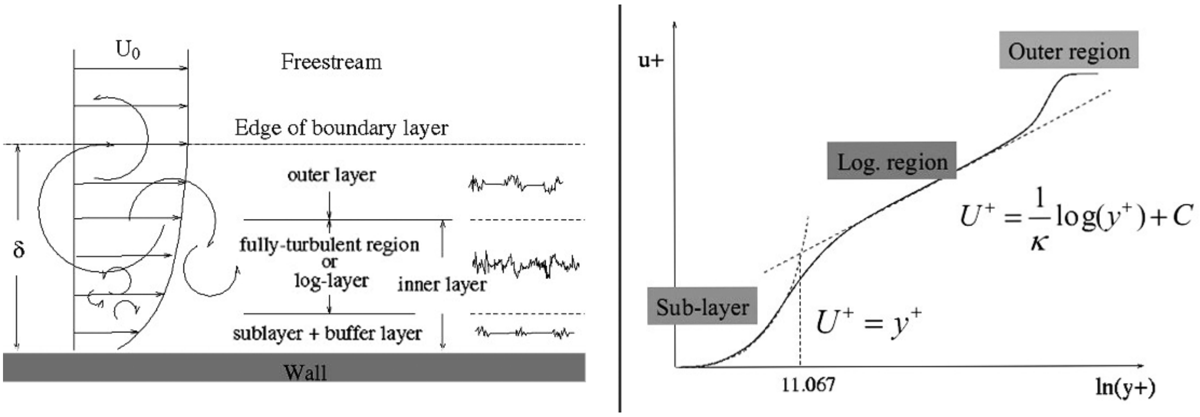

Figure 2.2: Structure and velociy profile of a turbulent boundary layer

According to [3], a mesh resolution of $y^+ \leq 2$ should be sufficient to resolve the sublayer with a k-ω model whereas a standard k-ϵ model would require a mesh resolution of $y^+ \leq 0.2$. The k-ω model of Wilcox is however strongly sensitive to the boundary conditions whereas the k-ϵ model is generally well known for over predicting the kinetic energy at the stagnation points and for missing the flow separation. Therefore, Menter [79] introduced a blending between the k-ω model in the wall vicinity and the k-ϵ model in the outer region. The switch between both models is done by the use of a blending function F_1 depending on the wall distance. The two transport equations read:

$$\frac{\partial(\rho k)}{\partial t} + \frac{\partial(\rho \overline{u}_i k)}{\partial x_i} = \tilde{P}_k - \epsilon_k + D_k \tag{2.8}$$

$$\frac{\partial(\rho \omega)}{\partial t} + \frac{\partial(\rho \overline{u}_i \omega)}{\partial x_i} = \alpha \frac{\omega}{k} \tilde{P}_k - \epsilon_\omega + (1 - F_1)\rho \frac{2}{\sigma_{\omega_1}} \frac{\partial k}{\partial x_j} \frac{\partial \omega}{\partial x_j} + D_\omega \tag{2.9}$$

The terms P_k, ϵ_k and D_k represent the production term, the dissipation term and the destruction term in the k-equation ($k = \frac{1}{2}\left(\overline{u'^2_1} + \overline{u'^2_2} + \overline{u'^2_3}\right)$) while σ_K, σ_{ω_1} and $\sigma_{\omega_2}$are 3 constants. A production limiter is used for ($\tilde{P}_k$) in the SST model to prevent the build-up of turbulence in stagnation regions. These terms take the following formulation:

$$\begin{aligned}
P_k &= \mu_t \frac{\partial u_i}{\partial x_j}\left(\frac{\partial u_i}{\partial x_j} + \frac{\partial u_j}{\partial x_i}\right) \qquad \rightarrow \qquad \tilde{P}_k = \min(P_k, 10 \times \beta^* \rho k \omega) \\
\epsilon_k &= \beta^* \rho k \omega \quad \text{with} \quad \beta^* = 0.09 \\
D_k &= \frac{\partial}{\partial x_j}\left[\left(\mu + \frac{\mu_t}{\sigma_K}\right)\frac{\partial k}{\partial x_j}\right] \\
\mu_t &= \rho \frac{k}{\omega} \\
\epsilon_\omega &= \beta \rho \omega^2 \\
D_\omega &= \frac{\partial}{\partial x_j}\left[\left(\mu + \frac{\mu_t}{\sigma_{\omega_2}}\right)\frac{\partial \omega}{\partial x_j}\right]
\end{aligned}$$

In this equation, F_1 is equal to zero away from the surface (k-ϵ model) and switches over to unity inside the near wall boundary layer (k-ω model). The turbulence eddy viscosity ($\nu_t = \mu_t/\rho$) is then defined by:

$$\nu_t = \frac{a_1 k}{\max(a_1 \omega, \left|\overline{S}\right| F_2)} \tag{2.10}$$

where $\left|\overline{S}\right|$ is an invariant measure of the strain rate and F_2 is a second blending function allowing to limit the maximum value of the eddy viscosity (which may be over-estimated) and ensure the Bradshaw relation [22].

Bardina [8] carried out an intensive comparison of the performances of various turbulence models and concluded that the SST model was the most appropriate model to treat most of the engineering applications. The SST model has been used as kernel in the CFX solver to develop the DES and the SAS turbulence models. Both models have been used in the present work and will be defined later on.

2.2.5 Large Eddy Simulation (LES)

The philosophy of Large Eddy Simulation (LES) corresponds to solve the large and energetic scales of turbulence and to model the effect of unresolved scales on the resolved scales. This idea is based on the notion that the small scales are assumed to follow a more universal behavior and therefore can be modelled. The flow field is therefore decomposed into a large scale or grid scale (GS) component and a subgrid scale (SGS) component. Each field variable Φ is represented as a sum of spatially average value $\langle\Phi\rangle$ and a fluctuating part Φ': $\Phi = \langle\Phi\rangle + \Phi'$. The GS component is obtained as a result of filtering the entire domain with a filter function G and a filter width $\bar{\Delta}$ which defines the smallest resolved scale:

$$\langle\Phi\rangle(x,t) = \int\int\int_{-\infty}^{\infty} \Phi(x-s,t)\, G(x.s;\bar{\Delta})\, ds \tag{2.11}$$

The filtering operation is applied to the Navier-Stokes equations to obtain the equations governing the dynamics of the filtered quantities. These quantities are then solved directly for the grid scale turbulent motions, while the effect of the subgrid scales is approximated using an SGS model. Most of the SGS models which have been proposed are semi-empirical, such as the classical Smagorinsky model [110] where $\nu_t = \left(C\bar{\Delta}\right)^2 \times \bar{S}$ with $\bar{S}$ the velocity gradient. The definition of the subgrid scale model is decisive in the implementation of the LES method and many works have been done to propose a dynamic SGS model. Further information on SGS can be found in [104] while an overview over LES and its application in aeroacoustics can be found in [120].

Formally LES and RANS approaches solve the same equations. The main differences concern the modelling of the Reynolds stress and the fact that the LES is inherently unsteady:

$$\overline{u_i' u_j'} \;\rightarrow\; \langle u_i' u_j' \rangle - \langle u_i' \rangle \langle u_j' \rangle \tag{2.12}$$

2.2.6 Hybrid methods

a/ Detached Eddy Simulation (DES)

In the LES approach, the Navier Stokes equations are filtered using a spatial operator with a filter-width proportional to the local grid spacing. This aspect makes a direct connection between the level of resolution of turbulence scales and the mesh refinement. In an attempt to overcome this restriction, Spalart [112] proposed a hybrid method which combines features of classical RANS formulations with elements of LES methods. This concept called Detached Eddy Simulation (DES) is intended to take advantage of both methods by covering the boundary layer by a RANS model and switching into a LES mode in detached regions. This allows the calculation to capture the instability of shear layer and the development of coherent structures in the wake with more accurate prediction of the unsteady forces than can be obtained by steady or unsteady RANS methods. The switch for the DES is achieved by comparing the modelled turbulence length scale and the grid spacing.

DES belongs to the category of seamless hybrid turbulence models, in opposition to the so-called zonal methods. Both categories are differentiating from each other through the transition between RANS and LES formulations and the treatment of the so-called grey area existing in this particular region. In case of zonal approach a physical interface has to be defined. Based on the SST model developed by Menter, Strelets [115] proposed a model able to switch from the SST-RANS model to an LES model in regions where the turbulence length scale, L_t, predicted by the RANS model is larger than the local grid spacing. The length scale used in the computation of the dissipation rate in the equation for turbulence kinetic energy is replaced by the local grid spacing (Δ).

$$\epsilon = \beta^* k\omega = \frac{k^{\frac{3}{2}}}{L_t} \quad \rightarrow \quad \frac{k^{\frac{3}{2}}}{C_{\mathrm{DES}}\Delta} \quad \text{for} \quad C_{\mathrm{DES}} \cdot \Delta < L_t \quad \Delta = \max(\Delta_i) \quad L_t = \frac{\sqrt{k}}{\beta^* \omega} \tag{2.13}$$

The maximum edge length is chosen to return to a RANS formulation in the attached region. The destruction term in the k-equation of the SST-DES model of Strelets was modified as follows:

$$\epsilon = \beta^* k\omega \rightarrow \beta^* k\omega F_{\mathrm{DES}} \quad \text{with} \quad F_{\mathrm{DES}} = \max\left(\frac{L_t}{C_{\mathrm{DES}} \cdot \Delta}, 1\right) \tag{2.14}$$

with $C_{\mathrm{DES}} = 0.61$.

A major drawback of the DES method is the explicit grid dependency of the method. In regions where the local surface grid spacing is less than the boundary layer thickness, the limiter may become active in the attached portion of the boundary layer and induce premature and unphysical flow separation. Spalart proposed a so-called Delayed DES model [113] to overcome this problem. To avoid/reduce the grid induced separation effect, Menter [85] proposed to shield the boundary layer and use the blending functions of the SST model to formulate a zonal DES limiter. In CFX, the function F_{DES} proposed by Strelets to modify the destruction term is modified as follows:

$$F_{\mathrm{DES-CFX}} = \max\left(\frac{L_t}{C_{\mathrm{DES}} \cdot \Delta}(1 - F_{\mathrm{SST}}), 1\right) \quad \text{with} \quad F_{\mathrm{SST}} = 0, F_1, F_2 \tag{2.15}$$

$F_{SST} = 0$ recovers the Strelets model. F_1 and F_2 are the two blending functions of the SST model.

Based on both k-ϵ and k-ω models, the constant C_{DES} of the SST-DES model needs to be calibrated. Therefore a blending is used to generate the overall model constant as follows:

$$C_{\mathrm{DES}} = C_{\mathrm{DES}}^{k-\omega} \cdot F_{\mathrm{SST}} + C_{\mathrm{DES}}^{k-\epsilon} \cdot (1 - F_{\mathrm{SST}}) \tag{2.16}$$

The two constants were evaluated by Strelets as: $C_{\text{DES}}^{k-\omega} = 0.78$ and $C_{\text{DES}}^{k-\epsilon} = 0.67$.

The same numerical schemes are used for the DES model in CFX as the one suggested by Strelets: a second order upwind-biased scheme is used for the RANS region and a second-order central difference scheme is used in the LES region. This is necessary to avoid excessive numerical diffusion in the LES regions.

In the present study, the SST-DES implemented in ANSYS-CFX is used to compute the wall pressure fluctuations generated over a simplified automotive rain gutter. The focus will be put on the influence of the mesh resolution for accurate resolution of the structures but also of the wall pressure fluctuations.

b/ Scale Adaptative Simulation (SAS)

The Scale Adaptive Simulation (SAS) turbulence model was presented in 2003 by Menter and co-workers [81]. They demonstrated that a derivation of the RANS model, the SAS formulation, was able to detect the already resolved structures and to allow the evolution of a turbulence spectrum in unstable regions.

Generally, a main characteristic of all existing RANS formulations is their intrinsic dissipative nature making them insensitive to physical (flow) instabilities which could physically lead to fully developed unsteady flow, unless the instabilities are above a certain critical level as would be the case for e.g. a cylinder in cross flow. However, with regards to the fundamental similarity existing between the momentum equations resulting from the RANS and LES approaches, there is no reason for an improved RANS model not to be able to predict turbulent structures. The role of the small scales is only to take out kinetic energy from the system, therefore a detailed knowledge of the subscale structures is not necessary to solve the problem (like in the LES theory). According to Menter [81], the obstacle rests on the overestimation of the eddy viscosity level by standard 2-equations formulations in unsteady conditions. Therefore, the idea behind SST-SAS model is to add an additional production term in the ω-equation which is sensitive to resolved fluctuations. The objective of the SST-SAS model is to detect the unsteadiness of the flow and increase the production term in the ω-equation in unsteady regions while reducing k and the turbulence eddy viscosity.

When the flow equations resolve turbulence, the length scale based on the velocity gradients is much smaller than the one based on time-averaged quantities. For this reason Menter proposed to use the von Karman length scale, $L_{\nu K}$ as scale determining variable for his SAS-SST model. The ratio between the modelled turbulence length scale and the von Karman length scale is used to dynamically adjust the resolved structures in a unsteady RANS (URANS) simulation, which results in a LES-like behavior in unsteady regions of the flow field. At the same time, the model provides standard RANS capabilities in stable regions. It allows the development of a turbulence cascade up to the grid resolution into detached regions without or small grid dependency. For shear-flows, the von Karman length scale in 1D reads:

$$L \approx L_{vK} = \kappa \frac{S}{U''} = \kappa \left| \frac{\partial u/\partial y}{\partial^2 u/\partial y^2} \right| \tag{2.17}$$

where S is the absolute value of the strain-rate and $\kappa = 0.41$.

The whole development of the SAS model can be found in [82]. Here, only the relevant steps will be summarised. The starting point of the transformation process was the formulation of the two-equation $k - \Phi$ model with $\Phi = \sqrt{k}L$ and L an integral length scale. The formulation of the model based on Rotta's theory [101] revealed the presence of the second derivative of the velocity formulated as follows:

$$U'' = \sqrt{\frac{\partial^2 u_i}{\partial x_j \partial x_j} \frac{\partial^2 u_i}{\partial x_k \partial x_k}} \tag{2.18}$$

This is the relevant term around which the SAS model is built, making the turbulence length scale largely proportional to the von Karman length-scale $L_{\nu K}$. $L_{\nu K}$ is considered as a natural scale since it adjusts to the already resolved scales in a simulation and provides a length-scale, which is proportional to the size of the resolved eddies. Standard turbulence models always provide a length-scale proportional to the thickness of the shear layer. They do not adjust to the local flow topology and are therefore too diffusive.

In order to provide the SAS capability to the SST-model, the k-Φ equations have been transformed into the k-ω framework using the expression:

$$\Phi = \frac{1}{C_\mu^{0.25}} \frac{k}{\omega} \qquad \text{with} \qquad C_\mu = 0.09 \tag{2.19}$$

Consequently, the resulting SST-SAS model also benefits from the usage of the von Karman length-scale, working in pure SST mode in RANS region and activating the SAS formulation in the URANS region.

As relatively recent, the literature related application of SAS is rather limited. Nevertheless, several applications have been presented by Menter and co-workers ranging from academic cases [83] up to complete aircraft [84] and aeroacoustics of vehicle side mirrors [16]. One example of application of the SAS model to an internal combustion engine can be found in [61]. The reported applications of the model have demonstrated that the SAS-model is able to provide similar results as the SST-DES model while avoiding some uncertainties resulting from an explicit usage of the grid spacing and showing a lower grid dependency. A second advantage of SAS is its greater tolerance towards the selection of the time step as observed by Davidson [29] [30]. A comparison between LES and SAS simulations on the same grid but with different time steps highlighted the characteristic of the SAS concept to allow the model to adjust to the scales resolved by the grid and the time step and to produce turbulent structures suitable for the given resolution.

However this last point can represent a major drawback in the sense that the SAS model cannot be forced into unsteadiness by grid refinement. It has been shown that if the flow instability is not strong enough, the SAS model will simply remain in steady mode, whereas the DES model can be influenced reducing the grid spacing. In order to overcome this difficulty, Menter proposed a forcing method which will be presented later in the dissertation.

c/ Other models

A large amount of other methods or variations have been developed to compute unsteady flows. Among the most interesting, one can cite the Limited Numerical Scales model

(LNS) [9] based on a hybrid LES/RANS approach and implemented in the code CFD++. Based on this work, the group also developed a commercial aeroacoustic code (CAA++). Further details on the code and example of applications can be found on their website[1]. The mesoscopic approach introduced by the Lattice Boltzmann (LB) method represents also an interesting alternative. This method demonstrates good potential for the unsteady flow simulation but also for aeroacoustic applications[2]. Although not used in this work, these methods could also be applied to the cases investigated in this work and could be an interesting complement to the present work. The interested reader can also refer to [48] for further information on hybrid and URANS models.

d/ Synthetic turbulence

It is widely accepted that the specification of realistic (inflow) boundary conditions plays a major role in the accuracy of numerical simulations. If for RANS approaches, the description of a mean velocity and turbulence is enough, the definition of inflow conditions for LES or DNS is more difficult.

A common way to solve this problem is to use periodic boundary conditions or the results of previous simulations. Different research teams proposes to generate synthetic turbulence [63] [67] at the inflow. A basic technique to generate turbulent inflow consists in superimposing random fluctuations to a mean velocity profile. However the data generated do not exhibit any spatial or temporal correlations. Therefore filtering techniques have been developed to obtain better spatial and temporal correlations.

In addition to inflow conditions, techniques to generate synthetic turbulence have also been applied at the interface for explicit zonal RANS-LES method where the turbulence level is often too low [78].

As previously noted, hybrid models like DES or SAS may not be well suited to flows involving impingement, thin separation or indeed any region in which the local mesh undergoes an abrupt isotropic refinement and where the flow instabilities are not 'strong enough' to initiate the large-scale unsteady motions [29]. For DES, this results in the well known *grey area*, where the model switches to LES but the flow is not sufficiently resolved and the mesh behavior is undefined. In SAS this results in a steady state RANS. A way to solve this 'insufficiently unsteady' case consists in an explicit transfer of the statistically described turbulence kinetic energy into directly resolved turbulence kinetic energy. Here the generation of synthetic turbulence appears as a good alternative. Based on the work developed by Batten et al [10], Menter applied this idea and proposed a variation of the SAS model [80]. The idea is to introduce forcing terms in the momentum equations in order to transfer modelled turbulence energy into the resolved energy for flows which do not exhibit sufficiently strong instability in order to (naturally) switch to unsteady mode. A volume stochastic source term $F_{\omega_i} = \rho u_{f,i}/\Delta t$ and a corresponding sink term $F_{k_i} = -0.5\left(\rho u_{f,i}^2\right)/\Delta t$ are then respectively introduced in the momentum and k-transport equations in a confined user-specified flow region. An application of this technique will be presented in this work.

---

[1] http://www.metacomptech.com

[2] http://www.exa.com

2.3 From CFD to CAA

2.3.1 General considerations

Although ruled by the same equations, the requirements for aeroacoustic simulations can differ to those for fluid dynamics. Some of the main differences are summarised thereafter:

- Aeroacoustic problems are by definition time dependent as opposed to fluid mechanic problems which are generally time independent or involving only low frequency unsteadiness.

- Aeroacoustic problems are typical examples of multiple-scales problems and involve a wide range of frequencies. The length scale of the acoustic source is usually very different from the acoustic wavelength. The sound generated by turbulence is broadband with often three orders of magnitude between the largest and the smallest acoustic wavelengths. All these scales must be solved. The spectral resolution depends directly on the duration of the simulation. The numerical resolution of the high frequency waves represents a huge challenge to accurate numerical simulations.

- The amplitudes of acoustic waves are several orders of magnitude smaller than the average aerodynamic field amplitudes. Therefore, numerical schemes must present low numerical noise to be able to compute accurately the sound waves.

- In most aeroacoustic problems, the sound waves radiated into the far field is of interest. This implies that a solution must be uniformly valid from the source region to the measurement point at many acoustic wavelengths away. The waves must also be propagated with the correct wave-speeds. The long propagation distances impose the usage of CAA schemes presenting minimal numerical dispersion and dissipation. The numerical scheme should remain isotropic irrespective of the orientation of the computation mesh.

- The acoustic generation in fluid simulation is a non-linear phenomenon while its propagation is linear and can be described with the help of linear numerical solvers.

- Compressibility is essential in aeroacoustics while the fluid can often be considered as incompressible at low Mach number (M).

- In aerodynamics or fluid mechanics, flow disturbances tend to decay very fast away from a body or the sources. On the other hand, acoustic waves decay very slowly and reach the boundaries of the finite computation domain. The outgoing sound waves should not be reflected into the computation domain and risk to contaminate the numerical solution. Hence accurate radiation boundary conditions must be imposed at the exterior boundaries to assist the waves to exit smoothly.

2.3.2 Numerical requirements

a/ Numerical schemes

In contrast to CFD applications where generally 2nd order accuracy in space is sufficient for engineering purposes, the requirements are more stringent for CAA applications. The basic idea is to minimize the numerical dispersion (phase error) and the dissipation (amplitude) introduced by the discretisation for a chosen wavenumber range. The price to pay is a reduced consistency order of the given spatial discretisation.

The reduction of the dissipation imposes to use centered finite difference schemes. The optimization of the scheme consists then in minimizing the error between the exact wavenumber k and the effective wavenumber k_s over a large wavenumber range. The most famous CAA scheme is probably the so called DRP scheme (Dispersion Relation Preserving) proposed by Tam et Webb [118] and using a 7-point finite difference stencil. Many other numerical schemes have been proposed, see for example [18] and [20]. The resolution characteristics of some of them are represented in figure 2.3. These low dispersion and dissipation schemes allow to reduce the requirements on mesh and simulation times. The DRP scheme guarantees a 4th order accuracy of the spatial discretisation.

Different methods are here also available for the time discretisation. The most widely used is the low dissipation and dispersion Runge Kutta scheme (LDDRK) as implemented by Hu [59].

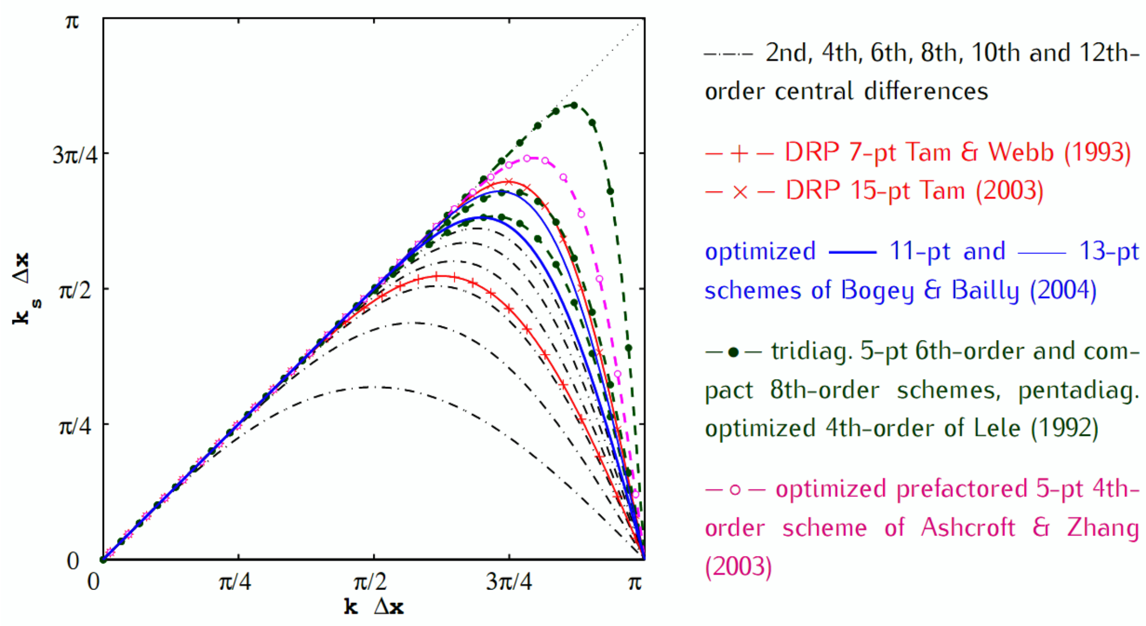

Figure 2.3: Resolution characteristics of several finite difference schemes (Representation of the wavenumber vs. the effective wavenumber)

b/ Boundary conditions

Two main types of boundary conditions are generally used in aeroacoustic: walls and external boundaries.

A wall is a non-penetration condition to which an additional condition such as adiabaticity may be added. The treatment of walls is generally done by using the concept of ghost points introduced by Tam and Dong [117]. The idea is to introduce additional nodes beyond the wall boundary (i.e. non-physical nodes typically situated inside the body). The pressure at such ghost point is evaluated so that the non-penetration condition at boundary $\vec{n} \cdot \vec{v} = 0$ is guaranteed, where $\vec{n}$ represents the wall normal vector and $\vec{v}$ the perturbation velocity vector.

In contrast the external boundaries of the domain must be able to allow acoustic waves to leave the domain without generating reflected waves. Another requirement on external CAA boundary conditions is to treat outgoing vorticity or entropy perturbations such that the generation of spurious noise sources is avoided. The radiation and outflow conditions introduced by Tam and Webb [118] can be enforced at external boundaries.

The Perfectly Matched Layer method (PML), originally introduced by Berenger [17], has become an important boundary treatment in all time-accurate numerical simulations. Originally developed for electromagnetic simulations, the principle has been extended to the simulation of many other wave propagation phenomena and was applied to the linearised Euler equations with a uniform and non-uniform mean flow [57] [58]. Finally, one can also defined a sponge layer by forcing a damping value in a defined layer attached to the external boundaries of the domain.

c/ Acoustic mesh

Generally, a mesh for fluid simulation is characterised by its high level of refinement close to the contour of the geometry in order to correctly capture the boundary layer as well as its wake. As soon as moving away from the geometry, the cells becomes quickly coarser generally with a ratio around 1.2 while so-called aspect ratios higher than 100 can be used.

On the contrary acoustic meshes must be homogeneous but also fine enough to be able to resolve the whole range of relevant wavelengths inside the whole domain without dispersion. Close to the wall, the acoustic mesh can be much coarser than the CFD mesh. It should just be fine enough for solving the smaller structures of interest and correctly representing the contour of the surface.

The cell aspect ratio is also important and must be kept as low as possible to keep a good resolution in all directions (isotropy requirement), a maximum of 10 is generally a good value. The ratio between the size of two consecutive cells must be small, 10% difference is generally a good start. To keep the isotropic character of the mesh, the smallest skewness angle of the cells must approximately be kept above 45° for quadrilateral cells. Shaping the grid cells as to be almost orthogonal to the surface of the geometry is generally good. However depending on the available grid generator, it may then happen that while smoothing, consecutive rows of cells present strong angle variations (see figure 2.4). These may introduce numerical instability. A *relaxation* of the direction of the different layers should then allow reducing this risk.

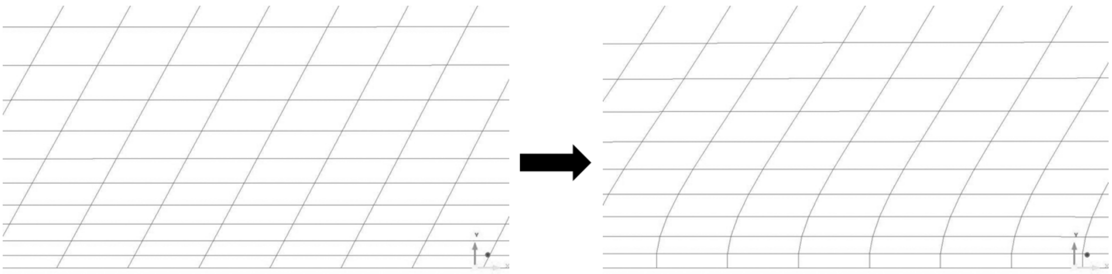

Figure 2.4: Representation of acoustic mesh before and after the smoothing

Finally cells at the external boundaries may be chosen as large as the ones in the far field using e.g. a sponge layer. Another technique consists into stretching the last 5 or 10 rows of cells in order to numerically filter the highest frequencies. A combination of both techniques is obviously possible as well.

d/ Damping and filtering

For stability reasons, very short wavelength components of the signal which cannot be represented physically correctly on a given computation grid must be suppressed. In addition the schemes used in CAA being low dissipative and dispersive, the aeroacoustic simulations are more sensitive to become unstable and divergent than CFD simulations. Hence it is generally recommended to use either artificial selective damping or filtering procedures to suppress the spurious oscillations.

Discussed by Tam et al [119], the artificial selective damping consists in introducing a sink term ($-\nu_{ASD}\widetilde{D}$ with ν_{ASD} representing the damping coefficient and $\tilde{D}$ a scalar damping operator) to the right hand side of the governing equations. The damping coefficient must be chosen in order that non-physical (purely numerically caused) components get efficiently damped while affecting the physical waves as little as possible and no numerical instability of the overall scheme is generated. A too high or too low value (due to the unsymmetrical spatial discretisation near boundaries) of the damping coefficient may lead to numerical instabilities. In some cases, one may use a so-called *Wall Damping* where the solution is only damped locally on slip walls or pre-defined damping spots for cases where the instability area can be clearly identified (e.g. sharp edges, grid singularities etc.). This method is generally used for the simulation with the DLR's CAA code PIANO (see 2.5) with a damping coefficient around 0.5.

The evaluation of the damping terms at each Runge-Kutta stage of each time step can be very time consuming and one may prefer to use a filtering procedure at distinctive time intervals instead. The solution is filtered without affecting the governing equations [107]. This method is generally faster than artificial selective damping but some adjustment must be carefully done to not deteriorate the solution. Different filters have been implemented in the code PIANO: a 6th order (N=3), a 8th order (N=4) and an implicit Pade Filter [71]. The implicit Pade Filter may be in some cases advisable although more time consuming and difficult to adjust.

2.4 CAA approaches

2.4.1 Direct approach

As acoustic fields respect also the Navier-Stokes equations, the most general approach consists in computing the acoustics in the whole domain by solving the Navier-Stokes equations for unsteady compressible flow. This approach is called Direct Noise Computation (DNC) and includes the resolution of both sound generation and propagation at the same time.

As previously discussed the disparity between the energy density of the hydrodynamic near-field and the acoustic far field represents several orders of magnitude. For subsonic flow, the energies in the far field are much smaller than those in the flow itself by a factor of $O(M^4)$, where M is the Mach number. It is then highly possible that the numerical noise due to the resolved hydrodynamic fluctuations may completely swamp the acoustic signal. In addition, the numerical cost of this approach grows with Re^3/M^4 and limits its use to very low Reynolds number and rather high Mach numbers, which in combination represent rather exotic flow problems which may be of academic use but generally not of technical interest.

Similar approaches based on LES have been used for predicting jet noise or cavity noise. The different properties of the generation and propagation of noise (linear vs. non linear, far-field vs. near-field, time dependent vs. (quasi) stationary, large vs. small spatial scale) require different trade-offs regarding computational schemes. The DNC remains currently out of reach for technically relevant flow and therefore most of computational aeroacoustic tools use nowadays are of hybrid type: sound generation due to aerodynamics is decoupled from the acoustic radiation process into the far field. This approach makes it possible to specifically tailor algorithms for both tasks.

As guidelines for a direct resolution of waves with ordinary CFD schemes, it is generally admitted that 30 iterations are minimally necessary to solve a wave and the total simulation time must be at least 10 times the period of the largest eddies. The time step is taken as $\delta t = f_{max}/30$ and the simulation real time must corresponds to $T = 10/f_{min}$, with f_{max} and f_{min} the limits of the frequency range of interest. In addition, spatially a minimum of 20 points per wavelength is necessary which limits the maximum size of the cells.

2.4.2 Hybrid approaches

As an alternative to direct methods, two-steps also called hybrid methods have been developed. In the first step, the acoustic sources are computed while the propagation of the acoustic waves in the acoustic field is computed during the second step. Two-steps methods rely on the assumption that noise generation and propagation are decoupled, in other words that the acoustic field has no impact on the flow. Aerodynamic field and acoustic field are intrinsically linked however for flows without strong aeroacoustic resonance phenomena (typically associated with self excited acoustically induced flow oscillations); one can make the hypothesis that there is no interaction between them. Different works are currently done on the interaction between the sound and structure but this does not belong to the scope of this work.

a/ Acoustic analogies

i. Lighthill's equation
Among the number of valuable acoustical analogies, the Lighthill analogy has probably a special place. It is associated with a seminal paper that almost started the era of research in aeroacoustics.

In 1952, by an exact recombination of the Navier-Stokes equations, Lighthill developed an analogy between sound generated by flows and the solution of a classical wave equation in an isentropic medium at rest, forced by appropriate volume sources. Derived from the fundamental equations of the fluid motion without any hypothesis, the Lighthill equation reads:

$$\frac{\partial^2 \rho}{\partial t^2} - c_0^2 \frac{\partial^2 \rho}{\partial x_i \partial x_i} = \frac{\partial^2 T_{ij}}{\partial x_i \partial x_j} \tag{2.20}$$

$$T_{ij} = \rho u_i u_j + \left((p - p_0) - c_0^2 (\rho - \rho_0) \right) \delta_{ij} - \tau_{ij} \tag{2.21}$$

where T_{ij} is Lighthill's stress tensor, δ_{ij} the symbol of Kronecker, τ_{ij} the viscous stress tensor p_0 and ρ_0 the pressure and density in a medium at rest and c_0 the speed of sound (typically all at large distance to the source).

The equation can be interpreted as a wave equation in a medium at rest with a source term of quadrupole nature (due to the double divergence). This concept is called *aeroacoustic analogy* as the aeroacoustic problem can be considered as analogous to an acoustic problem in a ficticious non-moving medium. As the left hand side of the equation can be identified as a wave operator, the right hand side represents the aeroacoustic sources. Three types of sources may be read from the Lighthill's stress tensor T_{ij}: the changes in flow velocities ($\rho u_i u_j$), the changes of entropy ($p' - a_\infty^2 \rho'$, for example temperature fluctuations due to combustion) and the changes in the viscous stresses (τ_{ij}).

For low Mach number applications where the flow can be considered as incompressible, the Lighthill's tensor can be simplified by noticing that the viscous effects and the entropy fluctuations are negligible in comparison to the velocity fluctuations and therefore writes as: $T_{ij} = \rho u_i u_j$.

Althought all methods from classical acoustics are immediately applicable and the solution of the aeroacoustic problem is simple, this analogy presents some drawbacks. The *source term* must be modelled. A major drawback is the loss of the physical meaning of the sources whenever convection/refraction effects on the sound wave are relevant. Sound propagation phenomena (refraction at shear- or boundary layers) appear as sources, although they are only kinetc effects.

ii. Other analogies

The Lighthill analogy was developed for free flow. Curle [28] developed an acoustic equation taking explicitly into account the effects of solid boundaries which can act as sources of noise, diffract the acoustic waves and thus change the radiation characteristic. Ffowcs Williams and Hawkings [50] extended the acoustic analogy Lighthill/Curle to the most general case of moving surfaces. On this basis, many attempts have been done to get analogies with more physical meaning.

There are two main categories of alternative analogies: those focusing on the physically appealing definition of the sources based on the vorticity of the flow such as Powell [100], Howe [56], Möhring [87] while keeping the concept of a second order (stable) generalised wave equation and those trying to eliminate as much as possible the propagation effects inherent in the Lighthill's sources term (Phillips [97] ad Lilley [73]).

iii. Implementation of Lighthill's analogy in FFT Actran/LA

A strong variational formulation of the Lighthill's analogy was derived by Oberai [92] and can be written as:

$$\int_\Omega \left(\frac{\partial^2}{\partial t^2} (\rho - \rho_0) - c_0^2 \frac{\partial^2}{\partial x_i \partial x_i} (\rho - \rho_0) - \frac{\partial^2 T_{ij}}{\partial x_i \partial x_j} \right) \delta\rho dx = 0 \quad \forall\, \delta\rho \tag{2.22}$$

where Ω is the computational volume and $\delta\rho$ the test function used in the finite elements. By applying the Green's theorem and integrating by part, one gets then:

$$\int_{\Omega} (\frac{\partial^2}{\partial t^2}(\rho-\rho_0)\delta\rho + c_0^2\frac{\partial}{\partial x_i}(\rho-\rho_0)\frac{\partial \delta\rho}{\partial x_i})dx = \underbrace{-\int_{\Omega}\frac{\partial T_{ij}}{\partial x_j}\frac{\partial \delta\rho}{\partial x_i}dx}_{\text{Volume sources}} + \underbrace{\int_{\delta\Omega=\Gamma}\frac{\partial \Sigma_{ij}}{\partial x_j}n_i\delta\rho d\Gamma(x)}_{\text{Surface sources}} \tag{2.23}$$

with $\Sigma_{ij} = \rho u_i u_j + (p-p_0)\,\delta_{ij} - \tau_{ij}$.

A volume and a surface source term can then be outlined from this equation. In case of fixed surfaces, the term Σ_{ij} is reduced to 0 and the previous equation can be rewritten in the frequency domain:

$$\int_{\Omega} k^2\rho_a\delta\rho - \frac{\partial}{\partial x_i}\rho_a\frac{\partial \delta\rho}{\partial x_i}dx = \int_{\Omega}\frac{1}{c_0^2}\frac{\partial T_{ij}}{\partial x_j}\frac{\partial \delta\rho}{\partial x_i}dx \tag{2.24}$$

where $k = \omega/c_0$ is the acoustic wavenumber and $\rho_a = (\rho - \rho_0)$ corresponds to the acoustic fluctuations of the volume mass.

This last formulation was implemented in the code Actran/LA and is solved to compute the radiated acoustic field. The two step procedure consists in firstly computing the aerodynamic sources by carrying out an unsteady CFD simulation. Spatial weight functions must generally be used to avoid the existence of spurious waves resulting from the truncation of the acoustic sources. The propagation of the acoustic waves is then computed using the finite element code Actran/LA in the frequency domain. Note that this method assumes a low Mach number, neglecting the convection and refraction effects. Typically for Mach number higher than 0.2 the Möhring's analogy is recommended and was recently implemented in the code. More information on this method can be found in the Manual of Actran [52].

b/ Perturbation approach

i. Linearised Euler Equations (LEE)

The Euler equations correspond to the general Navier-Stokes equations (2.3) with zero viscosity and heat conduction term. The hypothesis behind this simplification is that molecular viscosity/heat conductivity is negligible for the description of sound fields at moderate distance to the source. Valid also in far field, these equations can be used to compute an acoustic field. As the acoustic variations are in general much smaller than the hydrodynamic quantities, a linearised formulation of the Euler equations can be used. Considering small perturbations $(\rho', p', u_i{}')$ around a steady mean flow with density ρ_0, pressure p_0 and velocity $u_0 = (\overline{u_i}), i = 1, 2, 3$ and an ideal gas with isentropic exponent γ, the linearised Euler equations read:

$$\frac{\partial \rho'}{\partial t} + \bar{u}_j\frac{\partial \rho'}{\partial x_j} + \rho_0\frac{\partial u_j'}{\partial x_j} + \rho'\frac{\partial \bar{u}_j}{\partial x_j} + u_j'\frac{\partial \rho_0}{\partial x_j} = 0 \tag{2.25}$$

$$\frac{\partial u_i'}{\partial t} + \bar{u}_j\frac{\partial u_i'}{\partial x_j} + u_j'\frac{\partial \bar{u}_i}{\partial x_j} + \frac{\rho'}{\rho_0}\bar{u}_j\frac{\partial \bar{u}_i}{\partial x_j} + \frac{1}{\rho_0}\frac{\partial p'}{\partial x_i} = 0 \tag{2.26}$$

$$\frac{\partial p'}{\partial t} + \bar{u}_j\frac{\partial p'}{\partial x_j} + u_j'\frac{\partial \bar{p}}{\partial x_j} + \gamma p_0\frac{\partial u_j'}{\partial x_j} + \gamma p'\frac{\partial \bar{u}_j}{\partial x_j} = 0 \tag{2.27}$$

ii. Acoustic Perturbation Equations (APE)

Introduced by Ewert and Schröder [46], the acoustic perturbations (APE-4) are a modification of the linearised Euler Equations. The system solved for the pressure and velocity perturbations (p',u') in a medium with speed of sound c_0 is:

$$\frac{\partial p'}{\partial t} + {c_0}^2 \nabla.(\rho_0 u' + u_0 \frac{p'}{{c_0}^2}) = {c_0}^2 q_c \tag{2.28}$$

$$\frac{\partial u'}{\partial t} + \nabla(u_0.u') + \nabla(\frac{p'}{\rho_0}) = q_m \tag{2.29}$$

with q_c and q_m the source terms on the right-hand side. A complete formulation of the source terms can be found in [46].

Flow induced noise in cold flow is generally generated according to the vortex source term [47], therefore here the heat source contained in q_c is neglected. Also the viscous, entropy and non-linear terms are negligible for non heated flow of moderate Mach numbers. The major source term is then the Lamb vector:

$$q_m = -(\omega \times u)' = -\omega_0 \times u' - \omega' \times u_0 - \underbrace{(\omega' \times u')'}_{\approx 0} \tag{2.30}$$

A similar vortex source term appears in the acoustic analogies of Powell [100], Howe [56] and Möhring [87]. In the framework of the hybrid methods, the unsteady sound sources can be provided by an unsteady CFD method or a stochastic modelling on the basis of a RANS simulation. Altogether the APE system with the source (2.30) constitutes an acoustic analogy based on the wave operator of irrotational flow and using the vortex sound source distribution, which thanks to the nature of vorticity is a highly localised quantity in space.

Discussed in [47] the stability of the APE even for hydrodynamically unstable flows is accomplished by removing the vortical degree of freedom otherwise present in the linearised Euler equations. The APE system excludes all hydrodynamic instabilities and no CFL restriction related to spatial resolution requirement of non-acoustic modes limits the time-step. Vortex dynamics can however still be represented in the APE perturbation velocity field, but are entirely prescribed by the right-hand side source terms. Precisely, vortex sound sources on the one hand act as a direct sound source, describing the sound generation in free turbulence. On the other hand they act as a pure vorticity source in the APE enabling the description of sound generation of vorticity perturbations near edges. In [33] the analogy between the APE system and the Möhring's acoustic analogy is highlighted. The APE corresponds to the adjoint of the Möhring's equations.

As for the method developed in FFT Actran, the truncation of the sources of the APE can cause spurious sound sources which therefore must be smoothly spatially weighted. In addition the source should be gradually turned on at the beginning of the simulation to avoid an initial acoustic bang due to the sudden appearance of vorticity in the source domain.

iii. Other formulations

Further variations of the governing equations have been derived for different aeroacoustic purposes. Seo [106] for example introduces another but quite similar set of perturbation equations. Another field which is neither used in this work is the use of the Discontinuous Galerkin method (DGM) to numerically to discretise the equations and solve the aeroacoustic field [34]. For example, Bauer used the DGM to discretise the APE in combination with the RPM model [13].

c/ Acoustic sources

In framework of the hybrid methods, the unsteady sound sources can be either provided by an unsteady CFD method or by a stochastic modelling based on a RANS simulation.

i. Unsteady CFD sources

A presumably accurate noise prediction methodology to compute acoustic sources consists in computing the near field turbulence with a large eddy simulation (LES) or a direct numerical simulation (DNS). As explicitly mentioned in the Lighthill analogy, the velocity fluctuations can be used to describe the acoustic sources. Here one has to keep in mind that the results of the aeroacoustic simulations will be directly dependent on the results of the CFD. The acoustic far field is computed by solving the propagation equation such as the APE or the Lighthill equation.

ii. Stochastic acoustic sources

A direct simulation of the sources can be too time consuming to be used in a design process during which numerous evaluations of design modifications are required. Therefore one may prefer to use a stochastic turbulence model to recreate the unsteady character of the flow and to model the acoustic sources. Steady RANS simulations provide information on turbulence length scale and time scales which can be translated by empirical relations into sound source information.

From statistical noise theory, one can show rigorously that knowledge about the one- and two-point statistics of turbulent sound sources is sufficient for the prediction of the far-field spectra and directivities, see [45]. The two point space-time correlation reads:

$$R(\mathbf{x}, \mathbf{r}, \tau) = \overline{\psi(x, t)\psi(x + r, t + \tau)} \tag{2.31}$$

Steady simulation only provide one-point statistic of the flow-field. Therefore, the RANS one-point statistics have to be augmented with appropriate models for the spatial and temporal correlation functions.

Based on this assumption, many stochastic model techniques have been developed for the definition of the acoustic sources. One of the first attempts of generating artificial or synthetic turbulence was done by Kraichnan [68] and further improved by Karweit [62]. The unsteady velocity field was reconstructed in physical space from a finite sum of discrete Fourier modes. However this approach does not account for anisotropy or convection effects and is non-local in character, such that a given distribution of the statistical turbulence quantities cannot be reconstructed correctly. Bechara et al [14] followed this idea to propose the Stochastic Noise Generation and Radiation (SNGR) and to compute the noise generated by a jet. The simulation was performed in the frequency domain. They firstly computed a collection of spatial turbulent fields. Independent the turbulent signals represent a white noise in time which should be filtered to get a correct temporal correlation. This method presents two major drawbacks: firstly it requires a large memory since the turbulent velocity field should be generated and filtered in advance and secondly it still does not account for any convection effects and therefore cannot represent proper spatio-temporal correlations of the turbulence quantities. Bailly et al. [7] [6] [21] proposed some modifications to take into account convection effects. However the generated turbulent field suffered from a lack of proper time correlation. Billson proposed an extension of the model and introduce a better time-correlation between the velocity samples by using the previous velocity sample to compute the next one. Applied to the prediction of jet noise, all the methods over estimate the far field noise; especially for problems with highly non-homogeneous distribution of turbulence quantities (e.g. edge noise problems) the SNGR approach turned out to be a too crude representation of turbulence for the description of turbulence related sound sources. Smirnov et al [111] proposed a modification version of Karweit's technique which allows to generate a non-homogeneous anisotropic turbulent field. From the correlation tensor of the original flow field and length and time scales, the procedure allows to obtain a time dependent flow field (divergence free) for a homogenous turbulence and nearly solenoidale for inhomogeneous turbulence. This method was applied for initial inlet boundary generation in LES. The tensor scaling proposed by Smirnov has been used in a simplified way by Batten to compute the Reynolds-stress tensor. Batten developed the Random Fluid Generator (RFG) to generate fluid and sound sources and implemented the RFG into the code CAA++, cf [10] and [11]. One can also refer to [86] for further information on SNGR model.

Ewert proposed an alternative time-domain techniques to model unsteady broadband sound sources called Random Particle Mesh (RPM). The procedure generates fluctuating quantities, which very accurately resolve the local RANS statistics and which have Gaussian shaped correlations. In statistical approach, a widely used function to model a two point space-time correlation is based on Gaussian and exponential functions and reads:

$$R(\mathbf{x},\mathbf{r},\tau) = \hat{R} \quad exp\left[-\frac{|\tau|}{\tau_s} - \frac{\pi(\mathbf{r}-\mathbf{u_c}\tau)^2}{4l_s^2}\right] \tag{2.32}$$

The parameters τ_s and l_s define the time and length scale correlations and $\hat{R}$ denotes the mean square value of the correlated quantity for vanishing separation space r and time τ. u_c represents the convection velocity. Any to be modelled fluctuating quantity $\psi(x,t)$ is generated by spatially filtering a convecting white noise field. The RPM method generates a fluctuating vector potential by computing a spatial convolution of spatio-temporal white noise with a filter kernel. For a n-dimensional problem, it reads:

$$\psi(x,t) = \underbrace{\int ... \int_{As}}_{n\times} \hat{A}(x')G^0(|x-x'|, l_s(x'))U(x',t)dx' \tag{2.33}$$

where G^0 is a filter kernel, $\hat{A}$ is a local amplitude function, U denotes the spatio-temporal white noise field and ψ is the realised fluctuating quantity. The parameter l_s specifies the width of the filter kernel.

In 2D and for a k-ω model, the parameters $\hat{R}$ and l_s read:

$$\hat{R} = \frac{4 l_s^2 \bar{k}}{3\pi} \tag{2.34}$$

$$l_s = \frac{c_l}{C_\mu} \frac{\bar{k}^{\frac{1}{2}}}{\omega} \tag{2.35}$$

the ratio c_l/C_μ can be estimated to 6.0 [44].

After applying the spatially filtering procedure to generate the fluctuating quantities, the discrete realization of convective white-noise is made possible by the introduction of random particles on an auxiliary mesh (patch). The random particles are advanced by using an area-weighted mean of the mean-flow from neighboring mesh points. The acoustic field is then computed by solving the APE system with the stochastic sound sources. The practical implication of the model is described in [45] and [33]. Some fundamental elements will be presented in section 2.5.3.

2.4.3 Kirchhoff-Helmholtz method

An alternative approach consists in separating the computational domains in two: an acoustic source generation domain and a propagation domain. In this case, the Kirchhoff-Helmholtz method [77] or the Ffowcs Williams-Hawkings (FW-H) equation can be used to compute the far field. The idea consists in defining a surface which encloses all the sound sources and the domain in which non-linear effects are dominant. This surface can be real, i.e. identical with the surface of aerodynamic bodies or a surface inside the flow domain surrounding the aerodynamic area containing sources. This surface is then used as input to a wave equation to solve the acoustic far field (where the dynamics of perturbations is linear). Volume integrals outside the surface can also be used in the case of the FW-H equation. This method has not been used in the framework of this study but it offers a convenient method to extend the computational area of the acoustic far field.

2.5 DLR aeroacoustic code PIANO

The code PIANO is a research code permanently under construction and developed at the Institute of Aerodynamics and Flow Technology (Division Technical Acoustics) of the DLR (German Aerospace Center) in Braunschweig. The name PIANO stands as abbreviation for Perturbation Investigation of Aerodynamic NOise. Designed to compute the aeroacoustic noise generation and acoustic wave propagation in non-uniform flows, different approaches are available. The simulation concept within which the code is used is based on a given time-averaged mean flow field, less expensive and easier to handle than unsteady simulations. Initially a localised (vortical) perturbation is injected in the flow upstream of the source and the acoustic field resulting from the interaction between the perturbation and the geometry is computed by solving the linearised Euler equations in the time domain. The acoustic perturbation equations [46] and the stochastic modelling formulation [44] developed by Ewert have been implemented, increasing the capacity of the code. Three methods to model the acoustic sources are available and presented underneath (cf figure 2.5):

- Injection of a single test-vortex (pressure and entropy pulse can also be used)
- External acoustic sources
- Stochastic reconstruction of turbulence fluctuations for modelling of the APE source terms

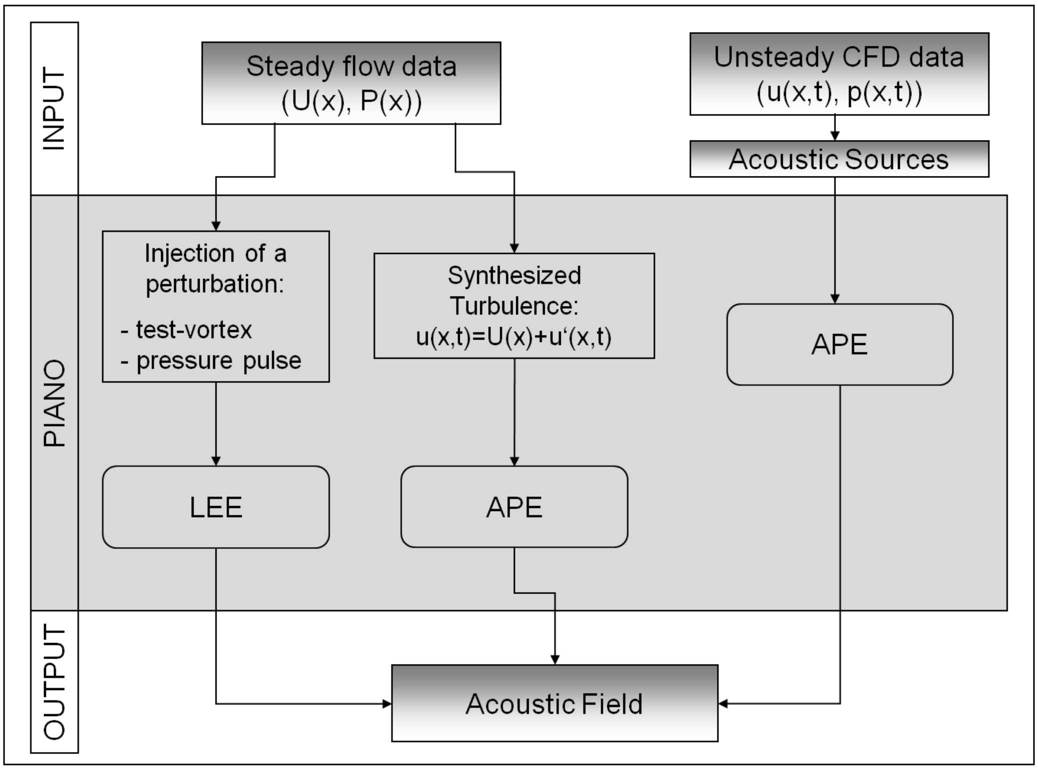

Figure 2.5: Description of the different computational strategies within PIANO

The spatial discretisation is realised by the 7-point stencil DRP scheme developed by Tam and Webb [118], while the time discretisation is done with a 4th order Runge Kutta scheme, either the classical explicit 4 or 6 stages Runge Kutta schemes or the well known low dissipation, low-dispersion Runge Kutta (LDDRK) algorithm. The users dispose of a wide possibility of appropriate boundary conditions as well as numerical damping or filtering to ensure the stability of the simulations. The code requires block structured meshes. Further information on the handling and specific functions of the code PIANO can be found in [33]. The 1st order linear interpolation of the CFD results (steady or unsteady) on the acoustic mesh is performed before using PIANO.

A non-linear version of the LEE has been developed and is available in PIANO. Considering each variable as the sum of its mean flow value and a perturbation, $\alpha = \bar{\alpha} + \epsilon\alpha'$, the non linear disturbance equations are obtained. The coefficient ϵ represents the magnitude of the disturbance (i.e. $\epsilon = 0$ corresponds to the LEE).

$$\frac{\partial \rho'}{\partial t} + u_i'\frac{\partial \rho_0}{\partial x_i} + \left(\bar{u}_i + \epsilon u_i'\right)\frac{\partial \rho'}{\partial x_i} + \rho'\frac{\partial \bar{u}_i}{\partial x_i} + \left(\rho_0 + \epsilon \rho'\right)\frac{\partial u_i'}{\partial x_i} = S_1 \tag{2.36}$$

$$\frac{\partial u_j'}{\partial t} + u_i'\frac{\partial \bar{u}_j}{\partial x_i} + \left(\bar{u}_i + \epsilon u_i'\right)\frac{\partial u_j'}{\partial x_i} + \frac{1}{\bar{\rho}}\left(1 - \epsilon\frac{\rho'}{\rho_0}\right)\left(\frac{\partial p'}{\partial x_j} + \rho'\bar{u}_i\frac{\partial \bar{u}_j}{\partial x_i}\right) = S_2 \tag{2.37}$$

$$\frac{\partial p'}{\partial t} + u_i'\frac{\partial p_0}{\partial x_i} + \left(\bar{u}_i + \epsilon u_i'\right)\frac{\partial p'}{\delta x_i} + \gamma\left(p'\frac{\partial \bar{u}_i}{\partial x_i} + \left(p_0 + \epsilon p'\right)\frac{\partial \bar{u}_i}{\partial x_i}\right) = S_3 \tag{2.38}$$

where the right hand side terms describe any external sources.

2.5.1 Single-test vortex injection approach (STVI)

Based on a steady flow simulation, the first approach consists in injecting a single-test vortex in the flow upstream the geometry. The acoustic field resulting from the interaction of the vortex (convected by the flow) with the geometry is computed by solving the linearised Euler equations. The vorticity is described by a Gaussian stream function and the corresponding velocity field:

$$\Psi = r_0 V\sqrt{\frac{e}{\ln 4}}e^{-\ln 2\left(\frac{r}{r_0}\right)^2} \tag{2.39}$$

$$r = \sqrt{(x - x_0)^2 + (y - y_0)^2} \tag{2.40}$$

$$u_1 = \frac{\partial \Psi}{\partial y} = -V\sqrt{2e\ln 2}\frac{y - y_0}{r_0}e^{-\ln 2\left(\frac{r}{r_0}\right)^2} \tag{2.41}$$

$$u_2 = -\frac{\partial \Psi}{\partial x} = +V\sqrt{2e\ln 2}\frac{y - y_0}{r_0}e^{-\ln 2\left(\frac{r}{r_0}\right)^2} \tag{2.42}$$

where V is a measure of the vortex strength, r_0, x_0 and y_0 denote respectively the length scale and the position of the perturbation vortex. Due to gradients of the RANS mean flow in the boundary layer, the corresponding pressure/density perturbation field of the initial vortex conditions cannot be specified analytically, leading to the generation of an initial artificial pressure pulse. This can be either damped or the first pressure pulse can be ignored when reading the data. The technique has already been applied to different applications such as trailing edge noise [75] [76], slat noise [38] and duct noise [114].

NOTA: when using a probe in the field with this method, the signal registered is the acoustic answer of the interaction between one vortex and the geometry. Although this vortex can be seen as a representation of the turbulence, it remains different to the real turbulence. Firstly it is only one vortex with one length scale and also because the characteristic of an appropriate test-vortex remains difficult to assess. Therefore the noise level observed during the simulation cannot be compared to experiment. When making a spectrum out of the signal, one has to keep in mind that the phenomenon is transient. However it offers good possibilities for comparing different designs. The simulation concept of this approach is related to the hypothesis, that turbulence represents a stochastic sequence of eddies (vortices) and that sound generation at edges is related to the interaction of these vortices with the edge. In this sense the consideration of one test vortex represents the elementary process of how the edge transforms vortical perturbations into sound in comparison with edges of different design.

2.5.2 Hybrid unsteady CFD / CAA approach

Proposed by Ewert [47], the method is based on the acoustic perturbation equation (APE) system with the Lamb vector as source term representing the right hand side of (2.28) and (2.29):

$$\vec{S} = (0, q_x, q_y, 0)^T, (q_x, q_y)^T = \vec{\omega} \times \vec{u} - \overline{\vec{\omega} \times \vec{u}} \tag{2.43}$$

Once computed an unsteady CFD simulation, the computed velocity fluctuations are used to compute at each time step the Lamb vector. The radiated acoustic field is simulated by solving the APE system with the computed Lamb vector as right hand side. This method was previously applied to compute trailing edge and combustion noise and will here be used to compute the broadband noise generated by a rain gutter.

2.5.3 Random Particle Mesh approach (RPM)

As seen in 2.4.2.c.ii, one can also use stochastic models to compute acoustic sources. Ewert introduces the RPM modelling in [42] as an alternative for setting up the sources in the right hand side of the APE system. In the current implementation in PIANO a source patch (i.e. an auxiliary mesh) is constructed following the paths of the mean flow streamlines. The streamlines start along an upstream seeding line to a defined downstream position. The left picture in figure 2.6 shows some streamlines over a rain gutter profile whose initial streamlines are equidistantly distributed along a seeding line. The associated source domain is depicted on the right side.

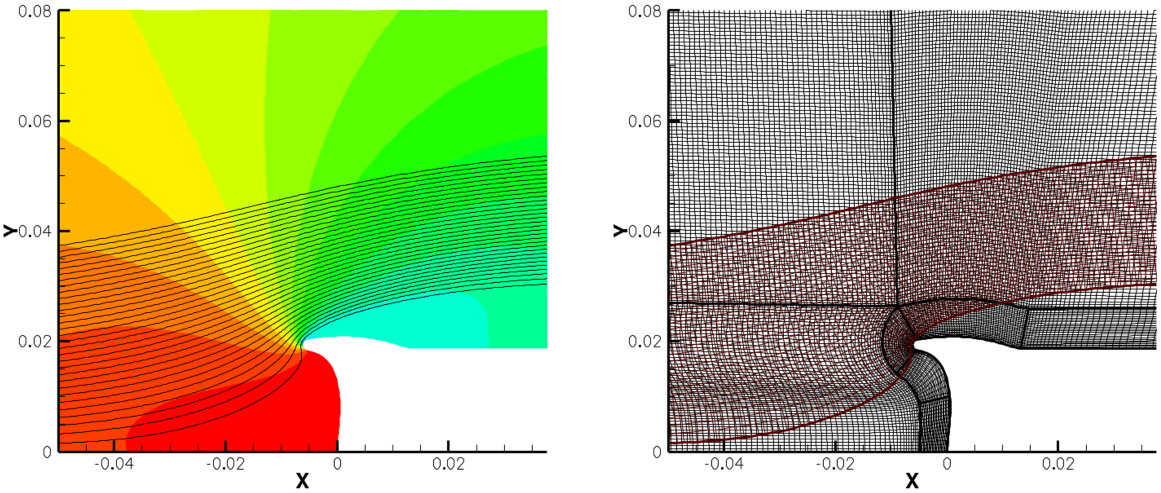

Figure 2.6: Streamlines and pressure field (left) Resolved source domain (Patch) and curvilinear multiblock CAA mesh (right)

Fluctuating quantities are then generated by spatially filtering white noise. The discrete realisation of convective white-noise is realised through the introduction of random particles along each streamline, whereby a constant drift time separation (RPM Δt) between the particles is realised. The RPM time step determines the time increment after a random particle enters or leaves the patch area. As the maximal time to reach the downstream border of a source patch depends on the consider streamline, the number of discrete particles also varies accordingly. The RPM Δt and the number of streamlines determine the total number of random particles involved as well as the size of the area surrounding each discrete particle. As a rule of thumb, the RPM Δt is generally chosen larger than five times the CAA time step. The random particles are advanced by using an area-weighted mean of the mean-flow from neighboring mesh points. The spatial filtering is realised by interpolating the random values onto the neighboring CAA mesh points and applying subsequently a sequence of 1D filtering operations [43]. The algorithm used to compute the stream functions is then:

- at each CAA time increment, the random particles are convected downstream
- if a particle crosses the downstream border, the particle is deleted and the first upstream position is updated with a new random value
- the random field is then filtered and simultaneously interpolated onto the CAA grid

The use of an intermediate source mesh allows evaluating source terms and further derivatives which are easier to compute on cartesian meshes. In addition since the mean flow field is mapped on the cartesian mesh, the propagation of particles can be computed conveniently with sufficient accuracy by mapping the local flow velocity from the surrounding hosting cell corners to the particle location.

As the synthetic turbulence model contains all turbulence scales up to the frequency cut-off of the approximative white noise-realisation used in the RPM method, there is a high chance that sound sources with too small scales to be resolved in the source region by the CAA mesh will be generated. Since these small scales could give rise to spurious acoustic waves, a length scale limiter has been introduced to restrict the resolved length scale to a smallest value being resolved by the CAA mesh. In PIANO this function is accomplished by using the effective length scale defined by:

$$l_s = \max(l_s, l_{\text{limit}}) \tag{2.44}$$

with l_s as prescribed by equation (2.35) and l_{limit} as an appropriate grid related lower length scale bound. Finally one has to define a upper and lower fade for the patch.

2.6 Concluding remarks

In this chapter an overview of different techniques and methods for CFD and CAA has been addressed in relation to the present work. Many methods with different levels of complexity have been introduced. It was shown the emergence of stochastic models to generate turbulence with mainly two purposes: either recreating more realistic boundary conditions or reconstructing turbulent sources.

Two trends are seen nowadays in the computation of aeroacoustics: either a direct computation of the noise which remains limited to low Reynolds application or the use of hybrid models based on unsteady CFD acoustic sources or on reconstruction terms. Finally the main features of the DLR's code PIANO have been presented. Two applications for internal and external flows will be proposed in the next chapters.

CHAPTER 3

Flow-induced noise in a duct containing a plate

3.1 Introduction

At low cruising speed HVAC systems (Heating, Ventilating and Air Conditioning) are generally considered as an important source of noise by car passengers. In order to continually improve passenger car acoustic comfort and to predict it as early as possible in the development, effective numerical methods are needed to simulate the noise generated by external flows as well as the noise produced by duct flows in HVAC systems.

The aim of this part is to present a first application of two fast computational aeroacoustic methods based on the Linearised Euler Equations (LEE) including 1st order non linearities and Acoustic Perturbation Equations (APE) to compute the acoustic field produced by a flat plate in a two-dimensional duct. The two methods used to investigate the noise produced are the injection of a single test-vortex in the flow and a stochastic sound source modelling both implemented in the DLR's CAA code PIANO. The other aim of this work is to assess some the major features of these two methods. The chosen configuration consists in a 2D duct containing a flat plate located midway between the duct walls and at zero angle incidence, see figure 3.1. The leading edge of the plate is round while the trailing edge is sharp.

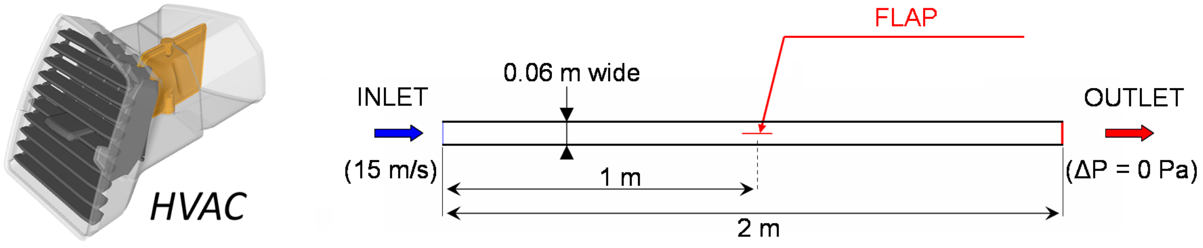

Figure 3.1: Description of the duct geometry

The generation of sound by flows around bluff bodies has been known for many years [116]. In 1955, Gerrard [54] studied for example the sound produced by the flow passing a circular cylinder and showed that the sound frequency was equal to the vortex shedding frequency. In a series of experiments on flat plate cascades Parker [94] showed that purely acoustic resonances (unrelated to mechanical vibration) may be excited by the vortex shedding process. He showed that this process does not require any mechanical vibration of the plate and corresponds therefore to an interaction between the unsteady flow around the plate and the sound field. He also found that each mode can only exist at a critical chord to pitch ratio. Each acoustic resonance is associated with a clearly defined resonant mode with observed pressure fluctuations on the order of the magnitude of the dynamic pressure. Therefore to avoid serious structural damages, the shedding frequency should not coincide with any of the possible acoustic resonance. Using a numerical relaxation technique, Parker [95] was able to compute the resonant frequencies of these acoustic modes in good agreement with experimental results.

In contrast to completely open systems where all modes are leaky (meaning exhibiting decay due to radiation loss), bodies in ducted domains may sustain so-called trapped modes; i.e. confined to the vicinity of the obstacle and almost not radiating energy. For a thin flat plate on the centreline aligned with the duct walls, the simplest acoustic and trapped mode was defined by Parker [95] as a 2D β-mode. Peak pressure amplitudes occur on the duct walls above and below the mid-chord positions while pressure nodes occur on the centre plane upstream and downstream of the leading and trailing edges, see 3.2. The acoustic velocities oscillate back and forth around the leading and trailing edges. The acoustic pressures are opposite in phase above and below the plate. When the flow velocity is adjusted so that the vortex shedding frequency coincides with that resonant frequency, a loud resonant sound level can be generated. Various methods were applied to compute for such test case the so-called Parker modes: Franklin [51] used a variational formulation, Nayed and Huddleston [89], Evans and Linton [40] and Duan [35] applied the mode matching method while Koch [64], Evans and Linton [39] and Woodley and Peak [126] used the Wiener-Hopf technique. Evans and Porter [41] showed that trapped modes could also exist above the first cut-off frequency while Duan et al. [36] extended this analysis above the first cut-off frequency for different configurations of waveguides.

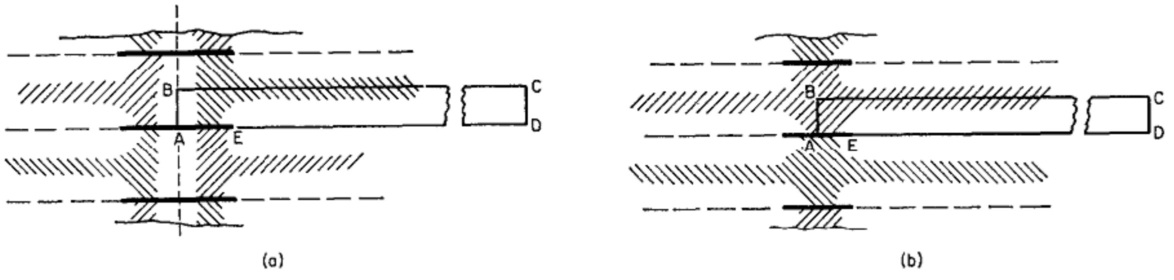

Figure 3.2: Principal two-dimensional modes: (a) Node at mid-chord (mode α); (b) antinode at mid-chord (mode β). — plates; – – nodes; |||| regions of high S.P.L. [95]

Welsh and Gibson [122] showed that only particular resonant modes were excited when a single plate was located in a duct. These modes correspond to those which have high acoustic velocities (pressure nodes) near the trailing edge of the plate. The acoustic modes with velocity nodes near the duct walls were not excited. Welsh et al. [123] analysed the effect of the flow velocity on different Parker modes in a duct and pointed out that by modifying the flow velocity, the vortex shedding frequency could lock up/down to the acoustic resonance frequency. The velocity range over which the vortex shedding is locked to the acoustic resonance frequency differs for different plate geometries (ratio chord/thickness) and of the trailing edge geometry. It was found that depending of the flow velocity, a plate with a semi-circular trailing edge locked up and down, i.e. the vortex shedding frequency was higher (respectively lower) than the corresponding natural Strouhal frequency, while a plate with a square trailing edge only locks up. Finally, by replacing the semi-circular trailing edge by a square one, they noticed a reduction of 14 dB of the sound pressure level (SPL). They also observed that the vortex being shed from the plate with semi-circular trailing edge was less intense and conclude that the vortex was absorbing less acoustic energy resulting therefore into higher sound pressure level.

3.2 Preliminary comments

In [32], some calculations on a similar test case have already been presented by the author of this work. By using the single test-vortex injection and the RPM methods introduced in the previous chapter, it was shown that resonance phenomena identified as Parker modes could be simulated with accuracy with both methods. A good agreement was found between the simulations and the analytical work done by Koch [64]. In addition the simulations performed with the single test-vortex injection method revealed the existence of a vortex street downstream the rounded trailing edge at a Strouhal number close to 0.2. It was also shown that the interaction between the β-Parker and the vortex shedding resulted in the production of further resonance. When using the RPM modelling, the vorticity was filtered by the APE system and only the acoustic modes were simulated. Depending of the length of the flat plate, it was shown that different modes with both methods acoustic modes could be simulated.

Following this paper [32], a validation experiment was built in the DLR's acoustic wind tunnel in Braunschweig. In addition, the duct was longer and narrower and the trailing edge of the flat plate was sharpened than in [32]. New numerical simulations have then been performed with this geometry and are presented thereafter. A wider range of frequencies has also been investigated and the results have been compared to the representation proposed by Duan [36].

The chapter is organised in three parts. The experimental set-up and results are firstly presented. The methods followed for the computation are then described and finally the results of the simulations are discussed.

3.3 Experimental analysis

3.3.1 Experimental set-up

The experimental tests were performed in the DLR's Aeroacoustic Wind Tunnel in Braunschweig in the framework of a student work[1]. The duct is 2 m long, 60 mm high and 210 mm wide. The section ratio is about 3.5 which allow to consider this case as 2D for the simulations. A 2 mm thick flat plate (t_p) is located midway between the duct walls with a zero incidence angle. The flat plate was fixed to the side walls of the duct. Its leading edge was round while the trailing edge was sharp. During the experiment five different oncoming flow speeds (5, 10, 15, 20 and 25 m/s) and three lengths (l_0) of flat plate have been investigated, see table 3.1. The height of the duct is denoted d_0 and the thickness of the flat plate t_p.

Table 3.1: Plate's length and chord/pitch ratio

Designation	Length (mm)	l_0/d_0	l_0/t_p
Short	39.7	0.65	19.85
Medium	78.1	1.28	30.05
Long	143.4	2.35	71.70

The noise level in the duct is measured with a free field microphone B&K 1/2″ Type 4133 mounted in a turbulence screen UA-0436[2] from B&K, figure 3.3. The turbulence screen is specially designed to attenuate the turbulence noise when measuring airborne noise in ducts or wind tunnels. The turbulence screen with the microphone is fixed on the ground of the duct and the noise is measured at 6 positions along the flow axes (0, 23, 79, 159, 339, 500 mm). The position X = 0 mm corresponds to a microphone positioned under the flat plate at about the middle of its chord. The microphone is then moved downstream.

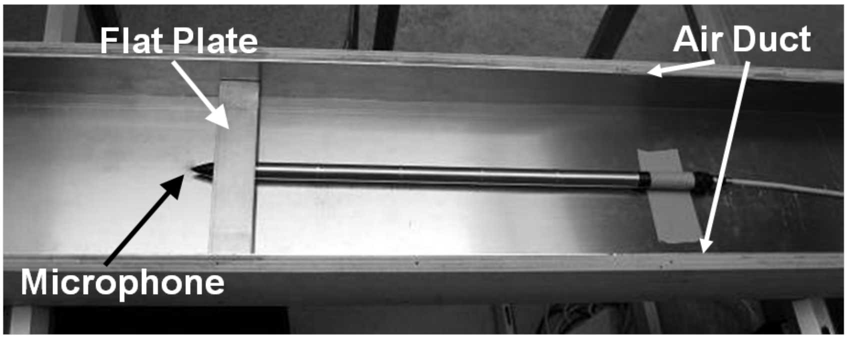

Figure 3.3: Turbulence screen positionned in the duct under the flat plate

Koch proposed an analytical formulation to predict the acoustic resonance frequencies of plate cascades restricted to low inflow speed. Duan [36] extended the work of Koch to

---

[1] G. Signoretta, *Experimental investigation of noise generation on a thin plate inside of a rectangular duct*, DLR Intern Report

[2] http://www.bruelkjaer.de/doc/bp0577.pdf

the prediction of the leaky modes, see figure 3.4. The notation (m, n) is commonly used to order the resonant modes, m denotes the number of nodal lines between the leading and trailing edge while n denotes the number of nodes between two plates. The dimensionless frequency (f^*) was defined by Koch [64] as:

$$f^* = \frac{f \cdot d_0}{c_0} \tag{3.1}$$

with f, d_0 and c_0 the frequency, the height of the duct and the sound velocity respectively.

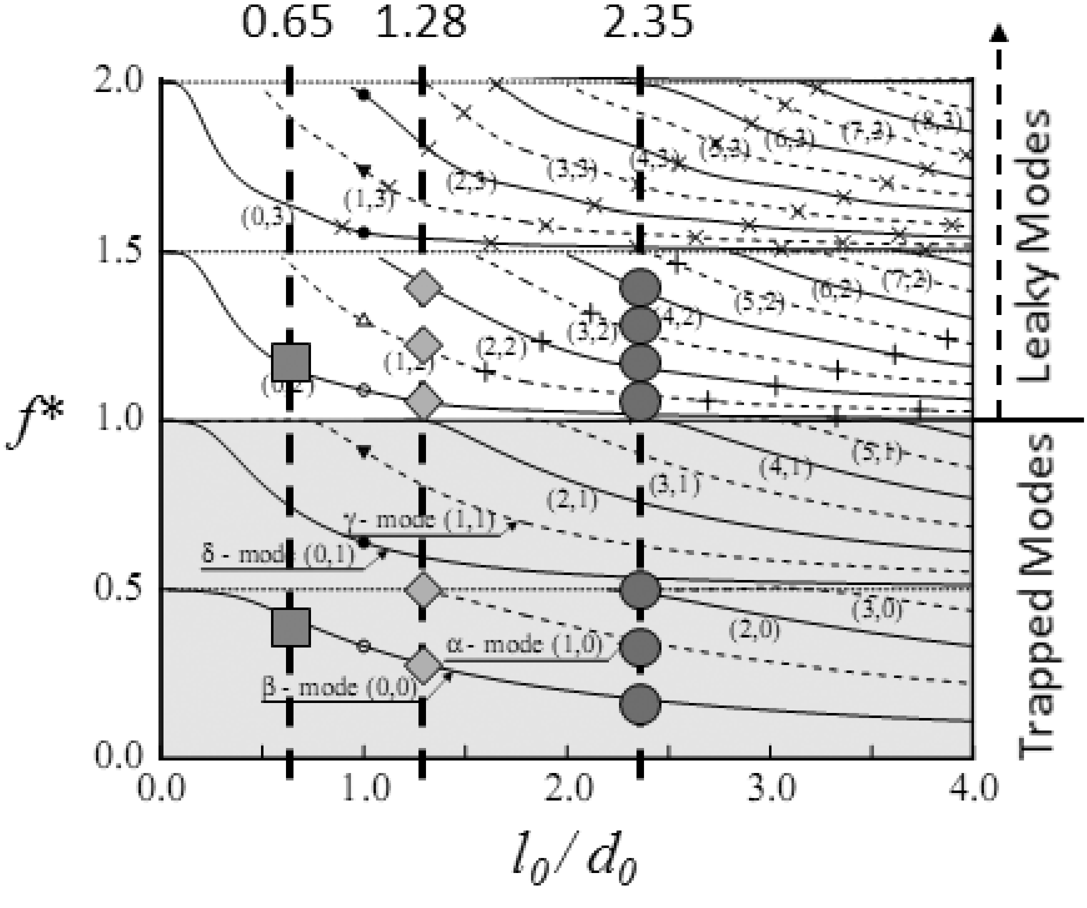

Figure 3.4: Parker mode resonances with trapped and leaky modes: the reduced frequency f^* as function of the ratio l_0/d_0 (plate's length divided by the duct's height) after Duan [36]. The shaded area marks Parker's trapped mode domain.

The frequencies of the acoustic resonances for the three flat plate lengths studied in this work may be predicted from this graph. These are gathered in table 3.2. However, as explained by Koch [64] and by Welsh and Gibbson [122], the graph was proposed for a case of parallel plate cascades. In the particular case of a single plate in a duct, the modes with an odd number of nodes between the plates do not occur. This means that no resonance modes for f^* between 0.5 and 1 are expected. Leaky modes corresponding to a dimensionless frequency f^* between 1 and 1.5 will also be numerically investigated in this work.

Table 3.2: Reduced frequency (f^*) of the Parker modes for the three considered plate's length according to Koch

l_0/d_0	β - mode	α - mode	δ - mode	γ - mode	(2,0)	(2,1)	(3,1)
0.65	0.42	-	0.74	1	-	-	-
1.28	0.28	0.49	0.59	0.8	-	1	-
2.35	0.18	0.35	0.56	0.62	0.49	0.75	0.9

3.3.2 Experimental results

The spectra obtained for different positions under the flap in the case of an inflow speed of 15 m/s and a medium plate's length are represented on the left part of the figure 3.5. Peaks at f^* of 0.03, 0.28, 0.41, 0.49, 0.57 and 0.65 can be identified. The measurements were done with only one microphone. Hence it is difficult to identify the modes from the signals. The use of several flush-mounted microphones may have been interesting to better identify the modes. However an analysis of the associated wavelengths and the use of graphs of Duan (figure 3.4) allows to identify some of them. The highest noise level was found for X = 79 mm and the lowest was found for the position further downstream (X = 500 mm). The raw experimental data were unfortunately not available anymore and it was not possible to redo them for the dissertation.

The lowest frequency ($f^* \approx 0.03$) corresponds to a wavelength $\lambda \approx 2$ m which corresponds to the length of the duct. The peaks observed at the frequencies $f^* \approx 0.28$ and 0.49 correspond to the β- and α-Parker modes. The other peaks cannot be clearly identified and should lead to further investigations but were no subject in the present work. An overall decay of - 30 dB/f^* for the microphones at X = 23 mm and X = 79 mm and of - 25 dB/f^* at 0 and 339 and 500 mm can be found from figure 3.5 (left). By examining the amplitudes for different microphone positions, figure 3.5 shows that there is a clear intensity distribution representing the respective mode structures.

Position A is located under the flat plate at 80 % of its chord. For different plate lengths, the position of the microphones was accordingly adapted. The spectra obtained at this position for three different flat plate's lengths is presented on the right hand side of figure 3.5. The number of resonances increases with the length of the plate. Without considering all the peaks, main peaks are found at f^* of 0.18, 0.35 and 0.49 for the longer plate. Peaks at f^* of 0.28 and 0.49 are found for the medium plate's length and one peak at f^* of 0.42 is found for the shorter plate. According to the prediction made by Koch, the first frequency for each length corresponds to the β-Parker mode, while the second frequency corresponds to the α-Parker mode for the two longer plate lengths and the third frequency found for the longer plate corresponds to the mode (2,0) according to their denomination.

The influence of the inflow speed on the resonance for the medium and long plate's length is presented in figure 3.6. For both lengths an increase of the inflow speed leads to an increase of the noise level. However the position of the peaks does not change with the speed which confirms that all peaks correspond to acoustic resonances. Due to the background noise level of about 42 dB, almost no peak can be identified for a inflow speed of 5 m/s.

The effect of the inflow velocity on the acoustic intensity at the resonances can be

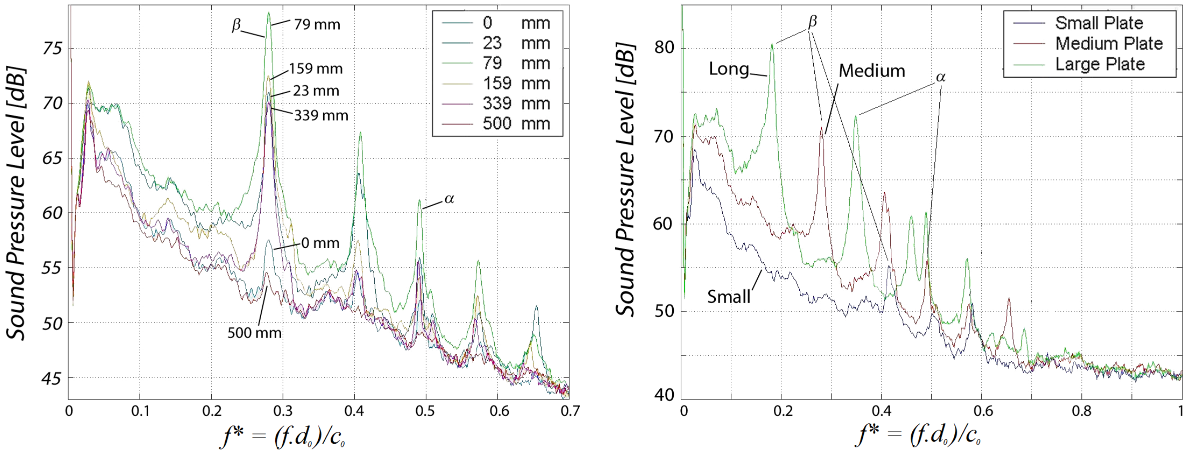

Figure 3.5: Left: Pressure level measured at different positions as function of the dimensionless frequency f^* for the case l = 1.28 d and U_{mean} = 15 m/s [X = 0 mm corresponds to middle of the plate's chord] Right: Pressure level measured at point A for different plate's lengths at U_{mean} = 15 m/s. The point A is located under the plate at 80 % of the plate's chord. d_0 and c_0 represent respectively the height of the duct and the sound velocity.

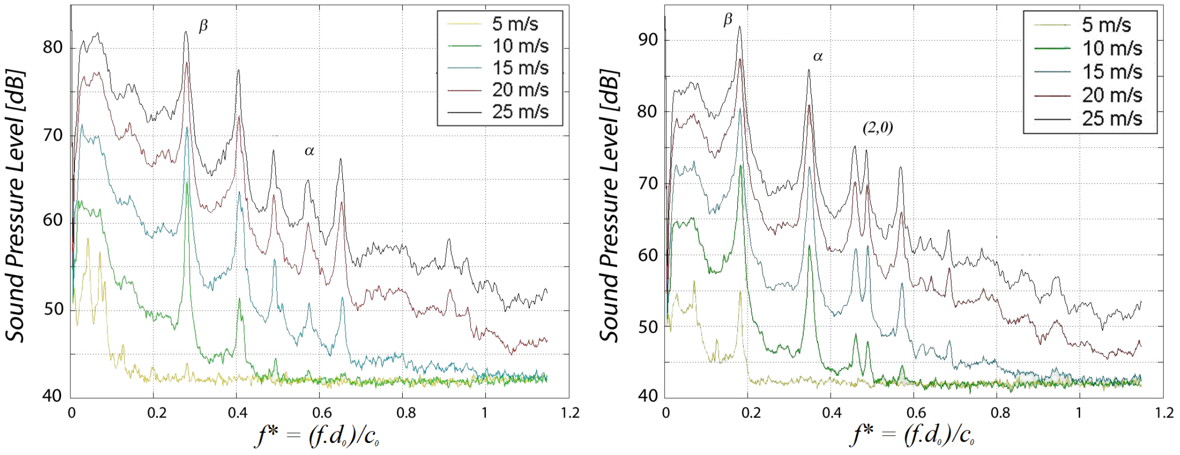

Figure 3.6: Pressure level measured at point A for different mean inflow velocities for the medium (left) and long (right) plate's lengths

quantified by plotting in a logarithmic scale the square of the pressure fluctuations (which is directly proportional to the acoustic intensity) versus the inflow velocity and defining the best fitting curve, cf. figure 3.7. One can first observe that the individual modes indeed seem to follow a well defined power law as they appear to fall onto a straight line in the logarithmic plot. Two clearly different scaling exponents were found for the β- and α-Parker modes for both plate's lengths. The acoustic intensity scales as $I_\beta \sim U^{5.3}$ and $I_\alpha \sim U^{6.1}$ for the β and α-Parker modes respectively. Interestingly, the fact that the exponent decreases for the beta mode, representing the more acoustically compact source is in contrast to aeroacoustic sound generation in free flows without resonance. The precise

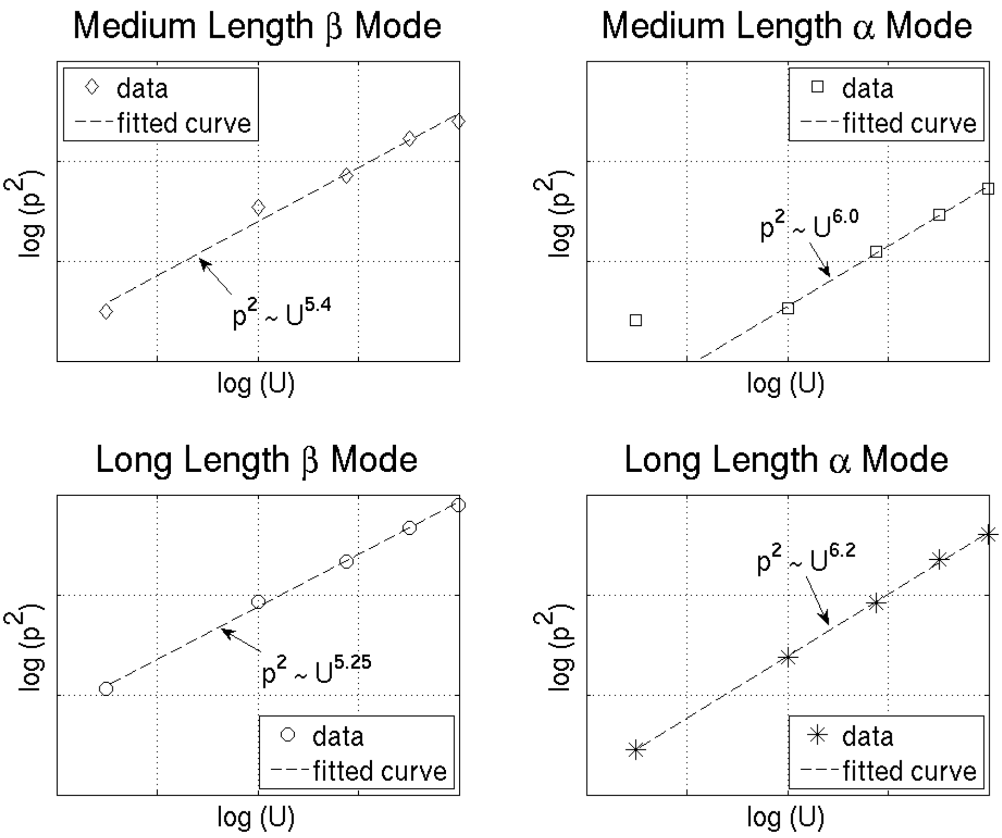

Figure 3.7: Evaluation of the scaling factor between the acoustical intensity at the β- and α- resonances and the inflow speed for the long and medium plate's lengths

reason for these values of scaling must be identified and requires further investigations.

3.4 Numerical methodology

Looking for computationally efficient methods, two methods based on steady RANS simulations have been used. The first method is the single test-vortex injection while the second approach is the stochastic turbulence modelling introduced by Ewert [43].

3.4.1 Simulation of the mean flow field

For both methods a steady state flow field is firstly required to initiate the acoustic calculation. Two CFD grids of respectively 83 000 and 175 000 nodes were used to compute the steady flow field. The main difference between both grids was the refinement level around the leading and trailing edges. In addition two different turbulence models (SST and k-ϵ) were used to compute the velocity field, see figure 3.8.

The RNG k-ϵ and SST models on the same mesh produced different results. The solution with the SST model shows a recirculation area around the trailing edge as well as some recirculation areas on each side of the plate around the leading edge. The k-ϵ shows

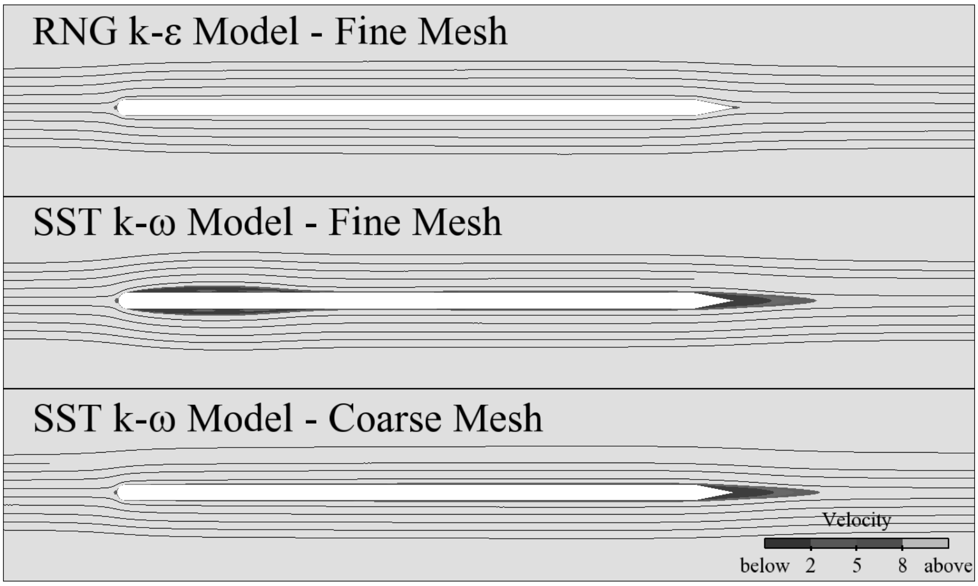

Figure 3.8: Computed Mean Flow around the Flat Plate with different CFD models and mesh refinement; $U_{mean} = 15$ m/s, values given in [m/s]

a flow completely attached around the flat plate. When using the same SST model with the coarser mesh, the same flow behaviour is found around the trailing edge however no recirculation is found around the leading edge. The mesh is not fine enough to capture the separation at the leading edge. In overall, the SST model on the fine mesh seems the more realistic. The effect of the CFD solutions on the acoustic results will be investigated in the next section. Finally, the steady flow field has been computed for four different inflow speeds. The Reynolds number based the duct's height (Re_{d_0}) and the plate's thickness (Re_{t_p}) are gathered in table 3.3.

Table 3.3: Reynolds Number (d_0 = duct width and t_p = plate's thickness)

	5 m/s	10 m/s	15 m/s	20 m/s
Re_{d_0}	19 500	39 000	58 500	78 000
Re_{t_p}	650	1 300	1 950	2 600

Furthermore two block-structured acoustic meshes have been created. The finer mesh is composed of 225 000 nodes while the coarser one has 127 000 nodes. The maximal sizes of the mesh in the area of interest were respectively 3 and 4 mm. Using a 7 stencil point spatial scheme, the maximal resolution of the mesh is then 16 and 12 kHz (e.g. f^* 2.8 and 2.1).

A linear interpolation of the steady flow field on the acoustic mesh is performed with Ensight [26].

3.4.2 Single Test-Vortex Injection method (STVI)

Based on the well known mechanism of sound generation due to the interaction of vorticity with an object, the method consists in injecting a single vortex in the flow which will generate noise by interacting with the flat plate located midway in the duct, see figure 3.9. The acoustic field is then computed by solving the LEE and derivatives thereof. The sequence of pictures illustrates the typical mechanism of sound generation and the formation of vortices behind the flat plate.

The initial vortex was positioned on the median line of the duct. Its length scale was set to $r_0 = 6.4 \times 10^{-2}$ chord length while its dimensionless strength was set to 0.1 and non-linearity parameter ϵ was set to 10% and introduced into the non-linear variant of the LEE.

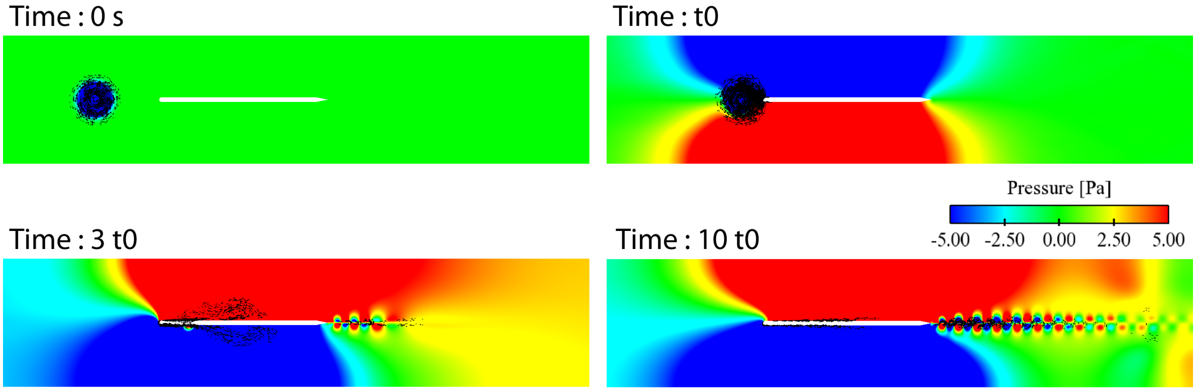

Figure 3.9: Evolution of a CAA simulation with STVI. The pressure field and velocity vectors are represented in the figure.

3.4.3 Random Particle Mesh method (RPM)

Instead of using only one vortex, one can simulate a wide range of turbulent structures with different length scales. This is the aim of the stochastic method developed by Ewert [45]. The method is based on the spatial filtering of white noise to reconstruct the noise sources over an auxiliary mesh called patch. The patch is built from the mean flow streamlines and must cover the source area (or areas). The acoustic field generated by the interaction of the unsteady turbulent sources with the geometry is then computed by solving the acoustic perturbation equations (APE).

The turbulence kinetic energy field computed with RANS is shown as first picture in figure 3.10. A snapshot and the time averaged of the reconstructed turbulence kinetic energy are presented at the top right and bottom left of the figure. A representation of the computed Lamb vector completes this figure. The patch shown in the picture at the bottom left is composed of 40×500 cells which corresponds to a representative cell size of $5 \cdot 10^{-5} \times 7 \cdot 10^{-5}\ mm^2$. Due to the symmetry of the case, only one patch positioned in the upper half plane was used. The use of patches on both sides of the trailing edge would simply result in an increase of 3 dB of the overall noise level.

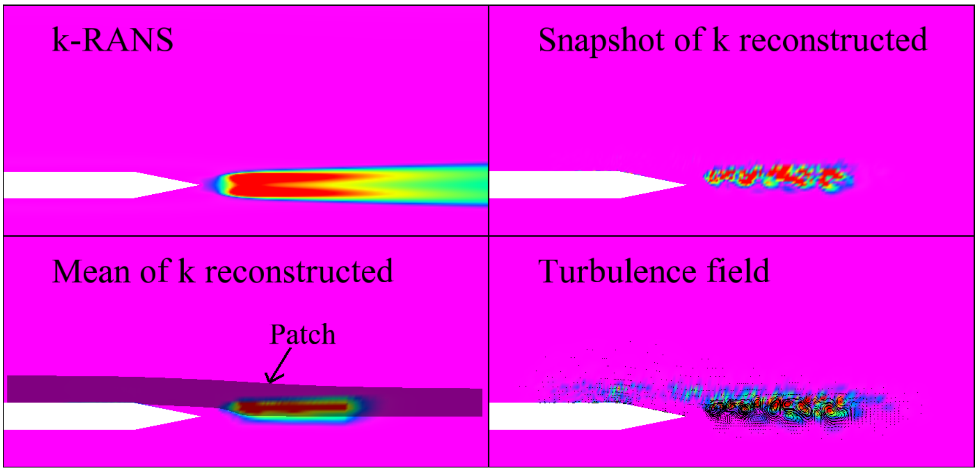

Figure 3.10: Turbulence kinetic energy computed with RANS (top-left). Snapshot of the reconstructed turbulence kinetic energy field (top-right) and time averaged reconstructed turbulence kinetic energy field (bottom-left). Snapshot of the computed Lamb vector and vortices (bottom-right). The darker area (in figure bottom-left) represents the domain covered by the patch.

3.5 Results

To study the acoustic resonances occurring in the duct, several 'virtual' probes have been defined, see figure 3.11. Point A is located 80 % of the chord length of the plate and point B is located 3.5 times the chord length behind the flat plate. The temporal signal is registered at each point. The spectra are obtained from the temporal signals by computing the power spectral density according to Welch's method [121] and using a Hanning window with an overlap of 50 %.

The results of the different simulations performed with single test-vortex injection are firstly presented followed by the results with the stochastic model. For each method the influence of some numerical and physical parameters have been studied.

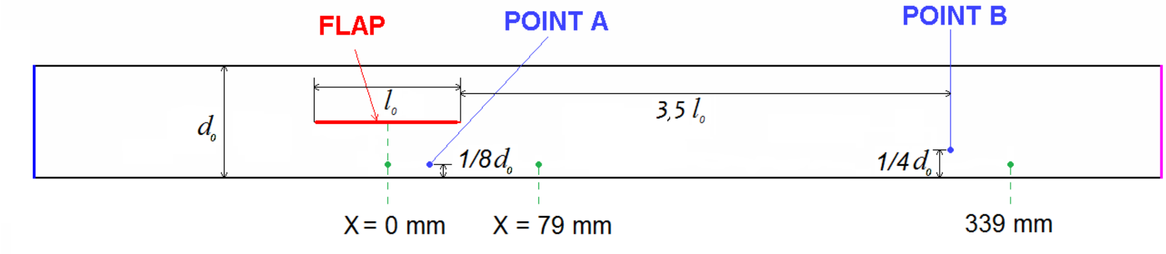

Figure 3.11: Representation of the positions of the virtual probes

3.5.1 Single Test-Vortex Injection method

a/ First observations

The results of the acoustic simulations have been produced based on the steady flow field computed with SST model and the coarser CFD mesh. The spectra for different microphone's positions are presented in figure 3.12. These spectra presents less resonances than the spectra obtained experimentally, however few peaks can be outlined for $f^* = 0.28$, 0.5, 0.85, 1.1, 1.25 and 1.43. The first two frequencies are identical to those found in the experiment and corresponds to the β and α- Parker modes. In this case, the lower noise level is found for the point further downstream in the duct while a highest noise level was found at X = 0 mm for the β- Parker mode and at X = 79 mm for the α- Parker mode. The spectra at point B confirms that the first duct cut-on frequency ($n = 1$) occurs at $f^* = 0.5$ for low Mach number (M). Above this frequency propagating waves other than plane 1D waves can exits.

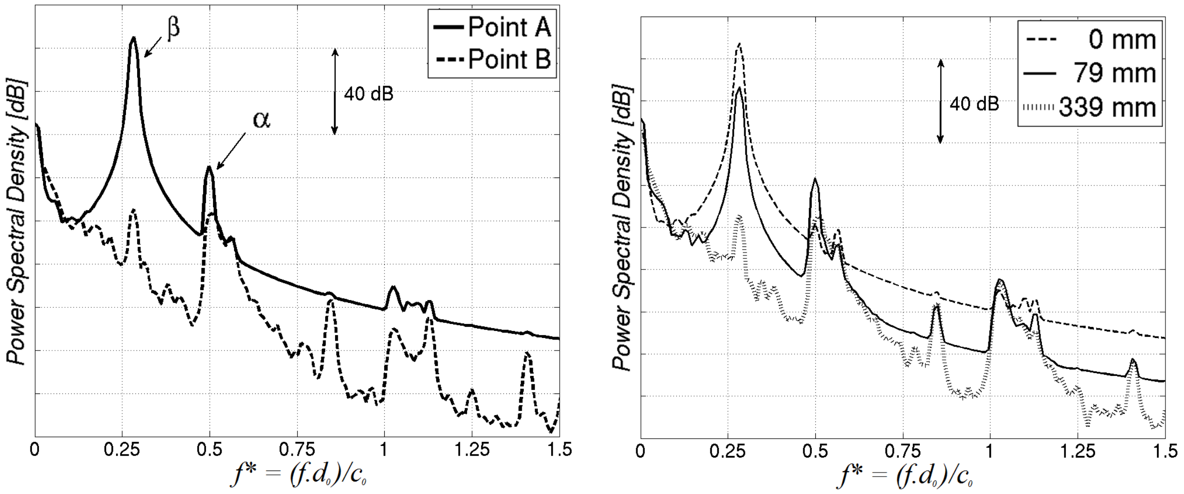

Figure 3.12: Spectra at different positions along the duct [$U_{mean} = 15$ m/s and $l_0/d_0 = 1.28$ (medium)]

Simulations performed with the coarser and finer acoustic meshes deliver similar results and it will not lead to further discussion. Nevertheless, the acoustic simulations on the finer acoustic mesh were carried out previously and the results of the simulations presented in this work are those performed on the finer acoustic mesh.

A representation of the acoustic modes can be obtained by carrying a Fourier transformation at every node of the mesh. The acoustic modes corresponding to the frequencies previously mentioned are shown in figure 3.26. The pictures **a**, **b**, **f**, **g** and **h** represent the modes β, α, (0,2), (1,2) and (2,2) as identified by Duan, cf figure 3.4. While for low frequencies (pictures **a**, **b**) no propagating modes can be seen along the duct, the situation changes for higher frequencies. Propagating (higher order duct modes) waves can be identified on pictures **c**, **d**, **e** and **f** as expected for frequencies larger than the first cut-on frequency $f_c^* = 0.5$. The wavelength (λ_x) of these propagating waves can be computed for a given Mach number (M) and a mode number (n) using the following equation:

$$\frac{\lambda_x}{d_0} = \frac{(1-M^2)}{-f^*M + \sqrt{f^{*2} - (\frac{n}{2})^2(1-M^2)}} \tag{3.2}$$

As noticed in figure 3.9, a vortex street due to the LEE develops behind the trailing edge of the flat plate with a frequency of about 1600 Hz for a mean flow speed of 15 m/s. This frequency corresponds to a value of 0.21 of the Strouhal number, defined as $St = f \cdot t_p/U$ with t_p the thickness of the plate and U the mean inflow velocity.

A simulation was also performed on the same flat plate but without duct. In this case, no resonance occurs but a short duration vortex shedding which cannot be shown in the spectrum was found by observation of some oscillations in the wake for a short time period. The vortex shedding frequency was lower in this case (1360 Hz, e.g. St = 0.18 and $f^* = 0.24$). Such observation would indicate that the considered (sharp) trailing edge is developing a self sustained *vortex street* only under the influence of an acoustic resonance (duct). The modification of the frequency of the vortex street tends to indicate that in presence of the duct a acoustic triggering phenomena happens between the vortex street and the β-Parker mode. This case is known as *gap tones* and was studied by C.K.W Tam and Ph. Morris. They explain the occurrence of a tone at the trailing edge of a slat of a high lift wing system by a combination of a wake instability behind the slat trailing edge and the main wing in its vicinity, which acts as a *reflector* of acoustic perturbations from the trailing edge. Only this feedback mechanism could explain the flow oscillation at the trailing edge and the corresponding tone. For a von Karman vortex street to occur without acoustic feedback, one needs a so called *absolute instability* in the wake. If the wake is only *convectively unstable* a mechanism is needed which feeds perturbations back to upstream the trailing edge which seems to be what happens here. A representation of the spectra obtained at the point A for simulations with and without duct around the flat

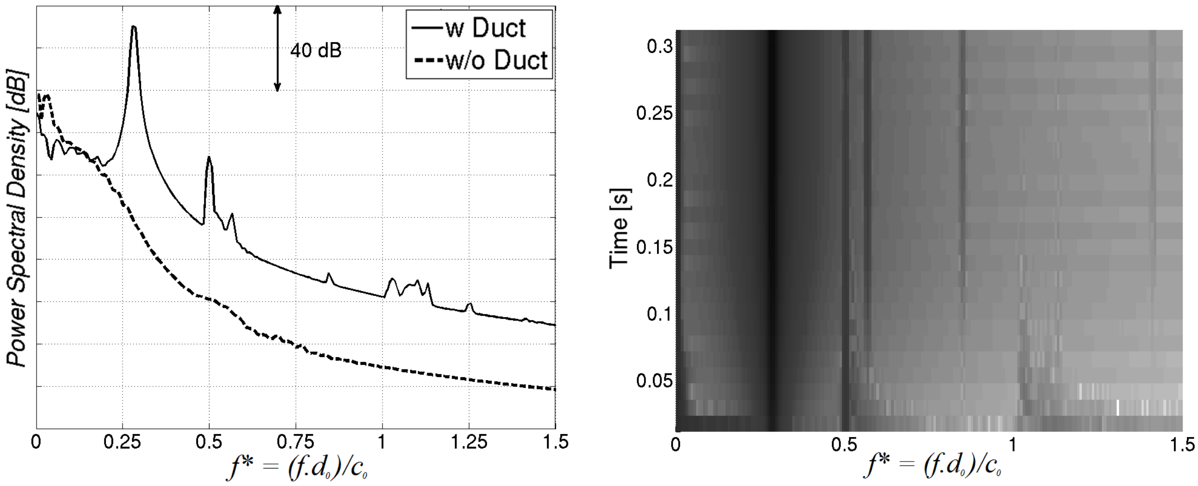

Figure 3.13: Comparison of the spectra at point A computed in both cases with and without duct (left) and computed spectrogram at point A for the configuration with the duct (right). [$U_{mean} = 15$ m/s and $l_0/d_0 = 1.28$ (medium)]

plate are presented in figure 3.13 (left). The overall noise level is lower in the case without duct and no resonance was found.

A spectrogram of the pressure signal registered at point A is presented in figure 3.13 (right). In addition to the main frequencies, one can notice that the intensities of the α-Parker mode and of the modes with a f^* slightly higher than 1 decrease over the time after the passage of the perturbation (vortex) due to radiation losses. On the contrary, the intensity of the modes associated with the vortex street and its harmonics increases for this speed (U_{mean} = 15 m/s).

b/ Study of numerical parameters

i. CFD solutions

Based on the three different computed steady flow solutions three aeroacoustic simulations have been performed with the single vortex injection method and using the same input parameters and the same acoustic mesh. The time signals and spectrum computed at point A for the three cases are plotted in figure 3.14.

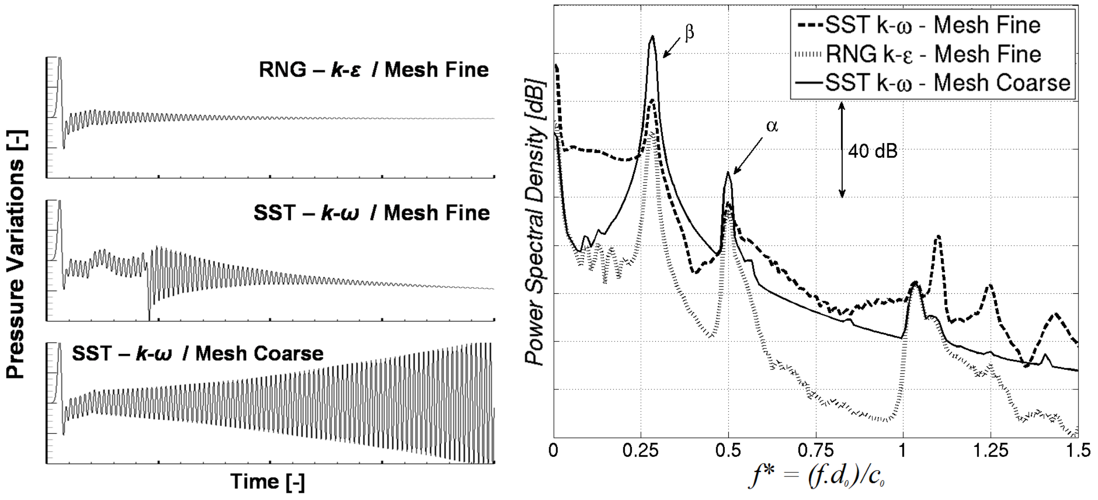

Figure 3.14: Time signal and spectrum at point A for different initial CFD solutions, [U_{mean} = 15 m/s and l_0/d_0 = 1.28 (medium)]

The time signals indicate very different behaviours although in the three cases a similar first peak is observed. This peak corresponds to the introduction of the test-vortex in the flow field. A fast decrease of the envelope of the pressure variations level is found for the simulation based on the RNG k-ϵ model. After a transient phase, the simulation based on the SST model and the finer mesh exhibits a higher level of pressure of fluctuations which quickly decrease. Instead of going back to zero the mean value of the pressure fluctuations reaches a negative value. The pressure field at the end of the simulations presents a different stable configuration as the one predicted by the CFD simulation, see figure 3.15. Further investigations should be done to clarify the mechanisms occurring in this specific case. The intensity of the signal obtained with the simulation based on the same SST model and the coarser mesh increases. In fact when letting the simulation going further, the amplitude of the pressure fluctuations reaches a maximum before to slightly decrease.

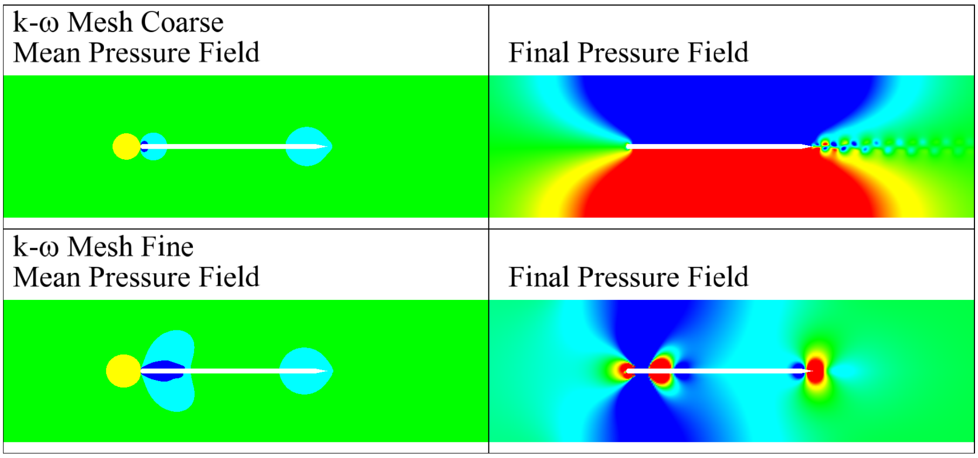

Figure 3.15: Representation of the mean pressure field computed with RANS and the computed field at the last time of the CAA simulation based on the SST model with the coarse and fine mesh at $U_{mean} = 15$ m/s

The very different shapes and the transient character of the time signals require to be careful when computing the spectrum. The first peak was removed from the time signals. The remaining signals were multiplied by a Hanning window and used to compute the spectra. Note that the STVI method was originally not done to compute spectra. The resonance occurring in the duct allow however to compute them in this specific case. In the three cases the β- and α-Parker modes are visible but with different acoustic levels. The highest levels for these both modes are found for the simulation with the SST model and the coarser mesh while after $f^* = 1$ the simulation based on the same turbulence model but with the finer mesh presents the higher noise level and three peaks above $f^* = 1$ can be identified which corresponds to the three modes identified by Duan. The simulation with the RNG model presents the lowest noise level but also the lowest number of peaks which indicates the importance of the flow simulation around the trailing edge. This study shows that although depending on the CFD solutions the main Parker modes were simulated with the same frequency in all three cases.

The deviating character of the pressure fluctuations found for the simulation based on the SST, the high noise level found for the β mode in case of the coarse mesh and the increase of the noise level found for this frequency in the spectrogram seem to indicate a coupling phenomenon occurring between the vortex shedding and the β Parker mode. In addition to the locking-up phenomenon occurring at this speed more energy from the initial vortex is also transferred to the resonance. However further investigations should be carried out to understand why the three models show so different behaviours.

ii. Effect of non-linearity

Illustrated by figure 3.16, three simulations were performed with different levels of non-linear terms included in the Euler equations. A strict use of the linearised Euler equations ($\epsilon = 0$) results in a spectrum where only the β mode raises. The noise level is also higher due to unlimited asymptotic growth in this case. The simulations with a rate of 5 % and 10 % of non-linear terms show almost identical results and allows the existence of other modes. The asymptotic formation of the acoustic sources is a non-linear phenomenon. Figure 3.16 clearly indicates that for the non-linear case the typical alternating wake oscillation occurs while in the linear case the wake remains anti-symmetric (and is thus more efficient in the noise generation). Moreover one can clearly see the occurrence of higher harmonics of the beta mode, which is of course possible for the non-linear simulation only.

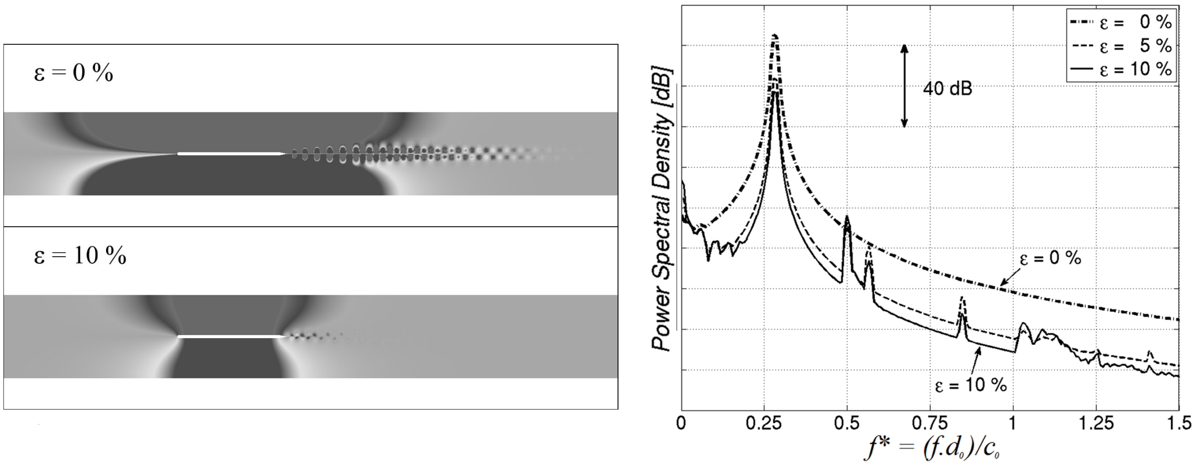

Figure 3.16: Representation of the pressure field and the spectra computed at point A for simulations performed with different levels of non-linearities included in the LEE, [U_{mean} = 15 m/s and l_0/d_0 = 1.28 (medium)]

Note also, that the spectra for the different levels of non-linearity (ϵ) lead to about the same spectra, which is expected at least in the time asymptotic behaviour. Therefore the use of non-linear terms is necessary in order to distribute the energy over all modes and not only in the first one.

iii. Magnitude and size of the initial vortex

The magnitude (V) and the size (r) of the initial vortex according to eq. (2.39)-(2.42) are chosen by the user, their values may be chosen according to following physical considerations. One can assume that the turbulence level i.e. the magnitude of the initial vortex scales with the mean flow speed. This guarantees also that for different mean flow speeds, the same absolute level of ϵ generates the same amount of non-linearity in the calculations. In addition the size of the vortex is limited by the mesh resolution. The 7-point stencil discretisation requires a minimum of 7 points to solve a vortex; otherwise the vortex may be dissipated during the simulation.

The spectra computed at point A for the simulations with different strength and size values of the initial vortex are presented in figure 3.17. An increase of the vortex's strength does almost not modify the amplitude of the β resonance, however it results in an increase of the amplitude of the α-Parker mode and of the modes with a frequency higher than $f^* = 1$, representing the second duct mode or the first "duct" mode in the space between the plate and the duct walls. The observed behaviour may be explained by the different durations of the transient phases until a fully developed (asymptotic) oscillation occurs. The excitation of the resonant system occurs due to the vortex and has to establish itself while those components of the vortex excitation, which are not resonant with the system, die out asymptotically. Obviously the strongest resonance (beta mode) is converging first, while the higher modes need more time. Especially in the high frequency domain, many degrees of freedom exist for pressure perturbations because the duct is cut on for higher duct modes. The higher the amplitude in the initial perturbation vortex, the higher duct modes get excited and correspondingly it takes more simulation time until they decay. It can be expected that the asymptotic result would be independent on the excitation. A low amplitude, the initial excitation obviously leads to a quicker converged solution.

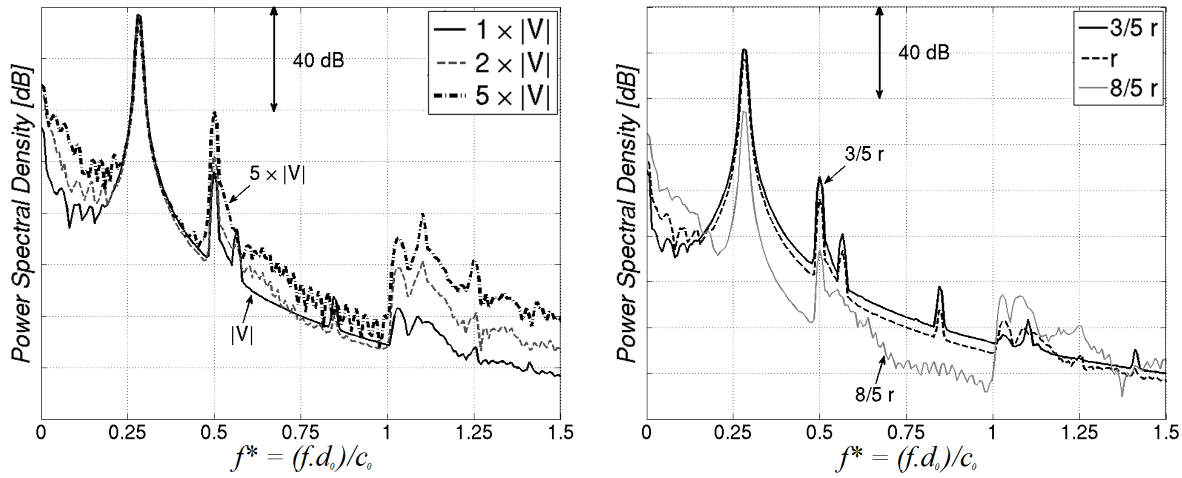

Figure 3.17: Influence of the magnitude and size of the initial vortex on the spectra observed at point A [$U_{mean} = 15$ m/s and $l_0/d_0 = 1.28$ (medium)]

A decrease of the size of the initial vortex leads to a similar result as using a small amplitude initial vortex perturbation. This may again be explained by the fact that for fixed vortex strength (V) the smaller sized vortex contains less perturbation energy as a whole and thus less non-resonant contributions need to die out before the system is free of transients. Therefore after a given computation time the simulation with the largest initial vortex size appears least converged.

Further investigation on the characteristics of the initial vortex (size, magnitude and sense of rotation) on the acoustic of a trailing edge can be found in [75]. The sense of rotation does not have any impact in this case as the geometry is perfectly symmetrical.

In conclusion, although the STVI approach appears relatively sensitive to the different parameters, it is a matter of experience to choose an initial perturbation which drives the solution as fast as possible to the fully developed oscillation. This happens preferably for small intensities of the initial perturbation vortex. Finally, this method appears mainly appropriate for carrying out A-B comparisons where few geometrical parameters change while keeping the simulation parameters fixed.

c/ Study of physical parameters

After this initial investigation all further simulations are based on the steady flow field computed with the SST model and the fine acoustic mesh. The length scale and dimensionless strength of the initial vortex are set to 5×10^{-3} and 0.1 while the non-linearity level for the LEE is set to 10%.

i. Inflow speed

The spectra computed at point A for three inflow speeds are presented in figure 3.18. The β- and α-Parker modes can be identified for the three velocities. However the overall level of the three curves is not ranked with the flow speed for the whole range of frequency as noticed during the experiment. A higher amplitude for the β mode is found for the inflow speed of 15 m/s than for the two other velocities (10 and 20 m/s).

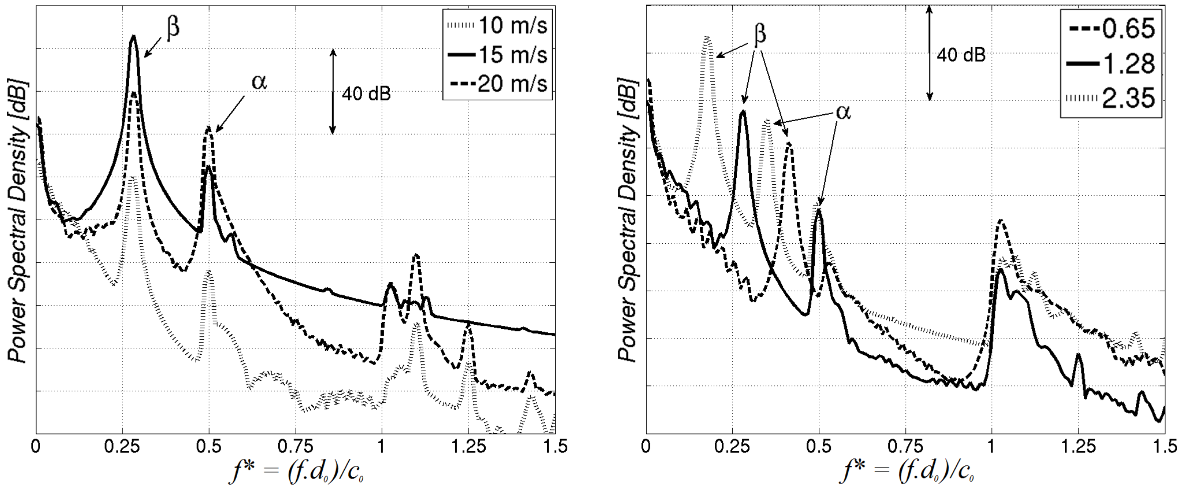

Figure 3.18: Investigation of the effect of the inflow speed (left) and of the flat plate's length (right), representation of the spectra at point A; $U_{mean} = 10\ m/s$

The pressure fluctuations for both simulations at 10 and 20 m/s decreases over time and reach zero. In addition the modes and the vortex street generated after the impact of the vortex with the leading edge disappear during the simulations. In contrast at 15 m/s, the intensity of the pressure fluctuations increases over the time due to the coupling between the vortex shedding while the β-Parker mode characterised by the same frequency. This does not occur for the other speeds, probably due to the absence of locking-up phenomena in these cases. At opposite to the spectrogram obtained for $U_{mean} = 15$ m/s the spectrogram for the cases at 10 and 20 m/s indicate a decrease of the energy level in the vortex shedding and Parker modes. The different values of the Strouhal number found for the different cases are gathered in table 3.4.

ii. Flat plate's length

To close this part on the use of single test vortex injection, the acoustic fields generated for different flat plate's lengths are investigated. For each plate length the point A is

Table 3.4: Strouhal number of the vortex shedding for different mean flow speeds

Plate's length	V = 10 m/s		V = 15 m/s		V = 20 m/s	
	f^*	St	f^*	St	f^*	St
0.65	/	/	/	/	/	/
1.28	0.15	0.17	0.28	0.21	0.30	0.16
2.35	0.18	0.2	0.18	0.13	/	/
1.68 (w/o duct)	/	/	0.24	0.18	/	/

located at 80% of the chord length. The spectra computed at point A for three different plate lengths are plotted in figure 3.18 (right) for U_{mean} =10 m/s. The frequencies associated to the different Parker modes varied also with the flat plate length. A representation of the different Parker modes computed for the different flat plate lengths is given in table 3.6. For the shorter plate, only the β mode is found while for the longer plate, the mode (2,0) is also identified. The frequencies found for the modes are in good agreement with the figure 3.4. The data displayed in the table 3.4 show that the Strouhal number of the vortex street varies with the length of the flat plate. The smaller the plate length is, the closer the Strouhal number is to the standard values of 0.2 for a cylinder.

3.5.2 Random Particle Mesh method

a/ First observations

Similar simulations as those performed with STVI have been carried out with the Random Particle Mesh (RPM) modelling. The acoustic field with the RPM modelling is computed by solving the APE system instead of the LEE as for the single test-vortex injection method. As stated before the APE system contains no vortical degree of freedom. Hence no vortex street can develop at the trailing edge. It is therefore to be expected that only modes are captured, which are due to the acoustic resonance in the duct. In order to sustain an asymptotic amplitude, the modes draw perturbation energy from the broadband flow fluctuations which are present according to the turbulent boundary layer flow past the plate.

The spectra obtained at different positions in the duct are presented in figure 3.19. Five peaks can be observed in the spectra for $f^* \sim 0.28$, 0.5, 1.1, 1.25 and 1.44. These five frequencies can also be clearly identified in the spectrogram, cf. figure 3.20. A major feature of the method is illustrated by the spectrogram: the RPM modelling produces turbulent excitations during the whole simulation and not only during the interaction of the vortex with the geometry as in the previous method. After a short transient phase at the beginning of the simulation this asymptotes into an unsteady but statistically stationary state while the resonant frequencies can be observed till the end of the simulation.

A simulation without duct was also performed and the spectrum is compared to the one obtained in presence of a duct. Both spectra show similar overall decays but no resonance occurs in the case without duct. The broadband floor of the spectrum decays with about - 25 dB/f^* which is similar to the value found for the experiment.

Maps of the acoustic field are presented in figure 3.27. These representations allow identifying the different modes. Therefore, the pictures **a**, **b**, **d**, **e** and **f** correspond to the

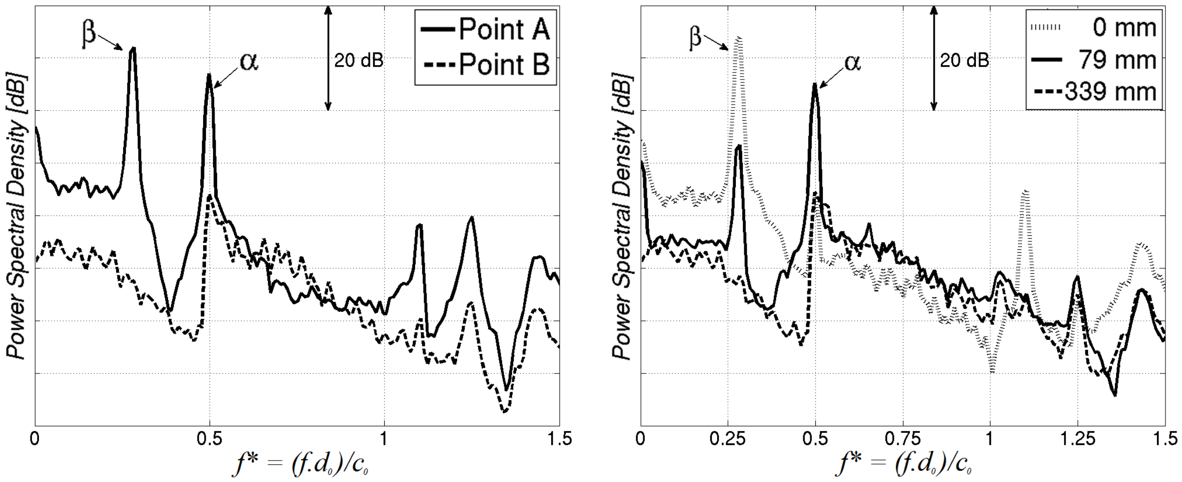

Figure 3.19: Spectra at different positions along the duct [$U_{mean} = 15$ m/s and $l_0/d_0 = 1.28$ (medium)]

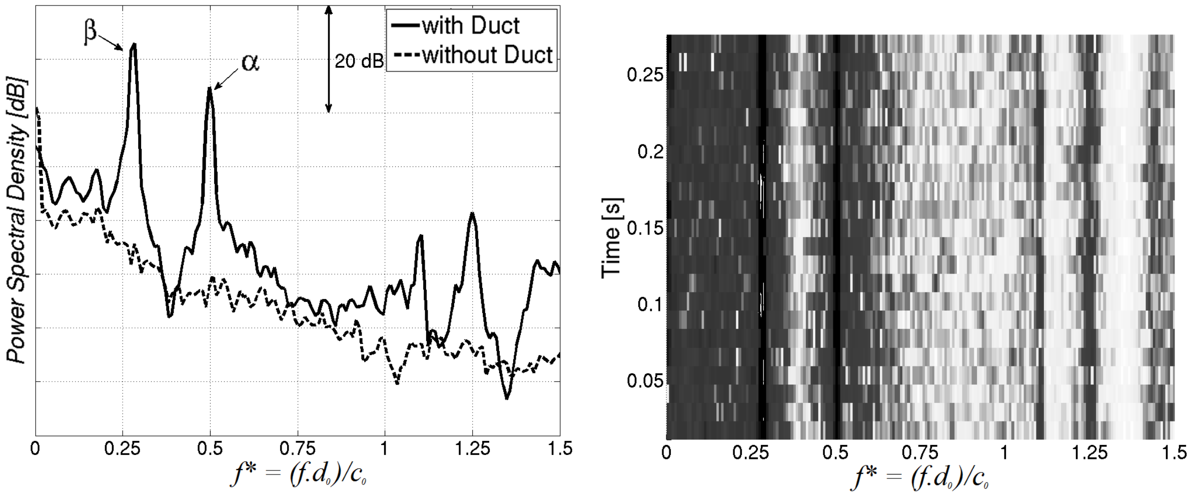

Figure 3.20: Comparison of the spectra at point A computed in both cases with and without duct and computed spectrogram at point A (right). [$U_{mean} = 15$ m/s and $l_0/d_0 = 1.28$ (medium)]

modes β, α, (0,2), (1,2) and (2,2) as identified by Duan, cf figure 3.4. Propagating waves can be identified in picture 3.27.c.

b/ Study of numerical parameters

i. CFD solutions

Aeroacoustic simulations based on CFD simulations with three different turbulence models have been performed. Almost identical spectra are obtained for both SST simulations with fine and coarse meshes as shown in figure 3.21. A similar spectrum at point A is obtained with the k-ϵ simulation but the curve seems shifted by about 20 dB. The CFD results show that the level of kinetic energy generated by the k-ϵ model is higher at the back of the trailing edge. Hence a higher turbulence level is reconstructed by the RPM modelling which explains the higher noise level. The over prediction of the turbulence level is a well known drawback of the k-ϵ model which is essential to control in the reconstruction model since the RPM modelling is based on the turbulence kinetic energy and the turbulence length scale.

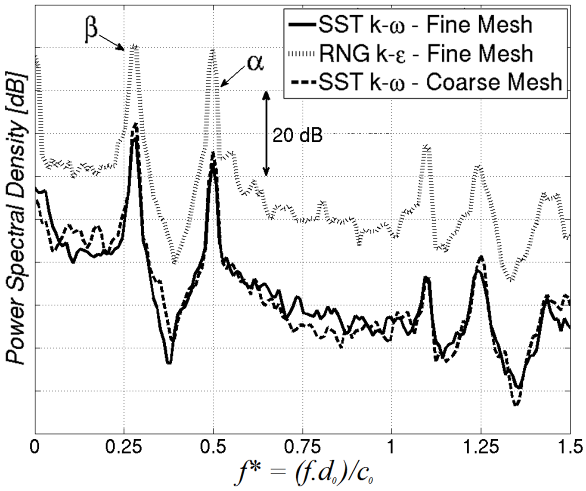

Figure 3.21: Spectra computed at point A based on different CFD simulations, [U_{mean} = 15 m/s and l_0/d_0 = 1.28 (medium)]

ii. RPM parameters

The main parameters of the RPM model are the time step between the generation of two particles (called RPM-dt) and the limiter length scale (l_{limit}). The limiter length scale defines the lower limit of the reconstructed turbulence structures. The upper limit of the length scales of the reconstructed turbulence is taken from the patch on which the value of the turbulent kinetic energy computed by the RANS simulation have been interpolated.

Different values of the RPM time step and RPM length scale have been used to evaluate their effect on the resonances. The resulting spectra computed at point A are gathered in figure 3.22. The computed spectra are almost identical and the resonances are predicted at the same frequencies. The RPM time step only affects the high frequencies. At high frequencies the amplitude of the resonance increases when increasing the time step while the amplitude of β- and α-Parker modes are hardly changed. Concerning the RPM limiter hardly no differences are found when using a value between 5×10^{-5} and 5×10^{-4}. A higher value of the limiter leads to an increase of the amplitude of most of the resonances but remains however limited.

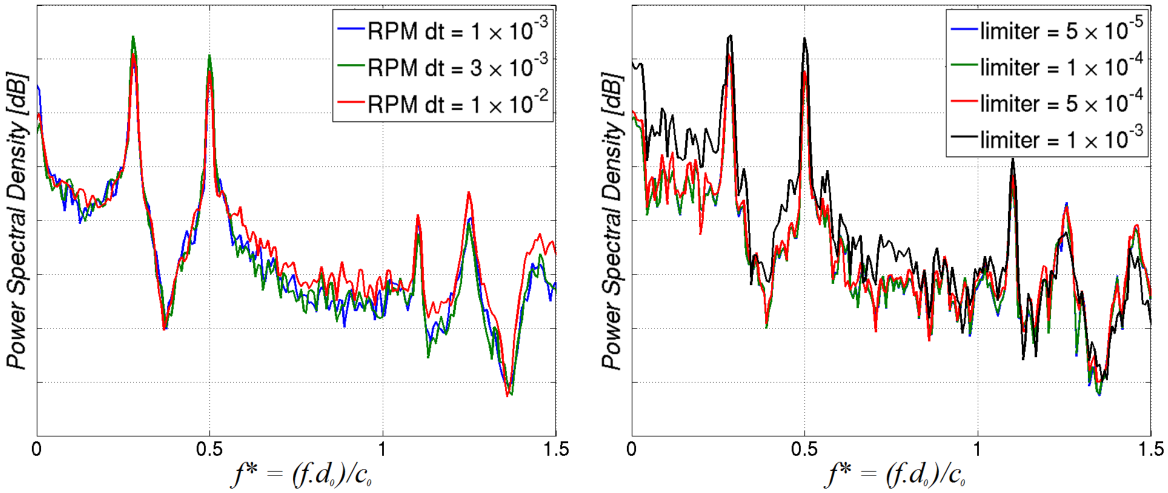

Figure 3.22: Effect of the RPM time step (left) and RPM limiter (right) on the spectra computed at point A; $U_{mean} = 15$ m/s and $l_0/d_0 = 1.28$ (medium)

c/ Study of physical variations

i. Inflow velocity

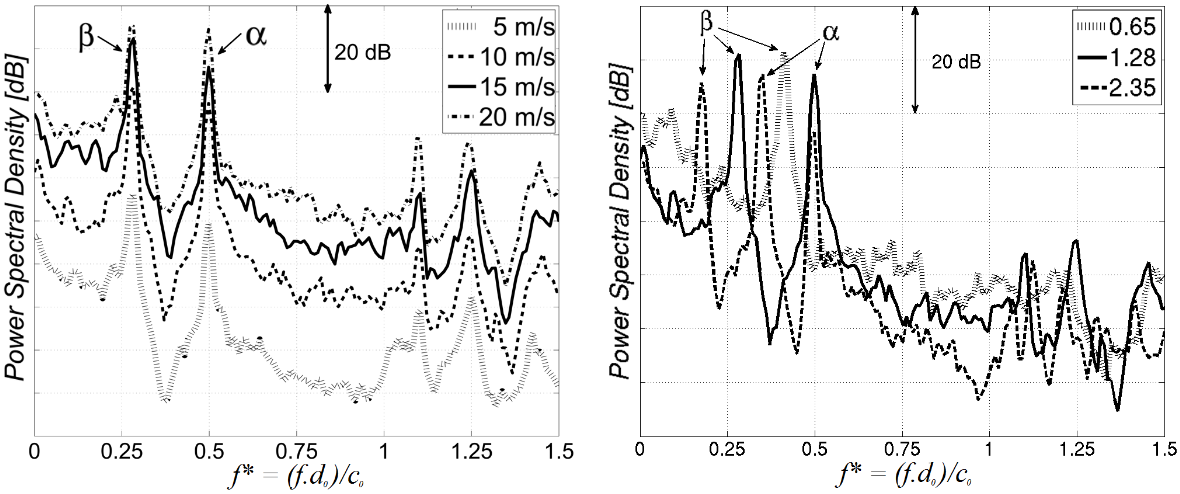

Figure 3.23: Effect of the inflow velocity (left) and flat plate length (right), spectra computed at point A; $U_{mean} = 15$ m/s and $l_0/d_0 = 1.28$ (medium)

Four different inflow speeds have been tested for the test case with the medium flat plate length. The spectra computed at point A for each speed are in ranked with the speed, see figure 3.23 (left). The higher noise level is found for the higher velocity like for the experiment. Based on the results of these simulations it was found that the amplitude of the β- and α-Parker modes scales as $I_\beta \sim M^{6.5}$ and $I_\alpha \sim M^{7.2}$. As by the experiment, the α mode is scaled with a higher factor than the β mode. The difference between the scaling factors found for the experiment and the simulations may come from the 2D character of the simulation. Note that the APE system contains no vortical degree of freedom, thus coupling effect between the vortex street and the Parker modes is excluded.

ii. Flat plate's length

The spectra computed at point A for the 3 different plate lengths are plotted in figure 3.23 (right). The frequencies associated with the different Parker modes varied with the flat plate length and the different Parker modes computed for the different flat plate lengths are represented in table 3.7. Similar modes were found as with the single test-vortex injection method.

The effect of the different parameters study in this part are gathered in table 3.5.

Table 3.5: Sum-up of the parameter studied carried out for the simulations performed with the RPM modelling

	β-mode		α-mode	
Increase of	Freq.	Ampl.	Freq.	Ampl.
RPM time step	-	$\sim$	-	↗
RPM limiter	-	↗	-	↗
U_{mean}	-	↗	-	↗
length l_0	↘	↘	↘	$\sim$

3.5.3 Further results: influence of the trailing edge

As a last comparison, the effect of the trailing edge was investigated. A comparison between the acoustic field generated by a flat plate in a duct with a rounded and sharpened trailing edge is proposed in figure 3.24. The two methods were applied for both configurations with an inflow speed of 15 m/s. The spectra computed with the single test-vortex injection method and the RPM modelling are presented in figure 3.25.

With the single test-vortex injection method, the β and α Parker modes are in both cases identically computed. However since the vortex street is characterised by the same frequency than the β Parker mode, harmonics are also found in the rest of the spectra. An overall higher noise level is predicted in the case with the rounded edge. The rounded trailing edge generates a von Karman vortex street even without the acoustic feed back of the Parker modes. This strongly (absolutely) unstable wake instability dominates the resonance and thus produces stronger higher harmonics compared to the plate with sharp trailing edge. In the latter case the acoustic feedback is required to sustain the oscillation.

The spectra computed for the simulations with RPM modelling are very similar for both configurations as can be expected. Interestingly, the amplitude of the β-Parker mode is increased by about 10 dB for the rounded edge configuration, just as for the single test-vortex method; moreover the α mode seems to stay independent of the trailing edge shape no matter which simulation method is used. The fact that the beta mode's amplitude is stronger for the rounded trailing edge is reasonable insofar as it is known that a) rounded edges generally convert more vortical perturbations into sound and b) the turbulence kinetic energy behind blunt bodies is generally higher than for sharp bodies, thus generating higher amplitudes.

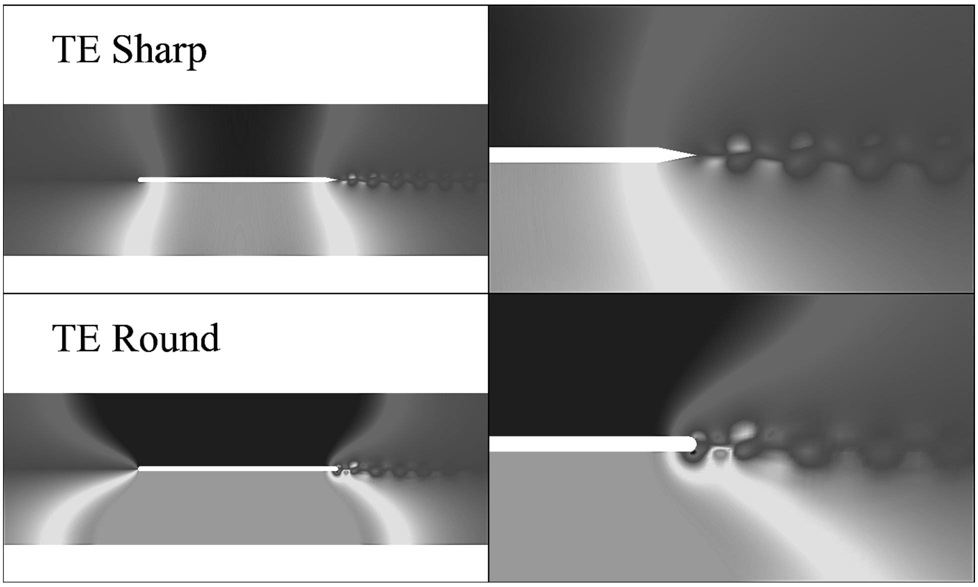

Figure 3.24: Comparison of the pressure field computed with a sharp (top) and a round (bottom) trailing edge

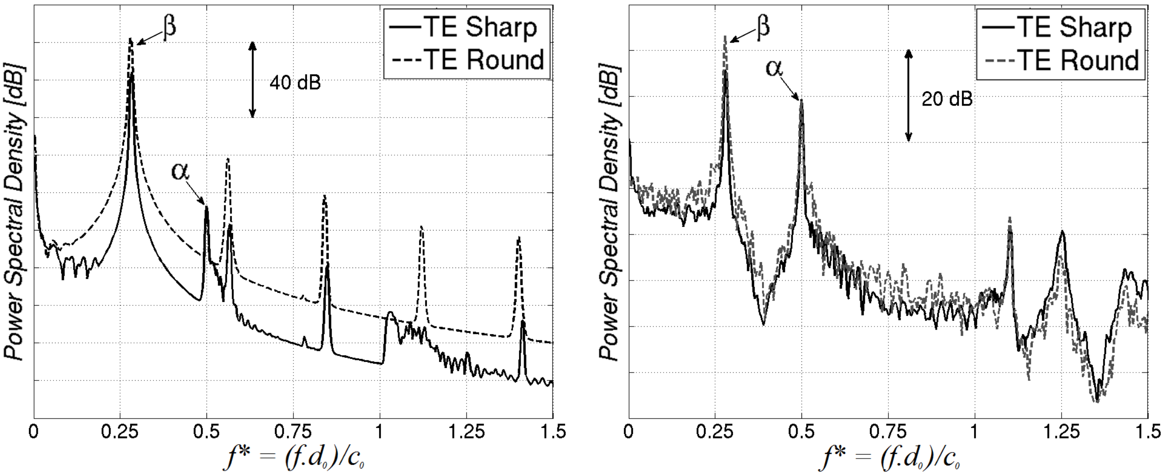

Figure 3.25: Comparison of the spectra observed at point A with sharp and rounded trailing edge computed with single test-vortex injection (left) and RPM method (right), $U_{mean} = 15$ m/s

3.6 Concluding remarks

A first application of two aeroacoustic methods based on steady RANS solutions has been proposed. The acoustic field produced by the flow in a duct with a flat plate positioned midway is studied by using the test-vortex injection method and the RPM modelling. Experimental and computational results have been presented. As demonstrated by Parker, purely acoustic resonance can occur even in the absence of mechanical vibrations. This work demonstrates that resonance phenomena identified as Parker type modes could be found experimentally and shows the ability of both numerical methods to simulate with accuracy these resonances. The frequency and mode representation computed by both methods are in good agreement between them but also with the analytical work done by Koch [64]. Both experiments and numerical simulations show the influence of the flat plate's length on the frequencies of the acoustic modes in agreement with the prediction of Koch.

It was shown that the test-vortex injection method allows to simulate the resonances although originally it was not made for it. The method delivers an answer to an impulse which in absolutely unstable flows or convectively unstable systems with acoustic feedback excites self sustained oscillations. Only short duration spectra should be evaluated for this computational approach and therefore a comparison between the results must be done carefully. The method was actually developed for an A-B comparison while using the same input parameters and it demonstrates its ability to deliver good results in this case. On the contrary the RPM model provides temporal signals which can be used for computing spectra. The method appears also less dependent of numerical parameters and less sensitive to instabilities. The RPM delivers results in good agreement with experimental and analytical data.

The studied geometry corresponds to a simplified version an automotive air duct. The methods could be further used to investigate the acoustic field in a real 3D automotive air duct.

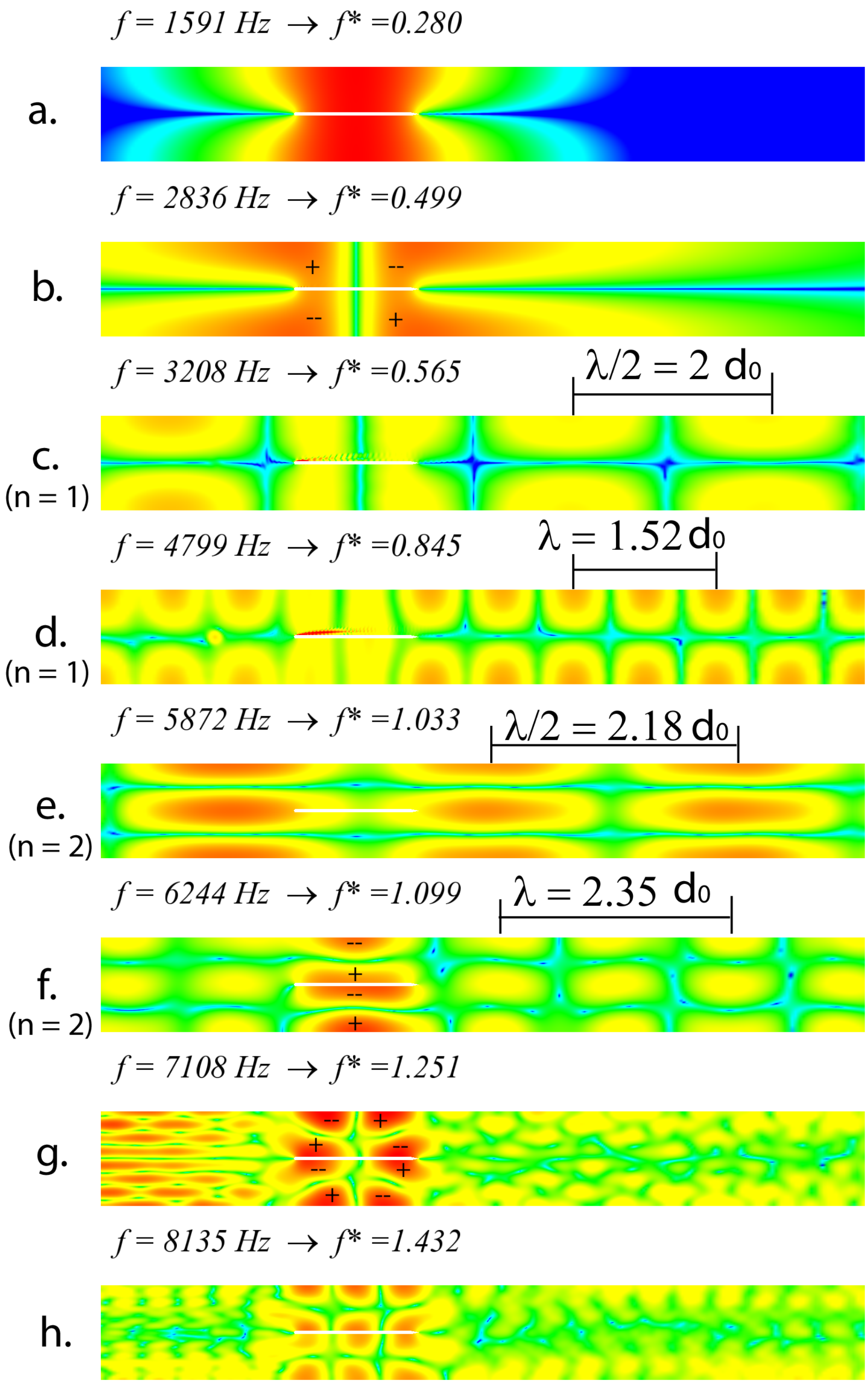

Figure 3.26: Pressure amplitude in the flow field for chosen frequencies computed with the single test-vortex injection method; $U_{mean} = 10$ m/s and $l_0/d_0 = 1.28$ (medium), the colour map differs from picture to picture. Pictures a and b correspond to the β- and α-Parker modes.

Short length (β mode)
f = 2354 Hz ⟶ f* = 0.414   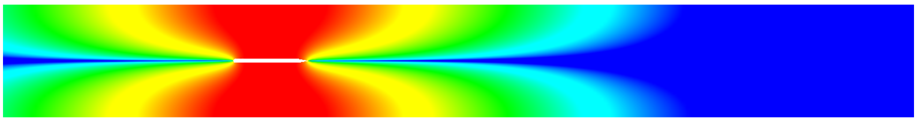
Medium length (β and α modes)
f = 1600 Hz ⟶ f* = 0.282   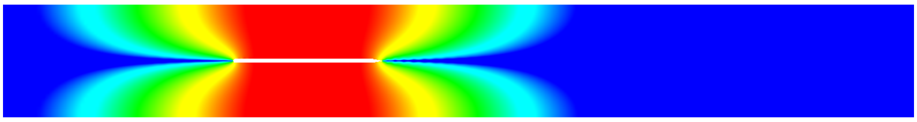   f = 2836 Hz ⟶ f* = 0.499   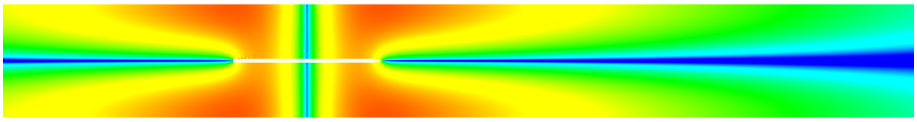
Long length (β, α and (2,0) modes)
f = 1009 Hz ⟶ f* = 0.178   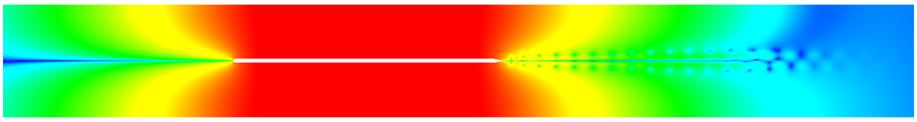   f = 1981 Hz ⟶ f* = 0.349   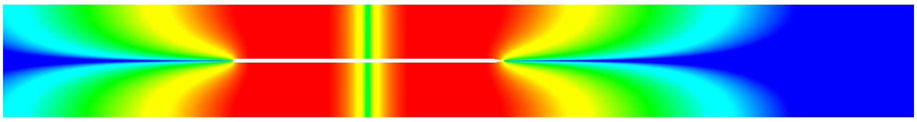   f = 2799 Hz ⟶ f* = 0.493   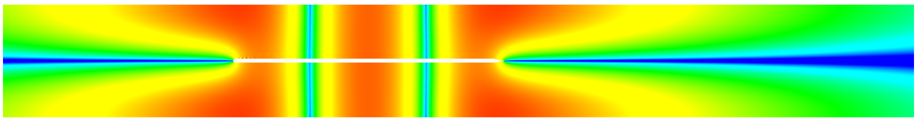

Table 3.6: Pressure amplitude of the Parker modes for different flat plate's lengths computed with single test-vortex injection method [U_{mean} = 10 m/s]; the colour map differs from picture to picture.

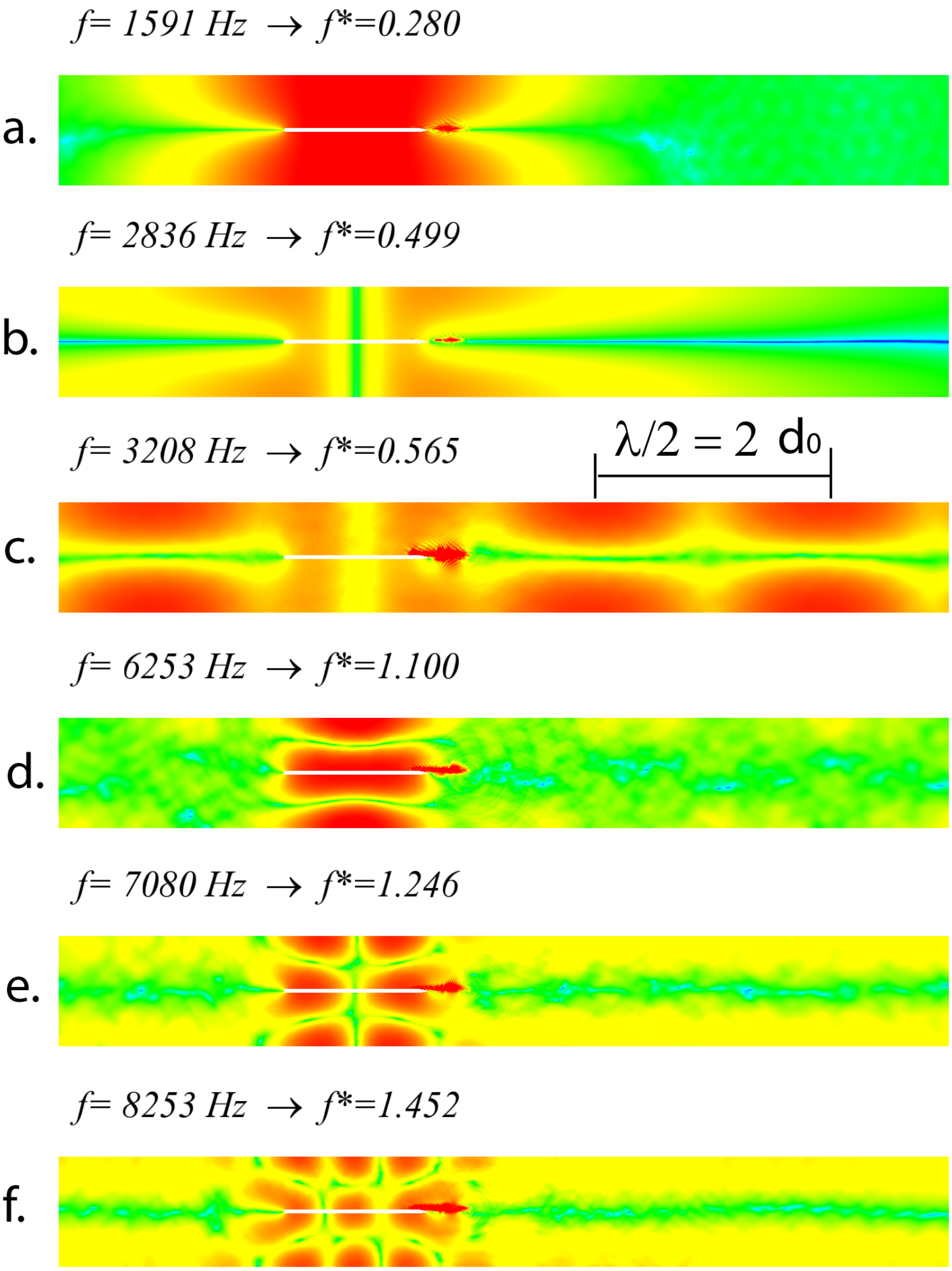

Figure 3.27: Pressure amplitude in the flow field for chosen frequencies computed with RPM modelling [$U_{mean} = 15$ m/s and $l_0/d_0 = 1.28$ (medium)]; the colour map differs from picture to picture.

Short Length (β mode)
f = 2354 Hz ⟶ f* = 0.414
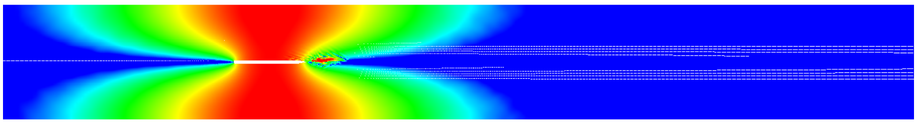
Medium Length (β and α modes)
f = 1591 Hz ⟶ f* = 0.280
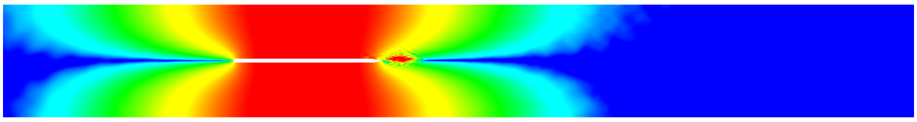
f = 2836 Hz ⟶ f* = 0.499
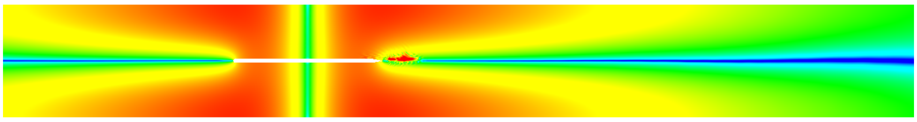
Long Length (β, α and (2,0) modes)
f = 1009 Hz ⟶ f* = 0.178
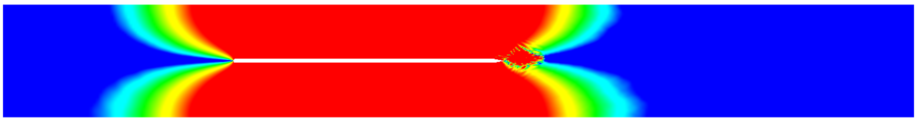
f = 1981 Hz ⟶ f* = 0.349
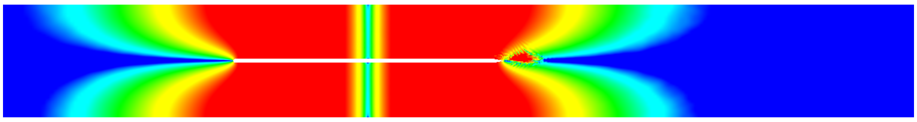
f = 2809 Hz ⟶ f* = 0.494
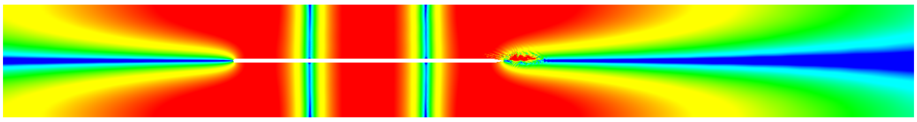

Table 3.7: Pressure amplitude for chosen frequencies in the overall flow field computed with RPM modelling [$U_{mean} = 10$ m/s]; the colour map differs from picture to picture

CHAPTER 4

Analysis of rain gutter aeroacoustics

4.1 Motivations

Side mirrors and A-Pillar are often pointed out as major noise sources due to their proximity to the driver's ears. One feature contributing to the overall noise level in the cabin is the rain gutter (RG) on the A-Pillar. This piece made out of rubber is similar to a long narrow channel placed along the side of the windscreen. Its purpose is to collect and drain the water that would otherwise flow from the windscreen and past the A-pillar along the side window, reducing therefore the visibility for the driver (figures 4.1 and 4.2). Aerodynamically speaking it can be seen as a turbulator creating highly turbulent flow in its wake, i.e. high pressure fluctuations leading to wind noise.

The flow passing over a rain gutter or more generally a forward facing step does not generate any resonances but produces broadband noise. A forward facing step is representative of many current industrial situations. It generally results from deliberate design features or/and manufacturing imperfections.

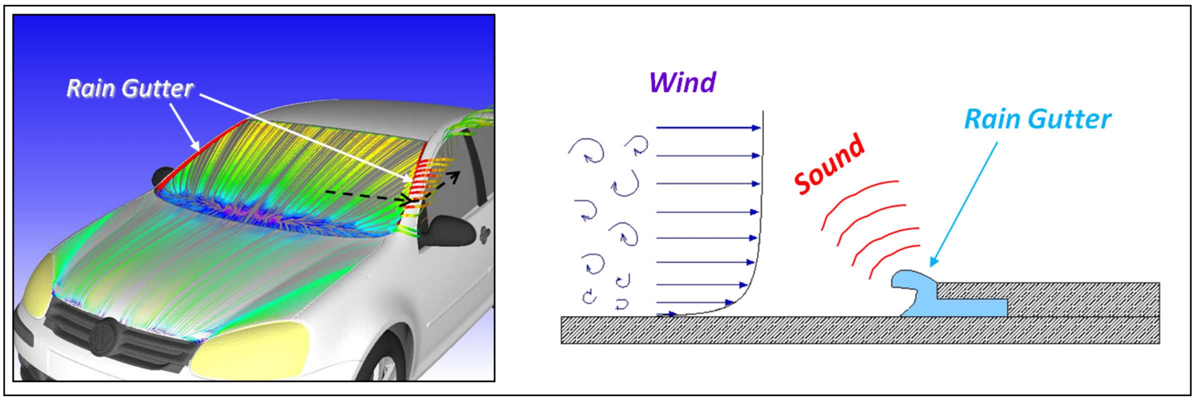

Figure 4.1: Description of a rain gutter

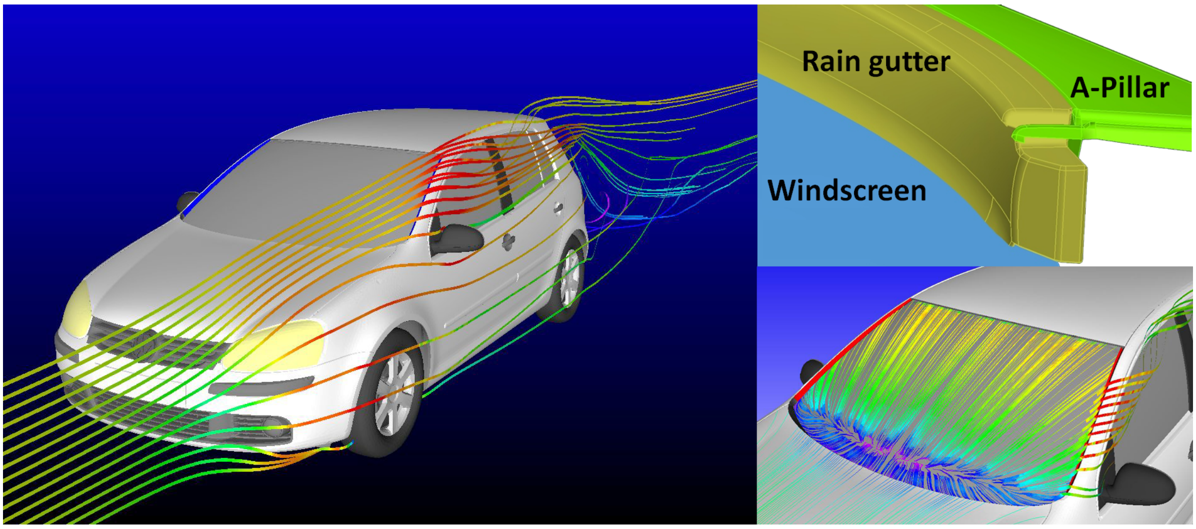

Figure 4.2: Flow Pattern Volkswagen GOLF, A-Pillar and rain gutter

In this chapter, some important results from the literature and current research on flow induced noise generated by rain gutters and forward facing step are firstly proposed. The present studied case is then described before to present the experimental results of the wind tunnel tests. The experimental work is completed by a numerical work. In this case four numerical methods have been used to compute the aeroacoustic field while the acoustic sources used in the different methods have been assessed with different turbulence models and stochastic modelling.

4.2 Literature review

4.2.1 Flow characterisation

On the market both types of vehicles equipped with or without a rain gutter exist. The height of the rain gutter can be very high, for example on the Volkswagen Golf Plus or the Mercedes Class-B. If it helps to reduce the quantity of water on the side window, it can also results in a higher wind noise level particularly in side wind situations. The height of the rain gutter is generally not constant but varies along the A-Pillar. Thick at its base (around 6 cm on a Volkswagen Golf Plus), it becomes thinner approaching the roof. Considering the streamlines' pattern on a windscreen (figure 4.1), one can see that the angle of the oncoming flow with the rain gutter also varies along the A-Pillar. Almost perpendicular at its base (90°), the angle between the oncoming flow and the rain gutter can reach a value of 30° at its top.

A section of the rain gutter can also be assimilated to a forward facing step (FFS). The flow around a forward facing step is generally represented by two recirculation areas, one in front of the step and one after, see figure 4.3. Several authors work on the prediction of the reattachment length [108] and show that a large discrepancy exist concerning the definition of the length of the recirculation bubble (X_L). The reattachment point can either be defined by the point where the streamline of the mean flow reaches the ground or as the mean place where the fraction of the flow going upstream is equal to those going downstream. Eaton and Johnson [37] shows that this length is very sensitive to the characteristics of the flows. In the case of a boundary layer's thickness on the order of the height of the step (h), the reattachment length is generally found between $3h$ and $5h$. Nevertheless no systematic study has been carried out on the height of the recirculation area (Y_b) but it is generally estimated around the step's height. Brungart [23] noticed that the ratio between the step's height and the wind tunnel's aperture can also have a significant impact on the recirculation's height.

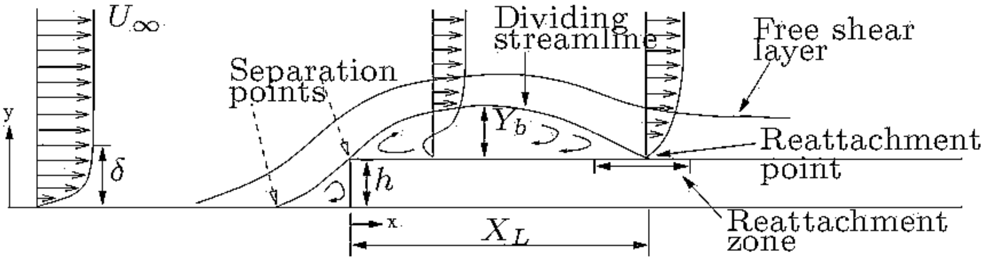

Figure 4.3: Recirculation over a forward facing step (FFS) [108]

The velocity in the recirculation area is found between 0.2 U_∞ and 0.3 U_∞ with U_∞ being the mean flow speed. After the reattachment, the mean velocity profile is not that of a boundary layer but tends to progressively get back to a logarithmic law as one moves away from the reattachment line. Farabee and Casarella [49] noticed that even $72h$ after the reattachment the velocity profile did not recover its normal shape. In particular the velocity fluctuations and Reynolds stresses present generally an excess of energy in comparison to boundary layer in equilibrium.

4.2.2 Flow-induced noise

Recently, many works have been done to tackle the simulation of the flow induced noise over side view mirrors [96] [98] [109] and the pressure fluctuations on the car's lateral windows [4] [31] [105]. Few works also addressed the problem of simulating the noise generated by a simplified rain gutter by using a facing elbow mounted on a flat plate [69] [90] or more basically a forward facing step [1] [5] [15]. However in these works the height was generally constant and the configurations were almost 2D. Becker [15] investigated the correlation between flow and acoustics on a forward facing step and showed the broadband character of the induced noise between 1 and 8 kHz. Using proper orthogonal decomposition, Bae et al. [5] [88] observed two different noise generation mechanisms for a Strouhal Number of about 0.1 and 0.5. These two phenomena correspond respectively to a monopole-type generated by the flapping motion of the shear layer and to a dipole-type generated by the breaking-off of the shear layer into eddies (due to Kelvin-Helmholtz instabilities).

Sabanca [103] used a perturbation method by introducing several vortices impacting three different profiles of forward facing step. He demonstrated that a rounded profile was about 13 dB quieter than the squared one and that the far field noise scales with

5.8th power of the flow stream velocity. Finally, Bauer [12] used a reconstruction of Fourier modes to compute the flow induced noise over a forward facing step. A patch on which the turbulent flow was reconstructed was placed in front of the FFS. The structures were then convected up to the FFS to generate noise. Although the study shows that at low frequency the noise was mainly radiated forward, no satisfactory spectrum could be presented.

4.3 Geometries and configurations

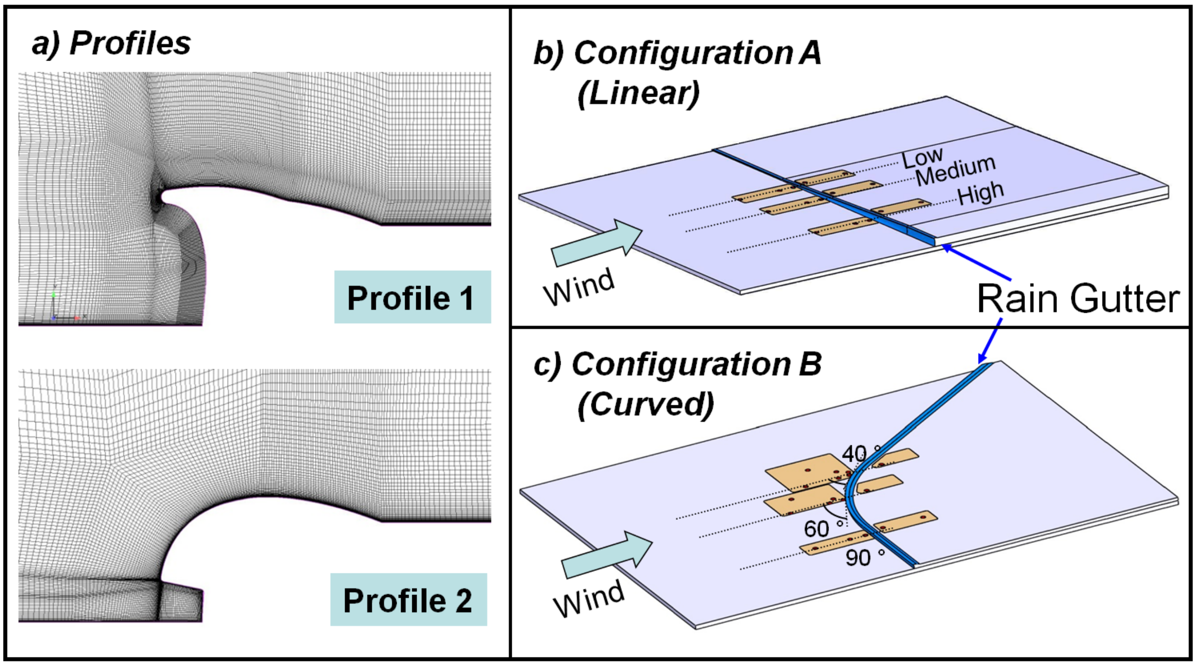

Figure 4.4: Geometry of the rain gutter's configurations

In this work, two different rain gutter section profiles are tested, see figure 4.4.a. The first profile presents a higher water channel and a sharper edge than the second profile. Shown in figure 4.1 and 4.4 the rain gutters are mounted on a flat plate and extended at their back by another plate. On a real vehicle the height of the rain gutter and the direction of the oncoming flow are generally not constant but change along the A-pillar. To evaluate these two parameters independently two configurations were designed. Figure 4.4.b represents a rain gutter with a height varying linearly from 10 to 42 mm (called *linear* or *configuration A*). The configuration shown in figure 4.4.c (designated as *curved* or *configuration B*) was designed to study the impact of different flow angles on the rain gutter. The angle between the flow and the rain gutter varies from 90° to 35°.

Note that the definition of the 3D shape was not identical for both rain gutter profiles. The upper part of profile 1 was translated and only the distance between the edge and the ground change. On the contrary the distance between the edge and the ground was kept constant for the profile 2 and only the radius of the upper part of the rain gutter was modified appropriately, see figure 4.5.

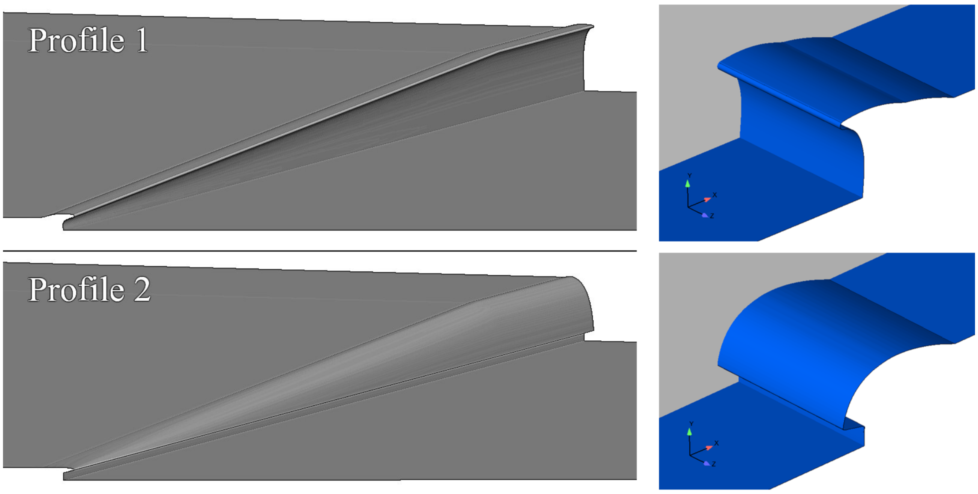

Figure 4.5: Representation of the two 3D rain gutters in configuration A

4.4 Experimental analysis

Experimental investigations were performed at DLR's aeroacoustic wind tunnel in Braunschweig (AWB) on the four test cases (2 configurations × 2 profiles), figure 4.6. The wind tunnel has an open section of 1.2 m × 0.8 m while the collector is 3 m × 3 m wide. More information on the characteristics of the wind tunnel can be found in [99]. The models were equipped with flush-mounted microphones placed in front of and behind the rain gutter. Three rows of microphones have been positioned in the flow directions to study three different heights of rain gutter for the configuration A and three oncoming flow directions for configuration B. In addition 10 free field microphones have been used to complete the set of data and to measure the directivity of the sound radiation. An array composed of 96 microphones (1/2") from Linear X was also used to identify the position of the sources. The flush-mounted microphones were 1/4" (B&K) and 1/8" (Gras) microphones type 40DP (working range: 6.5 Hz to 140 kHz). The microphones' signals were registered during 22 s at a sampling frequency of 45 kHz. A wind tunnel shear layer correction according to Amiet [2] was applied to the far field microphones signals.

4.4.1 Boundary layer

A comb of pressure probes was used to measure the boundary layer's thickness at 2 different positions in front of the rain gutter. A picture of the comb and a plot of the velocity profiles (for different inflow velocities and at 2 positions) are presented in figure 4.7. At the exit of the nozzle (X = -1 m) the boundary layer is 13 mm thick while its thickness reaches 23 mm further downstream (X = -0.57 m). The development of the thickness of the fully turbulent boundary layer may be represented by Nikuradse's law like $\delta(x) = 0.164 * Re_x^{0.861}\nu/U_\infty$[1]. The thickness of boundary layer was estimated to about 30, 29, 27 mm for the flow speeds of 30, 45, 60 m/s respectively when reaching the rain gutter (X = 0). This value is however higher than the height of the rain gutter itself.

---

[1] see e.g. H. Schlichting 'Grenzschichttheorie', 8. Auflage, Braun Verlag 1982

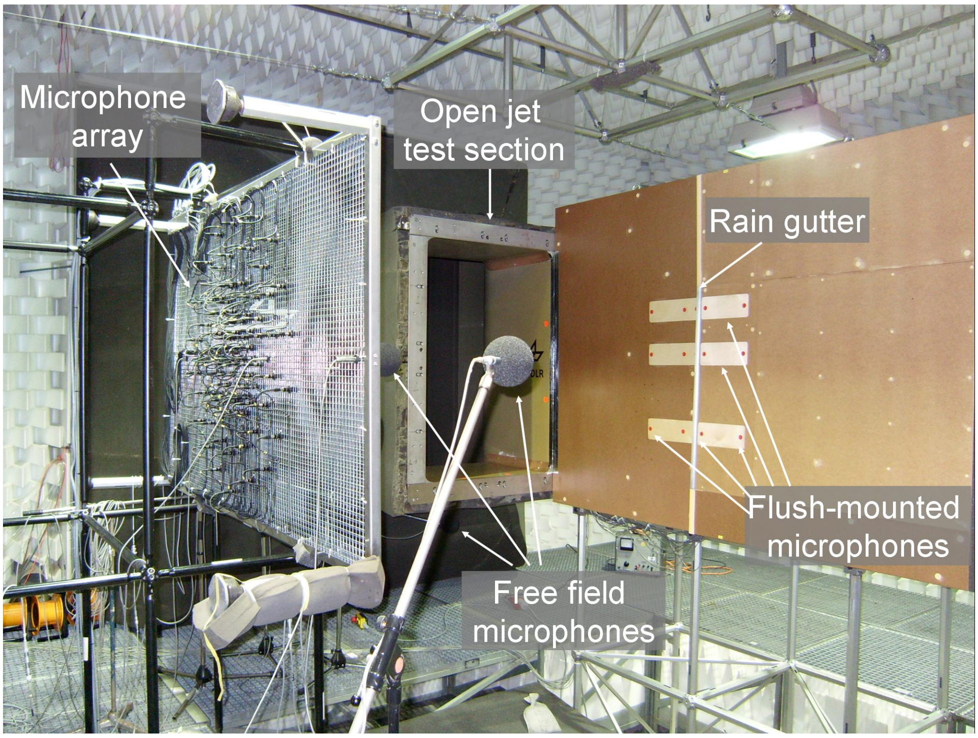

(a) linear configuration (A)

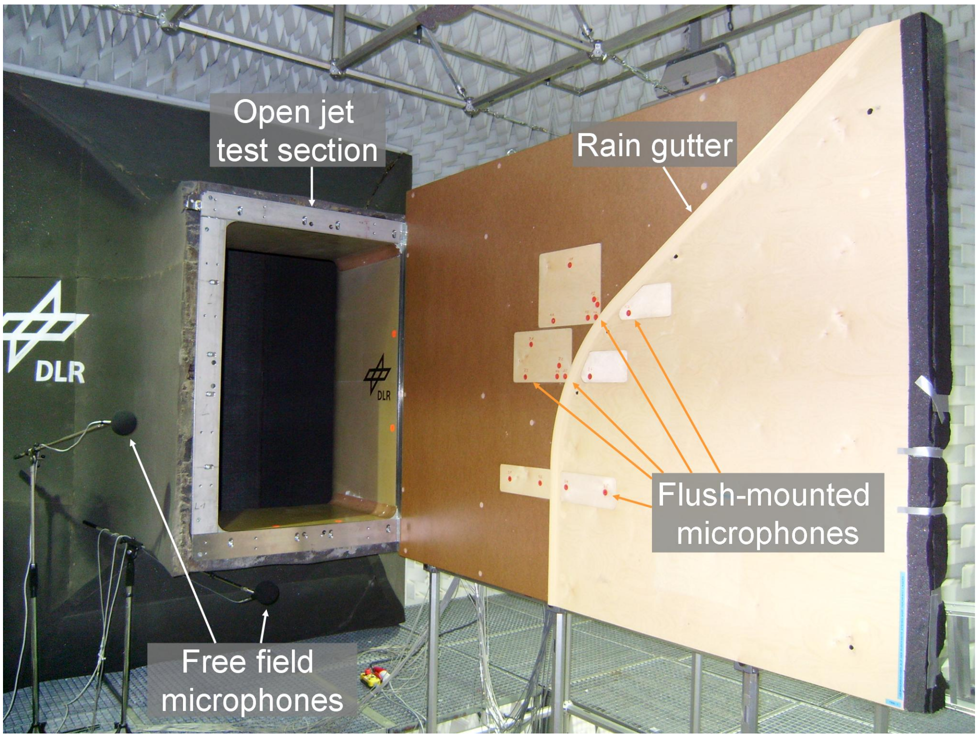

(b) curved configuration (B)

Figure 4.6: Set-up of the acoustic measurements (linear configuration (A) (top) and curved configuration (B) (down))

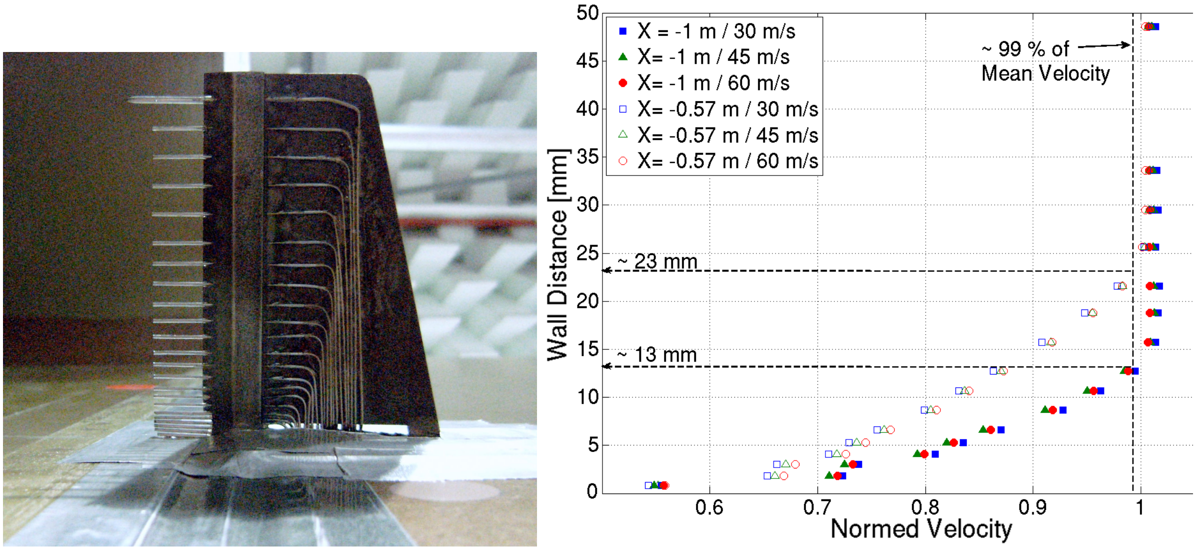

Figure 4.7: Evaluation of the boundary layer in the wind tunnel

This remark points out a critical aspect for the simulation particularly when using hybrid approaches. In fact the boundary layer is generally treated in steady mode and the instabilities are highly damped. Therefore the level of the instabilities may be too low to be able to switch from a steady state to an unsteady state. One can already perceive the challenge represented by such a configuration for hybrid CFD approaches.

This case represents an academic configuration and conclusions on this case cannot be directly transposed to the case of a real vehicle. On a real vehicle the flow in this area is for example expected to be more turbulent and the boundary layer thinner.

4.4.2 Flow visualisation

Oil painting has been used to visualise the flow pattern on the rain gutter. Pictures of the four different cases are presented in figure 4.8. Considering the linear configuration and profile 1 a large recirculation area is found downstream the rain gutter. For the middle section the size of the recirculation area is evaluated to 7.5 cm behind the edge which corresponds to almost 4 times the height of the profile. This size varies linearly with the height of the rain gutter from 2 to 11 cm. A small recirculation area appears also in front of the rain gutter. This area is about as long as the rain gutter's height.

For profile 2 no separation area is observed after the rain gutter. In fact only a constant recirculation area exists in front on the rain gutter. For the higher section of the profile the reattachment line can be directly seen on the rain gutter. This indicates also that the turbulence level is lower for profile 2 than for profile 1.

Considering the curved configurations a deviation of the flow is observed in front of the rain gutter. As previously a recirculation area behind the rain gutter is observed for profile 1 but not for profile 2. In this case a 3D vortex is formed behind the rain gutter similar to the A-Pillar vortex on a car. Compared to the linear configuration (A) the recirculation area is smaller in configuration B for a profile with the same height.

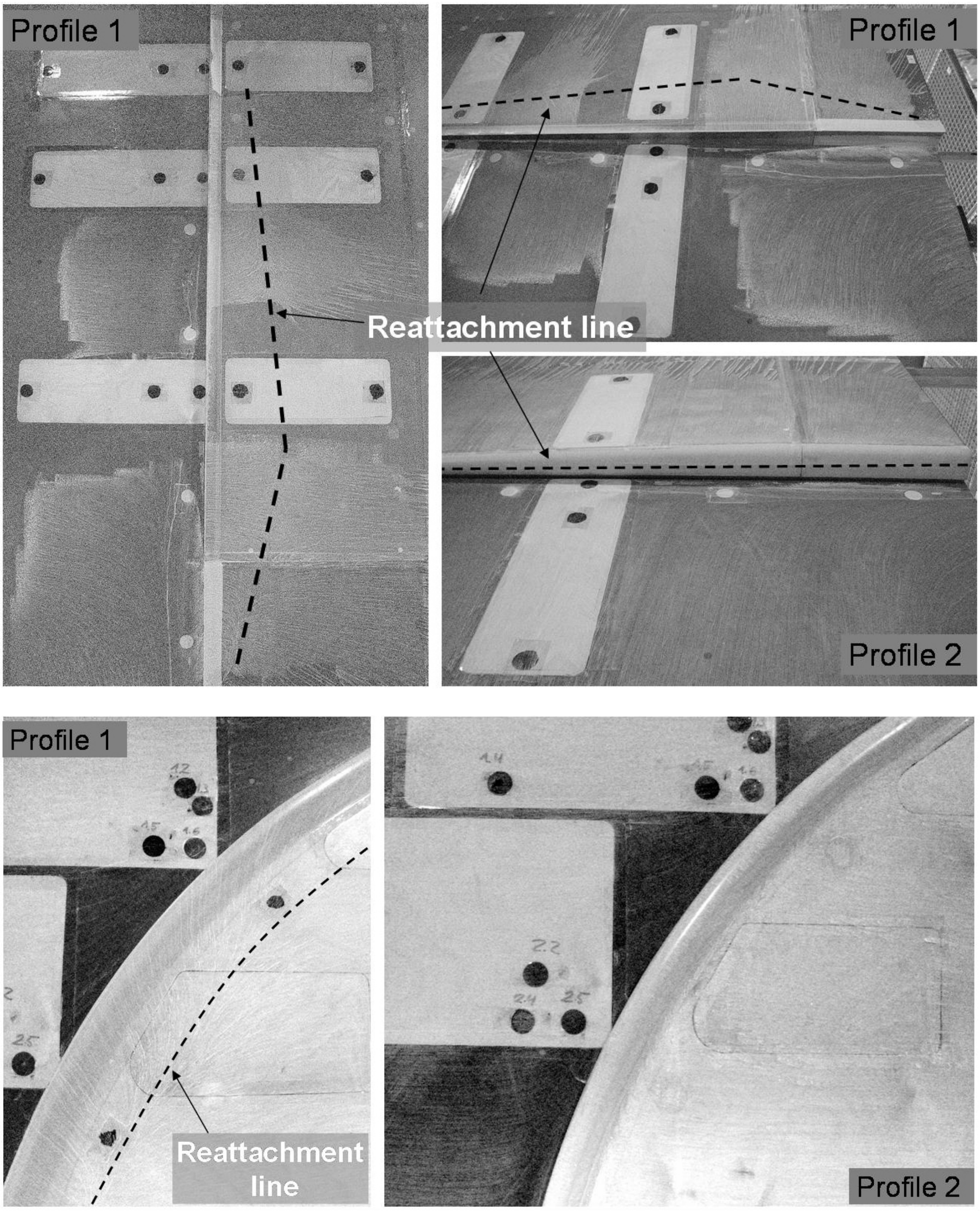

Figure 4.8: Flow pattern on the experimental rain gutter; configuration A (top) and configuration B (bottom)

4.4.3 Localisation of the sources

A microphone array was used to localise the acoustic sources. Some maps for three cases and at three different frequencies are presented in figure 4.9. The figures show that the noise sources are localised few centimeters (≈ 10 - 30 mm) in front of the rain gutter represented by the black line.

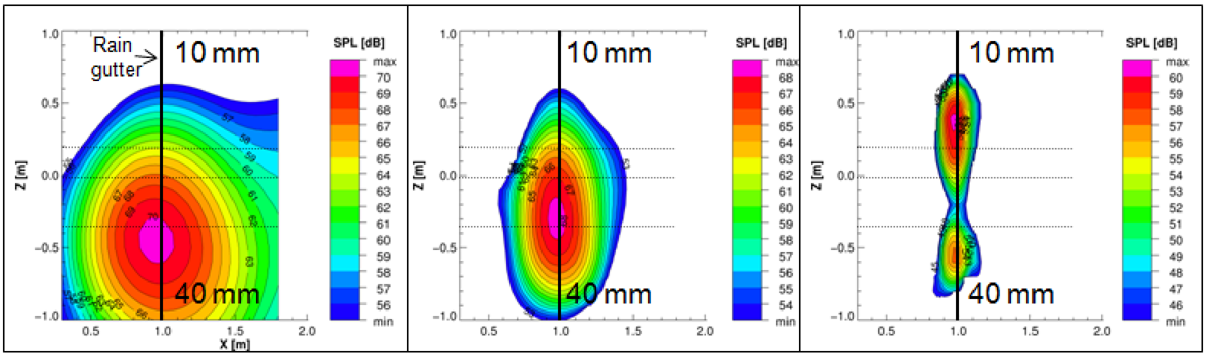

(a) Configuration A - Profile 1 at 1.25 kHz, 2.50 kHz and 6.30 kHz

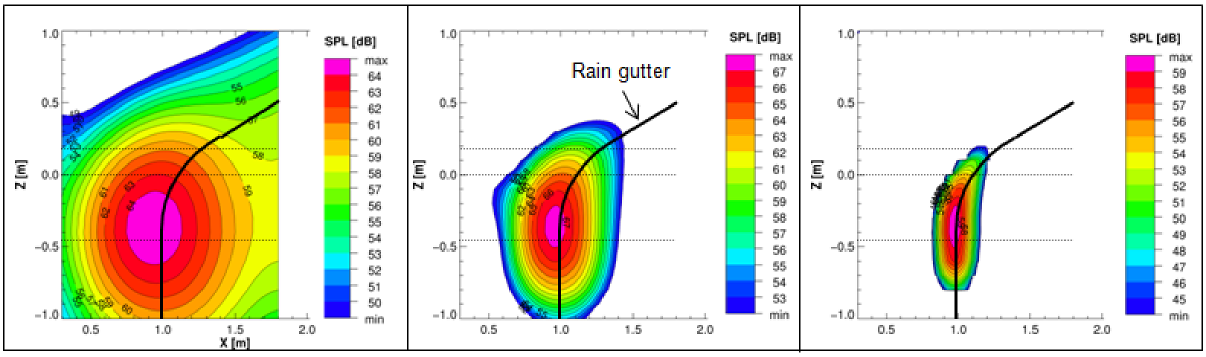

(b) Configuration B - Profile 1 at 1.25 kHz, 2.50 kHz and 6.30 kHz

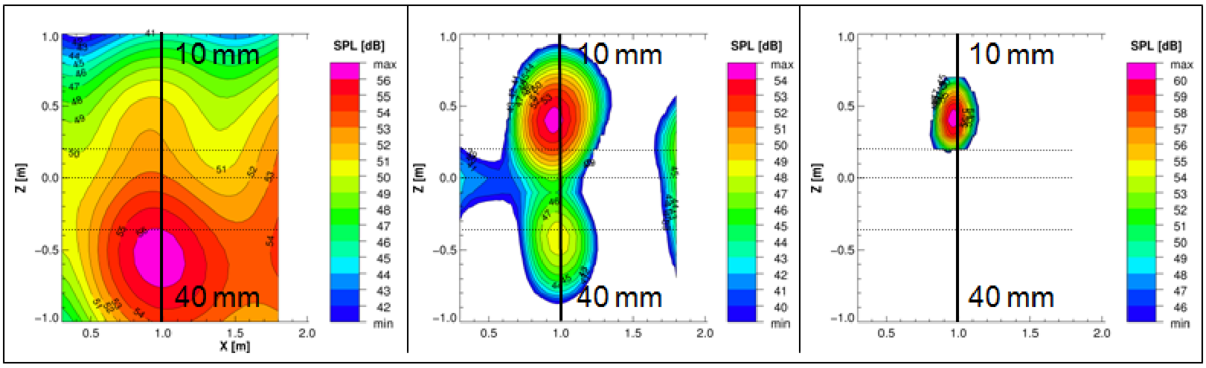

(c) Configuration A - Profile 2 at 1.25 kHz, 2.50 kHz and 6.30 kHz

Figure 4.9: Maps of the sound pressure level measured with the microphone array for three configurations: configuration A profile 1 (top), configuration B profile 1 (middle) and configuration A profile 2 (bottom); $U_{mean} = 45$ m/s

The first and third rows of the picture corresponding to the configuration A (linear) illustrate the localisation of the main sources at different frequencies for the configuration A. Low frequency components are mainly located on the thicker section of the rain gutter (bottom) while the higher frequencies are located on the thinner section. This remarks seems understandable considering that high frequencies corresponds to small wavelengths (λ) while lower frequencies correspond to longer wavelengths. A high noise level is found around 6 kHz for this configuration with the profile 2 (third row in figure 4.9). One element of explanation of this high noise level at 6 kHz can be found when considering a Strouhal number of 0.2 and the speed of sound. According to its definition this value characterise a length of 11 mm which corresponds exactly to the lower height of the rain gutter. The overall higher noise level observed for profile 1 masks this resonance.

For configuration B (second row) the higher noise level is found in the area where the oncoming flow is directly perpendicular to the rain gutter (bottom). Further maps obtained for four different configurations are presented in appendix.

4.4.4 Study of the near field acoustics

a/ Surface Pressure Level (SPL)

As indicated in figure 4.10, 15 or 18 flush-mounted microphones (FMM) are positioned upstream and downstream the rain gutter for the linear (A) and curved (B) configurations respectively. These microphones are located in three rows along the flow direction. For configuration B extra microphones are placed upstream in the direction directly perpendicular to the local tangent of the rain gutter. This was done in order to evaluate the correlations of the signals in this case. The numbering convention used for the graphs are defined in the same figure. For the linear configuration the numbers from 1 to 5 correspond to the thinner rain gutter profile while the numbers 11 to 15 correspond to the thicker part. The spectra presented in this section are 1/3 octave band spectra.

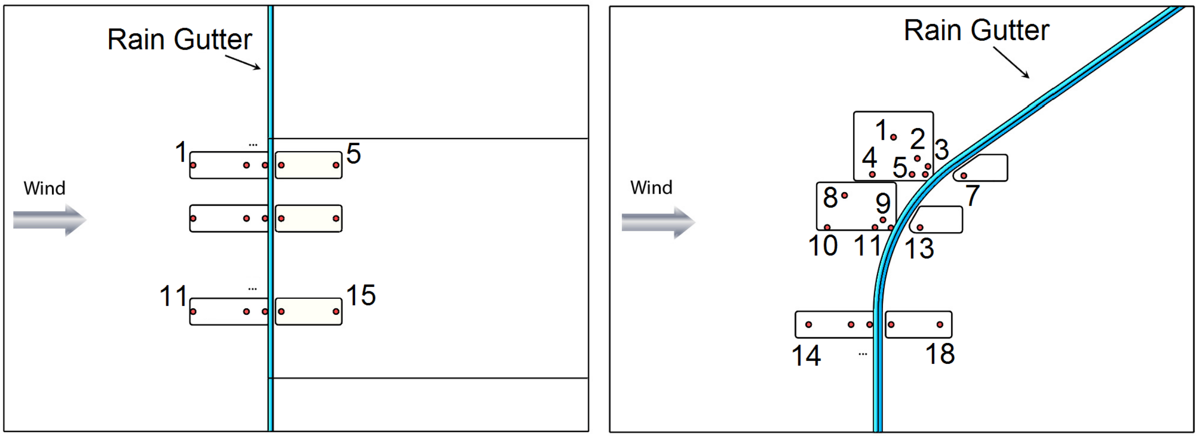

Figure 4.10: Numbering of the flush-mounted microphones: configuration A (left) and configuration B (right)

Table 4.1: Distance to the rain gutter of the 5 Flush-Mounted microphones along a row (X<0 corresponds to upstream positions)

Position	1	2	3	4	5
X [mm]	-288	-85	-17	45	250

The relative position of the microphones along a row are specified in table 4.1. The spectra measured by the five flush-mounted microphones positioned on the middle section of the rain gutter in configuration A and for both profiles are presented in figure 4.11. The pressure fluctuations registered from the microphones positioned in front of the rain gutter (points 6, 7 and 8) are very similar for both profiles. The main difference comes from the microphones positioned behind the rain gutter (points 9 and 10). Higher pressure fluctuations are found for profile 1 compared to profile 2. This statement supports the previous remark made concerning the length (X) of the recirculation area behind the rain gutter. The length of the recirculation is longer for profile 1 than for profile 2, synonym of a higher turbulence level behind the rain gutter.

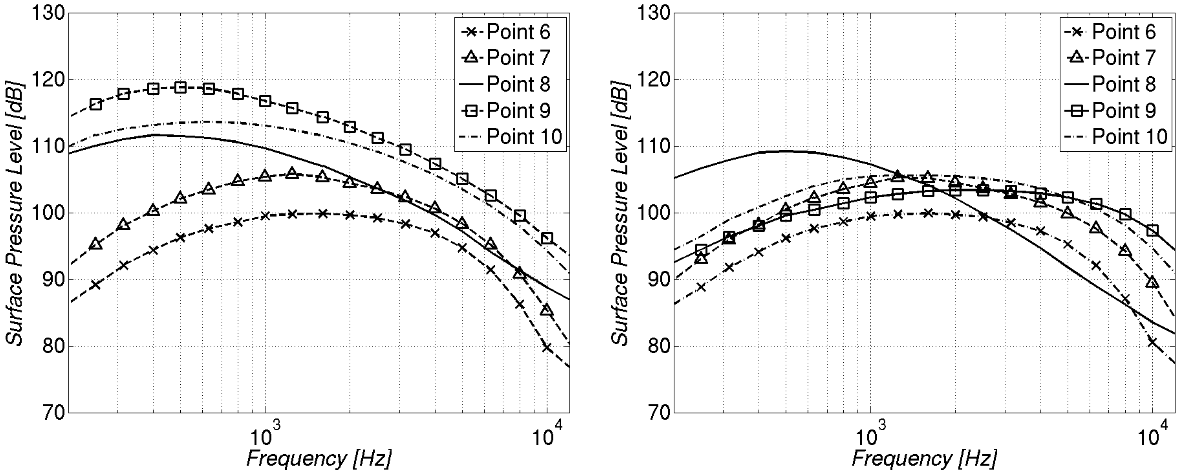

Figure 4.11: Measurements of the 1/3 octave surface pressure level for profile 1 (left) and profile 2 (right) in configuration A and with an oncoming flow speed of 45 m/s; the five microphones are placed along the middle line of the rain gutter as defined in figure 4.10; $U_{mean} = 45\ m/s$.

The general effect of the height variation on the surface pressure level is more difficult to outline, see figure 4.12. The surface pressure level in front and behind the rain gutter is presented for each RG's height. As a general tendency a shift in the frequency range of the maximum noise level is observed. In agreement with the maps obtained with the microphone array the high frequencies generally correspond to the thinner part of the rain gutter and the lower frequencies corresponds to its thicker part. However no ranking can be clearly found in term of overall sound pressure level. The frequency band corresponding to the maximum SPL does not vary linearly with the height. As mentioned before the height's variation was not only made by scaling or translating the profile but was more complex. Therefore the behaviour of the flow appears more disturbed than simply scaled. In addition the microphones were placed at the same distances to the rain gutter for all three heights, as the size of the recirculation area increases with the rain gutter's height the FMM were either inside or outside of the recirculation area resulting in different behaviours.

The effect of the flow direction (corresponding to configuration B) and oncoming flow speed are respectively presented in figures 4.13 and 4.14. It was found that the sound intensity scaled with a little bit more than the fourth power of the velocity (M^4). A reduction of the incoming flow angle tends to reduce the overall noise level. In addition

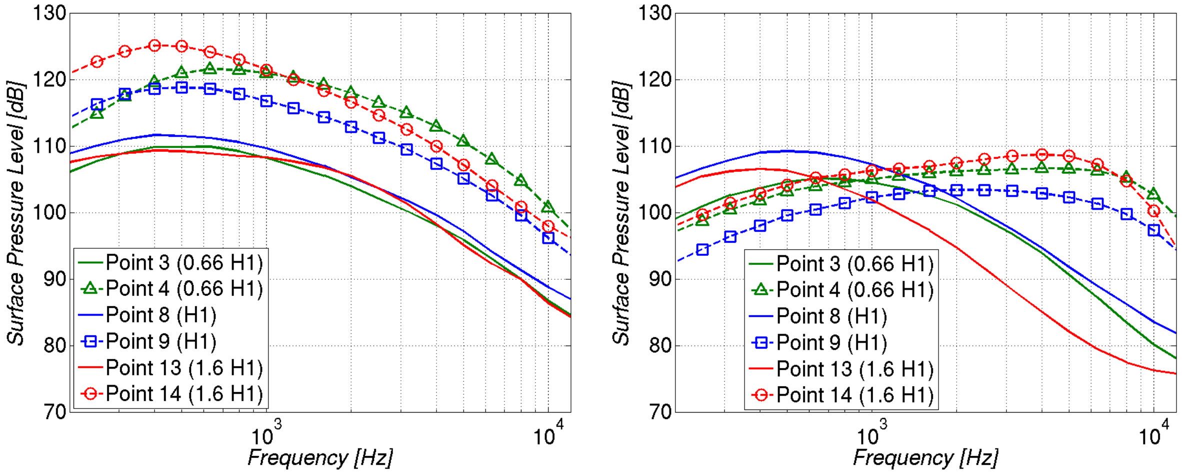

Figure 4.12: Measurements of the 1/3 octave surface pressure level in front and behind the rain gutter in configuration A for 3 different heights of rain gutter at 45 m/s, profile 1 (left) and profile 2 (right)

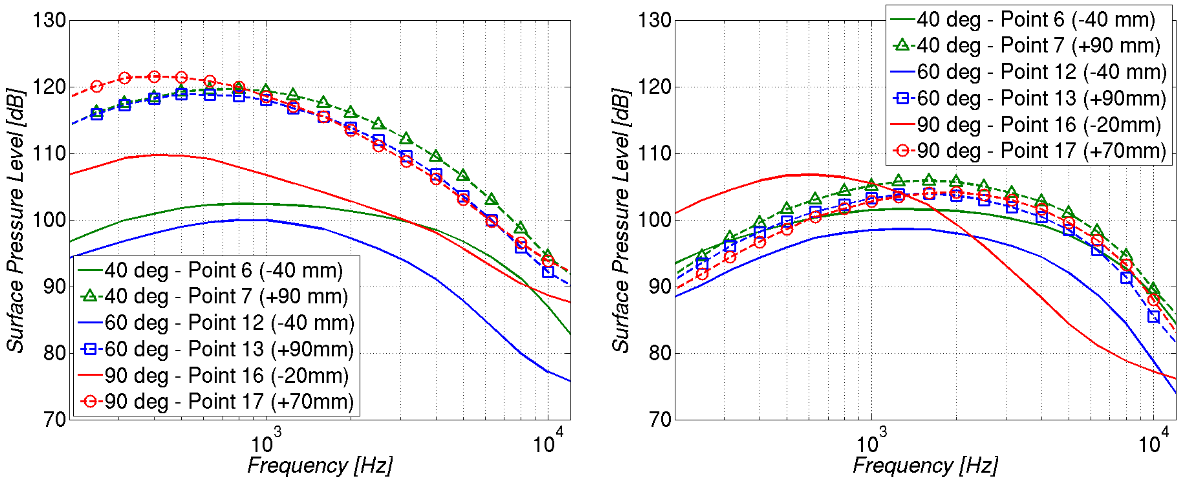

Figure 4.13: Measurements of the 1/3 octave surface pressure level in front and behind the rain gutter in configuration B for 3 different oncoming flow angles at 45 m/s, profile 1 (left) and profile 2 (right)

an increase of the oncoming flow angle appears leading to a reduction of the frequency at which the maximum SPL is observed.

Proportional to the square of the pressure (p^2), representations of the acoustic level (I) for each flush-mounted microphone and for both profiles are given in figures 4.15 and 4.16 for the configurations A and B respectively. The columns are normalised to the maximum acoustic intensity computed in each case. These plots confirm firstly that a higher noise level is found behind the rain gutter and that profile 1 is noisier than profile 2.

Considering only the configuration A (figure 4.15), the acoustic intensity of the signals

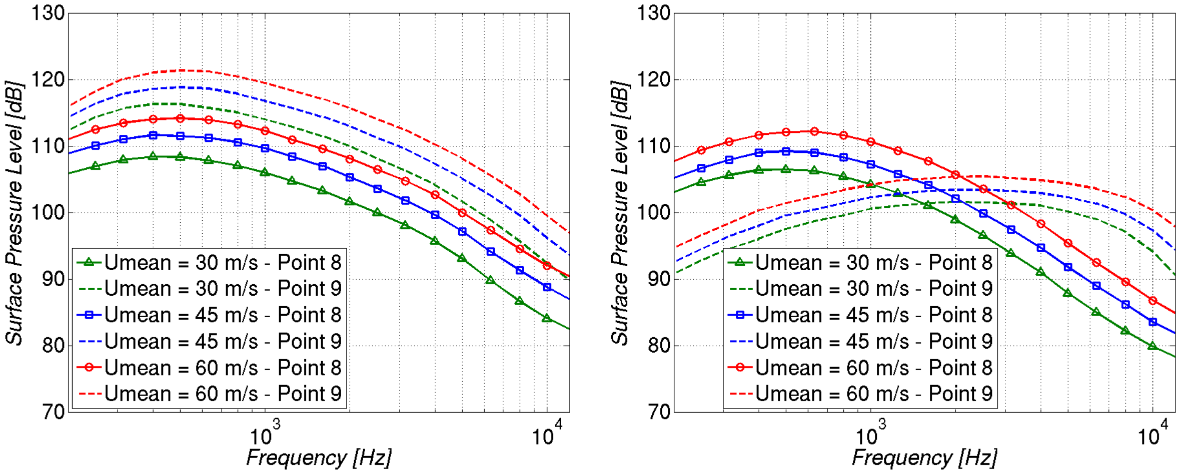

Figure 4.14: Measurements of the 1/3 octave surface pressure level in front and behind the rain gutter in configuration A for different oncoming flow velocities, profile 1 (left) and profile 2 (right)

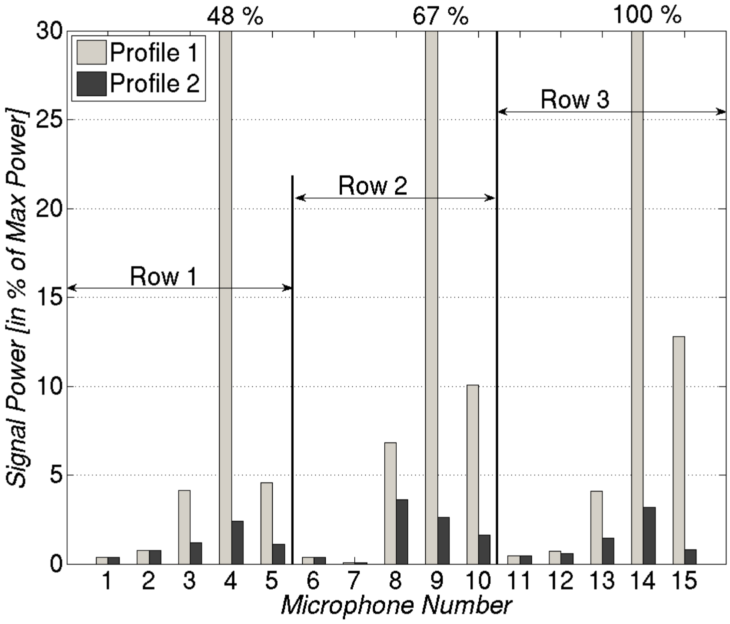

Figure 4.15: Comparison of the acoustic level measured for both profiles at each flush-mounted microphone - configuration A, $U_{mean} = 45$ m/s

measured by the flush-mounted microphones behind the rain gutter almost scales linearly with the height of the rain gutter. For configuration B (figure 4.16) the highest noise level is found for the microphone placed behind the rain gutter with an oncoming flow angle of 90° while in overall the lowest noise level is found for the middle section (raw 2). Considering the third row, the flow is then directly perpendicular to the rain gutter resulting in a bigger recirculation area. At the opposite, a large vortex takes place along the linear part of the rain gutter at the higher angle (raw 1) generating pressure fluctuations. Both phenomena are however moderate for the intermediate flow angle which results in lower pressure fluctuations; i.e. explaining the lower overall noise level.

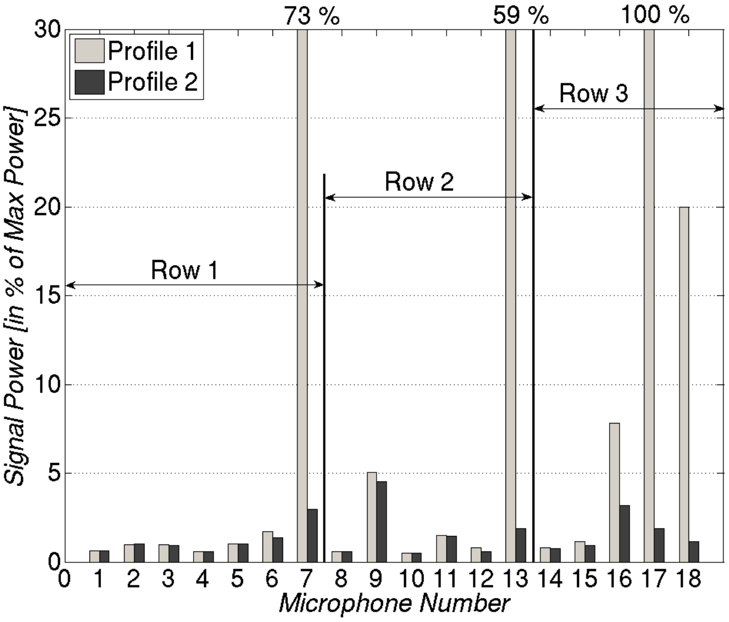

Figure 4.16: Comparison of the acoustic level measured for both profiles at each flush-mounted microphone - configuration B, $U_{mean} = 45$ m/s

b/ Coherence

To evaluate the relationship between two quantities, one can compute the coherence function by using the following formula:

$$\gamma = \frac{R_{xy}(f)}{\sqrt{R_{xx}(f) \times R_{yy}(f)}} \tag{4.1}$$

with R_{xy} the cross power spectral density and R_{xx} and R_{yy} auto power spectral densities of both signals.

Considering now 2 signals s_1 and s_2 registered at two different points, the previous formula allows evaluating the level of correlation between these two signals assuming that the same wave reaches both points.

The two signals are then defined by $s_1 = A_1 e^{i(\omega t - \vec{k}\vec{x}_1)}$ and $s_2 = A_2 e^{i(\omega t - \vec{k}\vec{x}_2)}$.

The cross-correlation is proportional to $e^{i(\vec{k}\cdot\vec{x}_2 - \vec{k}\cdot\vec{x}_1)} = e^{i(\vec{k}\cdot\Delta\vec{x})}$

while the phase of the coherence function is defined by:

$$\Delta\varphi = \vec{k}\cdot(\vec{x}_2 - \vec{x}_1) = \left\|\vec{k}\right\| \|\Delta\vec{x}\| \cos\alpha = k\ \Delta x\ \cos\alpha \tag{4.2}$$

with α the angle between the direction defined by the two points considered and the direction of the wave; $\Delta\vec{x} = \vec{x}_2 - \vec{x}_1$ and $\Delta x = \|\Delta\vec{x}\|$ and $k = \left\|\vec{k}\right\|$.
The phase velocity is defined by: $u_c = \omega/k$; by using eq 4.2, it reads:

$$u_c = \omega \Delta x \cos\alpha / \Delta\varphi \tag{4.3}$$
$$u_c = (2\pi f) \times \Delta x \cos\alpha / \Delta\varphi \tag{4.4}$$

The magnitude of the coherence gives then an indication of the level of coherence. According to the previous equation, the velocity of the wave between two coherent points is proportional to the slope of the phase (in radians) of the coherence function.

The coherence between the signals from different flush-mounted microphones have been analysed for an inflow speed around 45 m/s. Not presented here, similar coherence functions where found for the other velocities. Some coherence functions for the configuration A are presented in figure 4.17. The first and fourth rows present the coherence for both profiles and the two flush-mounted microphones directly placed in front of the rain gutter for the three microphone lines. A higher coherence is found for profile 1 than for profile 2. Under 500 Hz a linear behaviour is observed for the phase in all cases. This part corresponds indeed to the flow convection. Based on the previous formula a phase velocity around 40 m/s (i.e. the convection velocity) is found. One may expect that in this lower frequency range the signals are dominated by convecting turbulent (vortical) structures. This is to be expected since low frequency components can be associated with large scales in the turbulent boundary layer being somewhat correlated even for large separation distance of the sensors (here 68 mm). Any acoustic signal superimposed on these pressure fluctuations of the turbulent eddies are expected to be masked due to the dominance of these turbulence fluctuations. For higher frequencies only the first profile exhibits some coherence. The higher coherence values are found for the third row (mic. **12** vs. **13**) in the frequency range 6 to 9 kHz. The slope of the phase is here negative and a convection speed around 340 m/s is found. This indicates that acoustic waves are radiated upstream between these two microphones. The two others rows of microphones present the same phase decay but the magnitude of the coherence is lower. Nevertheless, this unique negative slope in the phase of the coherence function over most of the frequencies, except the very low ones, indicates clearly that here, sound dominates the correlation. This again is expected because vorticity-related higher frequency pressure fluctuations of the turbulent boundary layer are associated with small turbulent eddies which decay along their path from the upstream to the downstream surface pressure sensor. The above argument is again supported by the observation that the low frequency range, over which the convection slope is found (upper right diagram in figure 4.17) appears smallest for microphone pair **12/13**. The reason is that for this pair the observed large coherence is mostly determined by sound even down to quite small frequencies.

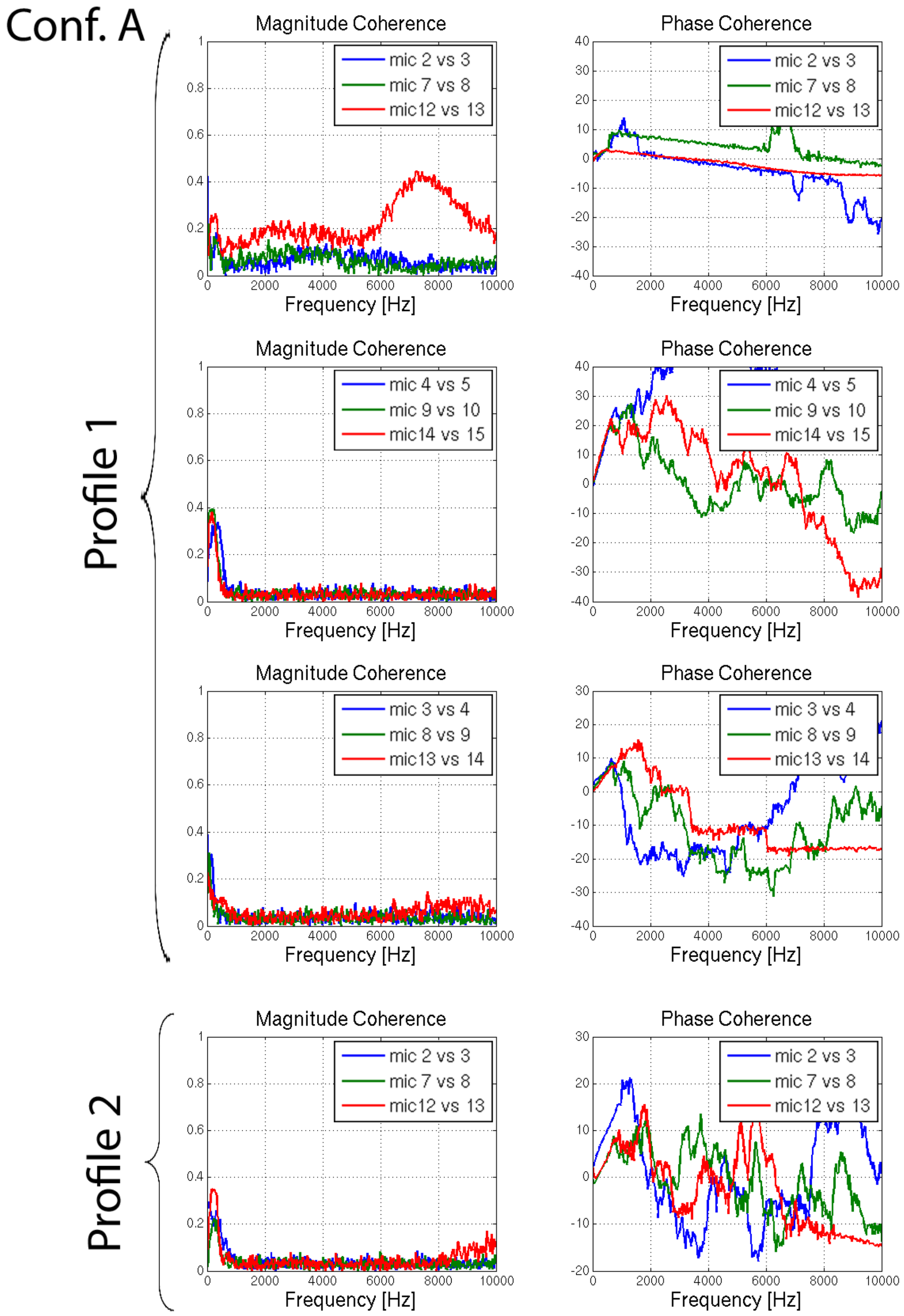

Figure 4.17: Coherence between microphones in configuration A: profile 1 and profile 2. The phase is in radians.

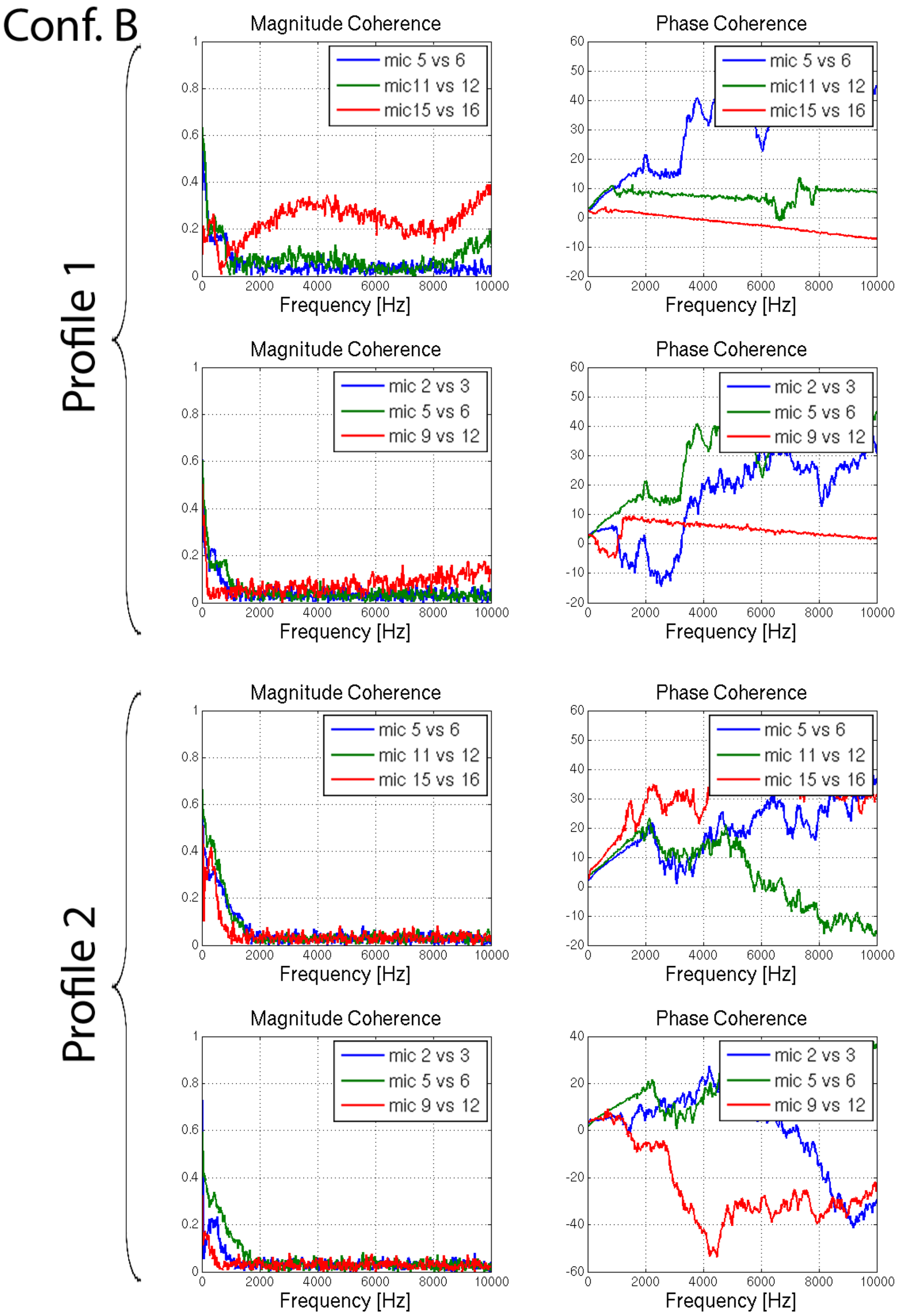

Figure 4.18: Coherence between microphones in configuration B: profile 1 and profile 2. The phase is in radians.

A very low coherence is found between the microphones positioned behind the rain gutter (row 2 in figure 4.17) over most of the frequency range, except very low frequencies. This fits nicely with the observation made before. The whole coherence is obviously dominated by large scale (low frequency) vorticity related pressure fluctuations. In this range the phase of the coherence displays an orderly positive slope, indication that there is a slow convective transport of the large scales downstream of the gutter. Although the higher frequency components are difficult to interpret, it is observed that there appears no dominant slope, indicating a pressure transport with the speed of sound as was the case in the microphone pairs in front of the gutter. The pattern seen at least for the microphone pair **9/10** and **14/15** indicate some low speed (i.e. non-acoustic) transport upstream which may be associated with the large flow separation bubble in this area.

The lowest coherence is seen for the microphone pairs, where one microphone is located before and one behind the rain gutter (row 3 in figure 4.17). Completely different physical phenomena seem to govern the pressure field closely before and closely behind the gutter. This at least indicates that the surface pressure dynamics close to the gutter is governed by sound on the upstream side, while it is governed by vortex dynamics on the downstream side. A consequence of this hypothesis would be that sound generation takes place at the front face of the gutter and sound is dominantly radiated to the upstream hemisphere.

The coherence of profile 2 is shown in the fourth row of figure 4.17. When compared the analogous measurement for profile 1 (first row of figure 4.17) one can observe that the coherence is strikingly smaller for profile 2 except for very low frequencies. This observation again supports the interpretation given before, namely that the low frequency coherence between the sensors come from turbulence related convective (i.e. non-acoustic) surface pressure fluctuations. Since profile 2 generates considerably less sound compared to profile 1, also the higher frequency pressure fluctuations are dominated by turbulence, which are largely uncorrelated for high frequencies. This in turn supports the hypothesis made for profile 1, namely that the coherence seen upstream the gutter is dominated by acoustics for a *loud* gutter.

As for configuration A also for configuration B, profile 1 exhibits higher coherence levels than profile 2, see figure 4.18. Until almost 2 kHz a good coherence is found for most of the cases presented with a propagation velocity around 40 m/s. At higher frequencies a good coherence is found for the first profile (loud) only, indicating again that for higher frequencies upstream of the gutter the coherence is dominated by sound. The coherence is higher where the flow hits the gutter the more perpendicularly. The behaviour at microphone pair **15/16** therefore largely corresponds to what was observed at configuration A. It is quite plausible that the coherence due to convecting turbulence is reduced at those positions where the flow hits the gutter under oblique angles (microphones **2**, **3**, **5**, **6**, **9**, **11** and **12**) because the convection direction is not pointing along the direction from the one to the other microphone. Moreover the overall coherence is smaller because at the swept parts of the gutter the noise generation is considerably lower. These high frequencies are also characterised by the sound velocity.

4.4.5 Study of the far field radiation

a/ Sound Pressure Level (SPL)

Ten far field microphones have been used to measure the radiated noise, the numbering and location of these microphones is presented in figure 4.19. The measurements of the 1/3 octave sound pressure level for three microphones (*H* before, *D* above and *I* behind the gutter line) are presented for both profiles and configurations in figure 4.20. As already pointed out when studying the signals of the flush-mounted microphones the noise radiated by the profile 1 is higher than by profile 2 by about 10 to 15 dB. The radiated noise level is also slightly higher for the configuration A than for configuration B.

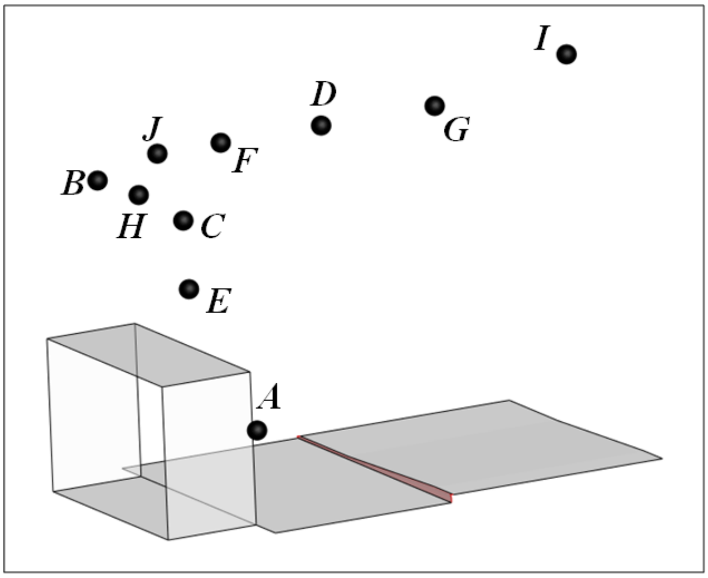

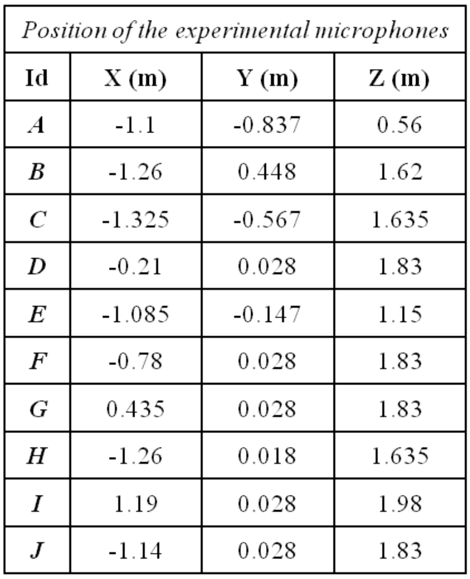

Position of the experimental microphones			
Id	**X (m)**	**Y (m)**	**Z (m)**
A	-1.1	-0.837	0.56
B	-1.26	0.448	1.62
C	-1.325	-0.567	1.635
D	-0.21	0.028	1.83
E	-1.085	-0.147	1.15
F	-0.78	0.028	1.83
G	0.435	0.028	1.83
H	-1.26	0.018	1.635
I	1.19	0.028	1.98
J	-1.14	0.028	1.83

Figure 4.19: Positions and designations of the far field microphones. Note that the coordinate system is different from the one shown in figure 4.9; here the spanwise direction corresponds to the y-axis , the spanwise centre of the gutter is located at y=0.

Considering the first profile, the maximum noise level is found for a frequency band around 2 kHz for the configuration A while the maximum is found around 3 kHz for the configuration B. The spectra for the second profile in configuration A is mainly marked by a maximum in the frequency band around 6 kHz while the spectra appears rather flat for the configuration B. For all cases the microphone *H* (in front of the RG) generally displays the highest sound pressure level among all three microphones. For high frequencies the sound pressure level appears to be lowest at the microphone placed behind the RG while the lowest sound pressure levels at low frequencies are seen at the microphone directly above the RG. This indicates that the maximum noise level is radiated forward, see figure 4.24. Shown in figure 4.21 it was also found that the shape of the spectra does not change with the inflow speed and that the intensity level scales with M^6 which according to Curle is indicative for a compact aeroacoustics sound source.

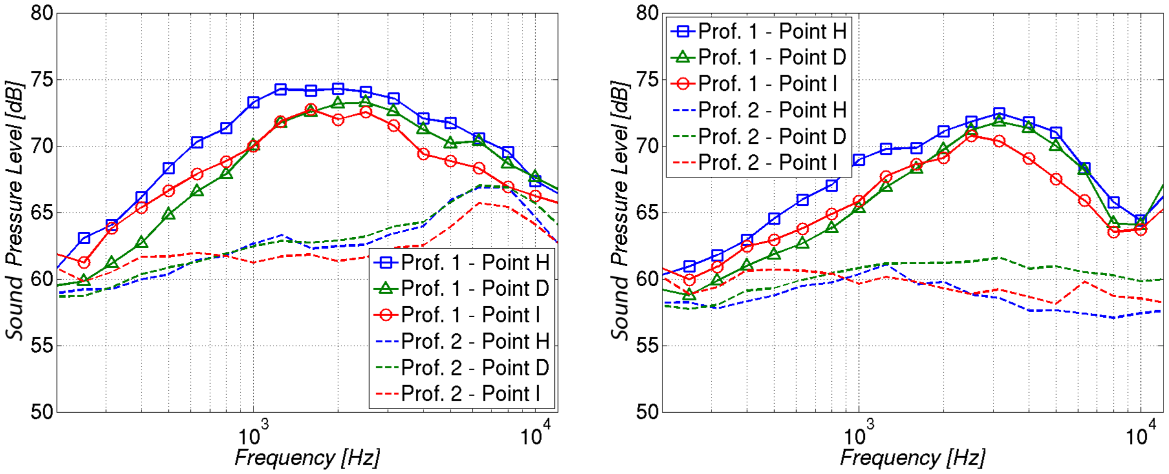

Figure 4.20: Measurements of the radiated 1/3 octave band sound pressure level for both profiles and configurations: configuration A (left) and configuration B (right) at $U_{mean} = 45$ m/s

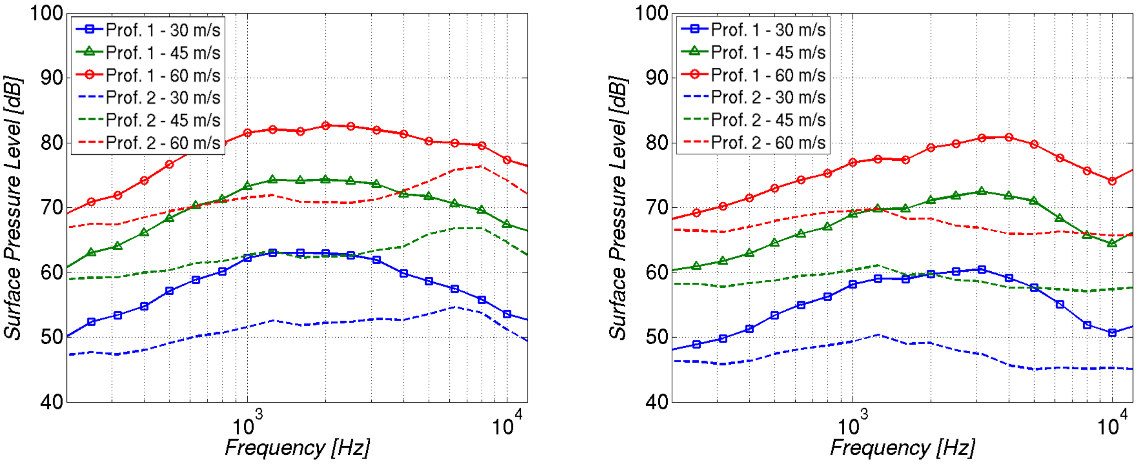

Figure 4.21: Measurements of the radiated 1/3 octave band sound pressure level for both profiles and for different oncoming flow speeds: configuration A (left) and configuration B (right) at $U_{mean} = 45$ m/s

b/ Coherence

Using the same coherence function as in the previous section, one can also analyse the coherence between the flush-mounted microphones (FMM) and the far field microphones (FFM) for both configurations A and B. The coherence for the configuration A is presented in figure 4.22. Only the results for profile 1 are presented here since no relevant coherence between the FMM and the FFM has been found for profile 2. The noise level of the profile 2 was lower than the one generated by the profile 1 and therefore probably masked by the surroundings to capture the coherence.

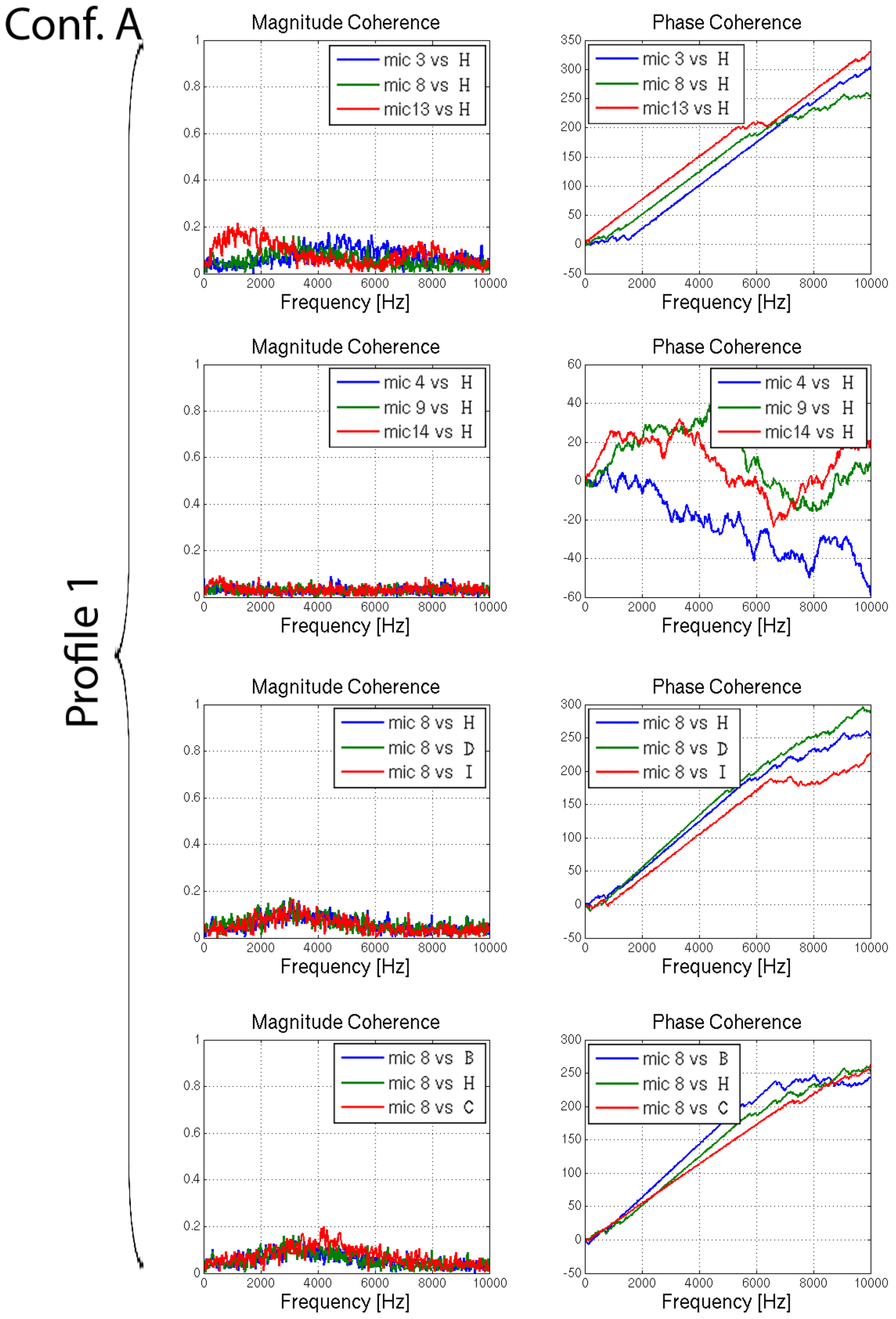

Figure 4.22: Evaluation of the coherence between flush-mounted and far field microphones for the configuration A and profile 1, magnitude and phase [rad] are presented

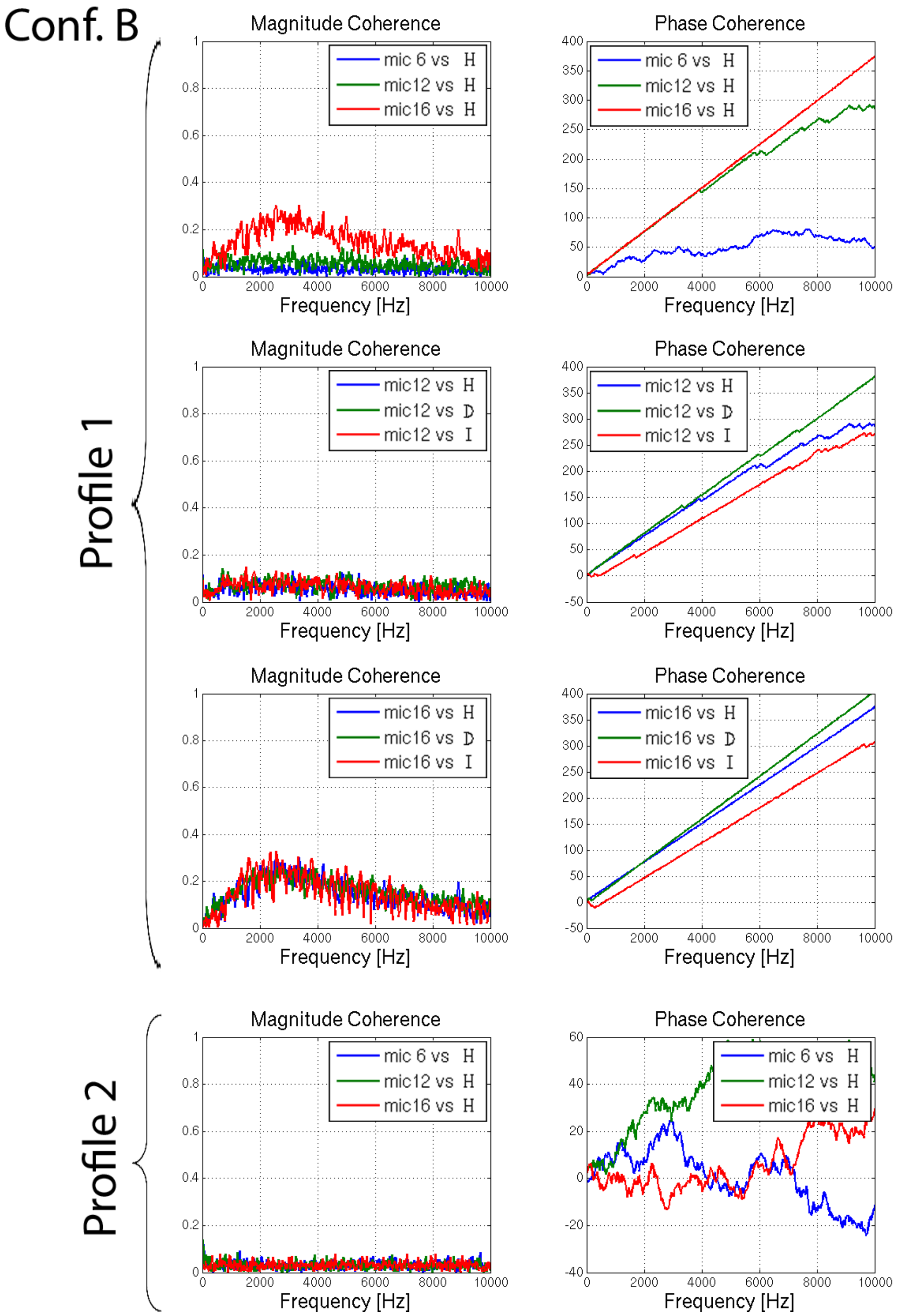

Figure 4.23: Coherence between flush-mounted and far field microphones for the configuration B for the profile 1 and profile 2

The upper row of this figure shows the coherence between the three microphones directly positioned in front of the rain gutter for the three heights and a microphone in upstream far field (named H). The magnitude of the coherence depends on the frequency range. Looking at the coherence magnitude (1st of the figure) the higher coherence is found for the thicker rain gutter at low frequency (under 2 kHz), between 2 and 4 kHz, a higher coherence is found for the medium part while the thinner part shows a good coherence between 4 and 6 kHz. A new increase of the coherence for the thicker part can be observed again for the highest frequencies. This correlates well with the previous remarks from the array maps. The propagation speed computed from the coherence phase was about 340 m/s indicating that the coherence reflects the propagation of sound waves.

The second row of diagrams in figure 4.22 illustrates the coherence between the three FMM microphones behind the rain gutter and the same far field microphone. However, no clear coherence is found which confirms that the noise sources are located in front of the rain gutter. The third row of diagrams in figure 4.22 illustrates the coherence between the flush-mounted microphone **8** placed in front of the rain gutter on the medium section and three far field microphones (H, D and I). In this case, all three show a good coherence between 2 and 4 kHz. This correlation is characterised by a velocity around 300-400 m/s (corresponding to the speed of sound +/- the convection speed depending if the point is in front or behind the rain gutter as well as convection/refraction related differences in the propagation direction of the sound waves compared to the direction between surface and free field microphone). The slopes are therefore also slightly different due to the variation of the distance between the microphones. Finally the fourth row of diagrams in figure 4.22 illustrates the coherence between the same surface microphone **8** and three far field microphones B, H and C having the same elevation but different positions in the spanwise direction. The three points shows good correlations however different propagation speeds are computed. This was also observed when considering the flush-mounted microphone **13** and the same three far field microphones (not shown here). The microphones B and H were found in perfect coherence but not with C. The asymmetrical design of the rain gutter is probably at the origin of this difference however some further investigations should be carried out to better understand these differences.

The coherence between the flush-mounted microphones and the far field microphones for the configuration B are presented in figure 4.23. The first top row illustrates for the profile 1 the coherence of the microphone directly placed in front of the rain gutter for the three different local gutter line sweep angles and the far field microphone (H). The second and third row in figure 4.23 illustrates the coherence functions between the flush-mounted microphones **12** and **16** corresponding to the oncoming flow angle 60° and 90° and the far field microphones H, D, I. Finally, the last row in figure 4.23 shows the coherence for the profile 2 with farfield microphone H. Very low coherence is found. From the first row of figure 4.23 it appears that the higher the angle, the higher the coherence with the far field is. This illustrates that most of the noise is coming from the part which is completely perpendicular to the flow. Looking at the rows 2 and 3 again emphasizes this finding. Generally it appears that the overall coherence for profile 1 in this configuration B is higher than for configuration A. This is explained by the fact that the sound generation in configuration B is spatially more localised as for configuration A, where contributions are relevant along the whole span of the rain gutter. Not presented here, no good coherence was found between the flush-mounted microphones behind the rain gutter and those in the far field. As for the studies of the straight configuration A this finding again supports the statement that the sound generation happens in front of the rain gutter, even for more complex shapes.

c/ Directivity

By computing the acoustic intensity of each far-field microphone the directivity for all cases can be represented. The directivity for both profiles in configuration A is given in figure 4.24 while the directivities for the configuration B are represented in figure 4.25. One can represent the overall directivity over all frequencies but one can also represent the directivity for different frequency bands which has been done here. The acoustic level on this graph is meaningless. For a better understanding, the values have been normalised and a factor was applied to each of them to get the curves on different levels vertically. For these plots the angle 0° is downstream of the rain gutter and the angle 180° is upstream. For the four cases a maximum noise level is found for an angle around 130° at low frequencies. At higher frequencies the behaviour looks more like a monopole. However the low number of far field microphones allows just getting an idea but does not allow to surely assess the directivity. These curves were obtained for an inflow speed of 45 m/s but similar curves were obtained at higher or lower speeds.

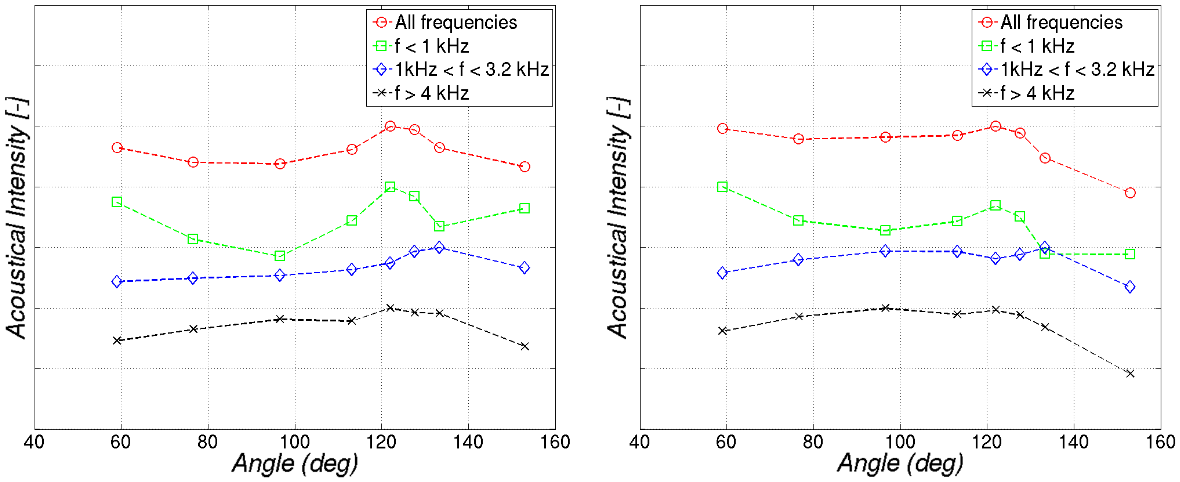

Figure 4.24: Representation of the directivity for configuration A for different frequency ranges: profile 1 (left) and profile 2 (right)

4.5 Numerical analysis

4.5.1 Flow simulations

In order to assess the differences between both profiles steady and unsteady flow simulations have been computed on an extruded section of the same profiles as those used for the experiment. Steady flow simulations were also performed on the same four 3D cases as

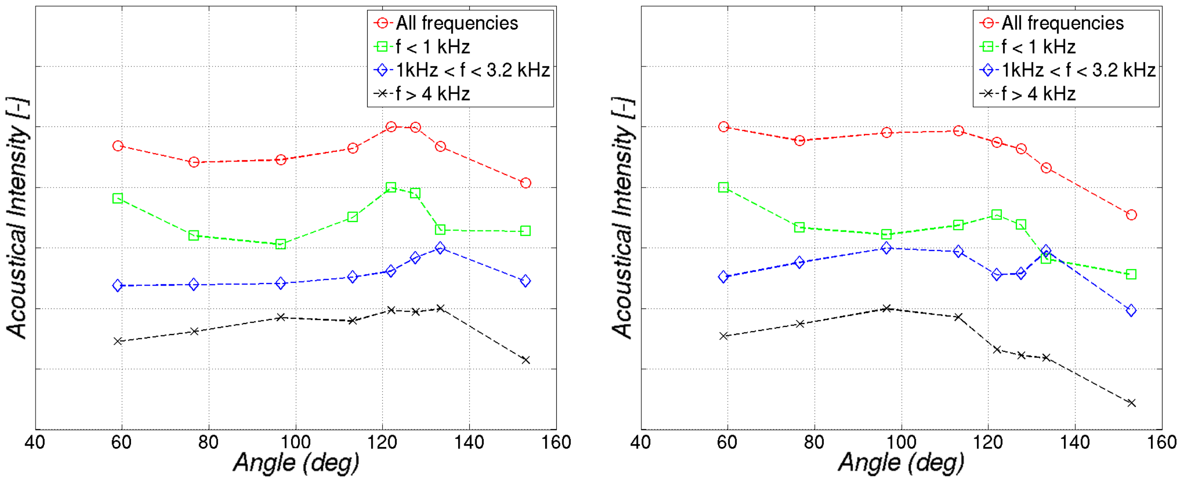

Figure 4.25: Representation of the directivity for configuration B for different frequency ranges: profile 1 (left) and profile 2 (right)

for the experiment (2 rain gutter's shapes × 2 configurations). In addition unsteady flow simulations were carried out on the configuration A with the sharp profile (1). Different turbulence models have been tested and the wall pressure fluctuations compared to the experimental data.

The models have been designed with the software CatiaV5 and the geometry was exported to the ANSYS IcemCFD mesh generator for structured computation grids. Block-structured meshes realised with hexahedral cells were used for this part. Further information on the meshes will be given in the different sections of this work.

a/ Comparison of the profiles

To get a first understanding of the flow topology for both profiles, fluid simulations are performed on an extrusion over 40 mm in the spanwise direction. The height of the rain gutter in this part is about 20 mm.

i. Meshing and set-up

The computational domain is contained in a box of 550 mm × 150 mm × 40 mm and the mesh composed of 3 400 000 nodes, see figure 4.26. The boundary layers are fully resolved with a resolution of y+ = 1, the resulting first cell at the wall is 12 μm. In 3D, the number of cells in the spanwise direction as well as the overall spanwise extent of the grid must be sufficient to avoid any non physical coherent turbulent structures and ensure the coherence of the structures. Spanwise grid spacings of 0.5 and 0.33 mm are respectively used for profiles 1 and 2 to ensure an appropriate coherence of structures in the spanwise direction. Not shown here, a first test on profile 1 with a spanwise grid spacing of 1 mm lead to incoherent results and unphysical large structures.

A uniform free stream velocity of 45 m/s (162 km/h) and a medium turbulence intensity are imposed at the inflow boundary of the computation domain. Based on the height of

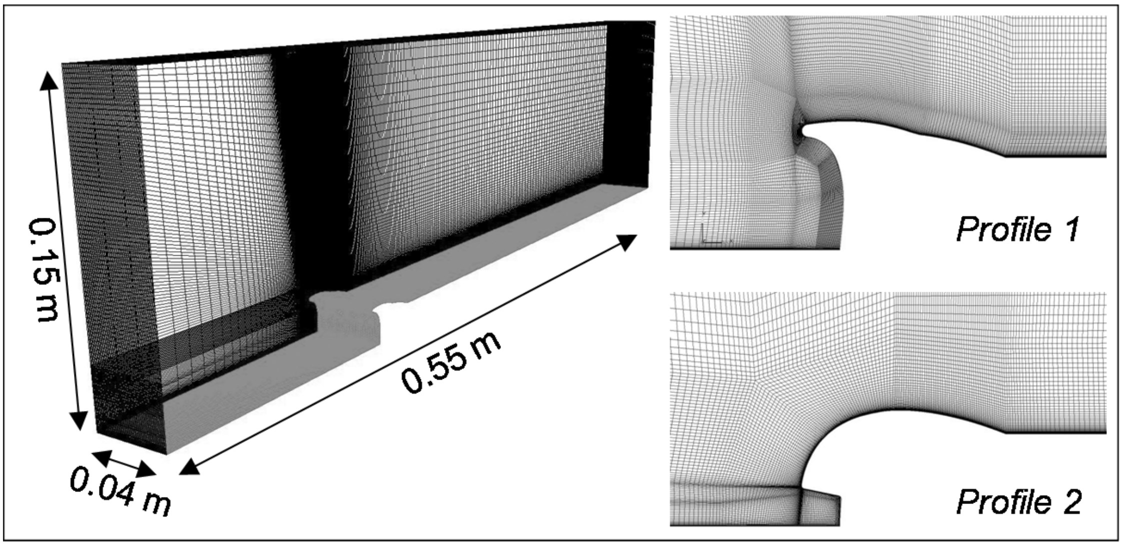

Figure 4.26: Computational 2D domains and meshes

the rain gutter the corresponding Reynolds number is 60 000 and the Mach number is 0.13. Pressure outlet, symmetry and periodic conditions are finally respectively applied to the outlet, the top and the sides of the domain.

The flow fields have been computed with the commercial CFD code CFX. Different models of turbulence have been used to compute the steady flow around the rain gutters while unsteady flow simulations were performed with the DES and SAS methods. A time-step of 5 μs was used to keep the Courant number under the unity. Based on the total length of the domain and the inlet velocity, the average time or geometrical timescale is 0.012 s. The disturbance period based on the rain gutter's height (around 20 mm) and free stream velocity can be estimated to 0.44 ms. Several thousand time steps have been simulated and only the last 0.1 s (20 000 time steps, i.e. 227 cycles) have been used to calculate the spectra data. This allows the turbulence to develop and overcome the start up transients. The pressure fluctuations were registered at four positions.

ii. Results

A representation of the steady flow and a snapshot of the unsteady structures for both profiles computed respectively with RANS SST model and DES are presented in figure 4.27. The simulations show that indeed the recirculation area behind profile 1 is larger than for profile 2 as previously noticed during the experiment. The streamlines are used to represent the steady flow while the variable Q is commonly used in CFD to represent the turbulent structures. The variable Q is defined by:

$$Q = -\frac{1}{2}\frac{\partial u_i}{\partial x_j}\frac{\partial u_j}{\partial x_i} = -\frac{1}{2}\left(S_{ij}S_{ij} - \Omega_{ij}\Omega_{ij}\right) \qquad (4.5)$$

with S_{ij} and Ω_{ij} the symmetric and anti-symmetric parts of the velocity gradient.

A representation of the velocity field and the kinetic energy computed with three different RANS turbulence models (RNG k-ϵ, SST and SST with the transition model implemented in CFX) over profile 1 is given in figure 4.28. The mean flow computed from

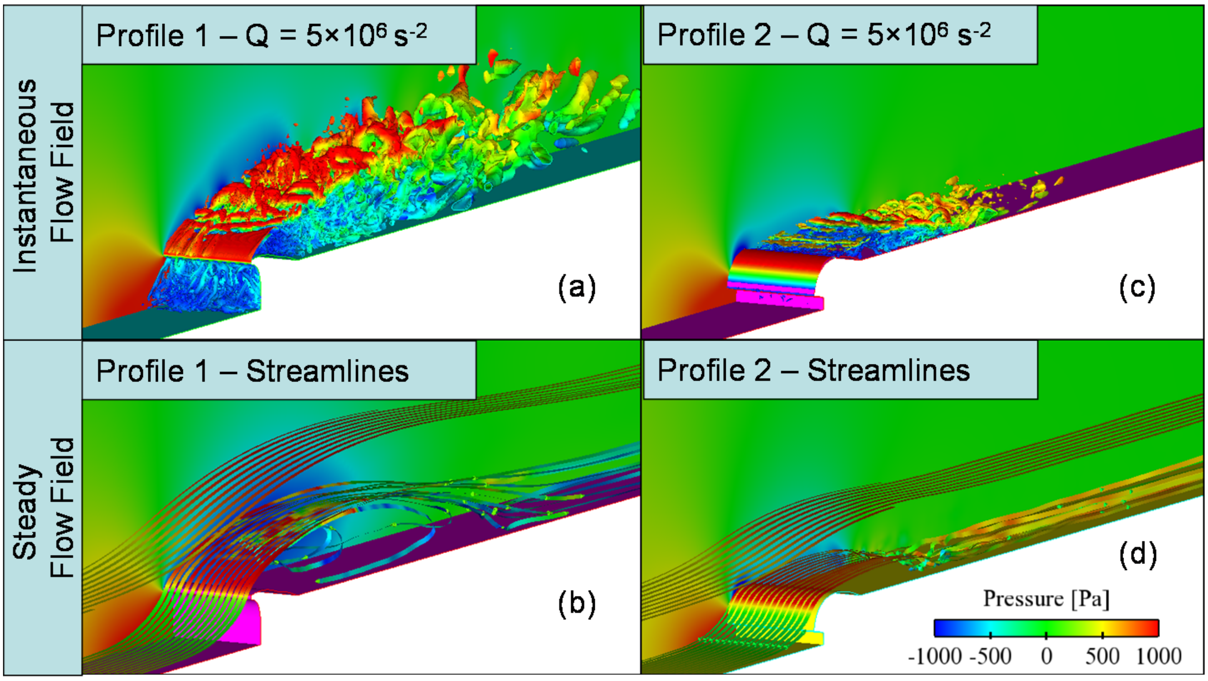

Figure 4.27: Representation of the flow structures and topology for both profiles with a free stream speed of 45 m/s

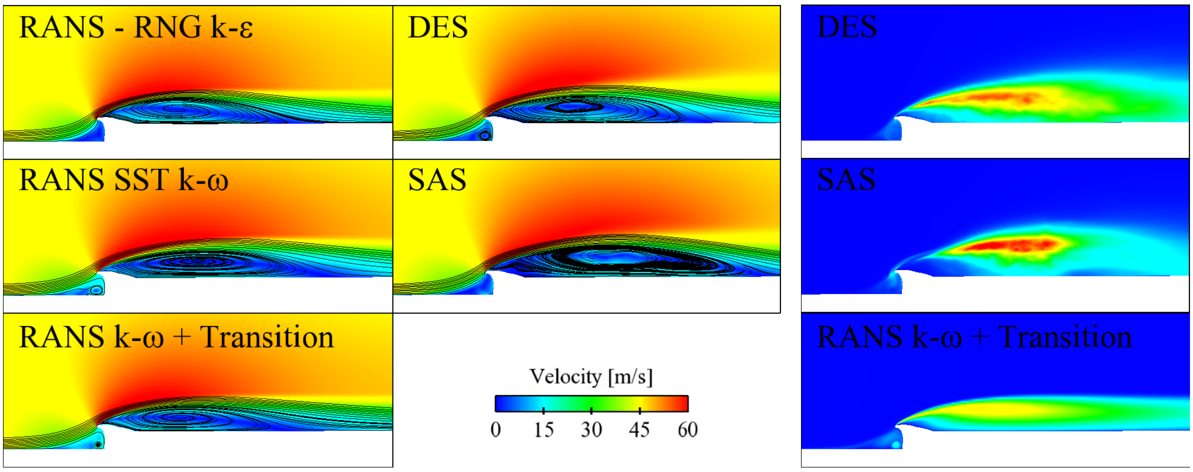

Figure 4.28: Comparison of mean flow velocity fields (left and centre) and turbulence kinetic energy (right) computed with different RANS turbulence models and time averaged data from unsteady flow simulations

the simulations with the DES and SAS models were also added. In all cases a separation occurs and the lengths of the recirculation, gathered in the table 4.2, are found between 16 and 23 cm behind the rain gutter. Both averaged unsteady models show a rather long recirculation area, the shortest one is found for the steady simulation with the transition model. The representation of the kinetic energy shows that the RANS simulation using the k-ω model with the transition model slightly underestimates the kinetic energy level in comparison to both unsteady simulations.

Table 4.2: Length of the recirculation bubble for the different turbulence models (*Tr. = transition)

	Steady RANS			Unsteady	
	RNG k-ϵ	SST	SST + *Tr.	DES	SAS
X_L [cm]	16.5	19.8	16	18.7	23

Compared to the experimental results, the computed lengths of the recirculation are much higher. A thick boundary layer was observed in the experiment while in this case a constant velocity profile was introduced in front of the rain gutter but not far enough to allow the development of a sufficiently thick boundary layer. Therefore a higher flow deviation occurs resulting in a bigger recirculation length. An appropriate velocity profile was used in the following simulations on the 3D cases in order to have the boundary layer thickness similar to the one in the experiment.

Snapshots of the turbulent structures using the variable Q computed with the DES and SAS for profile 1 and DES for profile 2 are presented in figure 4.29. If unsteady structures are computed in all three cases the turbulent structures computed with SAS appears less energetic and bigger than the structures computed with DES. The analysis of the flow shows that the frequencies of the breaking-off of the shear layer (see figure 4.30) for both profiles corresponds to St = 0.75 and 1.35 for the profiles 1 and 2 respectively.

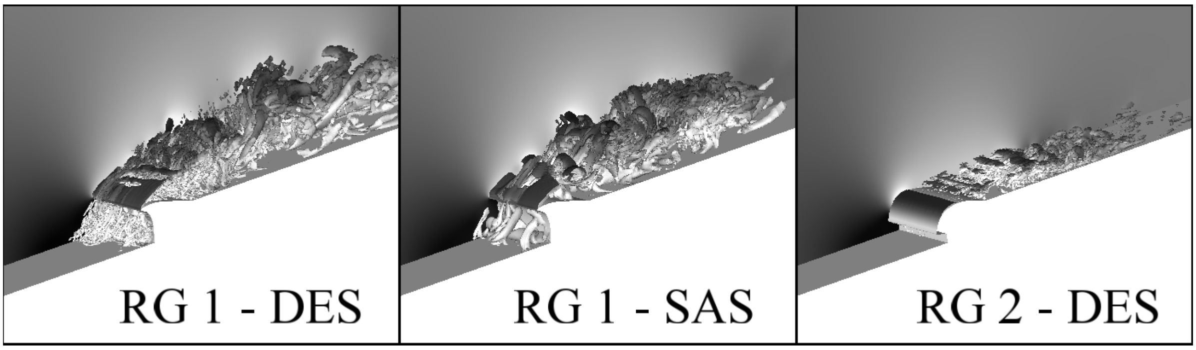

Figure 4.29: Unsteady simulations computed with different models, profile 1 with DES and SAS and profile 2 with DES

As mentionned in the set-up, the surface pressure fluctuations computed by the DES and SAS model generated by the unsteady flow over profile 1 have been registered at two positions in front of the gutter and two positions behind. These positions are identical to the ones use in the experiment (X = - 87 mm (point 2), - 17 mm (point 3), 45 mm (point 4) and 250 mm (point 5)). The signals were registered after a transient phase for a duration of about 0.1 s (20 000 time steps). The computed spectra are presented in figure 4.31. In both cases the measured pressure fluctuations behind the rain gutter (position 4 and 5) appear higher than the computed ones. However, different decays are found in both

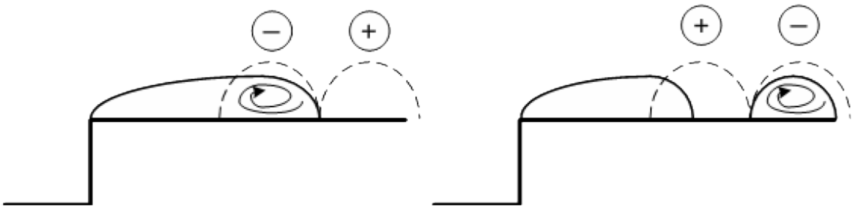

Figure 4.30: Illustration of the breaking-off of the shear layer for a forward facing step [5]

simulations. The decay of the spectra computed with the SAS model is higher than the one computed with the DES model. This illustrates the previous statement that bigger structures were computed by the SAS model than with the DES model. The narrow band spectra computed with the DES data seem presenting the best agreement with the experimental data in opposition with the SAS model. However the decay in the middle range seems slightly too high. A curve with a decay of -1 was added on the graph as reference.

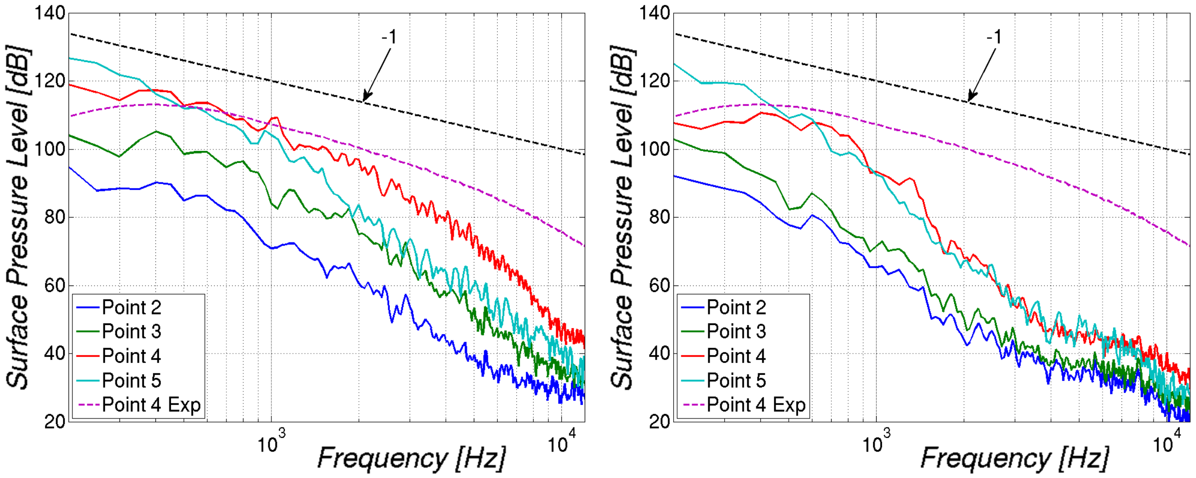

Figure 4.31: Spectra (narrow band) of the surface pressure level computed with DES (left) and SAS (right), Profile 1, 45 m/s

b/ 3D steady flow simulations

i. Set-up of the simulations

Steady flow simulations have been performed on the four cases (2 configurations × 2 profiles). The meshes used for the simulations are composed of two domains linked by a non-conformal interface (GGI). A low Reynolds number (i.e. highly resolved up to the wall) mesh was created for the core domain while a coarsened mesh was used for the outer domain. The nozzle of the wind tunnel as well as a large part of the experimental set up is also modelled in order to reproduce with the most fidelity the experimental conditions.

The domains are depicted in figure 4.32 and further information may be found in table 4.3. A mesh size of 25 to 28 mm was used in the spanwise direction.

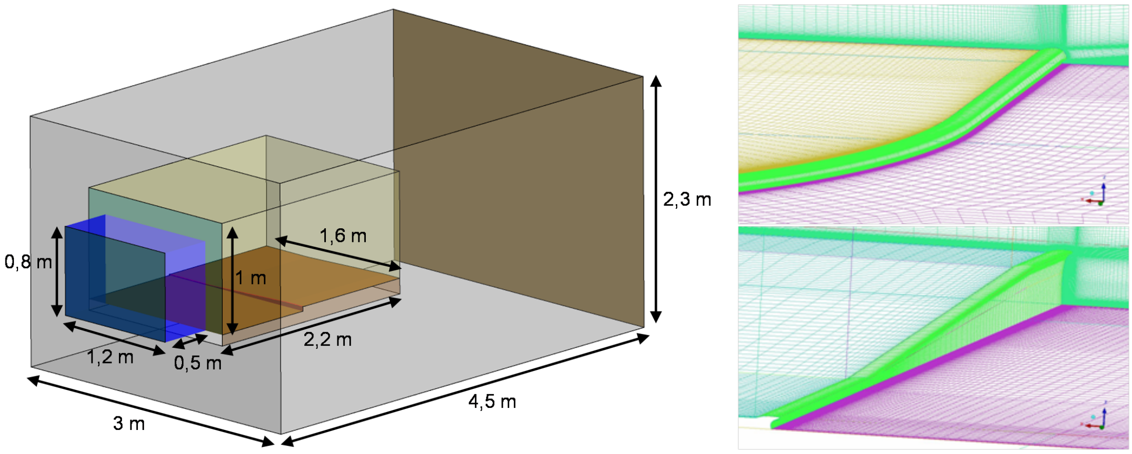

Figure 4.32: Computational 3D domains and meshes

Table 4.3: Number of nodes for each configuration

	Profile 1	Profile 2
Configuration linear (A)	Inner: 4 520 000 nodes (6 070 000 in total)	Inner: 4 900 000 nodes (6 500 000 in total)
Configuration curved (B)	Inner: 4 590 000 nodes (5 960 000 in total)	Inner: 4 520 000 nodes (5 910 000 in total)

To reproduce with the most fidelity the experimental conditions and adjust the height of the boundary layer in front of the rain gutter, an averaged velocity profile was applied at the inlet of the computational domain. Three flow speeds were tested: 30 m/s, 45 m/s and 60 m/s. The corresponding Reynolds numbers are gathered in table 4.4. At X = -1 m and -0.57 m similar velocity profile were obtained as the ones measured experimentally. In these conditions the boundary layer profile should be more realistic as in the previously discussed simulations.

Table 4.4: Reynolds number based on the rain gutter's height for the 3 studied sections

Inlet Velocity	Rain gutter 1			Rain gutter 2		
	0.66 H_1	H_1	1.6 H_1	0.61 H_2	H_2	1.67 H_2
30 m/s	26 500	40 000	64 000	22 500	26 000	60 500
45 m/s	40 000	60 500	97 000	33 500	54 000	90 500
60 m/s	53 000	80 500	129 000	44 500	72 500	121 000

ii. Results

The friction line patterns of configurations A on the thicker half span of the rain gutter

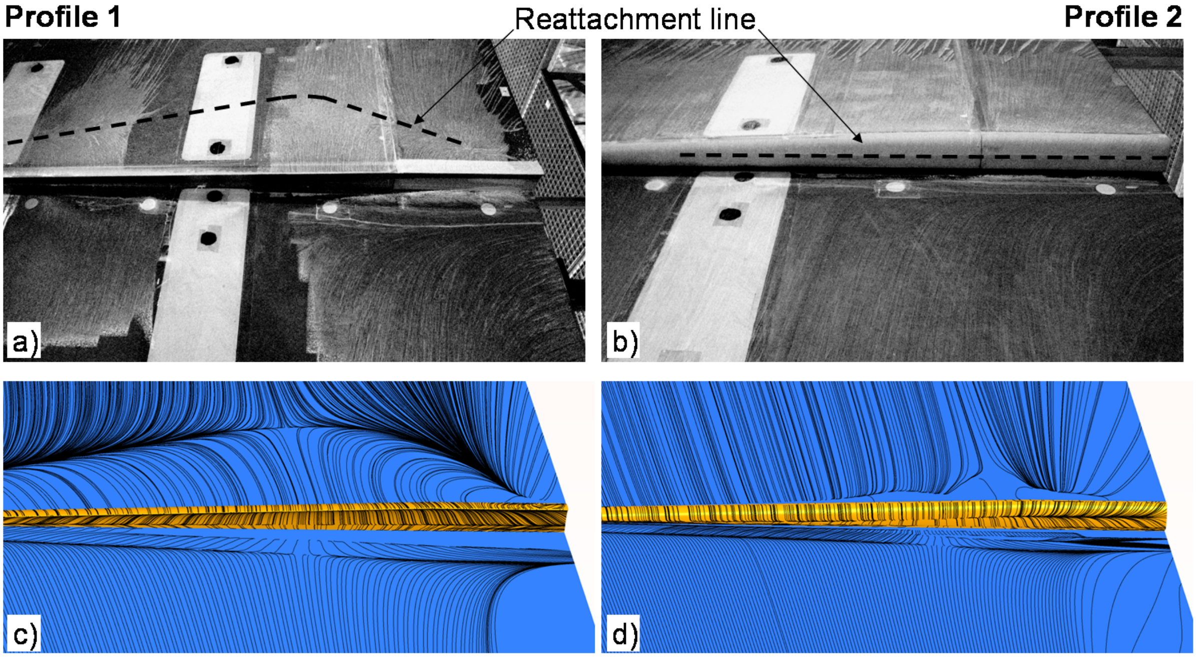

Figure 4.33: Friction line pattern of the 3D linear configurations of both profiles from experiments (1st row) and numerical simulations (2nd row)

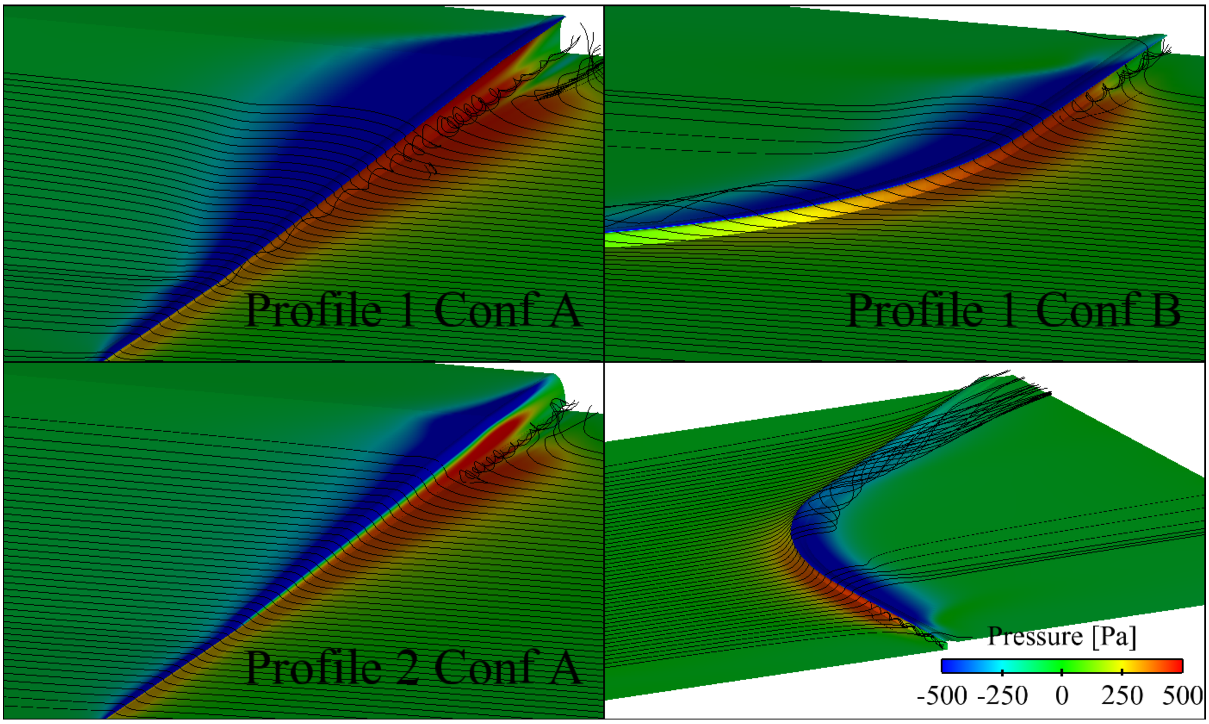

Figure 4.34: Representations of the 3D flow paths

for both profiles obtained experimentally (oil visualisation) and from the simulations are represented in figure 4.33.

The size of the recirculation area in front and behind the rain gutter increases almost linearly with its height (maximum separation length on the left hand side picture). Close to the right side edge of the rain gutter, the streamlines are highly deviated towards the spanwise direction showing another 3D effect which is explained with the wind tunnel shear-layer impinging on the gutter. Compared to the previous quasi 2D cases the plate behind the rain gutter was a bit higher reducing the size of the recirculation and leading for the profile 2 to almost no recirculation behind the rain gutter. On profile 2 one can also see that the reattachment line occurred on the middle of the thicker part of the rain gutter which is confirmed by the flow visualisation.

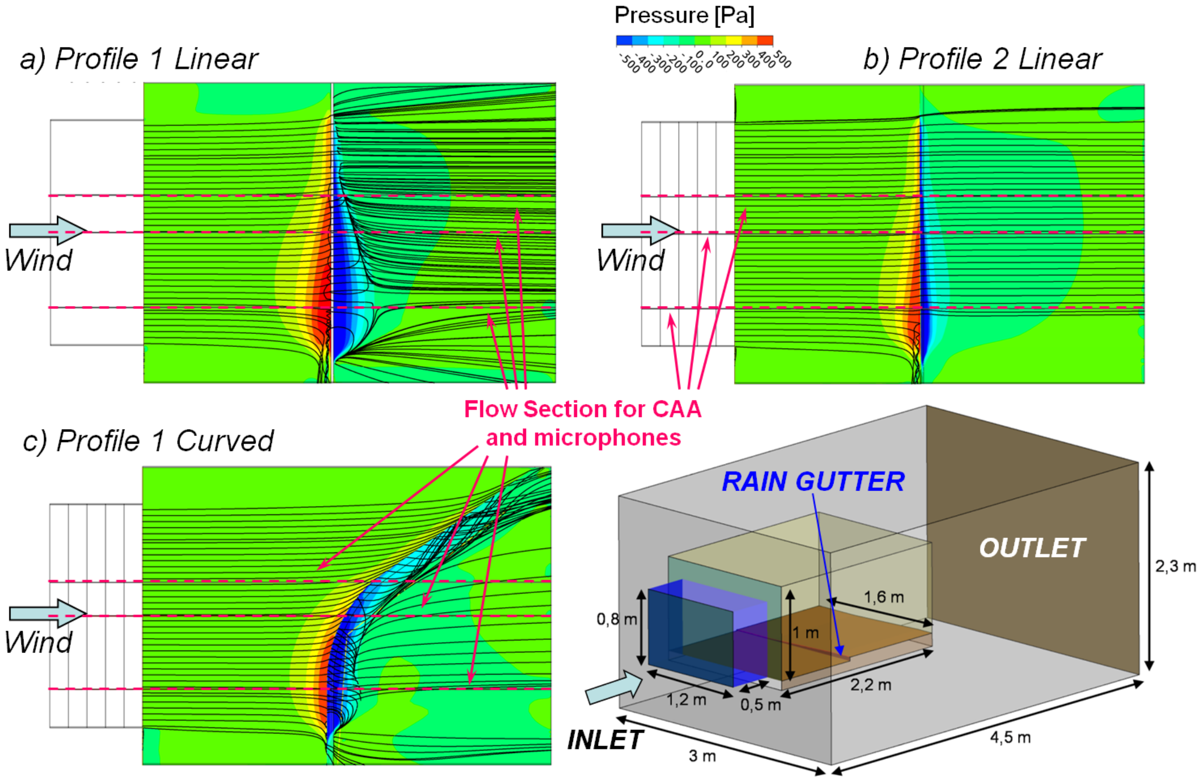

Figure 4.35: Flow topology (surface streamlines) of 3 different cases: profile 1 configuration A (top left), profile 2 configuration A (top right) and profile 1 configuration B (bottom left)

Figures 4.35 and 4.34 illustrate the flow pattern for three different configurations. The red lines in figure 4.35 depict the sections investigated further and also presented in figure 4.36. A recirculation area having a maximum length of about $6h$ (h being the rain gutter's height) was observed for profile 1. This value agrees well with the common value between 5 and 8 found in the literature for forward facing steps. Looking from the top, it can also be seen that only small cross flow effects occur at configuration A while for the curved configuration (B) a clear deviation of the flow direction can been seen upstream the rain gutter.

In configuration B, the inflow angle tends to reduce the size of the recirculation and a vortex is formed along the rain gutter which is not without reminding an A-Pillar vortex. One can finally notice that the thickness of the boundary layer in front of the rain gutter is almost as high as the rain gutter itself as desired.

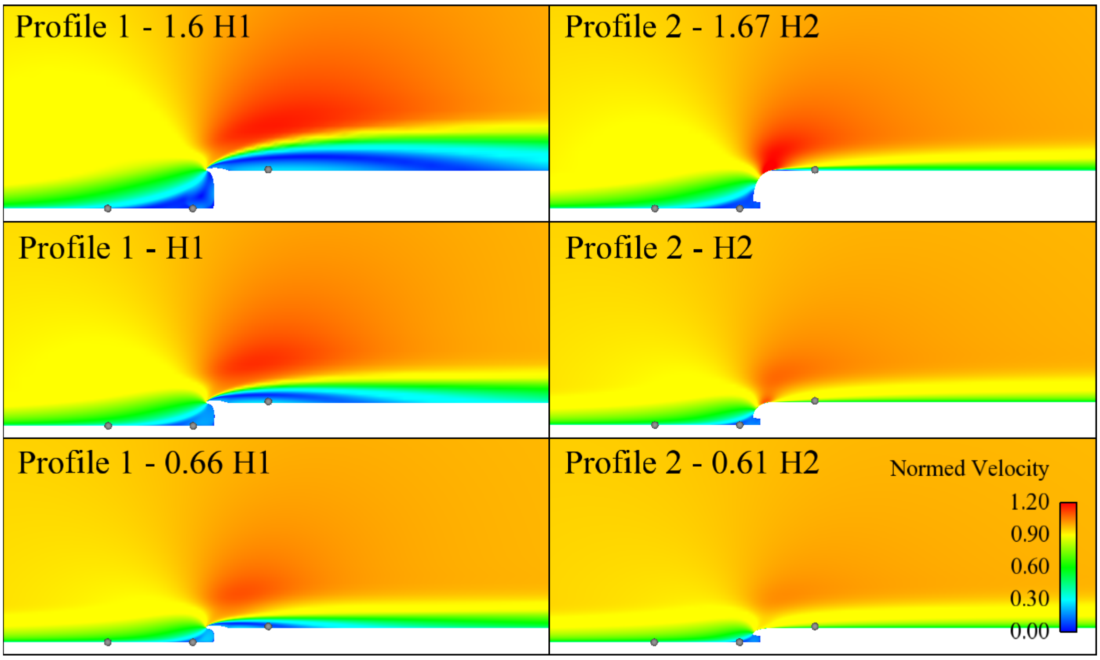

(a) Effect of the rain gutter's height for both profiles

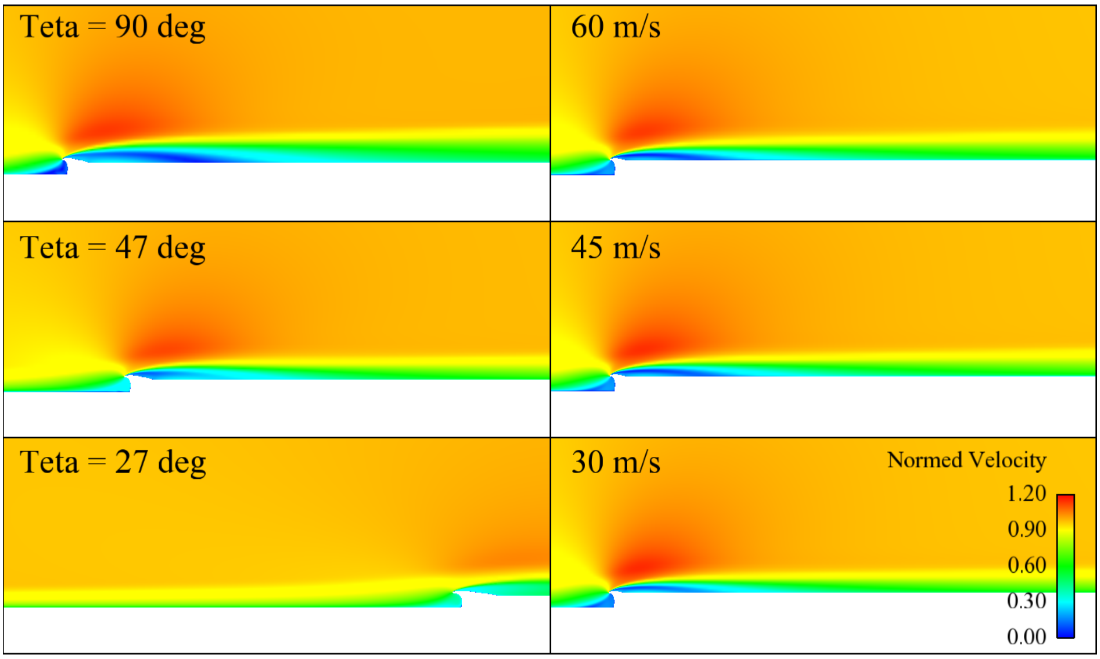

(b) Effect of the oncoming flow angle (left) and speed (right) for profile 1

Figure 4.36: Evolution of the flow topology against rain gutter's shape and height, flow angle and airspeed

c/ Unsteady 3D computations

i. Methodology and set-up

As explained in the first chapter, the pressure and velocity variations are a measure of the acoustic sources. For an unsteady computation, the resolution of the previous meshes is too low particularly in the spanwise direction. A complete refinement of the whole domain would on the contrary not be realistic since it would lead to a far too high nodes number. It was then decided to only compute the unsteady flow in a 100 mm wide box centred around the middle of the rain gutter, see figure 4.37. The spanwise slope of the rain gutter does not allow using spanwise symmetry or periodic conditions; therefore an interface between blocks representing different resolution levels was used. In total 3 domains were then created and linked via non-conformal interfaces. Due to the high cost of the simulations, only the linear configuration with profile 1 was meshed and simulated. As previously observed during the test, this corresponds to the noisier case with apparently the bigger recirculation area compared to profile 2.

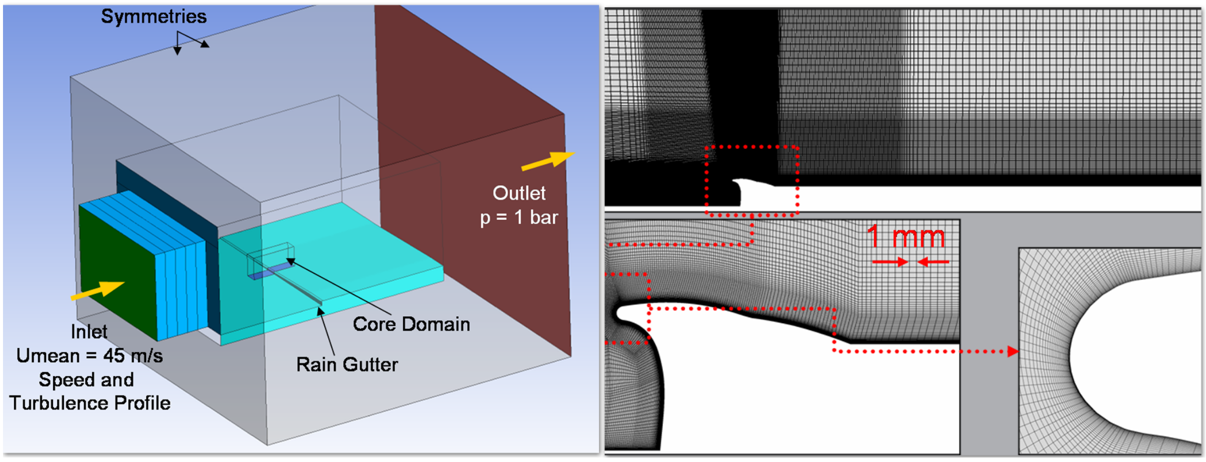

Figure 4.37: Computational CFD domain and zoom on the mesh in the core domain

The core domain (centred on the middle of the rain gutter, i.e. medium section) consists in a hexahedral block structured mesh of about 7 000 000 nodes (400 $mm \times$ 200 $mm \times$ 100 mm). The maximum size of the cells is 10.3 mm, allowing theoretically a resolution of the acoustic signal up to 16 kHz. The second and outer domains are composed respectively of 1 120 000 and 273 000 nodes resulting to an overall number of about 8 400 000 nodes.

Both DES and SAS formulations are used for the computation. A hybrid scheme switching automatically from second order upwind in RANS regions to second order central differencing in scale-resolved regions is used for the convection. The time step used for the simulation is 10 μs, maintaining a Courant number around 1. Thus, an averaged velocity profile corresponding to 45 m/s as well as an appropriate turbulence viscosity ratio is used at the inlet and an average static pressure condition is placed at the outlet. Based on the total length of the domain and the inlet velocity, the average time or geometrical timescale is 0.1 s. The disturbance period based on the rain gutter's height (around 20 mm) and free stream velocity can be estimated to 0.44 ms. Several thousand time steps have been simulated and only the last 140 ms (1400 time steps) have been used to calculate the spectra data. This allows the turbulence to develop and overcome the start up transients. According to Rung et al. [102], the numerical simulation requires 12 time steps per oscillation period to accurately represent the harmonic disturbances which gives here a limitation for the maximum frequency of 8.3 kHz (i.e. $1/(12 \times \Delta t)$). Using an overall simulation time of 140 ms, the minimun captured frequency is expected around 7 Hz.

ii. Results

Figure 4.38 gives a representation of the unsteady structures computed with DES and SAS by means of the variable Q at $5 \times 10^6 s^{-2}$ at some given point in time (snapshot). As the boundary layer was already fully developed in front of the rain gutter, a smaller recirculation particularly for profile 1 is expected.

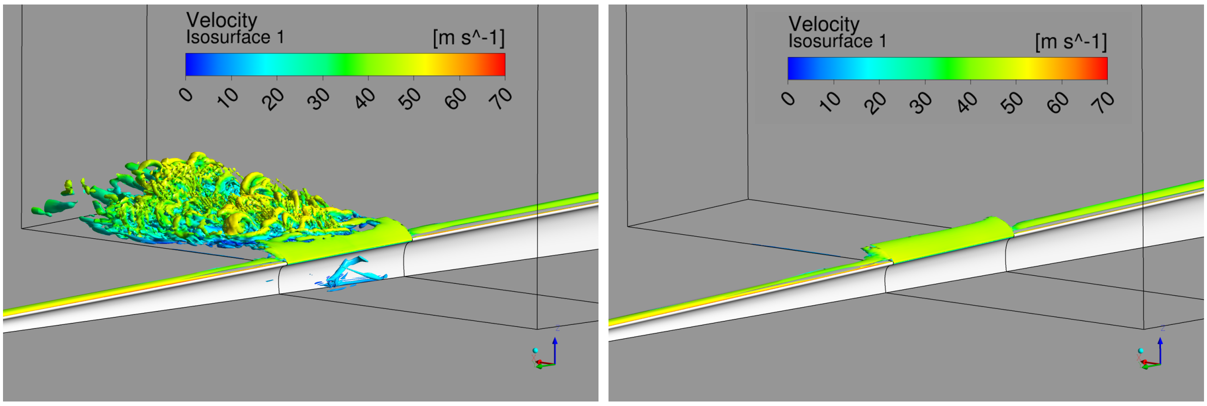

Figure 4.38: Snapshot of the turbulent structures using the isosurface of Q over profile 1 coloured with the velocity simulated with DES (left) and SAS (right)

A snapshot of the turbulence field computed with DES is presented in figure 4.38 (left). Compared to the simulations of the quasi 2D cases (see figure 4.29) also computed with DES, the structures in front of the rain gutter were here not so well resolved even if those behind the gutter seems to be reasonably well represented. This was observed although similar spanwise resolution was used. Two elements might be at the origin of these differences: the higher thickness of the boundary layer in this case which damps the instabilities and does not generate resolved turbulence before the rain gutter, the mesh might be too coarse for capturing all the frequencies.

The results of the simulation performed with the SAS-SST model delivers a quasi steady solution, figure 4.38 (right). Outlined by Davidson [29] and Menter [80] as a limitation of the SAS-SST model, in some cases, the flow can be too stable to switch in an unsteady mode and therefore provide a quasi steady solution. The large thickness of the boundary layer seems to be once again an important element of explanation as in the previous 2D extruded cases (computed for smaller boundary layer thickness), unsteady structures were well simulated. To overcome this difficulty, the new SAS with forcing model (SAS-F) introduced by Menter [80] and implemented in the development version of Fluent 12 has been used. The idea is here to introduce forcing terms in the momentum equations in order to transfer modelled turbulent energy into the resolved energy for flows which do not exhibit sufficiently strong instability to switch to unsteady mode. Therefore, a volume stochastic source term and a volume sink term are introduced in the momentum equations (cf. section 2.2.6.d) in a confined flow region defined by the user. Different attempts with different regions were tried but it was found that the best results were obtained for a zone of the height of the rain gutter and extending from the beginning of the core domain to the rain gutter. Thanks to this model, more turbulent structures were then simulated, see figure 4.39.

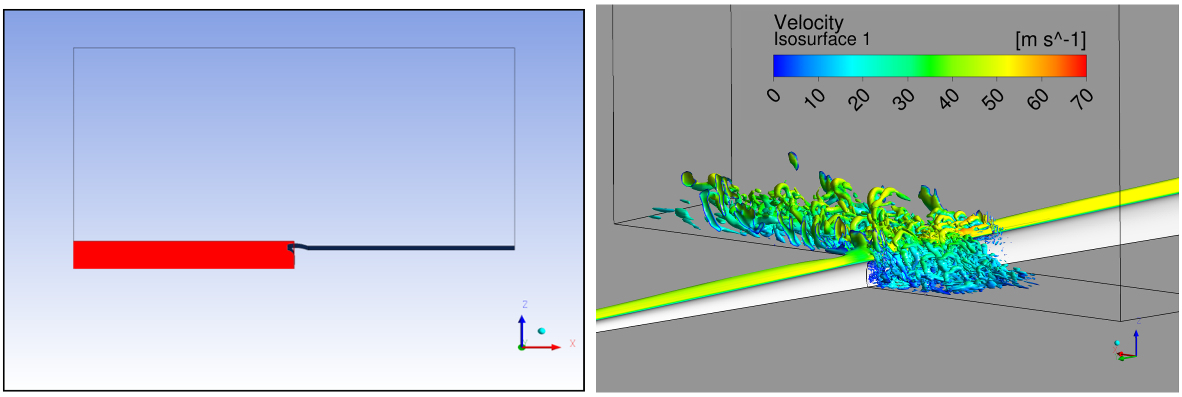

Figure 4.39: Representation of the forcing area (left) and snapshot of the turbulent structures using the isosurface of Q over profile 1 coloured with the velocity simulated with SAS with forcing(right)

The surface pressure spectra at the locations of the flush mounted microphones were computed using the formalism of Welsh and compared to the measured data in figure 4.40. A duration of 140 ms for the SAS and 96 ms were simulated for DES. Points 1 and 5 are actually placed outside the core domain, therefore in an area where the mesh is too coarse to capture the structures. The point 2 seems also too far upstream to the rain gutter. At point 3, the SAS-F presents a good agreement with the experimental results while for the DES simulation, the pressure fluctuations are under-evaluated confirming the inability of the model to catch the fluctuations in front of the rain gutter. For point 4, the SAS-F again shows a good agreement with the experiment. Here the results of the DES simulation provides a good agreement with experimental results only up to 2 kHz. After 3 kHz, on all DES spectra, a dramatic increase of the slope can be observed which might indicate a cut-off frequency due to the mesh resolution ($\sim$ 1 mm). This tends to confirm the lower dependency of the SAS model to the size of the mesh.
Note: one can evaluate the effect of the duration of the signals by computing the spectra for different signal lengths. Instead of taking the overall length (22 s) of the experimental signal, multiple signals with the duration of 100 ms (similar to the CFD signals) have been used to compute the spectra gathered in appendix. This illustrates the influence of the duration of the signals as well as the tolerance which should be observed when comparing the experimental results with the CFD results.

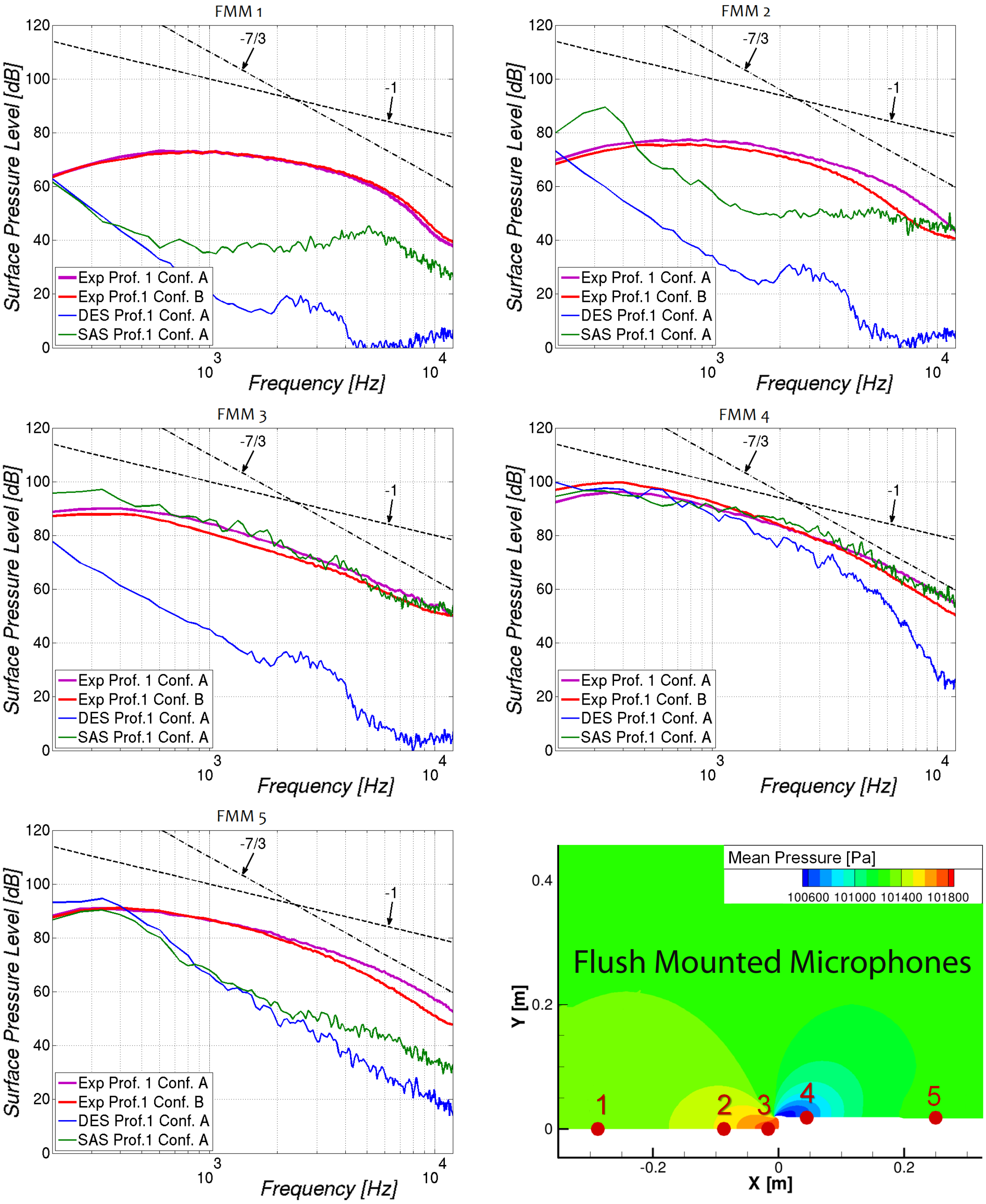

Figure 4.40: Comparison of the surface pressure level (experiment and CFD)

d/ Proper Orthogonal Decomposition (POD)

i. Definition

The Proper Orthogonal Decomposition (POD) technique was introduced in the late sixties by Lumley [74] in the context of fluid mechanics and is attractive in terms of identification of coherent structures. It offers the possibility of providing an optimal basis while the capturing the maximum of energy with few modes only by yielding a set of eigen-functions, which describes the dominant behaviour or dynamics of a given problem. The aim of POD is therefore to obtain a set of functions such that the average difference between the original flow and the reconstructed flow is minimised.

Closely related to POD the singular value decomposition (SVD) method is a mathematical method which enables to separate any set of data stored in a $m \times n$ matrix A to be rewritten such that $A = U\ S\ V^T$.

- U is an orthogonal matrix (size $m \times m$) such that $U^T\ U = 1$.
- V is an orthogonal matrix (size $n \times n$) such that $V^T\ V = 1$.
- S is a diagonal matrix (size $m \times n$) such that $S_{ij} = 0$ for $i \neq j$ and whose diagonal components are arranged in decreasing order and corresponds to the singular value σ_f of A.

The goal of POD is to obtain a modal system such that the difference between the original flow set $p(\mathbf{x}, t)$ and the computed POD modes $\phi_i(\mathbf{x})$ is minimised: $\left\|(p(\mathbf{x}, t) - \phi_i(\mathbf{x}))^2\right\|$ This is equivalent to maximising the correlation between the orthogonal modes and the original data set. The problem corresponds then to solve:

$$\int \left\langle p(\vec{x}, t)p(\vec{x'}, t)\right\rangle \cdot \Phi_i(\vec{x'})d^3(\vec{x'}) = \lambda_i \cdot \Phi_i(\vec{x}) \tag{4.6}$$

with $\left\langle p(\vec{x}, t)p(\vec{x'}, t)\right\rangle$ the spatial correlation (R_x) of the original data set z, Φ_i the spatial eigenvectors defining the shapes of the dominating modes and λ_i the eigenvalues defining the amplitude of these modes.
Equivalently, this can be written as:

$$(A\ A^T)U = \Omega\ U \tag{4.7}$$

with A the matrix representation of the original data z, U the matrix containing the spatial correlation eigenvectors (ϕ_i) and Ω the eigenvalues (λ_i).
From this equation one can then compute the spatial eigenvectors without computing the temporal ones (which can then be easily found using the relation $A = U\ S\ V^T$). The correlation matrix $(A\ A^T)$ has then a size of $m \times m$. This is particularly convenient for cases with high number of time steps but lower number of mesh nodes.

On the contrary the same methods can be used for cases where the number of mesh nodes is much higher that the number of time steps. The problem can then be written as:

$$(A\ A^T)U = \Theta\ V \tag{4.8}$$

with A the matrix representation of the original data z, V the matrix containing the temporal correlation eigenvectors (ε_j) and Θ the eigenvalues (μ_j).

Using the previous equation $A = U\ S\ V^T$ one can write:

$$A^T\ A = (U\ S\ V^T)^T \times (U\ S\ V^T) = V\ S^T\ \underbrace{U^T \times U}_{1}\ S\ V^T = V\ \underbrace{S^T \times S}_{\Theta}\ V^T \tag{4.9}$$

This gives $\left(A^T\ A\right) V = V\Theta$ which shows that $V\Theta = \Theta V$.

A major characteristic of the method is that the eigenvalues are equal in both cases for the same indices i and j: $\mu_j = \lambda_i = \sigma_f^2$ for $i = j$. The temporal eigenvector matrix V can be computed from the eigen-problem: $R_t\ V = \Theta\ V$. The spatial eigenvector matrix U can be obtained solving $U = A\ V\ S^T$. This method known as the method of snapshots delivers the same eigenvector matrix as directly with the spatial correlation matrix but save an important number of operations.

The field can then be reconstructed such that:

$$p(\mathbf{x}, t) = \sum_{i=1}^{n} \varphi_i(t)\lambda_i\phi(\mathbf{x}) \tag{4.10}$$

with φ_i the temporal eigenvectors, λ_i the eigenvalues and ϕ_i the spatial eigenvectors.

ii. POD analysis

In this section the POD was applied to a 2D section of the aerodynamic field computed with DES for both profiles, see figure 4.29. 500 timesteps were used for the computation. The pressure field at one time step for 99% of energy is represented in figure 4.41. A very good agreement is found between the reconstructed field and the original field without mean. On the POD the mean field was suppressed. The remaining 1 % of energy corresponds to very fine structures.

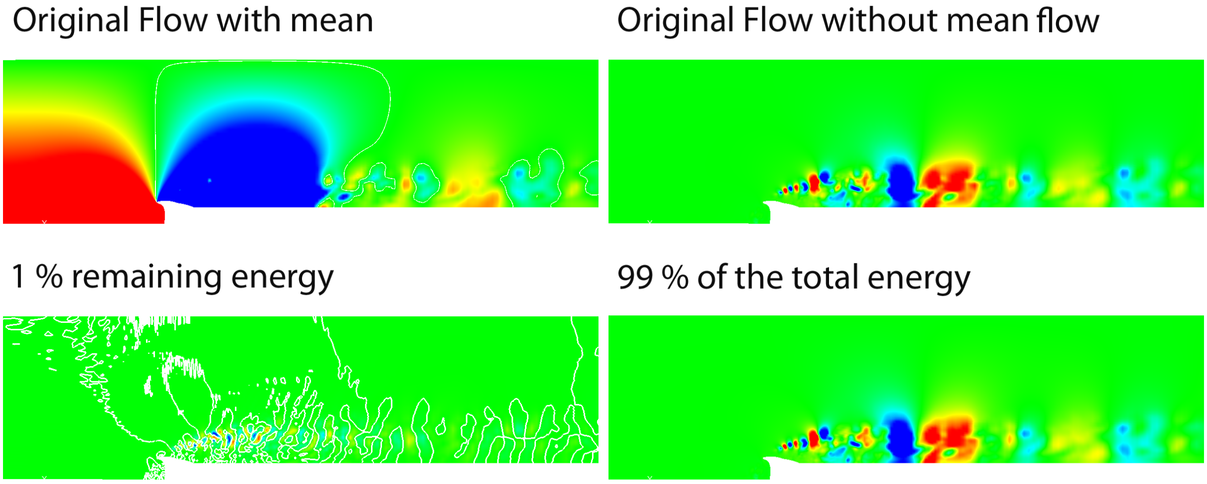
Original Flow with mean

Original Flow without mean flow

1 % remaining energy

99 % of the total energy

Figure 4.41: Original pressure field with and without mean (top left and right) and reconstructed pressure field using 99 % of the total energy (bottom right) as well as the remaining 1 % (bottom left)

This study shows that the correlation eigenvalues are directly linked to the energy of the flow. Hence it is possible to recreate the flow following specific modes in order to obtain a desired percentage of the total flow energy. The energy of the POD decreases extremely rapidly with increasing mode number enabling the reconstruction of the flow with a minimum number of modes and offering equivalent if not identical information concerning the flow. The number of modes necessary to obtain a certain percentage of the total energy can be normalised by the total number of modes N used for POD. Depending on the level of energy required this number stagnates and a threshold under which the reconstructed flow will always contain at least x% of the total energy can be defined. The frequency of the temporal eigenvectors increases with mode number. The POD eigenvectors and eigenvalues are specific to the time steps chosen to perform the POD. Therefore from one time step range to the next, different coefficients or spatial eigenvector values will be found. The reconstructed flow offers then a representation of the original flow with equivalent information but for a lower quantity of data. Finally as the POD technique inherently removes the stationary mode and only deals with the fluctuations, the flow structures are therefore immediately visible.

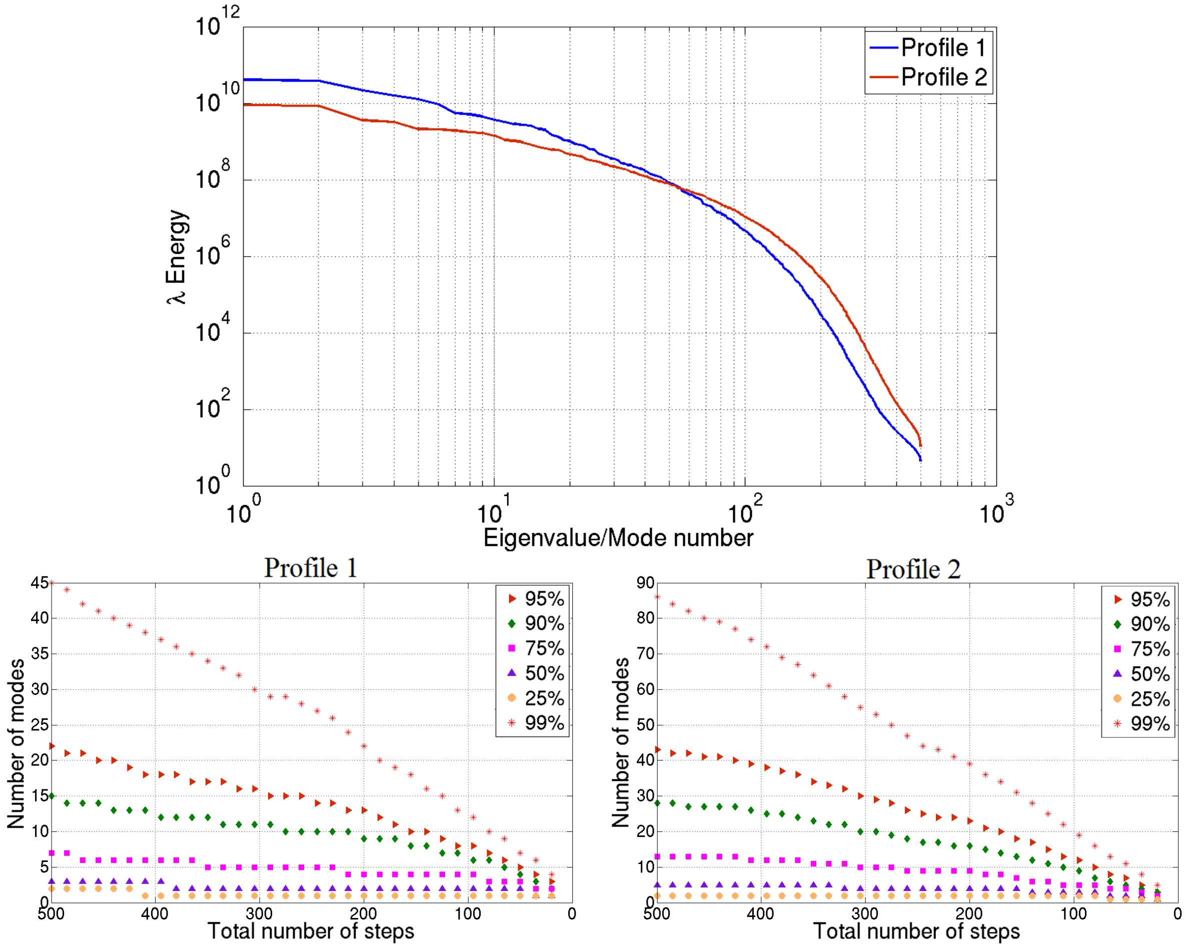

Figure 4.42: Modal energy distribution for both profiles (top), representation of number of modes necessary to reconstruct a signal with a given percent of initial total energy against the initial number of time steps for profile 1 (left) and profile 2 (right)

A representation of the modal energy distribution for both profiles shows that the first modes of profile 1 are more energetic than those of profile 2, see figure 4.42 (top)[2]. In

---

[2] Quentin Behagel, Master Thesis at Volkswagen, September 2009

addition the number of modes necessary to reconstruct a certain percent of total energy against the number of time steps considered is plotted in the bottom part of figure 4.42. It shows that 15 modes are necessary to reconstruct 90% of the total energy for profile 1 while almost twice as many modes (28) are necessary for profile 2. The analysis of the temporal eigenvectors shows that the frequencies of the first coefficients for the profile 2 are higher than the profile 1. Assuming that in general large structures are characterised by low frequency and smaller structures by higher frequencies, one can guess that the dominant structures for profile 2 are smaller than those for profile 1.

4.5.2 Acoustic simulations

a/ Simulations based on unsteady CFD simulations

A wide range of CAA methods was presented in chapter 2. Many of them are based on the solution of a propagation equation to compute the radiated field generated by unsteady acoustic sources previously computed by an unsteady compressible or an incompressible flow simulation. Two methods based on this technique have been used in this work. The first method consists in solving the APE system implemented in the code PIANO to compute the radiated acoustic field. The second method is based on a variational formulation of the Lighthill's equation. This approach was followed by the developers of the company Free Field Technologies and was implemented in the software Actran/LA. LA stands here for *Lighthill Analogy.* The sources take different formulations in the two approaches and need to be firstly computed before to solve the propagation equations. Both methods will be applied to compute the 2D acoustic field radiated by profile 1. The results of the unsteady simulations computed with the SAS-Forcing model were used to compute the appropriate acoustic source terms.

i. Computation with PIANO/APE

Methodology : Proposed by Ewert [46] the acoustic perturbation equations have been presented in chapter 2. The APE system corresponds to a modification of the LEE in which vorticity convection modes have been removed. The resolution of the APE system with appropriate source terms allows to compute the radiated acoustic field. The complete formulation of the source terms can be found in [46]. In most applications the sound generation is dominated by the vortex source term which takes the form of the Lamb vector in the APE system. In 2D the Lamb vector can be computed by using the following formulation:

$$L_{2D} = -(\omega_0 \cdot \vec{e}_z \times \vec{u}_t) - (\omega_t \cdot \vec{e}_z \times \vec{u}_0) \tag{4.11}$$

where $\vec{e}_z$ represents the unit vector along the z-axis, subscript "t" stand for *turbulent* and subscript "0" denotes the mean flow.

The process used to carry out a simulation based on the APE system with the code Piano is composed of the following steps, see figure 4.43:

- Compressible or incompressible unsteady flow simulation

- Computation of the mean flow and of the acoustic source term (Lamb vector) at each CFD time step
- Interpolation of the unsteady source terms and mean flow on the acoustic mesh
- Conversion of the files to the PIANO format and preparation of the input files
- Computation of the acoustic field by solving the APE

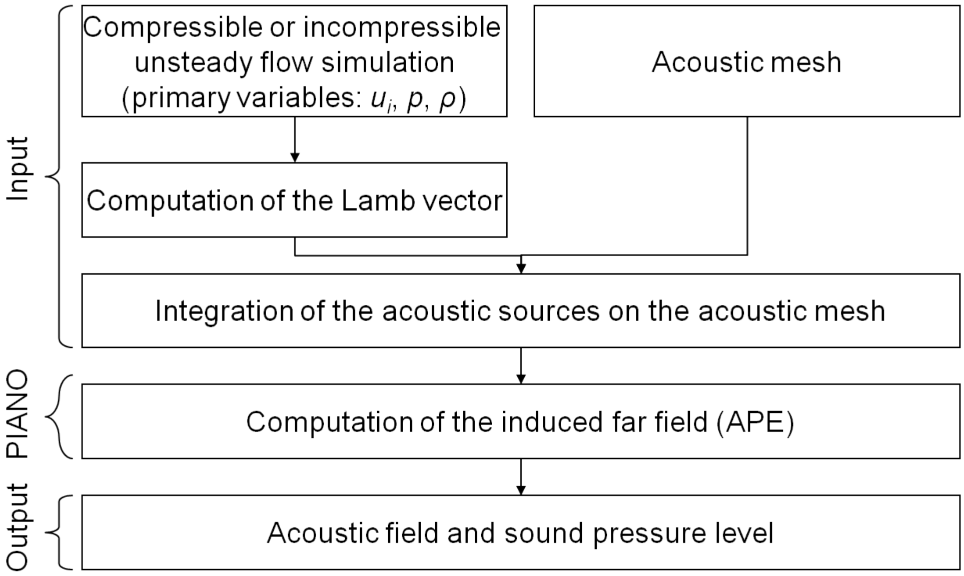

Figure 4.43: Strategy followed for the approach unsteady CFD / APE with PIANO

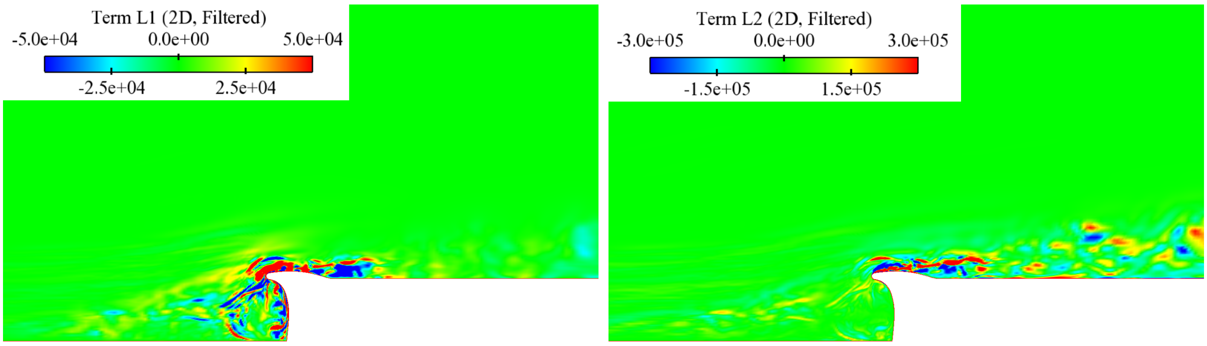

Figure 4.44: 2D representation of the acoustic sources for APE computed for the profile 1: components X (left) and Y (right) of the Lamb vector

Snapshots of the X and Y components of the Lamb vector around the rain gutter are presented in figure 4.44. The 2D Lamb vector was computed on the CFD mesh before to be mapped on a block-structured mesh of 13 blocks centred on the rain gutter and composed of about 370 000 elements, see figure 4.45 (left). The computation of the Lamb vector on the CFD mesh should generally be done before the mapping (1st order interpolation) in order to take advantage of the higher resolution of the CFD mesh around the geometry. The maximal cell size of the acoustic mesh was about 6 mm which when using a 7-point stencil DRP solver allows a resolution up to 8 kHz. The domain corresponds to a half circle of 1.5 m radius.

In order to smoothly reduce the amplitude of the sources when getting away of the rain gutter and avoiding truncation effects of the sources, a spatial filter based on a cosine function was applied, see figure 4.45 (right). The acoustic source terms were then computed by multiplying the Lamb vector field with the filter field. As the unsteady CFD domain was smaller than the acoustic domain the source term was set equal to zero at all the points outside the source area.

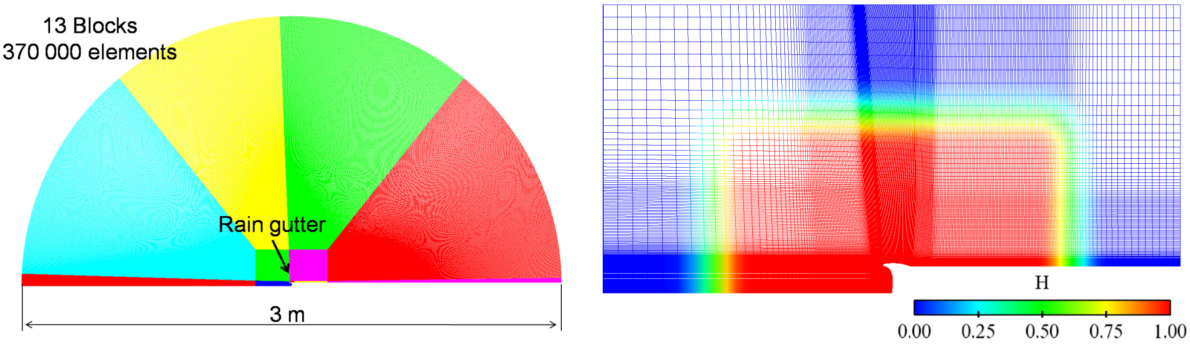

Figure 4.45: CAA mesh and spatial filtering used for the simulation

A dimensionless time step (dimensioned by the speed of sound) was set to 5×10^{-5} [-] to respect the CFL conditions. This value corresponds to a real time step of 0.15 μs. The higher time step of the CFD simulation (10 μs) implies the use of a quadratic interpolation of the acoustic sources at each acoustic time step. A sixth-order accurate implicit Pade filter was used to ensure the stability of the simulation. Several thousand time steps have been simulated and only the last 200 ms (real time) have been used to calculate the spectra data and the radiated acoustic field. This allows the turbulence to develop and overcome the start up transients.

Two simulations have been performed using either a long CFD simulation (140 ms) of about 1400 samples and a lower temporal resolution dt $= 1 \times 10^{-4}$ or a shorter CFD simulation (40 ms) with a higher temporal resolution $1 \times 10^{-5} s$ and about 4000 samples. According to the Nyquist criteria these time steps should allow frequency resolutions respectively up to 5 and 50 kHz. The idea was here to perform two simulations; one for the low frequencies and one for the high frequencies with the appropriate sources. However it was observed that both simulations predicted very similar noise levels in the low frequency range (100 to 500 kHz). Therefore only the results with the shorter simulations are presented.

Results : A snapshot of the radiated acoustic field is presented in figure 4.46. This figure shows an alternance of acoustic waves with different wavelengths. The radiated acoustic field is not symmetrical in front and behind the rain gutter. The asymmetry is due to the mean flow and it demonstrates that the convection is taken into account.

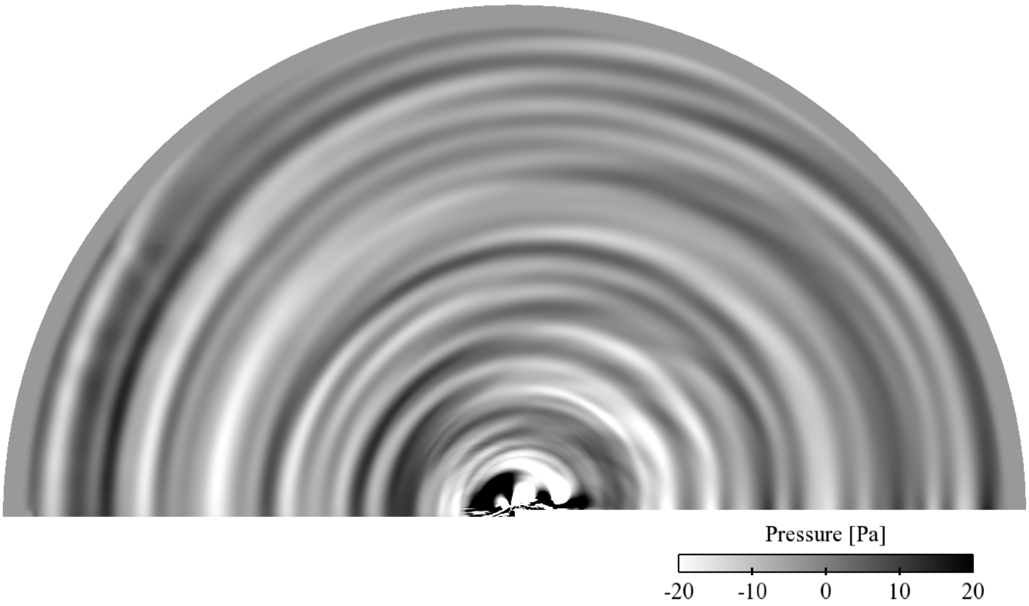

Figure 4.46: Acoustic field computed with APE

The narrow band spectra computed at three far field positions at a distance of 0.5 m from the rain gutter are presented on the left hand side of figure 4.47. The spectra show a broadband character. Above 4 kHz the power spectra density decays proportionally to a law with an exponent of -7/3. One can also rank the noise level measured at the different positions. The higher value is found for the microphones positioned upstream followed by the point situated downstream and finally the point above (90°). This indicates that a minimum is found at the vertical with at least two main directions: one forward and one backward.

The directivity pattern shown on the right side of the same figure was calculated by computing the acoustic intensity at 37 points placed at 0.5 m from the rain gutter. The acoustic intensity was computed using the following formula in order to take into account the convection effect and in which t_1 and t_2 represent the beginning and end times of the signal respectively:

$$I(\phi) = \frac{1}{M\cos\phi + \sqrt{1 - M^2\sin^2\phi}} \frac{1}{t_2 - t_1} \int_{t_1}^{t_2} p^2(r, \phi, t)dt \tag{4.12}$$

here ϕ is the polar radiation angle.

In order to visualise the directivity pattern for different frequency ranges, one can first perform a Fourier transform and compute the acoustic intensity for each frequency range. This was done here and the directivity pattern are represented in figure 4.47 (right). The arrow indicates the direction of the wind. For a better readability the level of the curves were differently scaled and should not be compared in magnitude. The energy level was much lower for the higher frequencies than for the lowest ones. Therefore it would not have possible to see the curves without a normalisation. The directivity pattern obtained when considering all frequencies highlights a main lobe forward and a secondary lobe backward with a minimum for the vertical directions confirming the previous remark. Similar directivity patterns are found when considering the low frequencies (up to 1 kHz) and the middle range. In contrast the directivity pattern obtained for the higher frequency shows a more sophisticated form with more lobes and particularly a lobe in a direction of 50° - 60° forward. A similar analysis will be done with the other methods and will lead to further discussions at the end of this chapter.

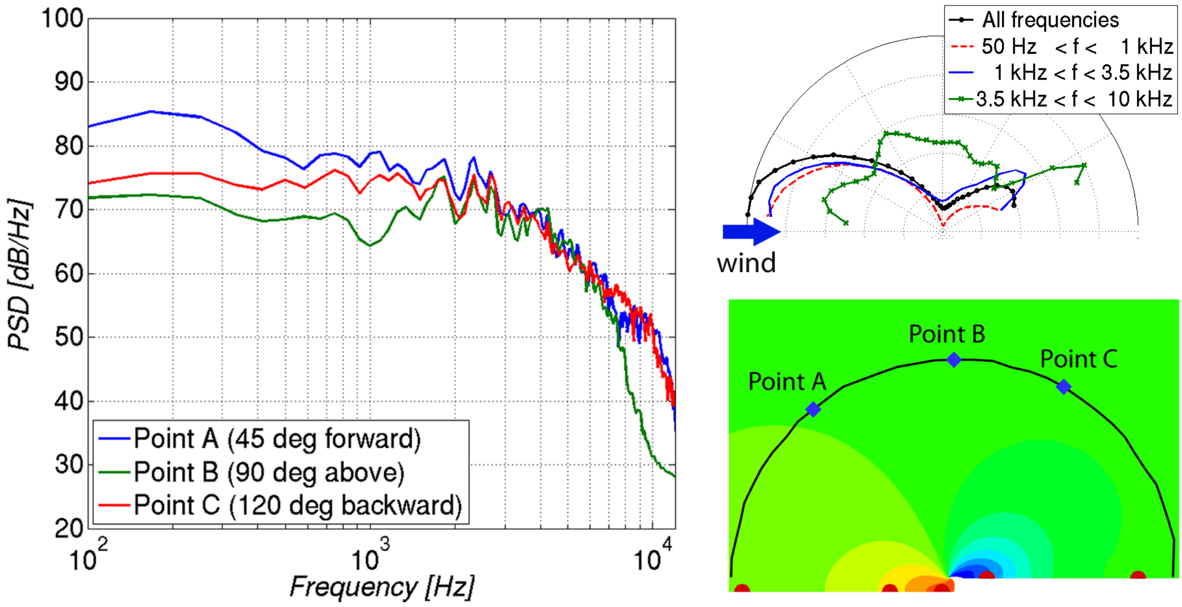

Figure 4.47: Computed spectra at three far field positions and directivity at r ∼ 25 h (0.5 m) simulated with APE and unsteady sources from CFD

ii. Computation with Actran/LA

Methodology : The code Actran/LA developed by the company Free Field Technologies (FFT) is based on the resolution of a variational formulation of the Lighthill equation introduced in [25]. Based on the Lighthill analogy the source terms used for the computation correspond to the simplified version of the Lighthill tensor and takes the form: $\frac{\partial^2 \rho u_i u_j}{\partial x_i \partial x_j}$. The process used for the simulation is illustrated in figure 4.48.

A new conservative interpolation scheme developed by Free Field Technologies and presented in [24] is applied. This interpolation consists in integrating source terms over the acoustic finite elements and allows preserving the energy contained in the source terms. In contrast with the previous method, the computation takes place in the frequency domain. Further information on the code can be found in the handbook [52].

A typical mesh for the code Actran/LA is composed of three zones: the inner domain which should include all the sources, a secondary zone called free acoustic domain and the external surface (or line in 2D) on which are applied the infinite elements. The 2D

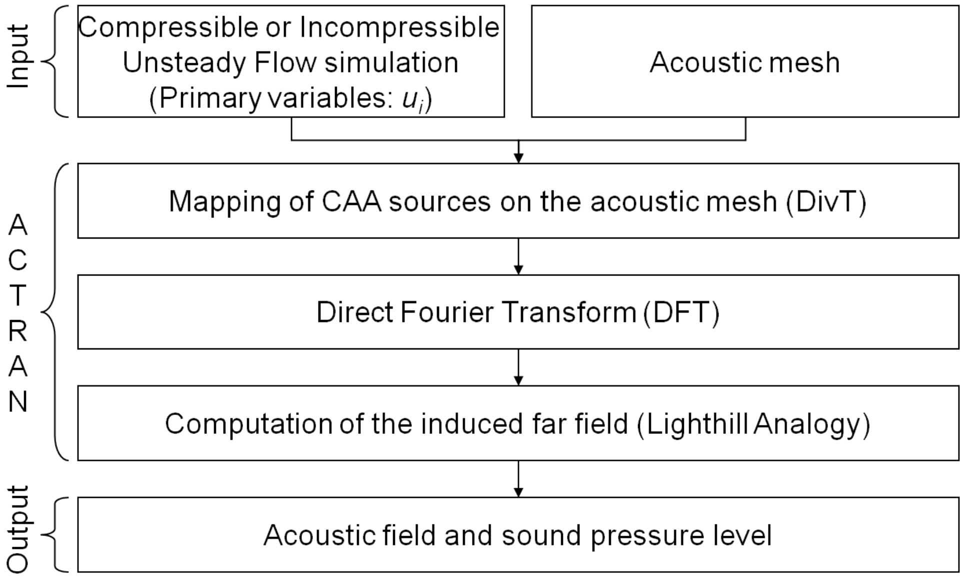

Figure 4.48: Strategy followed for the approach unsteady CFD / Actran/LA

acoustic mesh used for the simulation is presented in the left side of figure 4.49. The inner domain is composed of 36 225 triangular elements, the free field domain of 44 039 while the external line is composed of 442 elements. The maximal size of the elements is 7.5 mm. Four elements are required to solve a wavelength which allow a frequency resolution up to 11 kHz. After mapping the Lighthill sources on the acoustic mesh the sources are transformed in the frequency domain. A Hanning window is used to reduce the border effects.

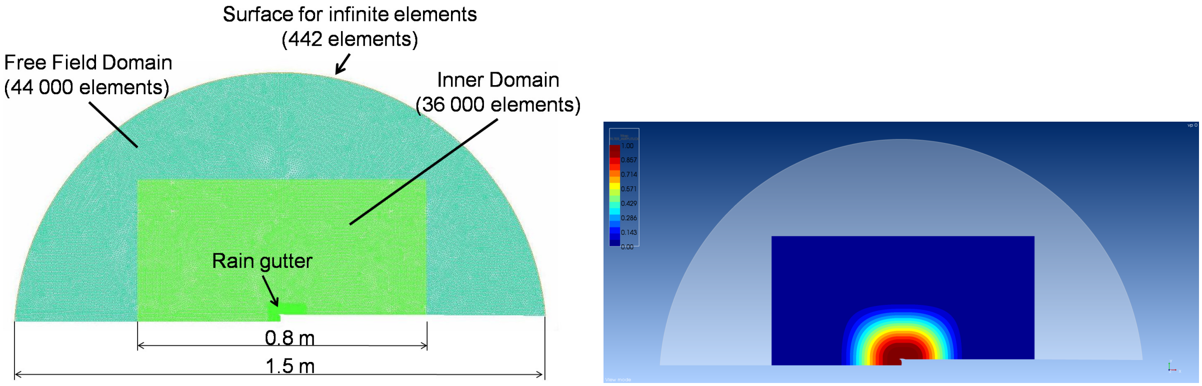

Figure 4.49: Mesh and spatial filter used for the computation with Actran/LA

As for the previous method one can apply a spatial filter in order to reduce the effect of a truncation of the sources. In this case the distance between the rain gutter and the end of the domain was rather short and lots of big structures were still present at the end of the domain. Hence spatial filter were used in order to avoid this truncation effect which at low frequencies might lead to the generation of strong artificial sources at the end of the domain. Different configurations of filters were tested and it was found that the best configuration corresponds to a cosine with very small inner domain and a long decrease to zero, see the picture on the right hand side in figure 4.49. As for the previous method, the acoustic simulations have been preformed with both set of CFD results (long and short simulations) obtained with the SAS-F model. Similar results have been found in both cases for the low frequencies therefore only the results with the short (but with the higher temporal discretisation) CFD simulations will be presented.

Results : The computed acoustic sources before filtering in the frequency domain as well as the computed acoustic field for three different frequencies (500 Hz, 1500 Hz and 5000 Hz) are gathered in table 4.5. At 500 Hz the source area is rather extended behind the rain gutter. At this frequency a suspect high pressure area appears on the acoustic map which looks like a typical problem of the downstream source truncation. However even by using different filters it was not possible to remove it. A similar but already smaller area appears at 1000 Hz but not anymore at 5 kHz. Therefore the low frequencies must be considered very carefully in this case as the truncation effects perturbe the low frequencies and contaminate the spectra.

Acoustic sources	Acoustic field
500 Hz	
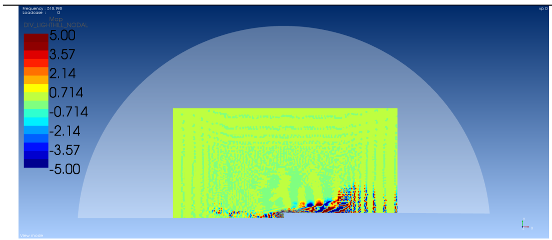	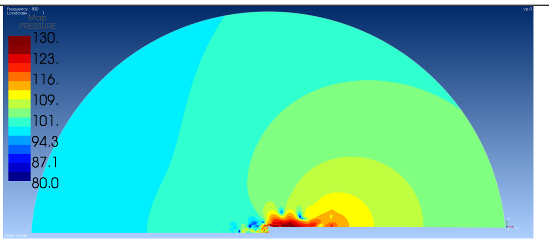
1000 Hz	
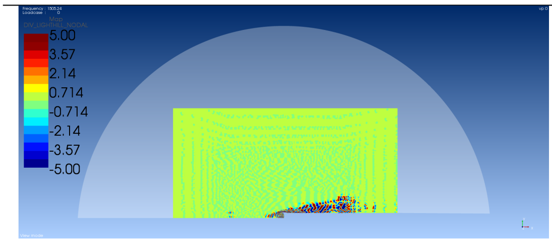	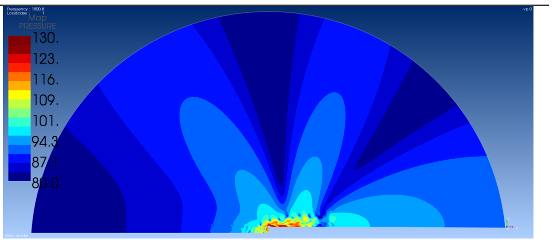
5000 Hz	
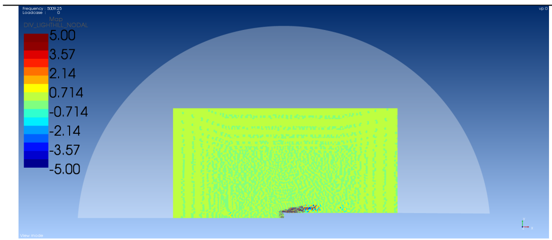	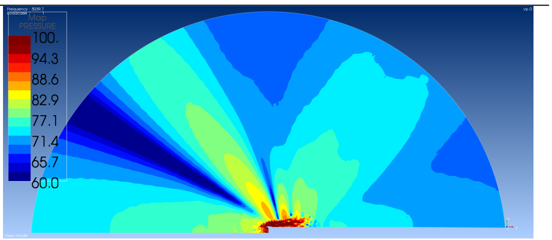

Table 4.5: Acoustic sources and field computed with FFT Actran/LA

The narrow band spectra computed at three far field positions and the directivity pattern at 0.5 m are presented in figure 4.50. The spectra at the three points are very similar and due to the truncation effect the higher noise level is found for the point downstream the rain gutter. A fast change in the decay appears after 5 kHz which could indicate a limitation of the resolution. The directivity seems rather disturbed by the truncation for downstream directions the low frequencies. However when looking specifically certain range of frequency, one can observe a dipole behaviour for the middle frequency range and a multipolar behaviour for the highest frequency range. In this last case a lobe in the direction around 60° is even found.

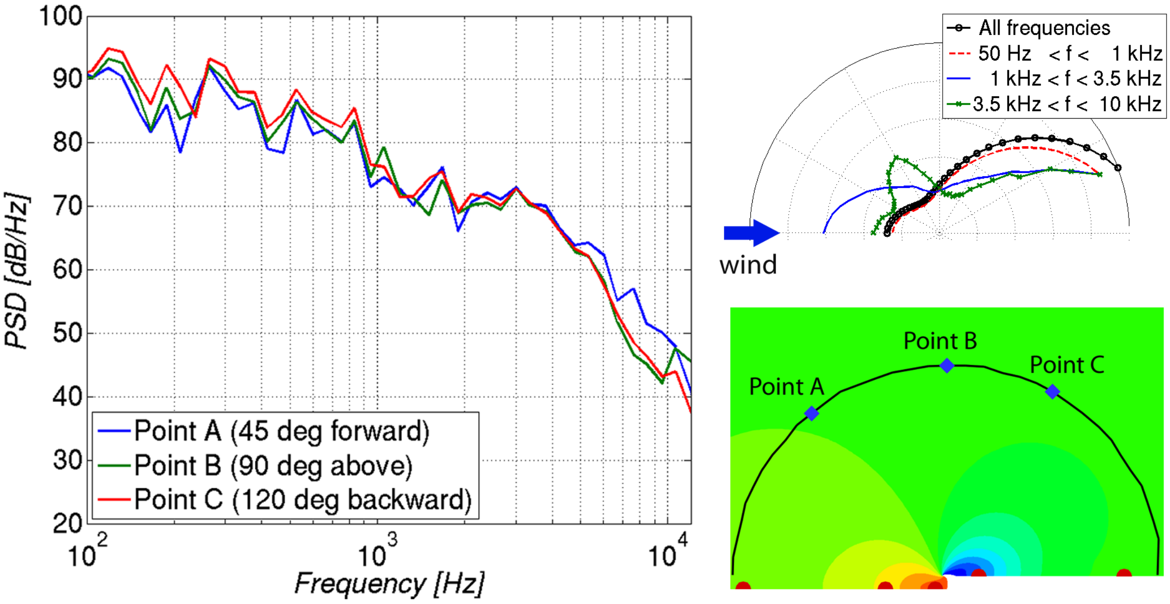

Figure 4.50: Computed spectra at three far field positions and directivity at r ∼ 25 h (0.5 m) simulated with Actran/LA

Finally simulations in 3D have also been performed in this case. It was shown that the noise level simulated was much lower. A representations of the acoustic field obtained at different frequencies are available in figure 4.51 while the corresponding spectra will be shown in the part relative to the comparison between methods.

b/ Steady CFD based simulations

In the next two sections the acoustic field will be computed by using the two methods already used for the prediction of the acoustic modes in the duct. 3D RANS simulations (previous section) have been computed for the different profiles and configurations. The deviation of the flow in configuration A is low enough to consider that the problem can be addressed in 2D. The mean flow was thus interpolated on a 2D structured grid similar to the one presented in figure 4.45.

The structured mesh generated for the rain gutter's profiles 1 and 2 were composed of 20 blocks and 250 000 elements and 13 blocks and 330 000 elements respectively. An overall damping of 0.5 was used in all cases.

Sponge layers were placed on the free space surroundings to avoid reflected waves. The spatial derivatives were approximated by the 4th order DRP-scheme and the time

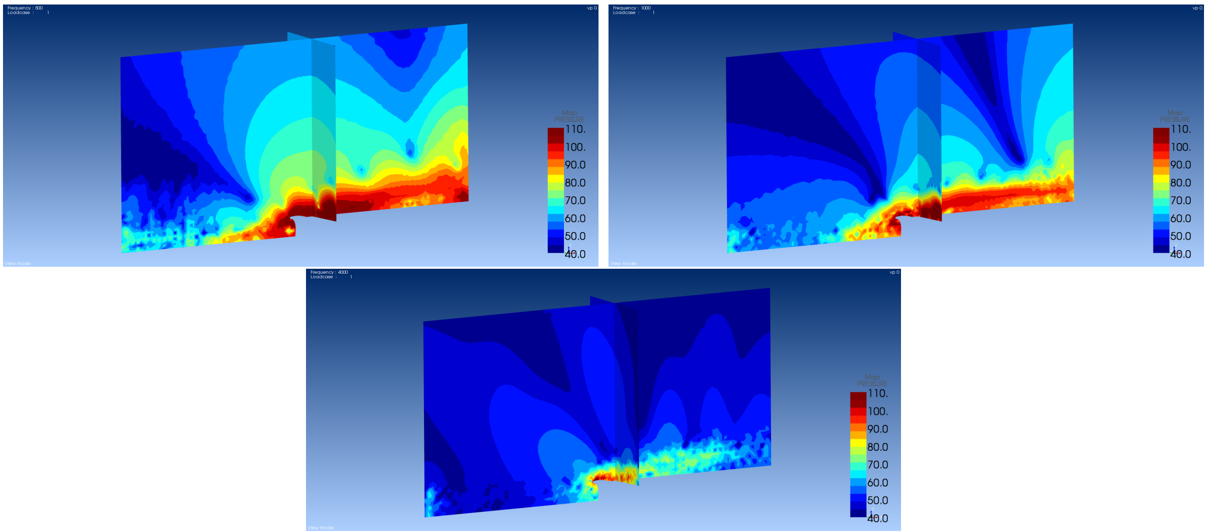

Figure 4.51: Representation of the 3D acoustic field computed with Actran/LA at a frequency of 500 Hz, 1 kHz and 4 kHz

integration was done by the standard 4th order Runge-Kutta procedure. The numerical methods applied within PIANO are described in [33].

i. Single Test-Vortex Injection method

Illustrated by figure 4.52 a single vortex is injected in the flow upstream the rain gutter. The noise radiated by the interaction of the vortex convected by the flow and the rain gutter is computed by solving the non-linear Euler perturbation equations. The initial vortex is positioned upstream of the rain gutter as to hit the edge of the rain gutter. Its dimensionless length scale is set to 2.5×10^{-3} while its dimensionless strength is set to 1×10^{-3}. The time step was also chosen very small (6.45×10^{-5} [-]) to respect the CFL condition.

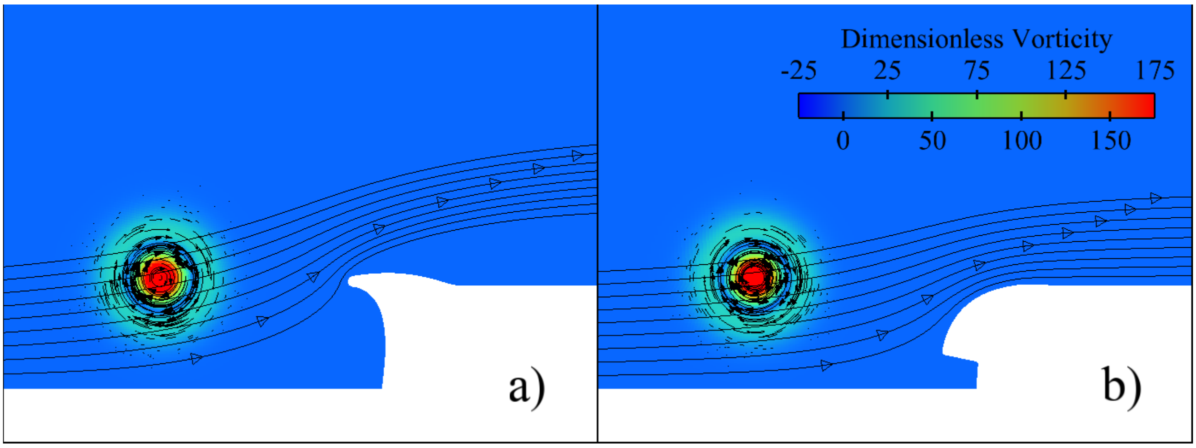

Figure 4.52: Representation of the initial vortex (profile 1 and profile 2)

The acoustic fields generated by both profiles are shown in figure 4.53. The graph demonstrates the higher sound level generated by profile 1 compared to profile 2. The vorticity around the rain gutter is represented on the right hand side of the picture.

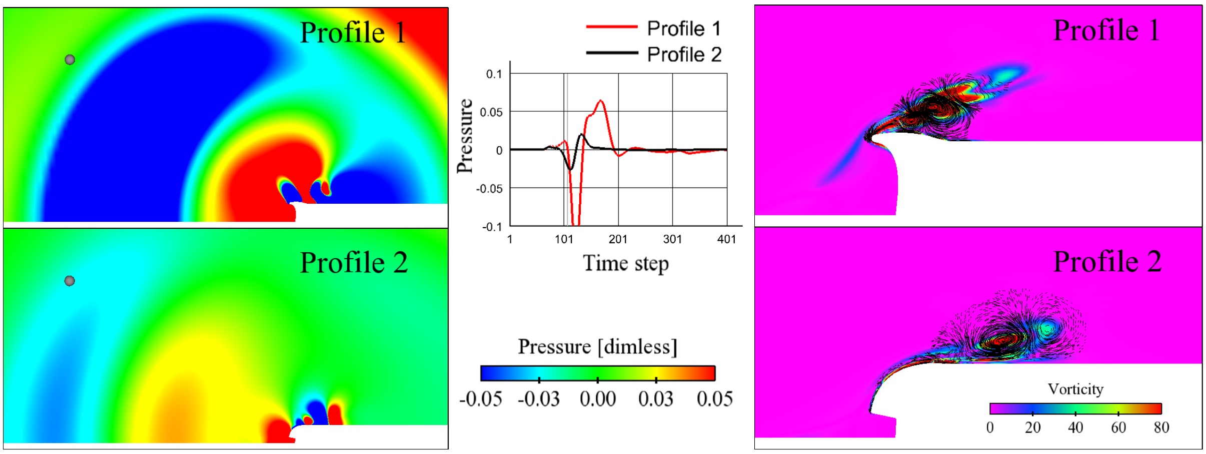

Figure 4.53: Radiated acoustic field computed with single test-vortex injection method for both profiles

The temporal signals registered at point 1 positioned upstream the rain gutter at an elevation angle of about 45 deg and a distance of 0.5 m for three different heights of the rain gutter are plotted in the left hand side of both figures 4.54 and 4.55 for profile 1 and profile 2 respectively.

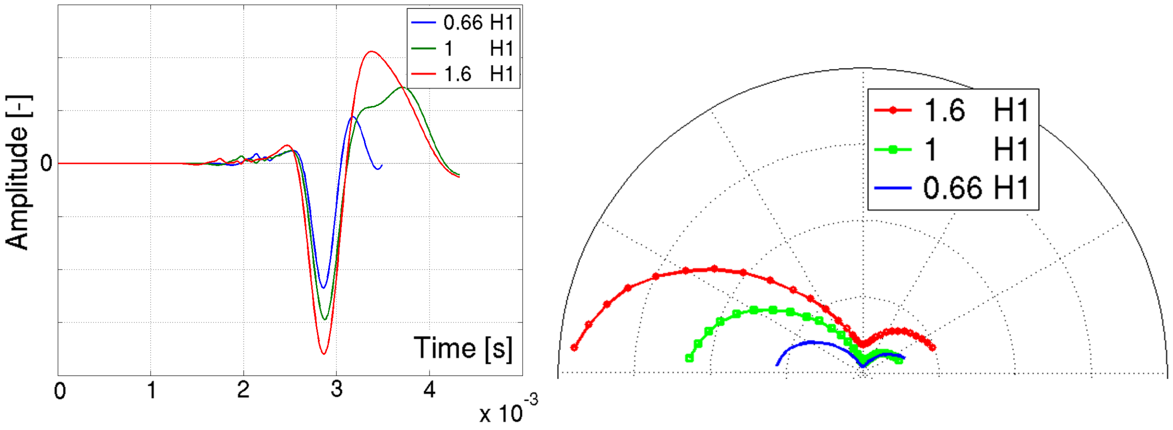

Figure 4.54: Time signal registered at a point $r \sim 0.5$ m and 45° forward the rain gutter simulated with the single test-vortex injection method for the profile 1 and for different heights. Presentation of the overall directivity for the different heights of profile 1

An opposite trend is found in both cases. The signals registered for the profile 1 shows that by increasing the height, the amplitude of the acoustic response increases. On the contrary the temporal signals registered for the profile 2 show that by increasing the height, the amplitude of the acoustic response decreases. One element of explanation for this remarkable acoustic design feature can be found in the shapes of the different profiles,

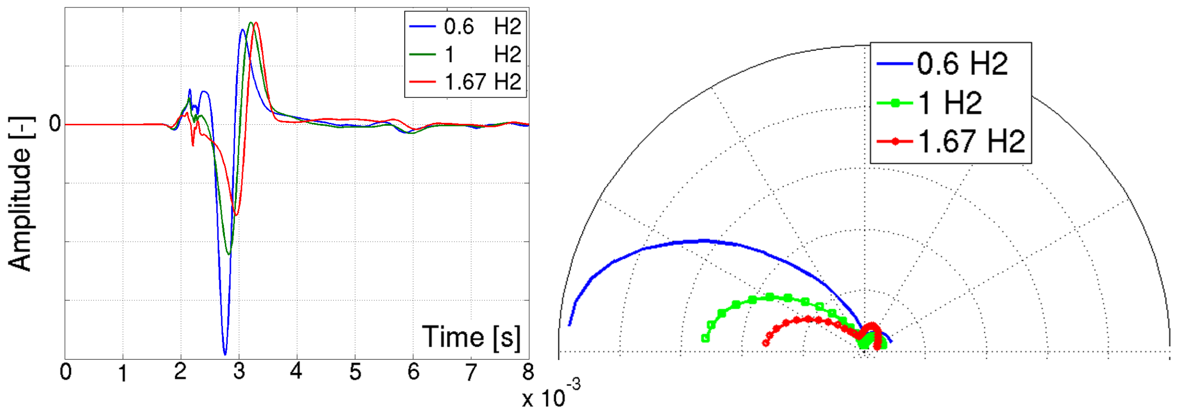

Figure 4.55: Time signal registered at a point $r \sim 0.5$ m and 45° forward the rain gutter simulated with the single test-vortex injection method for the profile 2 and for different heights. Presentation of the overall directivity for the different heights of profile 2

see figure 4.56. First it is remembered that the mechanism of sound generation is the interaction of the vorticity perturbations with the edges of the gutters. It is well known that the sound increases with the curvature of the edge and the flow speed by which the vortex passes the edge. In fact both influence the acceleration of the vortex, which is really the origin of the sound generation. By design the shape (curvature) of the edge at profile 1 is independent of its height. However, the flow speed of the boundary layer increases drastically with height and so the edge of a taller variant of profile 1 is located in a higher speed flow than that of a shorter variant. Hence the taller profile 1 generates more aerodynamic sound.

For profile 2 a different effect may govern the change in sound generation for different heights. Due to the design, the curvature of the gutter decreases considerably with height. This effect decreases strongly the acceleration of the vortex and less sound may be generated as for a short (and more curved) version of profile 2 provided the curvature effect over compensates the speed increase effect due to the higher position in the boundary layer for taller rain gutters.

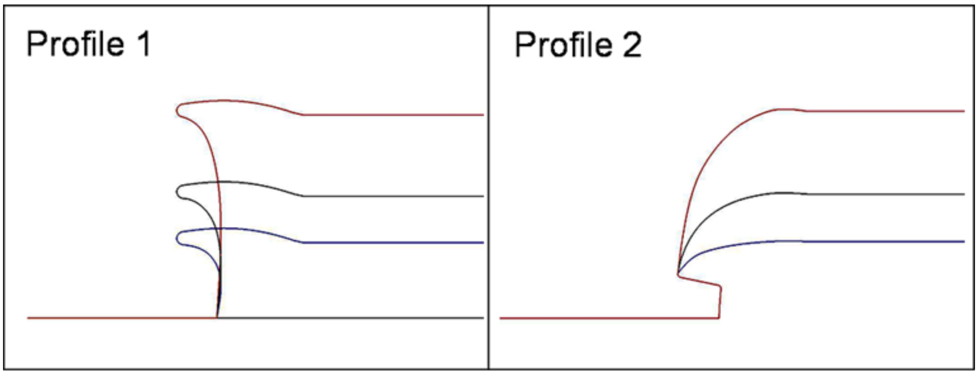

Figure 4.56: Representation of the different profiles for the three height considered

By computing the acoustic intensity at positions on a circle centred on the rain gutter the directivity pattern can be computed and plotted for all profiles. For both profiles the directivity shows a main radiation direction forward a minimum in the vertical direction and a second smaller lobe downstream of the rain gutter. Based on the acoustic intensity measured upstream one can find some scaling law for the different configurations. It was found that the acoustic intensity scales almost linearly (or inversely linear) with the height of the rain gutter: $p^2 \propto H^{1.2}$ and H^{-1} for the profiles 1 and 2 respectively. The scaling with the inflow velocity was found as: $p^2 \propto M^{4.8}$ and $M^{3.8}$ for profile 1 and profile 2 respectively. As known for cylindrical geometries, the acoustic results obtained in 2D can be extrapolated to 3D by increasing the exponent of the velocity scaling by 1.

ii. 3D simulations with single test-vortex injection method

To extend this work simulations on 3D cases with the same methodology have been performed. The simulations require to design specifically 3D block-structured meshes. These meshes were composed of about 10 to 11 million cells and 550 to 600 blocks depending on the case. The directivity pattern computed in 3D are similar to patterns found in 2D. The only difference concerns the acoustic energy level, lower in 3D, see figure 4.57 and figure 4.58. Further investigations should be done to understand this phenomenon.

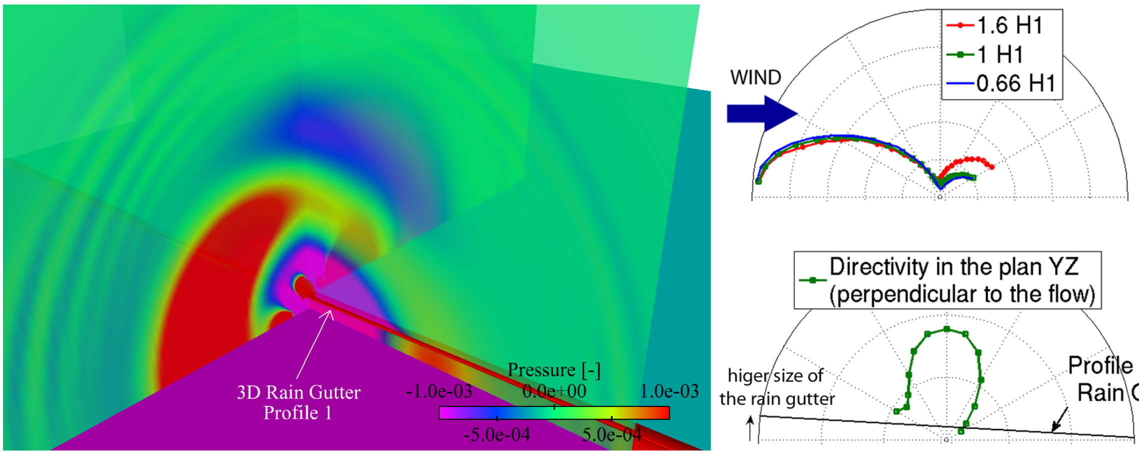

Figure 4.57: 3D pressure field computed with single test-vortex injection (left) and directivity pattern computed in the flow direction (right-top) and perpendicular to the flow direction (right-bottom)

iii. Random Particle Mesh

Methodology and set-up : Instead of injecting a test-vortex, the fluctuating turbulent velocities are set up by using the stochastic approach proposed by Ewert [43] and called Random Particle Mesh (RPM). The RPM is based on the spatial filtering of white noise to generate acoustic sources on an auxiliary mesh (called also patch) based on the streamlines of the flow. The streamlines are used to convect the particles which represent the turbulence and obtained from spatial filtering of white noise. The resulting turbulence data is used to compute the acoustic source term (Lamb vector), which is interpolated on the acoustic mesh. The acoustic field in then computed by solving the APE system.

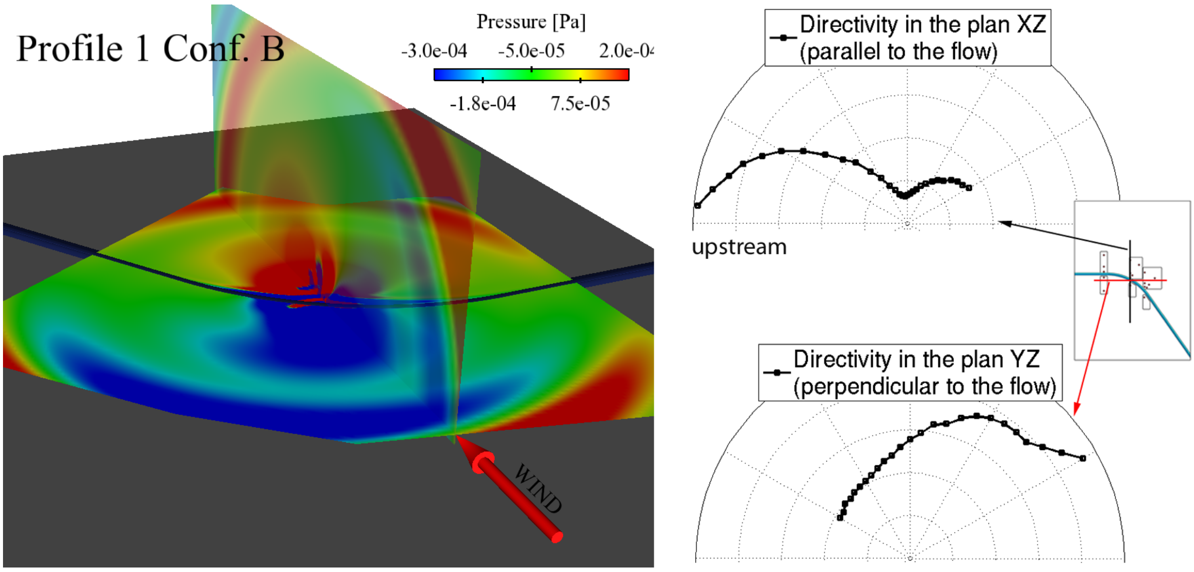

Figure 4.58: Directivity computed with single test-vortex injection in the direction of the flow (top right) and perpendicular to the flow (bottom right) in the case of 3D simulation configuration B

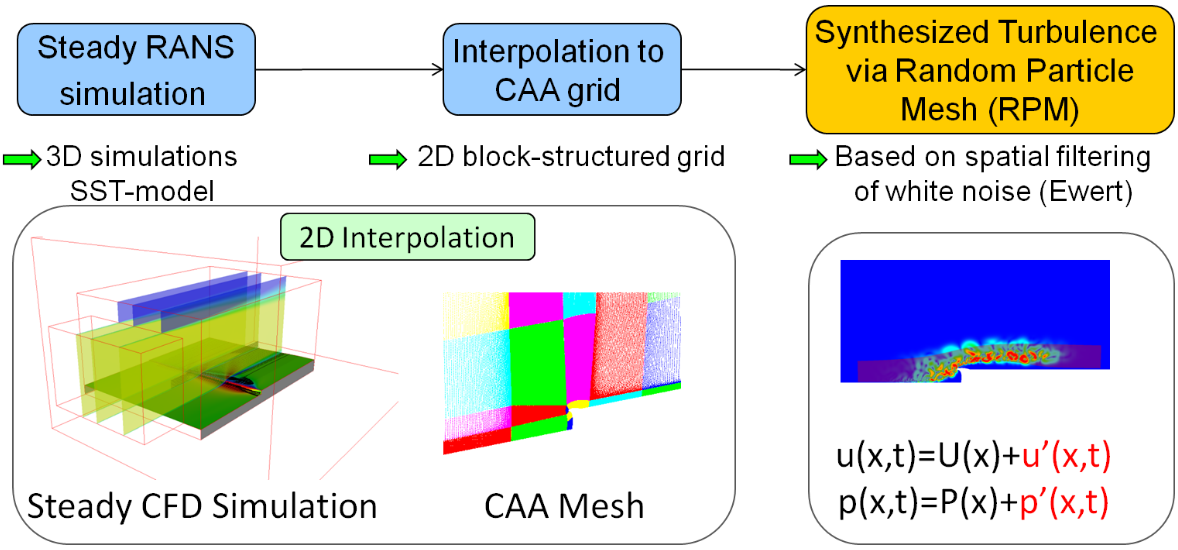

Figure 4.59: Computation process with RPM modelling

Limited up to the finalisation of this work to 2D cases only the effects of the rain gutter's height and of the inflow velocity have been studied. The mean flow was taken out of a 3D simulation to be interpolated on the 2D acoustic mesh. The process used for the simulation with RPM is described in figure 4.59. The particles are set-up at the inflow face of the patch and convected by the flow along the streamlines composing it. The interaction of the reconstructed sources and the rain gutter generates sound. For the rain gutter a patch was designed to cover a large area in front and above the rain gutter. This patch area is depicted for both profiles in figure 4.61. The patches are extracted from the streamlines computed by the RANS, see figure 4.60. In this case the patches were composed of 41 × 450 cells. For profile 1, one can notice the presence of an area above the rain gutter not covered by the patch. This area corresponds to the recirculation bubble generated at this profile. An alternative variant of the RPM method in which turbulence kinetic energy can be reconstructed inside recirculation zones was not yet available upon finalisation of this thesis.

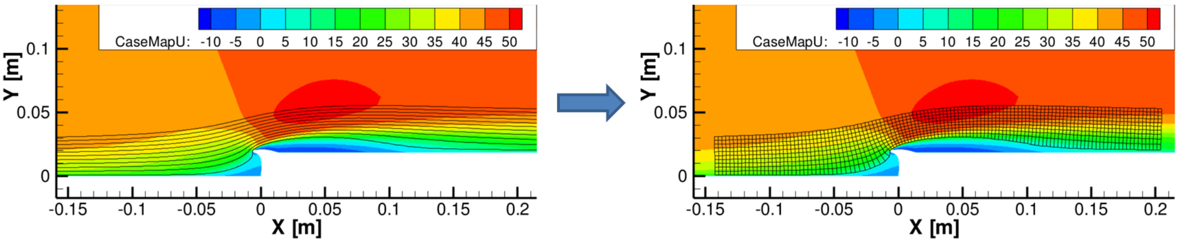

Figure 4.60: From the streamlines to the patch (Profile 1)

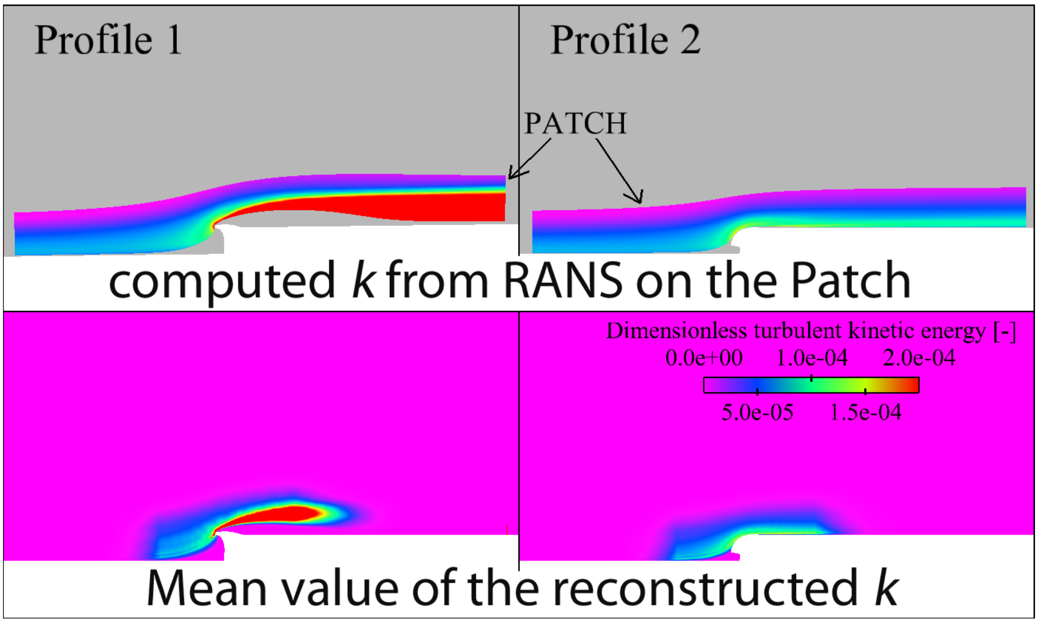

Figure 4.61: Representation of the turbulence kinetic energy and contour of the patches used for the computation in red

Different lengths and resolutions of patches can be used. Three different levels of mesh refinements on the patch were used to compute the radiated field. As the same results were found, only the results with the coarser patch will be presented here. Different heights of the patch were tested and it was found that in this case the streamlines far off the contour of the gutter have no influence. The most important phenomena occur in the first streamlines of the patch. The distance between the first streamline and the geometry may be of importance. Different lengths of patches were tested. A variation of the length of the patch did not show a major influence. However, it may be important that the length of the patch is long enough in order to be able to apply a smooth blending function to bring the amplitude of the sources to zero at the end of the patch and avoiding a truncation effect. Finally a major aspect concerns the resolution of the CAA mesh in this area. It is generally expected that the CAA must be fine enough to be able to resolve the smallest structures reconstructed on the patch.

RPM sources : In the current implementation of the code PIANO two different formulations can be used to model the acoustic sources. Both are based on the computation of the Lamb vector but differ in the quantity modelled. For the source type A the turbulent velocity fluctuations ($\vec{u_t}$) are modelled and the turbulent vorticity ($\vec{\omega_t}$) is derived from them. The source term A takes the form:

$$S_A = -\vec{\omega_t} \times \vec{u_0} - \vec{\omega_0} \times \vec{u_t} \tag{4.13}$$

On the other hand the turbulent vortcity ($\vec{\omega_t}$) is directly modelled for the source type B and the source terms B is simplified to:

$$S_B = -\vec{\omega_t} \times \vec{u_0} \tag{4.14}$$

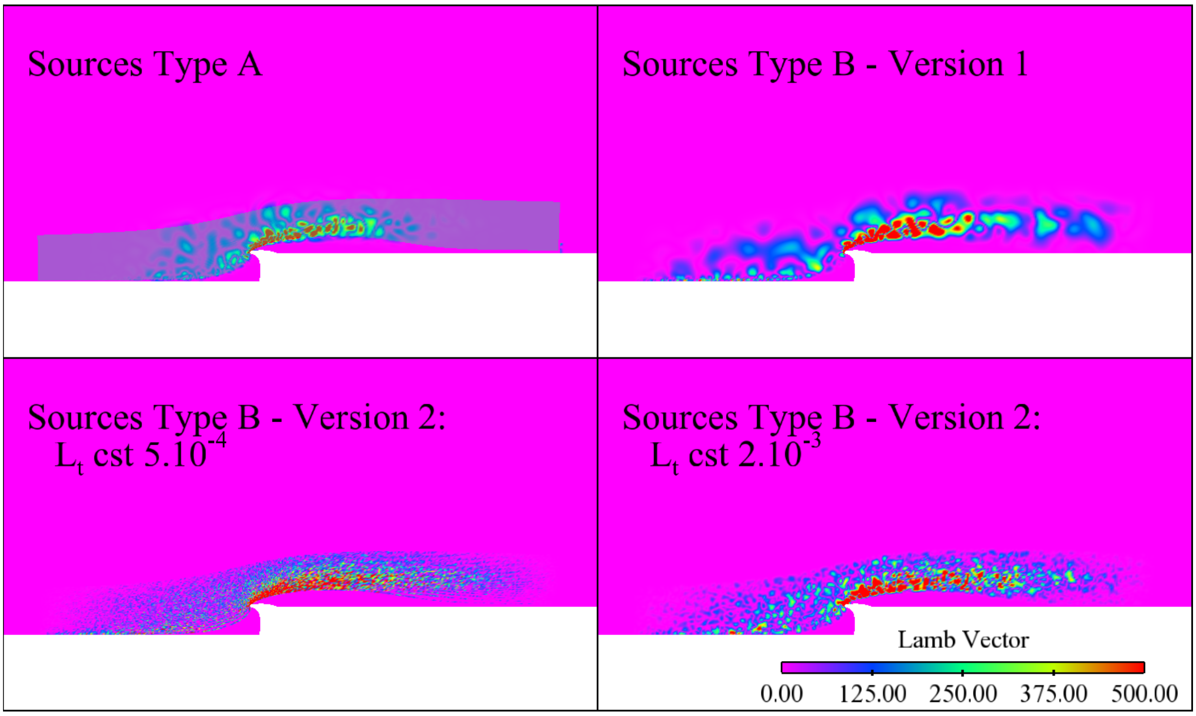

Figure 4.62: Snapshot of the Lamb vector reconstructed by the RPM modelling

In addition two variants of the source term B exist. In the first variant the length scale for the turbulence representation is taken from the patch and will be restricted by the RPM limiter (e.g. 3 times the grid resolution). Vortices with sizes varying in a range from the limiter up to all larger values contained in the patch will be generated. In the second variant vortices with only one size corresponding to the limiter will be created.

Snapshots of the Lamb vector computed in four cases are in presented in figure 4.62. In the first three cases the limiting length scale (L_t) was set-up to 5×10^{-4} while for the last picture the limiting length scale was equal to 2×10^{-3}. The sources type A appears slightly smaller than the sources type B (version 1). In both cases different sizes of structures are present. The smallest structures are close to the geometry and become larger when moving away of it. For the sources type B version 2 the turbulent structures have all the same size. This size depends directly of the length scale L_t. Therefore bigger structures are visualised on the last picture were the length scale limiter has been increased. It was therefore found that in the third case (picture bottom-left), although the value of length scale was the same as for the two previous cases the turbulent structures were much smaller. In the rest of the study, the fourth case with the higher length scale limiter will not be further investigated.

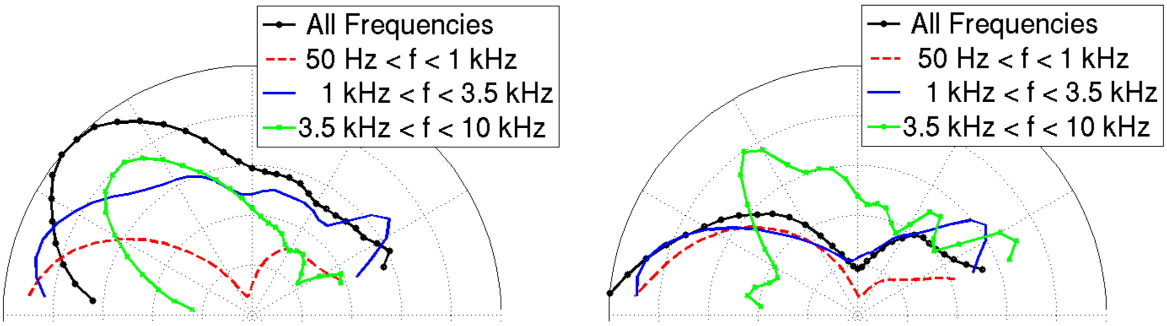

(a) RPM source type A (b) RPM source type B version 1

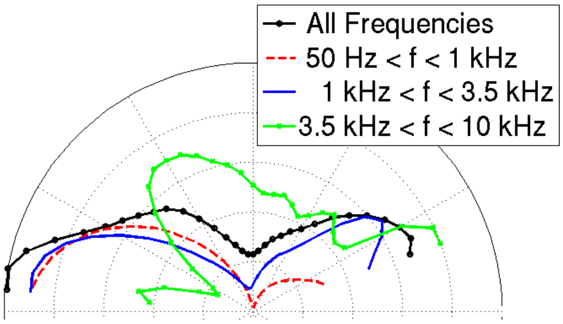

(c) RPM source type B version 2

Figure 4.63: Directivity with different sources models: type A (top-left), type B version 1 (top-right) and type B version 2 (bottom)

CAA simulations with the first three configurations (the three configurations with the length scale equal to 5×10^{-4}) were carried out. The directivity computed on a circle of radius 25 h (with h the height of the rain gutter) and centred on the edge of the rain gutter is depicted in figure 4.63. Narrow band spectra at three positions in the far field are plotted in figure 4.64.

The directivity pattern (over the whole frequency range) computed with both type modelling of source B presents a similar character while a different pattern is found for the modelling type A. A main lobe with an elevation around 40° is found for the modelling

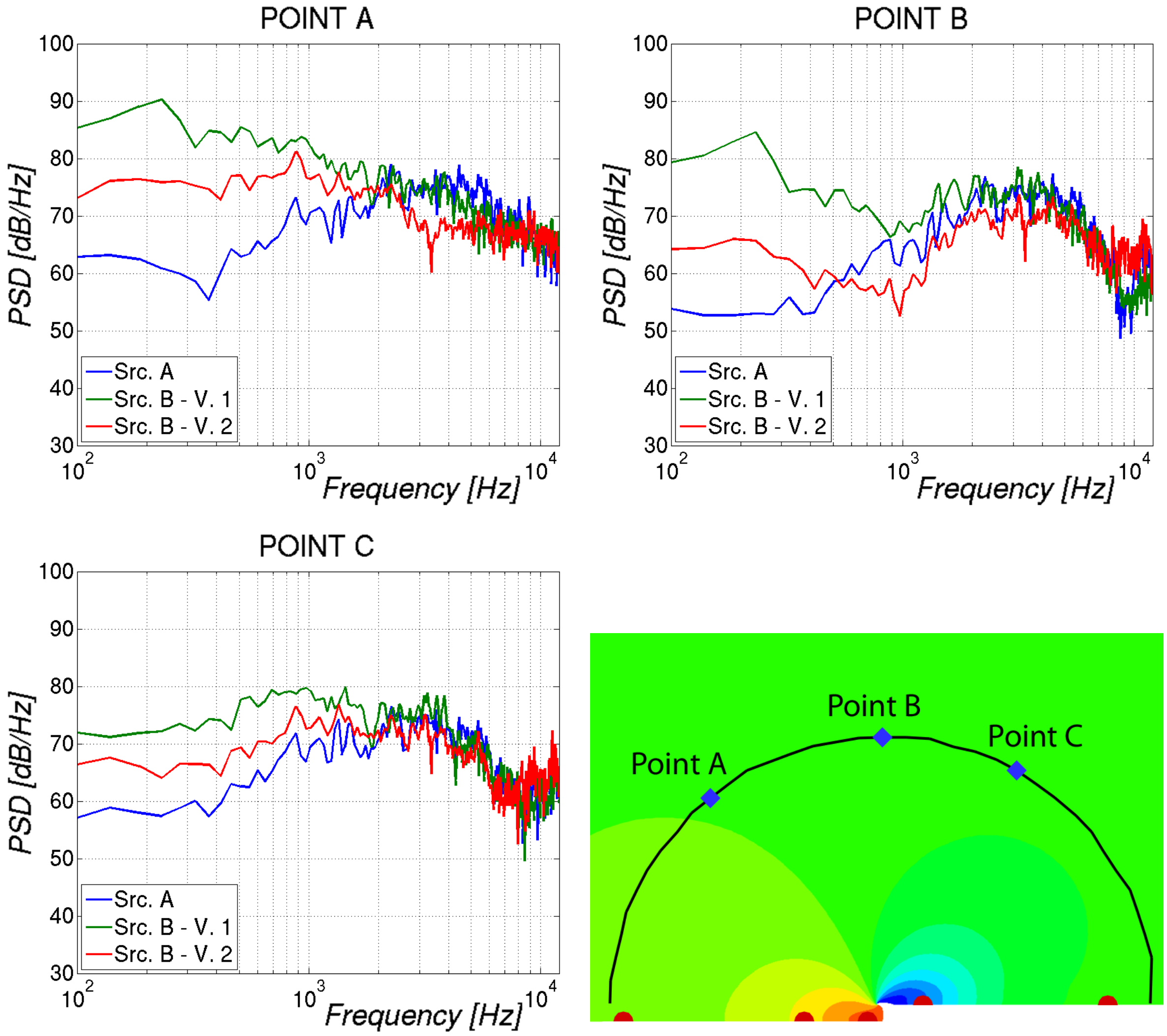

Figure 4.64: Narrow band spectra at 3 different positions and computed with different sources modelling: 45° forward (top-left), 90° above (top-right) and 120° backward (bottom-left)

type A while the directivity for the type B are relatively similar to those found with the methods based on unsteady CFD sources with a main lobe forward and a secondary lobe backward. A close look at the directivity pattern for different frequency ranges allows however to find more similarities between them. In fact when considering only the low frequency range a directivity pattern with a major lobe is found in the three cases while for the higher frequency range a main lobe with an elevation of 40 to 50° is found in all three cases. Therefore the three models show equivalent behaviour but the weighting of the different frequency ranges is different. The energy level in the high frequency range is higher with the modelling type A.

Considering now the spectra a lower noise level is found with the modelling type A (blue) for the low frequencies compared with the level predicted by the two simulations computed with the modelling type B. For frequencies higher than 2 kHz the spectra computed with the modelling A and the modelling B version 1 are extremely similar. The two types of source modelling seem to have an impact only on the low frequencies. The version 2 of modelling B exhibits an intermediate behaviour.

As we are mainly interested in the high frequencies the modelling type A seems the most appropriate in this case. Therefore, the acoustic sources for the simulations presented in the rest of the work will be carried out with this model. Nevertheless, the frequency dependent directivities for source B are in remarkable agreement with those obtained for the sources from unsteady CFD (see figure 4.47).

Remark: A test was also performed with the 3D corrections discussed in [45] and implemented into PIANO. However almost the same spectra were found, therefore no results will presented here. Further investigations would be required to properly investigate the 3D effect on the spectrum.

Differences between Profiles : The acoustic pressure fields computed for both profiles are presented in figure 4.65. The picture on the right-hand side represents the computed 1/3 octave spectra for both profiles at two positions in the far field at a distance r of 0.5 m (25 h) of the rain gutter, with h the height of the rain gutter. It can be seen in the pressure field and verified in the spectra that the profile 1 is much noisier than the profile 2 and produces also shorter wavelengths. The maximum SPL for profile 1 is found for a higher frequency band ($\sim$ 3 kHz) than for profile 2. In comparison with the experimental results the frequency bands of maximum SPL computed are higher for both profiles. One has to keep in mind that the simulation was 2D while the experiment was 3D.

A 3D configuration can be seen as superposition of the contribution of 2D sections along the span for which the frequency of maximal noise level depends on the height of the rain gutter (spanwise position respectively). Therefore the comparison between experiment and simulations has to be done carefully.

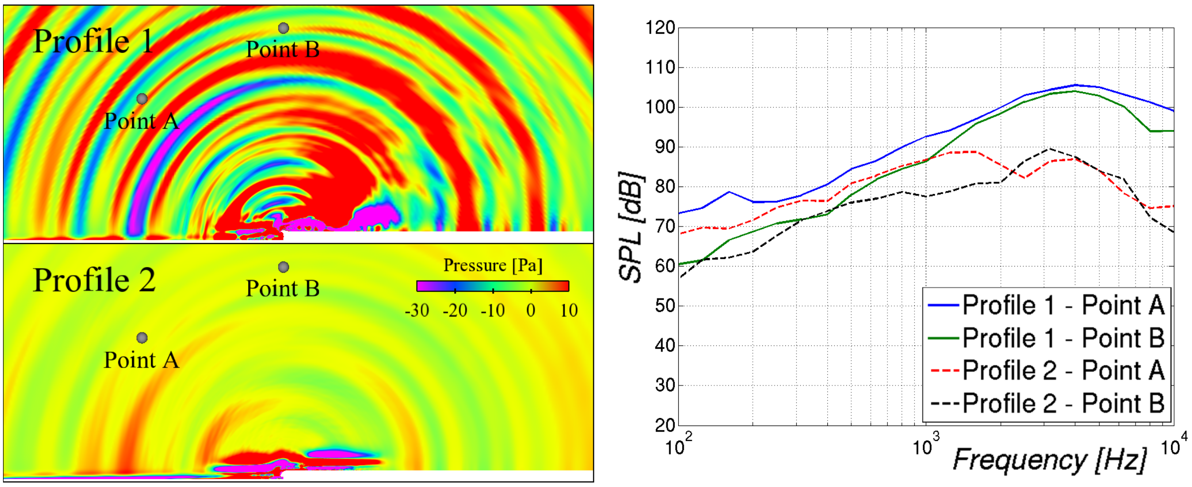

Figure 4.65: Acoustic field simulated with RPM model and corresponding simulated spectra at 2 positions

The directivity is presented in figure 4.66. Profile 2 shows mainly a radiation forward while profile 1 proposes for low frequency a main radiation forward but for higher frequencies a direction around 45° forward. The noise amplitude varies strongly between the different frequency ranges. For representation purposes the values have been normalised by their local maximum. The highest pressure levels were found for the frequency ranges of 3 - 4 kHz and 1 - 2 kHz for the profiles 1 and 2 respectively (coherent with the spectra). The directivity pattern of profile 1 appears also largely dependent on the frequency range. For example: lower frequencies (0 - 2 kHz) produced mainly a directivity forward like for profile 2, which by opposition is less frequency dependent. On the contrary for higher frequencies, the main lobe is found for an angle around 40 - 50° with respect to the horizontal which is also found in the overall pattern.

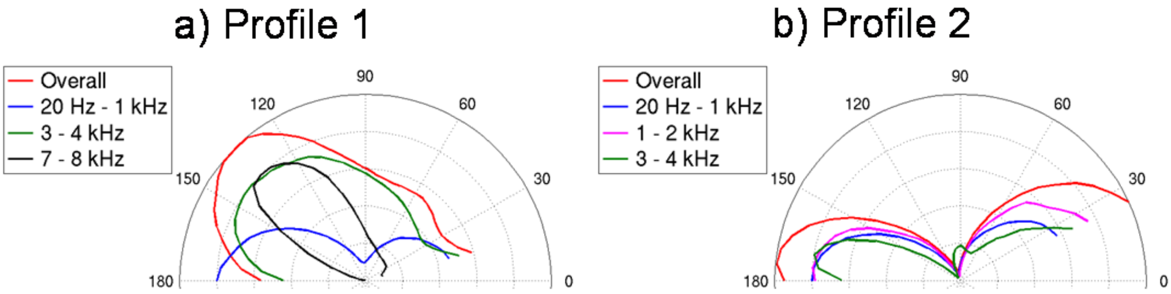

Figure 4.66: Representation of the directivity of both profiles for different frequency ranges

Inflow velocity effect : The sound intensity was computed with equation 4.12. To check the evolution against the Mach number, the sound intensity of each microphone was scaled to M^5 and normalised to the maximum noise level registered at 60 m/s, see figure 4.67. Good scaling effect is observed for both profiles. As 2D simulations always give one less exponent than 3D cases, the noise level in the far field is found to be scaled with M^6. This solution agrees well with the Curle's sixth power prediction of dependency of sound intensity to free stream Mach number for acoustically compact objects [28] and the results found with the test vortex injection method.

A minimum of SPL is found for $\Theta \sim 95°$ for profile 2 and a maximum for a direction around 170°. On the other hand, a maximum SPL is found for $130° < \Theta < 160°$ for profile 1 while a minimum SPL is noticeable behind the rain gutter. Spectra are plotted for a point at R $\sim 25h$ and $\Theta \sim 130°$, and show the reduction of the overall noise level with the flow speed but also a shift in the frequency of the higher SPL as previously noticed with the experiment.

Effect of the height : Figure 4.68 illustrates the modification of the directivity pattern against the height of the rain gutter for both profiles. The acoustic intensity was scaled with the rain gutter's height. In both cases the acoustical intensity scales almost linearly with the height of the rain gutter and same tendency is found for both profiles. An increase of the height leads here to an increase of the acoustic level. This behaviour differs for profile 2 of the behaviour observed with the test vortex injection method. One can also notice that the directivity patterns for the three heights of profile 2 are different.

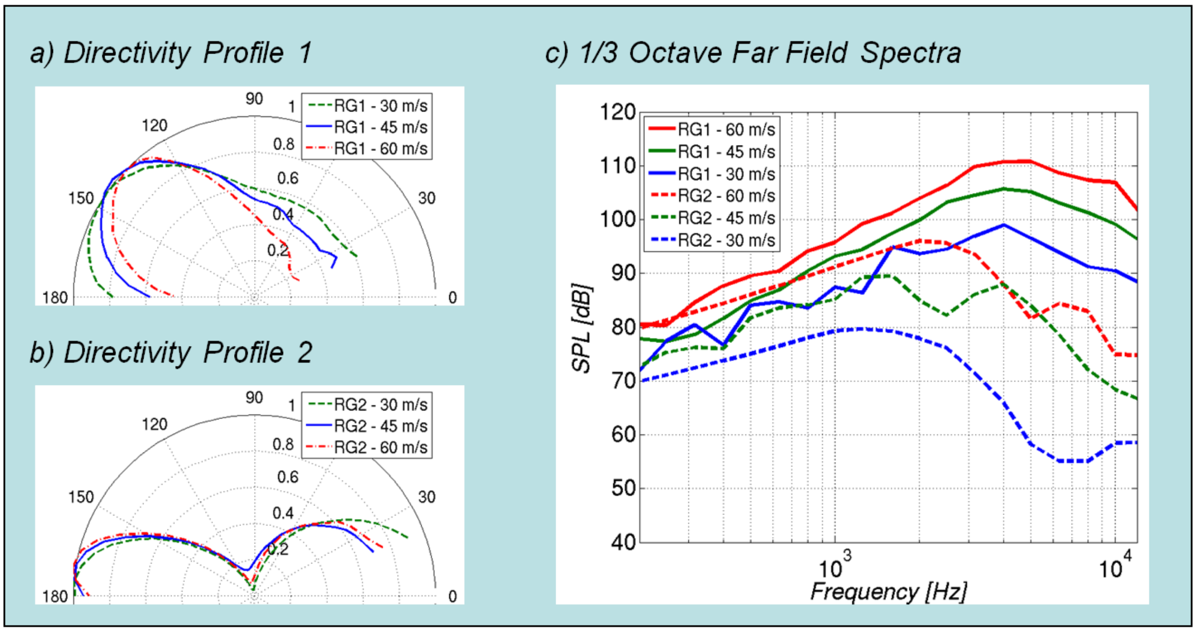

Figure 4.67: Normalised and scaled with M^5 directivity pattern and far field spectra of the profiles 1 and 2 computed with RPM model vs. inlet flow speed at R $= \sim 25h$ with h the height of the rain gutter

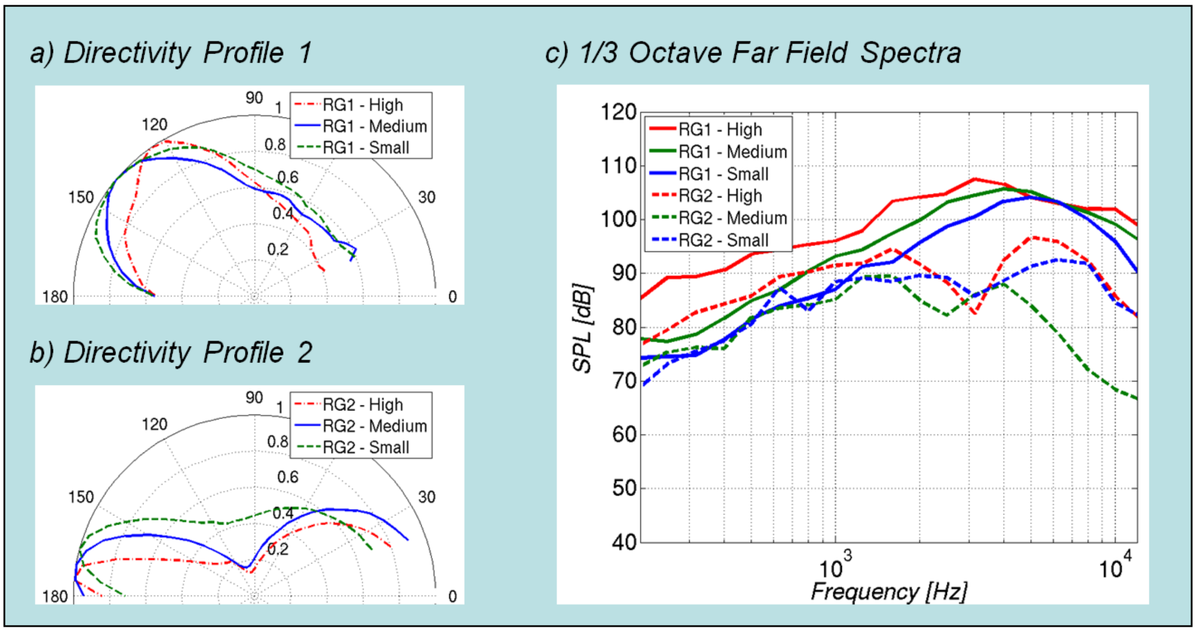

Figure 4.68: Normalised directivity pattern and far field spectra at 130° of the profiles 1 and 2 computed with RPM models vs. rain gutter's height at R $= \sim 25h$ with h the height of the rain gutter and $U_{mean} = 40\ m/s$

Shown in figure 4.56 the shape of the smaller height is less rounded and even appears similar to the shape of profile 1. Looking back now at the directivity, the angle of the main lobe is also reduced and approaches the directivity pattern found for profile 1. Note: if the small RG with profile 2 show the largest amplitude at radiation angle of 130° but the lowest spectrum, this is due to the normalisation in the directivity plot.

iv. Coherence

As in the experimental part the coherence function can also be computed for different points of the acoustic field simulated with RPM modelling. The numbering convention of the points is presented in figure 4.69 and the coherence function is presented in figure 4.70.

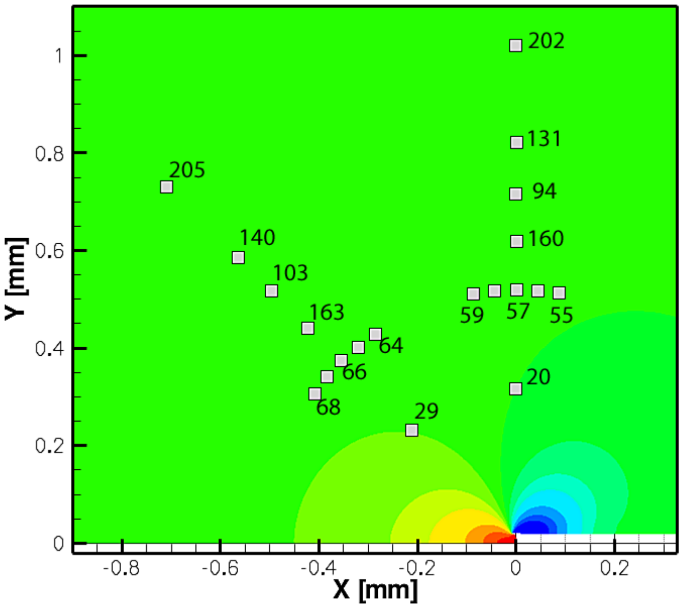

Figure 4.69: Numbering convention of the measurement points for the coherence

Two propagation directions are considered for the points: either five points positioned on a circle at constant radius and positionned with 5° distance or 6 points on a line starting from the rain gutter and making an angle of 45° with the horizontal.

The points positioned at the same distance of the rain gutter demonstrate a very high coherence between them. The phase illustrates the effect of the convection effect. On the contrary, the coherence between the point at $r = 0.5$ and the points placed on the same line but with a different distance decreases when the distance increases. In addition, the slope of the coherence phase increases proportionally to the distance between the points. The velocity found in this case is always the velocity of the sound which is expected as this is a purely acoustic phenomenon. Similar results have been found for the points positionned above the rain gutter, see Appendix.

c/ Corrections and comments

To be able to compare the experimental results with the results computed with the different methods several corrections should be applied. Since the acoustical domain was not big enough to include the position of the far field measurements the difference of distance

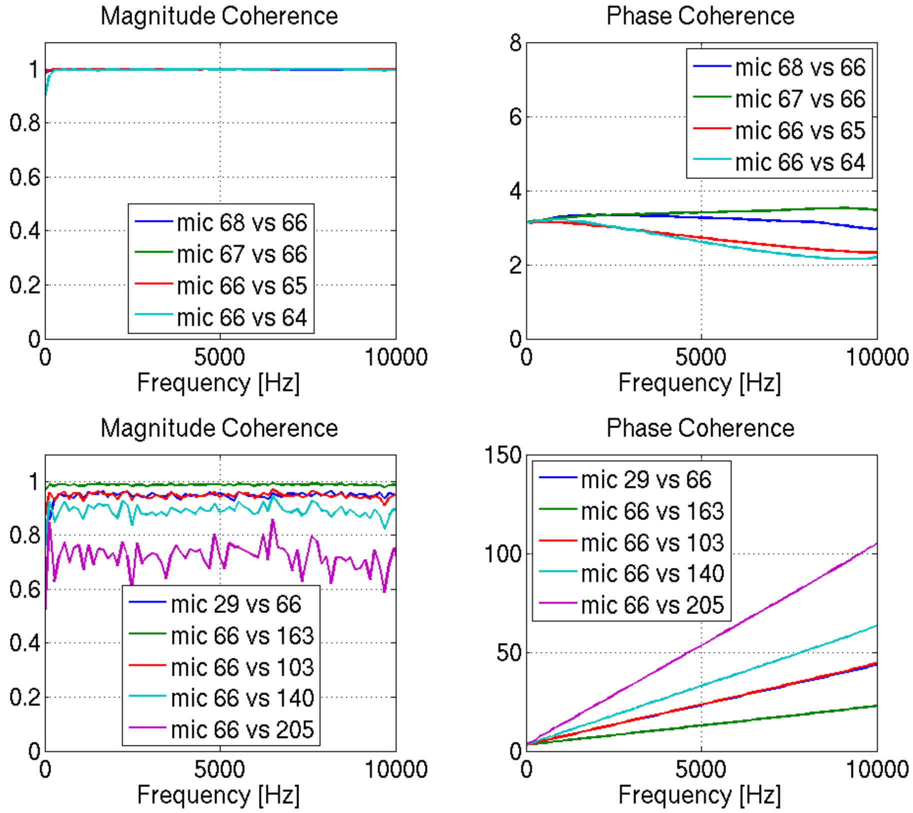

Figure 4.70: Coherence computed for different directions in the far field computed with RPM

must be compensated. In 2D this effect can be corrected as follows:

$$I_1^2 \times r_1^2 = I_2^2 \times r_2^2 \tag{4.15}$$

with I_1 and I_2 the acoustic intensity at two positions on a same direction and r_1 and r_2 the two distances.

The second correction corresponds to the difference between 2D simulations and 3D measurements. Obviously the complete 3D effect of the slope or curvature cannot be easily corrected. Oberai [93] and Ewert [46] discussed the possibility of using a correction factor for trailing edge noise. The evaluation of the correction factor can be done by using the general Green functions in 2D and 3D which can be written as:

$$G_{2D} = \frac{i}{4} H_0^{(2)}(k \cdot r) \tag{4.16}$$

$$G_{3D} = -\frac{1}{4\pi r} e^{-ikr} \tag{4.17}$$

with $H_0^{(2)}$ the Hankel function of the 0^{th} order and second kind.
Thus the correction factor takes the following form:

$$H(f) = \frac{G_{3D}}{G_{2D}} L_s = \frac{p_{3D}}{p_{2D}} \tag{4.18}$$

the definition of the length is discussed in Ewert [45] and can be written as:

$$L_s = C\frac{U}{2\pi f} \tag{4.19}$$

with C a constant generally equal to 2, U the mean flow velocity and f the frequency. The correction function is presented in figure 4.71. The function decreases almost linearly with the loglog representation.

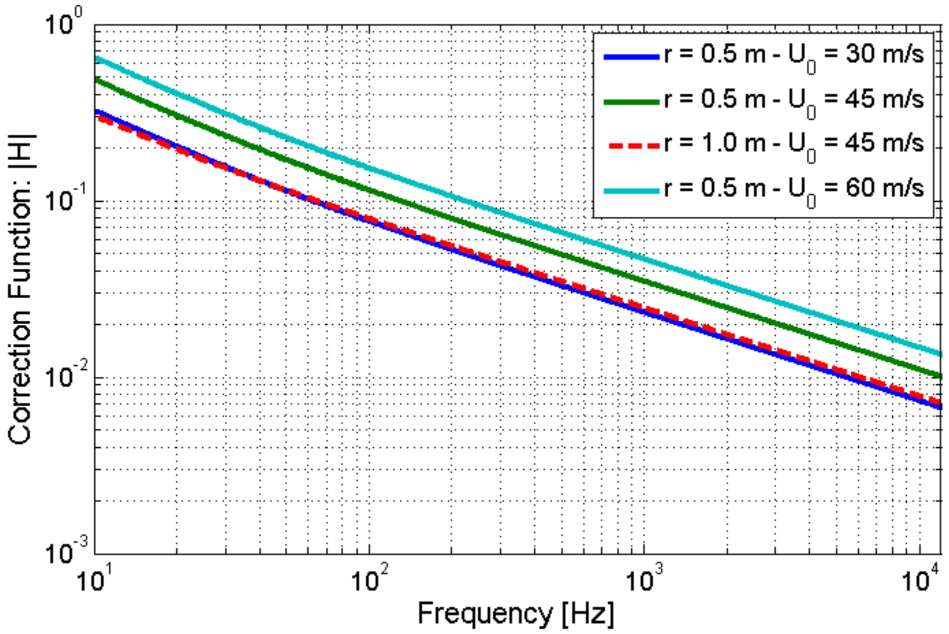

Figure 4.71: Representation of the 3D/2D correction function

The correction function (H) was applied to the simulations computed with the previous four methods used to compute acoustic field at a medium section of profile 1. 1/3 Octave spectra have been computed at three points positioned at 0.5 m from the rain gutter for each approaches and types of source modelling in case of RPM modelling are plotted in figure 4.72. The results are compared with the experimental results which have been corrected according to take in accound the difference of distance to the rain gutter. However as the experimental results were obtained with a rain gutter whose height was varying linearly, the spectra correspond indeed to the contribution of different heights. Therefore the spectra must be compared carefully.

The three methods show that the far field noise generated by the rain gutter is mainly distributed between 1 and 8 kHz as observed by Becker et al. [15]. The two 2D simulations based on the unsteady CFD sources show a reasonable agreement among each other and show a fair agreement with the experimental results in the frequency range 1 - 4 kHz. Although using spatial filtering, spurious acoustic sources were observed at the end of the source domain at low frequencies for the computation with Actran/LA. The different tests with different sizes of the filter did not allow to suppress the spurious sources which are responsible for the elevation of the noise level at low frequency and explain the difference

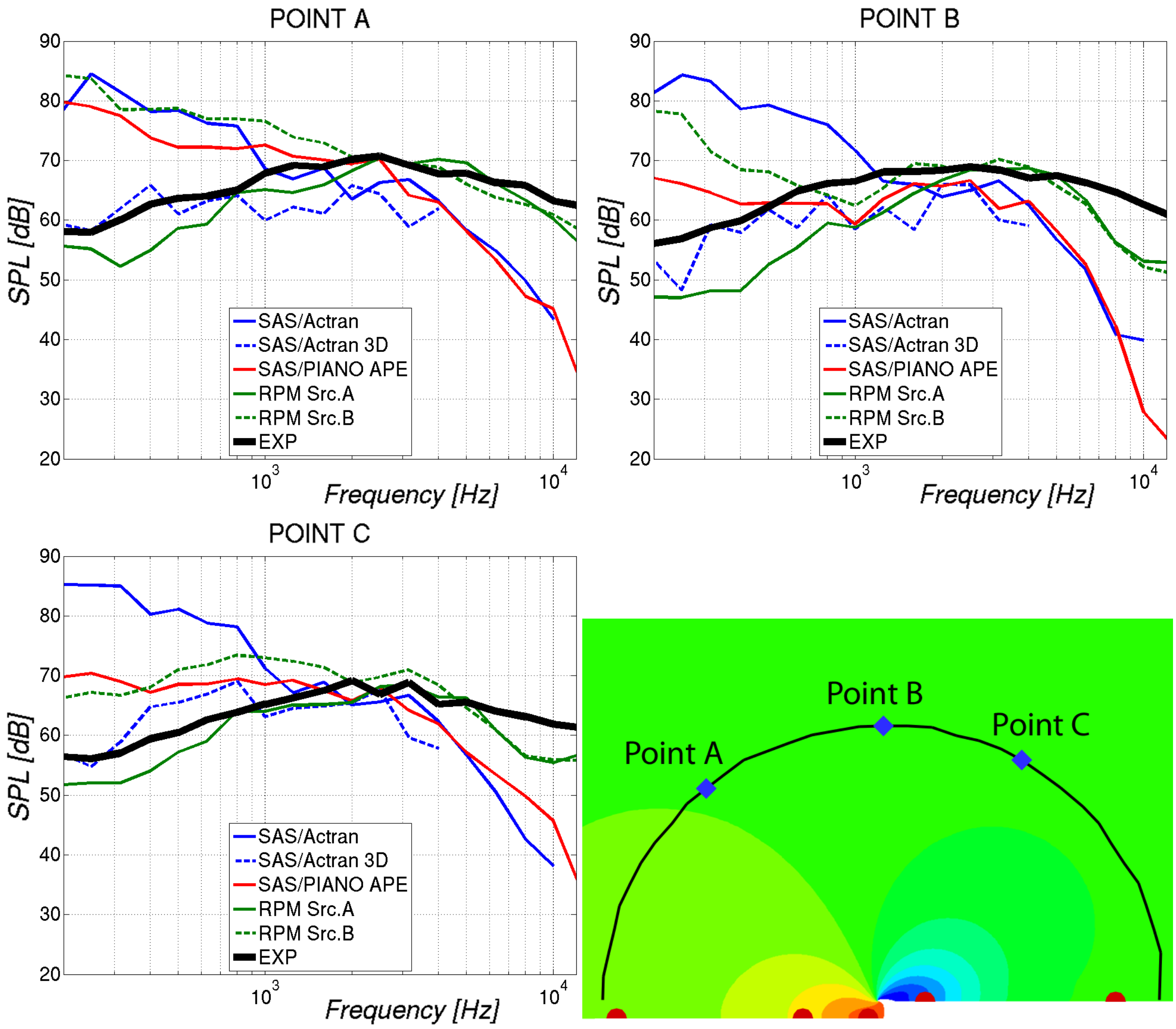

Figure 4.72: Comparison of the 1/3 octave band spectra measured and computed with the different CAA methods for the middle section of profile 1. Point A (top-left), Point B (top-right) and Point C (bottom left)

of the spectra computed with both approaches at low frequency. Further investigations on the effect of the spatial filter should be done.

Considering the simulations performed with the RPM modelling, it is found that the better correlations are found in the case of the RPM simulations with modelling type A. The computed spectra show here by far the best agreement with experimental results even when compared with the unsteady CFD based results. A better agreement was found for the complete modelling of the Lamb vector (source A) in particular at low frequency. Generally a large discrepancy between all simulations and the experiment is found for the low frequency range. One explanation may be the duration of the simulations which was too short. In the case of ACTRAN the simulations would require much more CFD time steps which is practically very difficult to do as it would result in a huge quantity of data. The same problem occurs for the simulation with PIANO/APE and unsteady sources. The main differences between the results of the simulation with PIANO and ACTRAN (particularly for the point upstream and downstream) may be due to the convection effect which is computed within PIANO but ignored in ACTRAN.

Although showing most promising results for the RPM modelling, longer simulations would need to be carried out for further improvement which however remains practically difficult to handle since the purpose of the method is to provide a comparatively quick computation of the acoustic field.

d/ Computational costs

As the aim of the study was to assess different numerical methods, some further comments on the applicability and computational costs must be considered. The code Actran/LA is a finite element code using non structured mesh whereas the code PIANO is a finite difference code and requires a structured mesh. The generation of structured meshes requires more work of the user and may be difficult to handle for complex geometry and three dimensional cases.

To assess the CPU requirements of the method, the duration of each simulation is scaled to a CPU time which corresponds to the time required to perform the simulations in the case where only one CPU is used. Obviously the computations were parallelised and the real time of the simulations were lower. For these simulations the two dimensional simulation with Actran/LA requires about 1 hour CPU time whereas 2 days CPU were necessary for the 3D simulation. In comparison, both computations with PIANO (RPM and unsteady CFD sources + APE) require about 15 days CPU time. Although as opposed to ACTRAN the PIANO computation provides complete time domain information (involving all frequencies) it remains to be clarified why the acoustic propagation part of these simulations was so time consuming since the generation of the initial RPM acoustic sources lasted only about 10 minutes. Finally the unsteady flow field simulation with SAS-forcing requires 3 620 CPU days. cf table 4.6.

The unsteady CFD simulation was the most expensive. The stated computation time ratio for the source representation from unsteady CFD and stochastic modelling of about 5-6 orders of magnitude illustrates the interest of stochastic modelling to represent acoustic sources. The possibility of using non-structured meshes and the resolution of the acoustic field in the frequency domain offers however a good alternative for engineering purposes when a good unsteady CFD solution is available.

Table 4.6: Duration of the simulations

CFD	Steady CFD	Unsteady CFD	
CPU time	4 days	3620 days	
CAA	RPM	Actran/LA	APE
CPU time	15 days	0.5 day	15 days
Total	19 days	3621 days	3635 days

4.6 Concluding remarks

In this chapter, an experimental and numerical study on two shapes of rain gutter and two different 3D configurations have been presented. These configurations were designed to study the effect of the height of the rain gutter and the effect of the direction of the oncoming flow. The height of the boundary layer was of a similar order as the height of the rain gutter. It was shown that the rounded shapes was about 10 dB less noisy than the sharp shape. The main acoustic sources are located in front of the rain gutter and the noise is mainly radiated forward. In addition the study reveals an increase of the rain gutter's height would lead to an increase of the noise level but also a modification of the frequency range of the maximum noise level. The variation of the flow angle results in the modification of the vortex behind the rain gutter and a reduction of the noise level which remains however difficult to quantify.

Furthermore the analysis of the coherence function reveals a good coherence between the signals in near and far field for the first profile while the coherence function was very low for the second profile. This is probably due to its low tendency to generate flow induced noise. Finally it was shown that the acoustic intensity of the flush-mounted microphones scaled with M^4 (corresponding to hydrodynamic pressure fluctuations) while the acoustic intensity scaled with M^6 in the far field. The signals in far field and near field presents a very good level of coherence for profile 1.

It was experimentally shown that the flow over the rain gutter generates a broadband noise and its level was largely influenced by the shape of the profile. The experimental work was performed in view to validate numerical methods.

Various flow simulations have been performed to compute the aeroacoustic field generated by the flow over the same rain gutters. At first steady and unsteady flow simulations were carried out. The results put in evidence the larger recirculation area produced by profile 1 compared to profile 2. Steady 3D RANS simulations show the existence of flow separation over both profiles of rain gutter which were somewhat larger than found during the experiment. 3D vortices were also found in the curved configuration which looks similar to the ones observed in the case of an automotive A-Pillar.

It was shown that getting the hybrid models into an unsteady state was not trivial. It firstly requires a very fine mesh. The DES shows a good ability to capture the turbulence downstream of the step but fails to compute the turbulence structure in front of the rain gutter. Downstream the rain gutter the spectrum shows only a good correlation with the experimental results up to 3 kHz. To solve the problem a finer mesh would probably be necessary but then would lead to a far too high computation effort. The simulation with the SAS model developed by Menter could not produce better results than a steady simulation. In order to give more fluctuating energy to the flow and being able to switch to an unsteady mode, the new forcing model presented by Menter was used. It consists in introducing statistic perturbations to energize the flow. Thanks to this method, rather good correlations were found for the pressure fluctuations upstream the rain gutter and a very good one was obtained even for high frequencies downstream the rain gutter. This method appears like a good tool in case where the flow is not energetic enough however it is not so easy to assess and further works should be done on this model.

The proper orthogonal (POD) method was used to get more information on the flow. It was demonstrated that by using it, one could reduce the order of points to represent the most energetic modes, it was particularly interesting to see that in the case of profile 1, 8 % of modes where necessary to represent 99 % of the whole energy.

Four numerical methods have then been used to compute the acoustic field induced by the flow over the automotive rain gutter. Two methods are based on wave operators and unsteady sources computed by CFD. The two other methods are based on steady flow simulations, i.e. single test-vortex injection method and RPM modelling. As observed during the experiment, profile 1 appears noisier than the profile 2. The different methods allow to visualise the directivity and it is shown that the noise is mainly radiated forward. Although wall pressure fluctuations computed by the unsteady flow simulation are in good agreement with the experimental measurements, the radiated fields computed either by Actran/LA or Piano/APE do not reproduce completely the acoustic field measured during the experiment. It highlights the difficulty of generating good acoustic sources for such application as well as the dependency on the quality of the CFD. The simulations computed with the RPM modelling demonstrate better agreement with the experimental dataset. The broadband character of the noise generated by the rain gutter seems better predicted however further investigations should be done to assess the method. Analogous speed scaling laws of the acoustic intensity were found with the simulation as the ones found during the experiment. Considering the computational effort it was also found that the RPM modelling offers an interesting alternative to quickly reproduce the unsteady character of the flow and allows to speed-up the simulation of the acoustic field.

CHAPTER 5

Conclusion and further remarks

5.1 Summary

Aeroacoustic considerations are nowadays becoming more and more significant for engineering applications. In the automotive context, Aerodynamic noises can be very loud and represent a real nuisance for the driver and the passengers at high speed. Therefore car manufacturers have invested massively during the last decades to build aeroacoustic wind tunnels in order to be able to investigate wind noise. However in order to cope with the continuous reduction of cost and duration of the development phases there is an increasing need for effective numerical methods to simulate the noise induced by external and internal flows and which could be systematically used in the early design phase of a vehicle.

The goal of this dissertation was to study the possibility of using hybrid aeroacoustic methods based on steady CFD RANS simulations to compute noise generated aerodynamically instead of performing expensive unsteady flow simulations. Two applications have been considered in order to assess the capabilities of different methods. The dissertation is organised in four parts.

Chapter 1 presents several examples of wind noise to make the reader aware of the variety of technical problems associated with aeroacoustics and to explain the framework and the objectives of this work. Chapter 2 introduces the fundamental aerodynamic concepts. It outlines the major differences between the requirements of an aerodynamic and an aeroacoustic simulation while demonstrating that CFD tools are generally inadequate when it comes to compute aerodynamic noise. Although providing good results for fundamental cases the use of direct noise computation (DNC) does not appear applicable to most of engineering applications. Therefore hybrid methods in which the simulation of the acoustic sources is separated from the propagation of the noise in the far field are nowadays widely used in industry to assess the wind noise. The acoustic sources can be computed in different ways. One can compute the velocity and pressure fluctuations in the near field via an unsteady flow simulation; but one can also use a model in order to reconstruct the unsteady character of the turbulence. Cost efficient, this last approach was largely applied in this work with the DLR's CAA code PIANO.

Chapter 3 is devoted to the first application: a duct containing a flat plate. Firstly presented, the experimental investigations show the existence of purely acoustic modes induced by the flow and identified as Parker modes. Two numerical methods based on a steady RANS simulation were used to compute the acoustic modes. The first method consists in injecting a single test-vortex upstream the object producing sound and solving the Linearised Euler Equations (LEE); the vortex is convected with the mean flow and interacts with the object (here plate). The interaction between this vortex and the geometry is representative of the flow induced noise source. The second method is the RPM modelling (Random Particle Mesh) to reconstruct the turbulent fluctuations while the far field was computed by solving the Acoustic Perturbation Equations (APE).

Both methods demonstrate their ability to predict with accuracy the acoustic modes. A good agreement was found between the results of the simulations, the experiment and the analytical work done by Koch [64]. It was found that the existence of a mode and the frequency associated were directly depending on the ratio between the length of the plate and the height of the duct. Although initially not designed to compute spectrum and acoustic resonance but to compare the acoustic answers of different geometries, this work outlines the injection of a test-vortex method allows to compute accurately the acoustical resonances in the duct. Originally the method delivers the acoustic response to a punctual perturbation. In this sense, the RPM modelling can be interpreted as the generation of multiple vortices with different length scales and is more appropriate to compute spectra. Finally it was particularly shown that in this particular case with acoustic resonance the simulation of the mean flow field can have a significant impact on the results and may be difficult to interpret.

Presented in chapter 4 the second application is an automotive A-pillar rain gutter. This chapter is divided in two main parts: the experimental work and the numerical simulations. The major results of the experimental investigations carried out in the DLR's Acoustic Wind Tunnel in Braunschweig on both rain gutter profiles have been presented in this work. It was particularly found that profile 1 was about 10 dB noisier than profile 2. 3D configurations were designed to study the effect of the rain gutter's height and the direction of the oncoming flow. The results show that the overall noise level scales almost linearly with the height of the rain gutter while an increase of the oncoming flow angle generally reduces the overall noise level. Using a microphone array, it was shown that the acoustic sources are located slightly in front of the rain gutter and that the position of the maximum noise level at a frequency moves with the height of the rain gutter. The correlation between the different microphones (far-field and near field) have been computed. Good correlations between the far field microphones and the flush-mounted microphones placed directly in front of the rain gutter were particularly found for profile 1 in the range 1 - 6 kHz. Finally it was found that the sound level in the far field scales with the 6th power of the mean flow velocity which according to Curle is indicative for a compact aeroacoustics sound source.

The topology of the flow over the same rain gutters was numerically assessed using steady and unsteady flow simulations. The steady and unsteady flow simulation showed the existence of flow separations behind both profiles. A longer recirculation area as well as a higher level of turbulence fluctuations were however found for profile 1 which confirms the higher noise level measured in this case. The simulation over configuration B reveals the existence of a three dimensional vortex similar to the one observed along the A-Pillar of a vehicle. Based on hybrid turbulence models (DES, SAS) unsteady flow simulations were performed over a part of the three dimensional linear rain gutter with profile 1. It was shown that making the hybrid models switch into an unsteady mode was not a trivial task. Requiring firstly a refinement of the mesh *in particular in the spanwise direction*, the height of the boundary layer almost as high at the rain gutter itself makes this switch particularly difficult. The DES demonstrates a good ability to capture the turbulence downstream the step but fails to really compute the structure in front of it. Downstream the rain gutter the spectrum shows a good correlation with the experimental results up to 4 kHz. The resolution of the higher frequencies would require even a finer mesh. It was found that the SAS model could not correctly switch into an unsteady mode and only delivers a steady solution. The new formulation of the SAS model with forcing terms introduced by Menter [80] was then used to increase the turbulence level in front of the rain gutter. The use of forcing terms allows getting a higher level of wall pressure fluctuations. A very good agreement was found between the simulation and the experiment even for frequencies between 5 and 12 kHz showing a lower dependency to the mesh resolution compared to DES. Proper orthogonal decomposition was finally used to study the flow. It highlights the dominant character of the first modes for profile 1 which are much more energetic than the ones of profile 2.

Four different methods have been tested to compute the aerodynamically induced acoustic field over the rain gutters. The first two methods are based on unsteady acoustic sources computed via an unsteady CFD simulation. In this work the results of the simulation with the SAS with forcing terms have been used. The computation of the acoustic field was then either computed by solving the APE system implemented in the code PIANO or the weak formulation of the Lighthill equation implemented in the code Actran/LA developped by FFT. The two other methods were the single test-vortex injection method and the RPM modelling as used for the duct. The RPM modelling was at the moment of this work limited to two-dimensional simulations, therefore all cases were treated in two dimensions and the original three-dimensional steady and unsteady flow fields were interpolated on two dimensional aeroacoustic meshes. In addition a 3D simulation was performed with the Actran/LA on a reduced portion of the rain gutter and with the single test-vortex method using full 3D block-structured meshes.

Both methods based on unsteady CFD sources (SAS-f) delivers similar results showing the equivalence between the methods. The limitation of the source domain results in a truncation phenomena of the sources. The truncation problem was not completely solved with Actran. The presence of spurious sources disturbed the results for the low frequencies. Although not delivering any spectra in the far field the single test vortex injection method allows to evaluate the directivity and to compare the noise levels produced by the different rain gutter profiles, heights and oncoming flow speeds. Similar scaling laws were found for the height ($\propto h$) and the flow speed ($\propto M^6$) as the ones found during the experiment. It was also confirmed that profile 1 was noisier than profile 2.

The simulations with RPM modelling indicate the same scaling laws. The influence of acoustic sources used in the RPM modelling to compute the acoustic field was also clearly put in evidence. It was demonstrated that using the source *type A* was leading to a dominance of the frequencies in the range 2 - 6 kHz while with the source *type B* the lower frequencies were further emphasized. The importance of the patch and particularly of the lines close to the geometry was also highlighted. Indeed the noise level can be very dependent on this last feature but remains very difficult to evaluate. Except for the RPM modelling, the methods show similar directivity patterns oriented forward. This difference comes from the dominance of higher frequencies for the RPM modelling which is confirmed by looking individually at the directivity patterns for different frequency ranges.

Based on the Green's functions a 2D/3D correction function (H) was introduced. This function was applied to compare the results of the different methods with the experiment. The RPM modelling (with source type A) shows the better overall agreement. However when looking in the range 1 - 5 kHz, all four methods show acceptable agreement with the experimental results. Two reasons can be advanced to explain the difficulty of the simulations with CFD unsteady sources. Firstly, it may indicate that the sources are difficult to simulate as it was shown in the aerodynamic part. Secondly, the 2D character of the simulation can represent an issue for the aeroacoustic simulation. One can notice that the 3D simulation computed with Actran/LA shows in comparison with the 2D simulations a better agreement with the experiment.

A large discrepancy of computational costs has been observed between the methods (i.e. 4 CPU days to compute the sources with RPM modelling vs. almost 10 CPU years to compute the sources with the unsteady CFD simulation). By computing the far field in the frequency domain, the code Actran/LA appears to be numerically more efficient than the simulations in the time domain. However the high cost to compute the unsteady acoustic sources made this method in overall more expensive than methods based on turbulence modelling such as the RPM modelling.

In a nutshell this work illustrates the possibility of computing the aerodynamic noise in the case of a ducted flow and of an external flow (rain gutter) using a stochastic source modelling. Different numerical approaches as well as some of the related requirements are investigated. A good agreement was found between the numerical and the experimental results.

5.2 Perspectives

Coming back to the list of points falling under the scope of this work and addressed in the introduction, it was shown that the stochastic model delivers results in good agreement with the experiment for both applications. It appears that computation of the acoustic sources is a key point. The different formulations of the RPM modelling illustrate this major feature. The set-up of the patch remains a delicate task and different attempts must be done to get a suitable set-up. While the method itself proves to be quite useful, it is recommended to invest more work in making the actual set-up more robust or user-friendly. The study illustrates also the possibility of using stochastic modelling for CFD. It was particularly shown that in this particular case where the SAS model was not unstable enough to switch into an unsteady mode, the introduction of stochastic terms allowed the model to switch into an unsteady mode.

In this study the aeroacoustic simulations were performed on 2D CAA meshes although the experiment was definitely 3D. At the moment of completion of this work a 3D version of the RPM modelling was under development but not available for this work. The possibility of carrying out 3D simulations represents a major issue since most of the applications are 3D. However the methods demonstrate a good ability to make comparison between two profiles which is often enough for many engineering applications. The use of the single test-vortex injection offers particularly a good alternative to quickly compute an A-B comparison between geometries.

For two-steps methods such as for Actran/LA or in PIANO where the simulation of the acoustic far field is based on acoustic sources previously computed by an unsteady CFD simulations, the quality of these CFD simulations has a major influence such that a poor simulation of the acoustic sources cannot lead to a favorable simulation of the acoustic far field. Shown in this work, the truncation of the sources plays an important role and must be carefully handle. As the analogy of Lighthill does not take into account convection effects, the Moehring analogy (similar to the APE system) was implemented in Actran/LA and could represent an interesting alternative to compute the acoustic far field in the presence of mean flow.

The study only deals with simulation of the sources and the propagation of the noise to the far field but not of the sound inside the passenger area. This would be the next step of the aeroacoustic simulation. The difficulty remains here to compute the pressure fluctuations on the windows and using a transfer function to compute the acoustic field in the cabin.

Currently the DLR's code PIANO is based on the finite difference method which limits the type of elements used. Up to now the code required structured meshes which may be very difficult and costs a lot of time to produce. The possibility of using unstructured meshes would make the use of the code easier. In addition the parallelization of the code is based on the blocks. Therefore the higher the number of blocks the easier it is to distribute them. However one has to be careful to the number of nodes in each block in order to make the parallelization as efficient as possible. When using RPM the RPM modelling is only carried out by one processor while the others compute the propagation of the acoustic field. Unfortunately it often happens that the RPM work depending of the RPM parameters is the most demanding work resulting in waiting time for the others processors. One has to be conscious that increasing the number of processor would not lead to any reduction of the computational time. This represents a key point to reduce the computational cost and be efficient.

Aeroacoustic issues in the automotive industry are currently mainly addressed by computing high-cost unsteady CFD simulations. Therefore stochastic modelling could represent a valuable alternative. However as presented in this work, a lot of preparation work is required to obtain good results. In addition due to the relative small amplitudes of the acoustic perturbations, small errors in the computation of the sources can result in inacceptable errors in the computation the acoustic field. Therefore if the tools are already able to deliver good results, it is now essential to make them more user-friendly, robust, automatic and faster in order to be used in a productive way and allow optimisation tasks.

List of Tables

List of Figures

Bibliography

[1] I. Ali and al. Aeroacoustic study of a forward facing step using linearised Euler equations. *Physica D: Non linear phenomena*, 237(14-17):2184–2189, 2008. 65

[2] R.K. Amiet. Correction of open jet wind tunnel measurements for shear layer diffraction. In *AIAA*, number 532, 1975. 67

[3] ANSYS-CFX. *CFX 11.0 modeling guide - Turbulence and near wall modeling*, December 2006. 11

[4] B. Arguillat and al. Measurements of the wave-number frequency spectrum of wall pressure fluctuations under turbulent flow. In *11th AIAA/CEAS Aeroacoustic Conference*, 2005. 65

[5] Y. Bae and al. Investigation of flow-induced noise from a forward facing step. In *19th Symposium of Japan CFD*, 2005. 65, 91, 142

[6] C. Bailly and D. Juve. A stochastic approach to compute subsonic noise using linearized Euler equations. In *AIAA Paper*, volume 99-1872 of *1*, 1999. 26

[7] C. Bailly, P. Lafon, and S. Candel. A stochastic approach to compute noise generation and radiation of free turbulent flows. In *AIAA Paper*, volume 95-092 of *1-6*, 1995. 26

[8] J.E. Bardina, P.G. Huang, and T.J. Coakley. Turbulence modeling validation, testing and development. Technical report, NASA Technical Memorandum 110446, 1997. 12

[9] P. Batten, U. Goldberg, and S. Chakravarthy. Subgrid turbulence modeling for unsteady flow with acoustic resonance. In *38th Aerospace Sciences Meeting, Reno, NV*, number 473, 2000. 16

[10] P. Batten, U. Goldberg, and S. Chakravarthy. Interfacing statistical turbulence closures with large-eddy simulation. *AIAA Journal*, 42(3):485–492, 2004. 16, 26

[11] P. Batten, E. Ribaldone, M. Casella, and S.R. Chakravarthy. Towards a generalized non-linear acoustics solver. In *10th AIAA/CEAS Aeroacoustics Conference*, volume 2004-3001, 2004. 26

[12] M. Bauer. Berechnung des Umströmungsgeräuches vorwärtesgeneigter Stufen mit Hilfe eines synthetischen turbulente Geschwingdigskeitsfeldes. Technical report, Forschungsverbund Leiser Verkehr - Akustische Simulationsverfahren - FKZ 19U1074A, 2005. 66

[13] M. Bauer, J. Dierke, and R. Ewert. Application of a discontinuous Galerkin method to discretize acoustic perturbation equations. *AIAA JOURNAL*, 49, 2011. 25

[14] W. Bechara, C. Bailly, P. Lafon, and S. Candel. Stochastic approach to noise modelling for free turbulent flows. *AIAA Journal*, 32-3, 1994. 4, 25

[15] S. Becker, M. Escobar, C. Hahn, M. Kaltenbacher, B. Basel, and M. Grünewald. Experimental and numerical investigation of the flow induced noise from a forward facing step. In *AIAA Aeroacoustics Conference*, 2005. 65, 125

[16] T. Belamri, Y. Egorov, and F. Menter. CFD Simulation of the aeroacoustic noise generated by a generic side view car mirror. In *13th AIAA/CEAS Aeroacoustics Conference*, 2007. 15

[17] J.-P. Berenger. A perfectly matched layer for absorption of electromagnetic waves. *Journal of Computational Physics*, 114:185–200, 1994. 19

[18] J. Berland, C. Bogey, O. Marsden, and C. Bailly. High-order, low dispersive and low dissipative explicit schemes for multiple-scale and boundary problems. *Journal of Computational Physics*, 224:637–662, 2007. 18

[19] M. Billson, L.E. Eriksson, and L. Davidson. Jet noise prediction using stochastic turbulence modeling. In *9th AIAA/CEAS Aeroacoustics Conference*, number 3282, 2003. 4

[20] C. Bogey and C. Bailly. A family of low dispersive and low dissipative explicit schemes for flow and noise computations. *Journal of Computational Physics*, 194:194–214, 2004. 18

[21] C. Bogey, C. Bailly, and D. Juve. Computation of flow noise using source terms in linearized Euler's equations. *AIAA Journal*, 42(2):235–243, 2002. 4, 26

[22] P. Bradshaw. *An introduction to turbulence and its measurement.* Pergamon Press, 1971. 12

[23] T.A. Brungart, G.C. G.C.Lauchle, S. Deutschland, and E.T. Riggs. Wall pressure fluctuations induced by separated/reattached channel flows. *Journal of Sound and Vibration*, 251(3):558–577, 2002. 65

[24] S. Caro, Y. Detandt, J. Manera, R. Toppinga, and F. Mendoca. Validation of a new hybrid CAA strategy and application to the noise generated by a flap in a simpified HVAC duct. In *15th AIAA/CEAS Aeroacoustics Conference*, 2009. 107

[25] S. Caro, P. Ploumhans, and X. Gallez. Implementation of the Lighthill's acoustic analogy in a finite/infinite elements framework. In *10th AIAA/CEAS Aeroacoustics Conference*, 2004. 107

[26] CEI. *Ensight user manual version 9.0.* Apex, USA, 2008. 41

[27] T. Colonius, S.K. Lele, and P. Moin. Boundary conditions for direct computation of aerodynamic sound generation. *AIAA Journal*, 31(-):1574–1582, 1993. 9

[28] N. Curle. The influence of solid boundaries upon aerodynamic sound. *Proc. R. Soc. London, Ser.A*, 231:505–514, 1955. 22, 121

[29] L. Davidson. Evaluation of the SST-SAS model: channel flow, asymmetric diffuser and axi-symmetric hill. In *in ECCOMAS CFD. TU Delft, The Netherlands*, 2006. 15, 16, 97

[30] L. Davidson. The SAS model: a turbulence model with controlled modelled dissipation. In *in 20th Nordic Seminar on Computational Mechanics Göteborg*, 2007. 15

[31] S. Debert and al. Fluctuations under turbulent flows enhanced methods for separation of propagative wavenumbers from wall pressure dataset. *JASA*, 123(5), 2005. 65

[32] H. Dechipre, M. Hartmann, J.W. Delfs, and R. Ewert. Aeroacoustic simulation based on linearized Euler equations and stochastic sound source modelling. In *Acoustics'08 Paris*, pages 1071–1076, 2008. 35

[33] J.W. Delfs and al. *Numerical simulation of aerodynamic noise with DLR's aeroacoustic code PIANO, PIANO Manual version 5.4.* Braunschweig, 2009. 24, 27, 28, 111

[34] P. Delorme, P. Mazet, C. Peyret, and Y. Ventribout. *Computational aeroacoustics applications based on a discontinuous Galerkin method*, volume 333-9. Comptes Rendus de l´Académie des Sciences, 2005. 25

[35] Y. Duan. *Trapped modes and acoustic resonances.* PhD thesis, Loughborough University, 2004. 34

[36] Y. Duan, W. Koch, and Maureen Linton, C.M.and McIver. Complex resonances and trapped modes in ducted domains. *Journal of Fluid Mechanics*, 571:119–147, 2007. 34, 35, 36, 37, 139

[37] J.K. Eaton and J.P. Johnston. Turbulent flow reattachment: an experimental study of the flow. *AIAA Journal*, 19(9), 1981. 65

[38] R. Edmunds and M. Fischer. Effect of Re-number, Ma-number and angle of attack on slat noise based on a test-vortex injected upstream of the slat-hook. In *11th AIAA/CEAS Aeroacoustics conferences*, number 2975, 2005. 29

[39] D. Evans and C. Linton. Trapped modes in open channels. *Journal of Fluid Mechanics*, 225:153–175, 1991. 34

[40] D. Evans and C. Linton. Acoustic resonance in ducts. *Journal of Sound Vibration*, 173:85–94, 1994. 34

[41] D. Evans and R. Porter. Trapped modes embedded in the continuous spectrum. *Q. Journal Mech. Appl. Math*, 52:263–274, 1998. 34

[42] R. Ewert. Slat noise trend prediction using CAA with stochastic sound sources from a random particle-mesh method (RPM). In *12th AIAA/CEAS Aeroacoustics Conference*, number 2667, 2006. iii, v, 4, 30

[43] R. Ewert. RPM-the fast random particle-mesh method to realize unsteady turbulent sound sources and velocity fields for CAA applications. In *13th AIAA/CEAS Aeroacoustics Conference, Rome*, number 3506, 2007. 2, 31, 40, 114

[44] R. Ewert. Broadband slat noise prediction based on CAA and stochastic sound sources from a random particle-mesh (RPM) method. *Journal of Computers & Fluids*, 37-4:369–387, 2008. 27

[45] R. Ewert, C. Appel, J. Dierke, and M. Herr. RANS/CAA based prediction of NACA 0012 broadband trailing edge noise and experimental validation. In *15th AIAA/CEAS Aeroacoustics Conference, Miami Florida*, number 3269, 2009. 25, 27, 42, 120, 125

[46] R. Ewert and W. Schroeder. Acoustic Pertubation Equations based on flow decomposition via source filtering. *Computational Physics*, 188:365–398, 2003. 24, 27, 103, 124

[47] R. Ewert and W Schroeder. On the simulation of trailing edge noise with a hybrid LES/APE method. *Journal of Sound and Vibration*, 270:509–524, 2004. 24, 30

[48] A. Fadai-Ghotbi. *Modélisation de la Turbulence en situation instationnaire par approches URANS et hybride RANS-LES*. PhD thesis, Université de Poitiers, 2007. 16

[49] T.M. Farabee and M.J. Casarella. Measurements of fluctuating wall pressure for separated / reattached boundary layer flows. *Journal of Vibration, Acoustics, Stress and Reliability in Design*, 108:301–307, 1986. 65

[50] J.E. Ffowcs-Williams and D.L. Hawkings. Sound generation by turbulence and surfaces in arbitrary motion. *Phil. Trans. Roy. Soc. London, Ser.A*, 264:321–342, 1969. 22

[51] R. Franklin. Acoustic resonance in cascades. *Journal Sound and Vibration*, 25:587–595, 1972. 34

[52] Free Field Technologies. *Actran 10.1 Users' Guide*. Louvain La Neuve, Belgium, 2010. 23, 107

[53] A.R. George. Automobile aerodynamic noise. In *SAE Paper 900315*, 1990. 1, 2

[54] J.H. Gerrard. Measurements of sound from circular cylinders in an airstream. In *Physical Society Section B*, volume 68, pages 453–461, 1955. 34

[55] M. Hartmann and H. Dechipre. Numerische Aeroakustik für Anwendungen im Automobilbereich. *ATZ VDI-FVT-Jahrbuch 2009*, pages 90–99, 2009. 3

[56] M.S. Howe. The generation of sound by aerodynamic sources in an homogeneous steady flow. *J. Fluid Mech.*, 67(3):597–610, 1975. 22, 24

[57] F.Q. Hu. On absorbing boundary conditions for linearised Euler equations by a perfectly matched layer. *Journal of Computational Physics*, 129-1:201–219, 1996. 19

[58] F.Q. Hu. On using perfectly matched layer for the Euler equations with a non-uniform mean flow. In *AIAA Paper*, number 2966, 2004. 19

[59] F.Q. Hu, M.Y. Hussaini, and J.L. Manthey. Low-dissipation and low-dispersion Runge-Kutta schemes for computational acoustics. *Journal of Computational Physics*, 124:177–191, 1996. 18

[60] W.H. Hucho, editor. *Aerodynamics of road vehicles - from fluid mechanics to vehicle engineering*. fourth edition, SAE International, Warrendale, PA, 1998. 2

[61] O. Imberdis, M. Hartmann, H. Bensler, D. Thevenin, and L. Kapitza. A numerical and experimental investigation of a DISI-Engine intake port generated turbulent flow. In *Journal of Engines - SAE 2007 Transactions*, 2007. 15

[62] M. Karweit, P. Belanc-Benon, D. Juve, and Comte-Bellot G. Simulation of the propagation of an acoustic wave through a turbulent velocity field: A study of phase variance. *Journal of Acoustic Society of America*, 89(1):55–62, 1991. 25

[63] M. Klein, A. Sadiki, and J. Janicka. A digital filter based generation of inflow data for spatially developing direct numerical or large eddy simulations. *Journal of Computational Physics*, 186:652–665, 2003. 16

[64] W. Koch. Resonant acoustic frequencies of flat plate cascades. *Sound of Vibration*, 88:233–242, 1983. iii, v, 34, 35, 37, 57, 132

[65] A. N. Kolmogorov. Die Energiedissipation für lokalisotrope Turbulenz. *Dokl. Akad. Wiss. USSR*, 32:16–18, 1941. 8

[66] A. N. Kolmogorov. Die lokale Struktur der Turbulenz in einer inkompressiblen zähen Flüssigkeit bei sehr großen Reynoldsschen Zahlen. *Dokl. Akad. Wiss. USSR*, 30:301–305, 1941. 8

[67] K. Kondo, S. Murakami, and A. Mochida. Generation of velocity fluctuations for inflow boundary conditions of LES. *Journal of Wing Engineering and Industrial Aerodynamics*, 67 & 68:51–64, 1997. 16

[68] R.H. Kraichnan. Diffusion by a random velocity field. *Physics of Fluids*, 13(1):22–31, 1969. 25

[69] S. Kumarasamy and K. Karbon. Aeroacoustics of an automobile A-Pillar rain gutter: computational and experimental study. In *SAE Conference*, 1999. 65

[70] P. Lafon. Application du modèle SNGR de génération de bruit au cas du diaphragme en conduit. Technical report, Rapport HP-63/95/32/A - Direction des Etudes et Recherches d´Electricité de France, 1996. 2

[71] S.K. Lele. Compact finite difference schemes with spectral-like resolution. *Journal of Computational Physics*, 103:16–42, 1992. 20

[72] M.J. Lighthill. On the sound generated aerodynamically. Part I: General theory. In *Proceedings of the Royal Society of London*, volume A211, pages 564–587, 1952. 2

[73] G.M. Lilley. The generation and radiation of supersonic jet noise. Vol. IV - Theory of turbulence generated jet noise, noise radiation from upstream sources, and combustion noise. Part II: Generation of sound in a mixing region. Technical report, Air Force Aero Propulsion Laboratory, 1972. 22

[74] J.L. Lumley. *The structure of inhomogeneous turbulent flows, in atmospheric turbulence and wave propagation*, pages 166–178. A.M. Yaglom and V.I. Tatarsky, eds. Nauka, Moscow, 1967. 99

[75] M. Lummer, J.W. Delfs, and T. Lauke. Simulation of sound generation by vortices passing the trailing edge of airfoils. In *8th AIAA/CEAS Aeroacoustics conferences*, number 2578, 2002. 2, 29, 49

[76] M. Lummer, J.W. Delfs, and T. Lauke. Simulation of the influence of trailing edge shape on the airfoil sound generation. In *9th AIAA/CEAS Aeroacoustics conferences*, number 3109, 2003. 29

[77] A.S. Lyrintzis. Review: the use of Kirchoff's method in computational aeroacoustics. *Journal of Fluid Engineering*, 116:665–676, 1994. 27

[78] F. Mathey. Aerodynamic noise simulation of the flow past an airfoil trailing-edge using a hybrid zonal RANS-LES. *Computers and Fluids*, 37:836–843, 2008. 16

[79] F. Menter. Zonal two equation k-ω turbulence models for aerodynamic flows. In *AIAA*, number 2906, 1993. 10, 11

[80] F. Menter and al. Scale-adaptive simulation with artificial forcing. In *3rd Symposium on Hybrid RANS-LES methods*, 2009. 16, 97, 133

[81] F. Menter, M. Kuntz, and R. Bender. A scale-adaptive simulation model for turbulent flow predictions. In *AIAA 41st Aeroaspace Science Meeting & Exhibit, Reno, Nevada, USA*, 2003. 14

[82] F.R. Menter and Y. Egorov. Re-visiting the turbulent scale equation. In *One hundred years of boundary layer research. Goettingen, Germany*, 2004. 15

[83] F.R. Menter and Y. Egorov. A scale-adaptive simulation model using two-equation models. In *AIAA, Reno, NV*, number 1095 in -, 2005. 15

[84] F.R. Menter and Y. Egorov. Turbulence modeling of aerodynamic flows. In *International Aerospace CFD Conference. Paris*, 2007. 15

[85] F.R. Menter and M. Kuntz. Development and application of a zonal DES turbulence model for CFX-5. Technical report, Ansys CFX Validation Report, 2003. 13

[86] M. Mesbah. *Flow noise prediction using the Stochastic Noise Generation and Radiation approach.* PhD thesis, Katholieke Universiteit Leuven, 2006. 26

[87] W. Möhring. On vortex sound at low Mach number. *Journal of Fluid Mechanics*, 4:685–691, 1985. 22, 24

[88] Y.J. Moon, Y.M. Bae, and M.H. Cho. Numerical investigation of the aerodynamic noise from a forward-facing step. In *Eccomas CFD*, 2006. 65

[89] A.H. Nayed and D.H. Huddleston. Resonant acoustic frequencies of parallel plates. In *12th AIAA Fluid and Plasma Dynamics Conference, Williamsburg*, number 79-1522 in -, 1979. 34

[90] N.N. Automotive rain gutter noise. Technical Report EX227, Application briefs from FLUENT, 2005. 65

[91] C. Noger. *Contribution a l´étude des phénomenes aéroacoustiques se developpant dans la baignoire et autour des pantographes du TGV.* PhD thesis, Université de Poitiers, 1999. 2

[92] A.A. Oberai, F. Roknaldin, and T.J.R. Hughes. Computational procedures for determining structural acoustic response due to hydrodynamic sources. *Comput. Methods Appl. Mech. Eng.*, 190:345–361, 2000. 22

[93] A.A. Oberai, F. Roknaldin, and T.J.R. Hughes. Trailing-edge noise due to turbulent flows. Technical Report 02-002, Boston University, 2002. 124

[94] R. Parker. Resonant effect in wake shedding from parallel plates: some experimental observations. *Sound of Vibration*, 4:62–72, 1966. 34

[95] R. Parker. Resonant effect in wake shedding from parallel plates: calculation of resonnant frequencies. *Sound of Vibration*, 5:330–343, 1967. 34, 139

[96] F. Perot. *Calcul du rayonnement acoustique d´écoulements turbulents basé sur des analogies acoustiques couplées aux simulations aérodynamiques instationnaires.* PhD thesis, Ecole Centrale Lyon, 2004. 65

[97] O.M. Phillips. On the generation of sound by supersonic turbulent shear layers. *J. Fluid Mechanics*, 9(1):1–28, 1960. 22

[98] H. Posson and F. Perot. Far field evaluation of the noise radiated by a side mirror using LES and acoustic analogy. In *12th AIAA/CEAS Aeroacoustics Conference*, 2005. 65

[99] M. Pott-Pollenske and J.W. Delfs. Enhanced capabilities of the aeroacoutic wind tunnel Braunscheig. In *14th AIAA/CEAS Aeroacoustic Conference, Vancouver*, number 2910, 2008. 67

[100] A. Powell. Theory of vortex sound. *J. Acousti Soc. Am.*, 36(1):177–195, 1964. 22, 24

[101] J.C. Rotta. *Turbulente Stroemungen.* Teubner Stuttgart, Germany, 1972. 15

[102] Rung and al. Sound radiated of the vortex flow past a generic side mirror. In *AIAA*, number 2340, 2002. 97

[103] M. Sabanca. Noise generated by turbulent flow over forward facing steps. *Computer and Fluids*, 38(7):1467–1479, 2008. 65

[104] P. Sagaut. *Large eddy simulation for incompressible flows. An Introduction.* Springer-Verlag, Berlin, 2nd edition edition, 2002. 12

[105] S. Senthooran, B. Crouse, G. Balsubramanian, D. Freed, S.R. Shin, and K.D. Ih. Effect of surface mounted microphones on automobile side glass pressure fluctuations. In *7th Mira International Vehicle Aerodynmics Conference*, pages 102–116, 2008. 65

[106] J.H. Seo and Y.J. Moon. Linearized perturbed compressible equations for low mach number aeroacoustics. *Computational Physics*, 2006. 24

[107] J.S. Shang. High-order compact-difference schemes for time-dependent Maxwell equations. *Journal of Computational Physics*, 153:312–333, 1999. 20

[108] M.J. Sherry, D.L. Jacono, J. Sheridan, R. Mathis, and I. Marusic. Flow separation characterisation of a forward facins ste immerser in a turbulent boundary layer. In *6th International Symposium on Turbulence and Shear Flow Phenomena*, 2009. 64, 65, 141

[109] R. Siegert and al. Numerical simulation of aeroacoustical sound generated by generic bodies placed on a plate: Part II - Prediction of radiated sound pressure. In *AIAA Conference*, number 1985 in -, 1999. 65

[110] J. Smagorinsky. General circulation experiments with the primitive equations. Technical Report 91(3), Mon. Weath. Rev., 1963. 12

[111] A. Smirnov, S. Shi, and I. Celik. Random flow generation technique for large eddy simulation and particle dynamics modelling. *Journal of Fluids Engineering*, 123:359–371, 2001. 26

[112] P.R. Spalart and al. Comments on the feasibility of LES for wings and on hybrid RANS/LES approach. In *Advances in DNS/LES, Proc. 1st AFOSR Int. Conf. on DNS/LES*, 1997. 13

[113] P.R. Spalart and al. A new version of detached eddy simulation, reistant to ambiguous grid densities. *Theoretical Computational Fluid Dynamics*, 20:181–195, 2006. 13

[114] C. Spehr, J.W. Delfs, O. Kornow, L. Krenkel, C. Wagner, A. Bouhaj, and A. Gommet. Simulation of flow-induced noise generation on orifice plates in air-conditionning ducts. In *14th AIAA/CEAS Aeroacoustics conferences*, number 3022, 2008. 29

[115] M. Strelets. Detached eddy simulation of massively separated flows. In *AIAA Paper*, 2001. 13

[116] V. Strouhal. Über eine besondere Art der Tonerregung. *Annalen der Phys J. und Chemie*, 5:216, 1878. 34

[117] C. Tam and Z. Dong. Wall boundary conditions for higher-order finite difference schemes in computational aeroacoustics. *Computational Fluid Dynamics*, 6:303–322, 1994. 18

[118] C. Tam and J. Webb. Dispersion-relation-preserving finite difference schemes for computationnal acoustics. *Computational Physics*, 107:262–281, 1992. 18, 19, 28

[119] C. Tam, J. Webb, and Z. Dong. A study of the short wave components in computational acoustics. *Computational Acoustics*, 1:1–30, 1993. 20

[120] C. Wagner, T. Huettl, and P. Sagaut, editors. *Large-Eddy simulation for acoustics.* Cambridge University Press, 2007. 12

[121] P.D. Welch. The use of fast Fourier transform for the estimation of power spectra: a method based on time averaging over short, modified periodograms. *IEEE Trans. Audio Electroacoustics*, AU-15:70–73, June 1967. 43

[122] M.C. Welsh and D.C. Gibson. Interaction of induced sound with flow past a square leading edged plate in a duct. *Journal of Sound and Vibration*, 67:501–511, 1979. 34, 37

[123] M.C. Welsh, A.N. Stokes, and R. Parker. Flow resonant sound interaction in a duct containing a plate, Part I: semi-circular leading edge. *Journal of Sound and Vibration*, 95:305–323, 1984. 35

[124] D.C. Wilcox. Re-assessment of the scale-determining equation for advanced turbulence models. *AIAA Journal*, 26:1414–1421, 1988. 10

[125] D.C. Wilcox. *Turbulence modeling for CFD.* DVW Industries, 2006. 10

[126] B. Woodley and N. Peake. Resonant acoustic frequencies of a tandem cascade, Part I: Zero relative motion. *Journal of Fluid Mechanics*, 393:215–240, 1999. 34

Acknowledgements

I would like to express my sincere gratitude to Dr. Markus Lienkamp, Mr. Oliver Schroeter, Dr. Klaus Droeder and Dr. Henry Bensler for their confidence and efforts all along the three and a half years spent in the research department at Volkswagen and who offered me the chance to conduct this study in the best conditions.

I want also to take this opportunity to thank Professor Jan Delfs for his guidance and encouragements during the preparation of this thesis.

I wish to thank Professor Sabine Langer as second referee for the work and Professor Kozulovic as president of the examination commission.

As I carried out this study with the support of the DLR Braunschweig, I gratefully acknowledged Mr. Michael Pott-Pollenske for his help during the experiments as well as Dr. Roland Ewert and Mr. Oliver Kornow for their advices and expertise in aeroacoustics and in the use of PIANO.

From the numerical side, I would like to sincerely greet Dr. Stephane Caro and Romain Leneveu from Free Field Technologies for their help and support provided together with their latest developments of Actran/LA as well as Dr. Florian Menter and Mr. Patrick Müller from ANSYS Germany for their support in the realization of unsteady flow simulation part.

I would like to sincerely thank also my colleagues at Volkswagen for their intensive support and friendliness and the all students with whom I shared a lot and long discussions with about aeroacoustics: Mr. Eric Pattyn, Mr. Gwenael Henry, Mr. Karim Hamiche and Mr. Quentin Behaghel.

Before closing this chapter, I have to express my deepest gratitude for his large contribution to this research work, his technical and scientific advices, my supervisor Dr. Michael Hartmann.

Finally, I remember the endless patience, understanding and encouragement of my family, my friends and especially my girlfriend Katharina Kuhlmann for her endless support and trust and without whom I would have never had the energy to finish it! Vielen Dank Schatz!!

Appendices

A.1 Maps from Microphone Array

Microphone Array - Configuration A - Profile 1

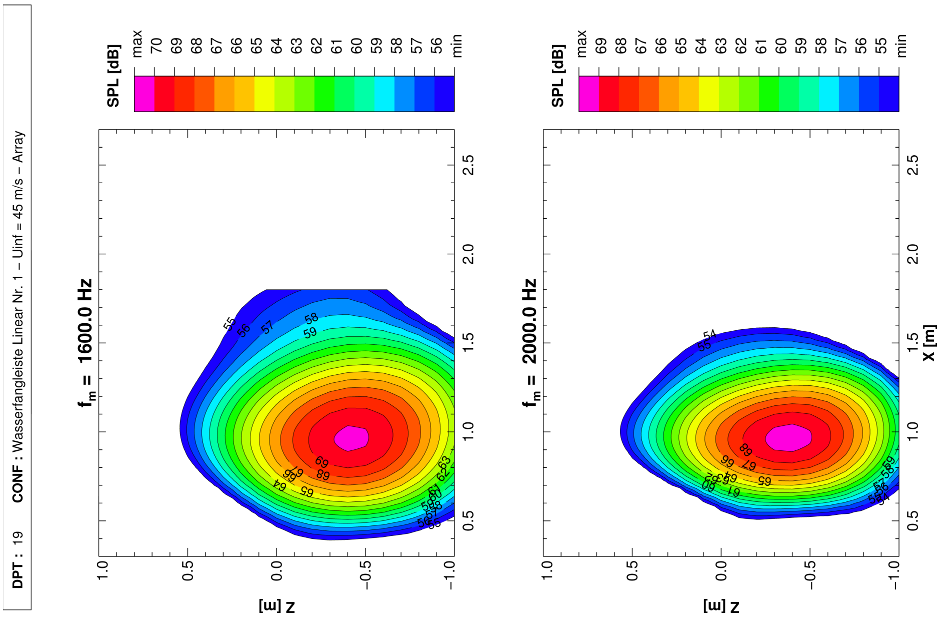

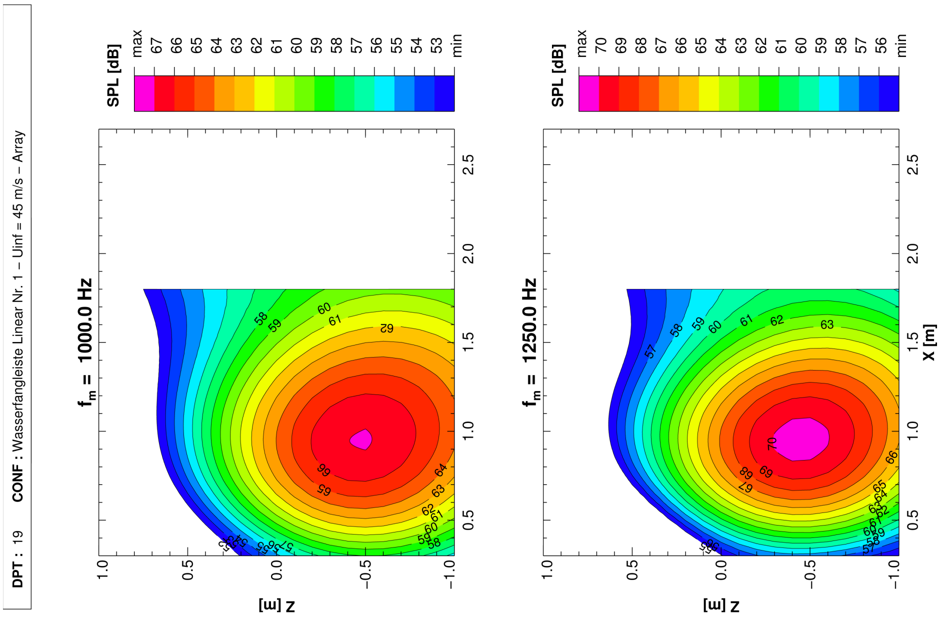

Microphone Array - Configuration A - Profile 1

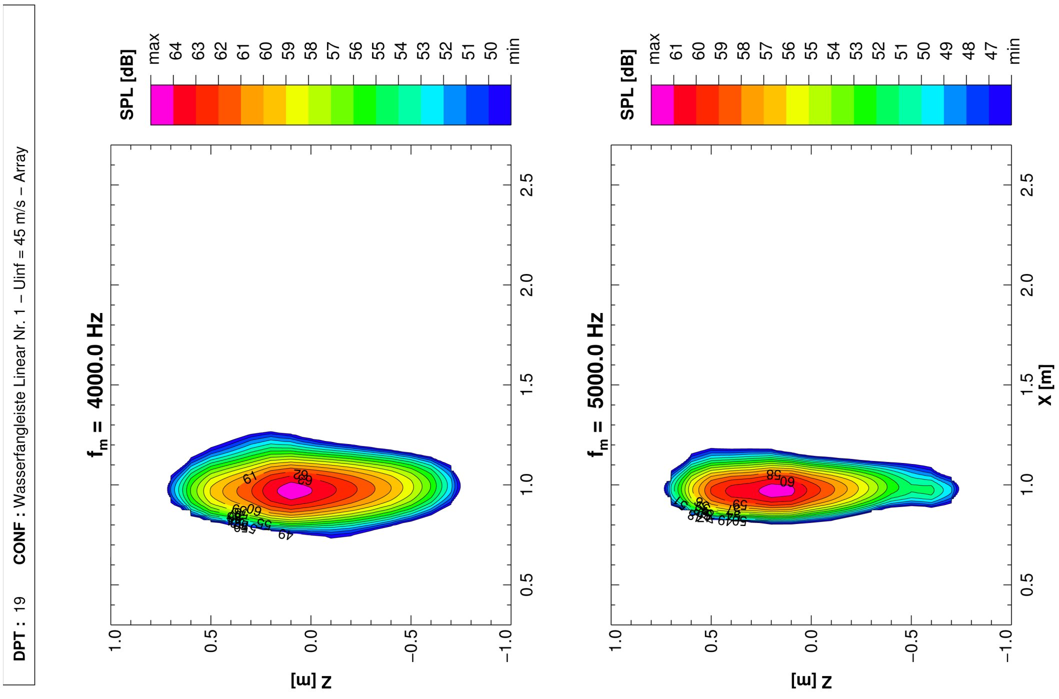

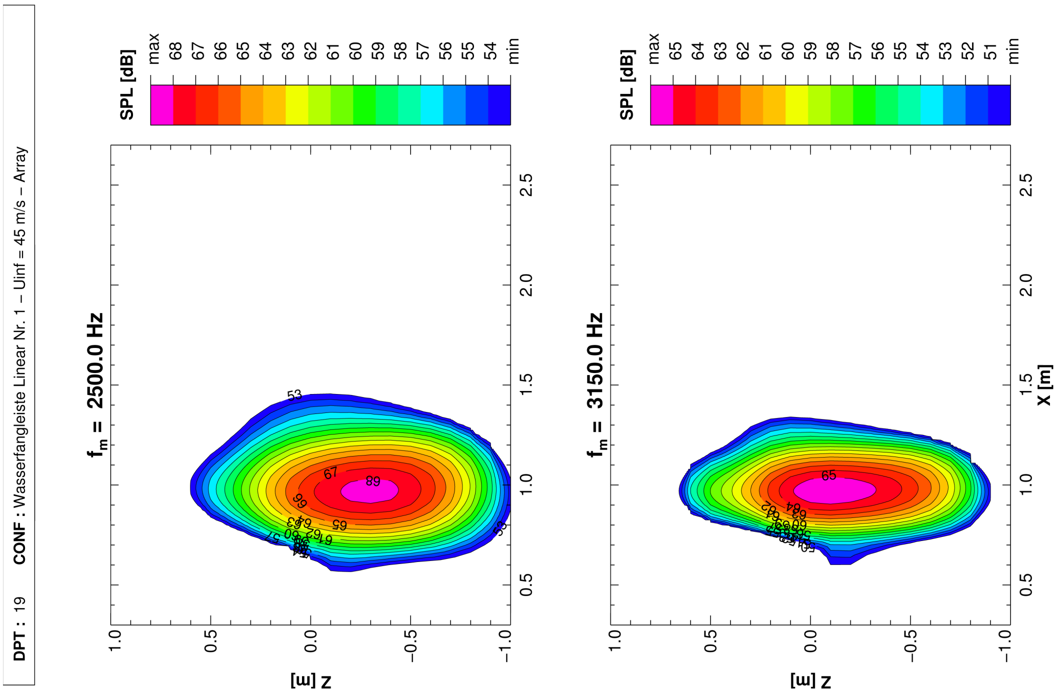

Microphone Array - Configuration A - Profile 1

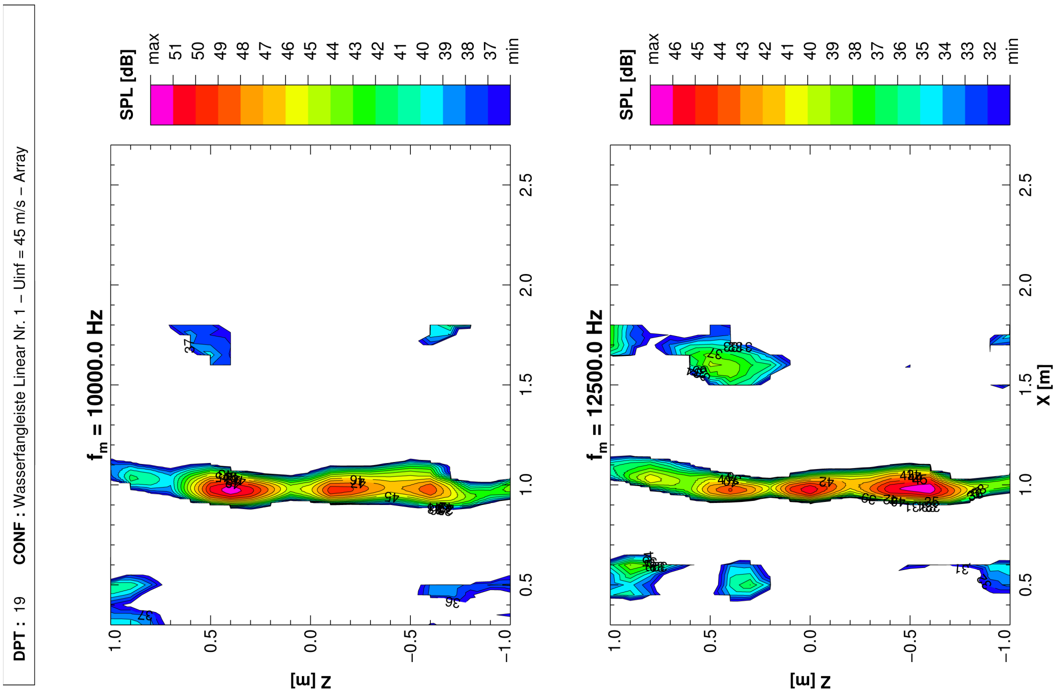

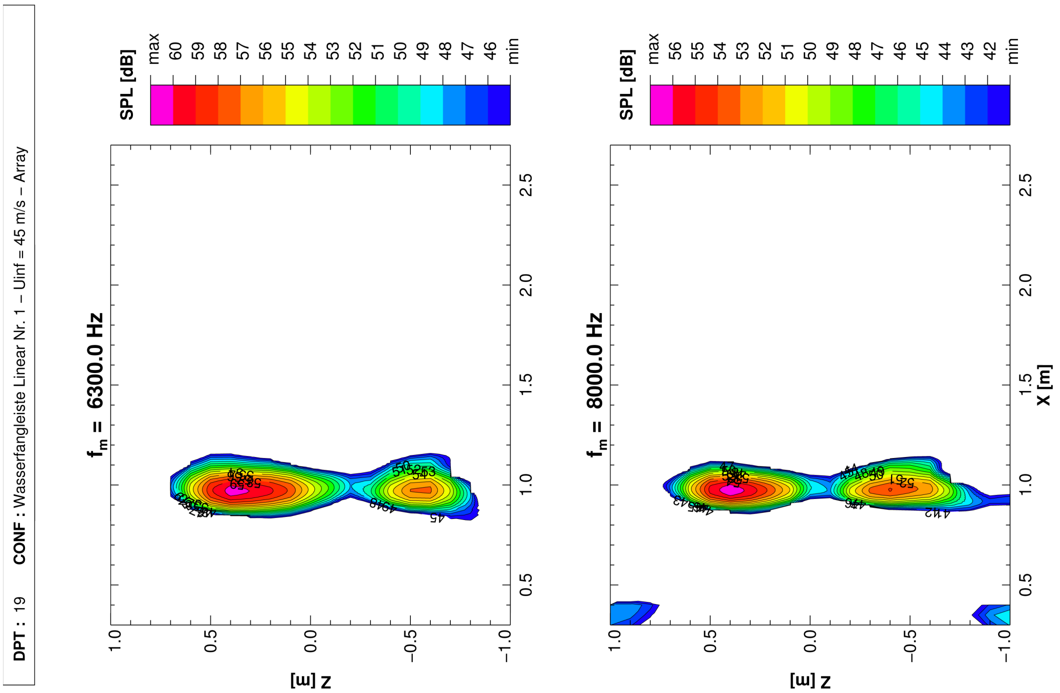

Microphone Array - Configuration A - Profile 2

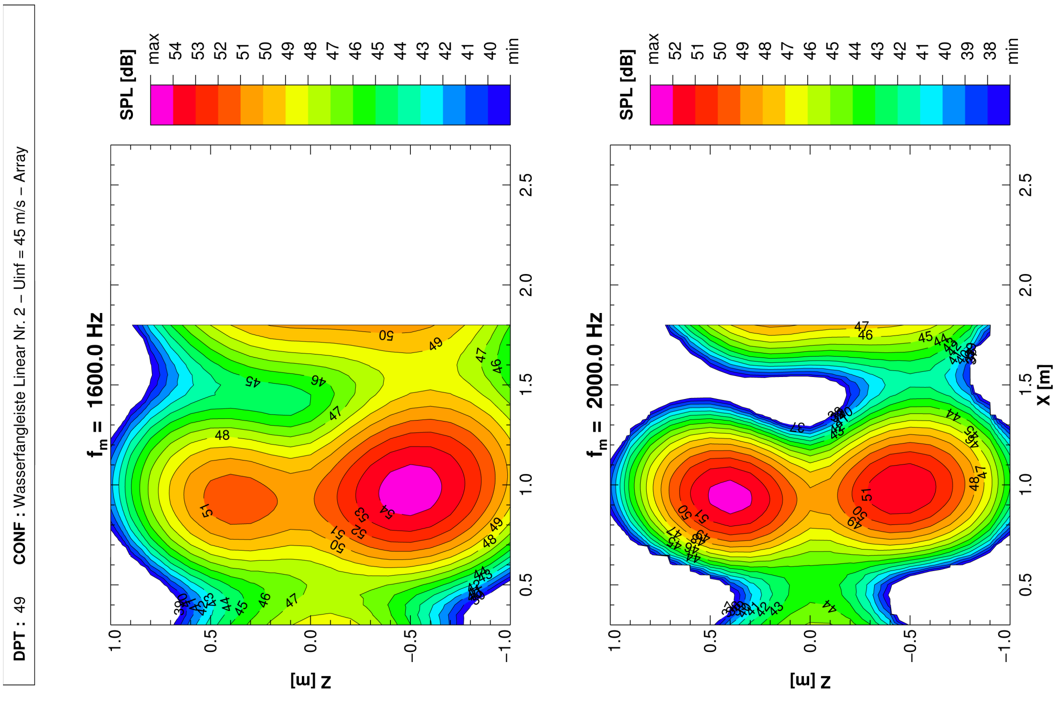

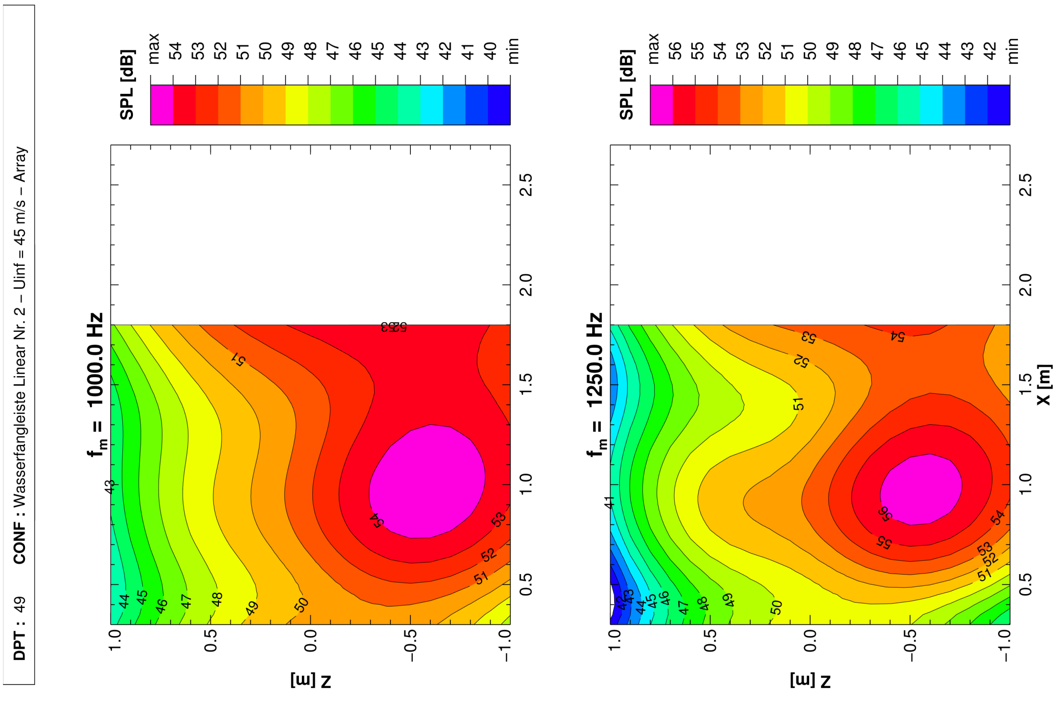

Microphone Array - Configuration A - Profile 2

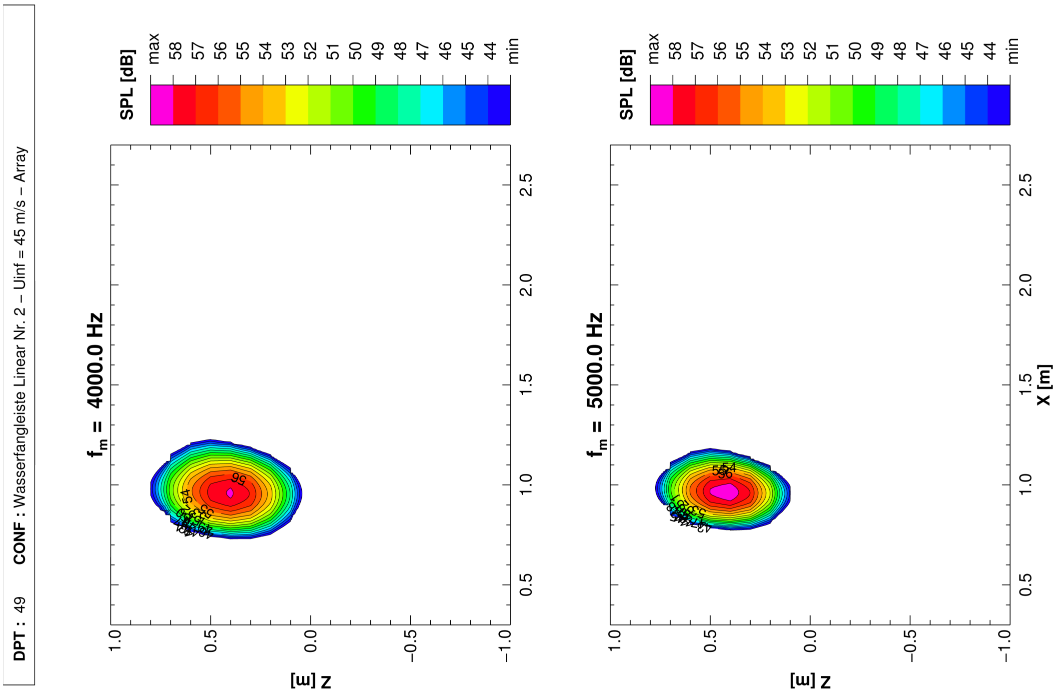

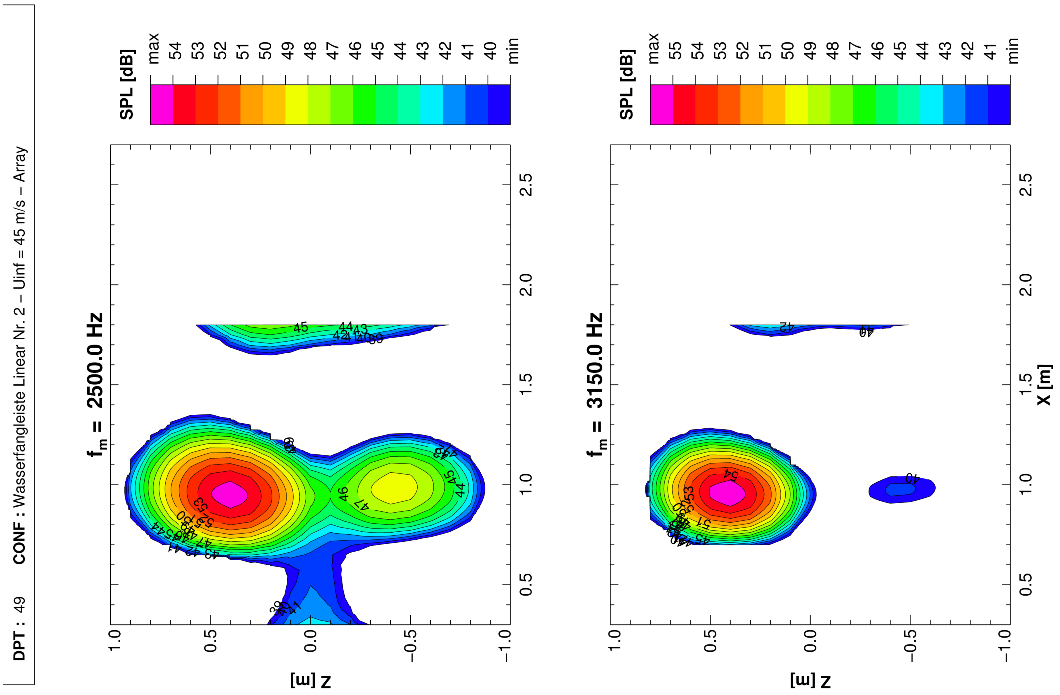

Microphone Array - Configuration A - Profile 2

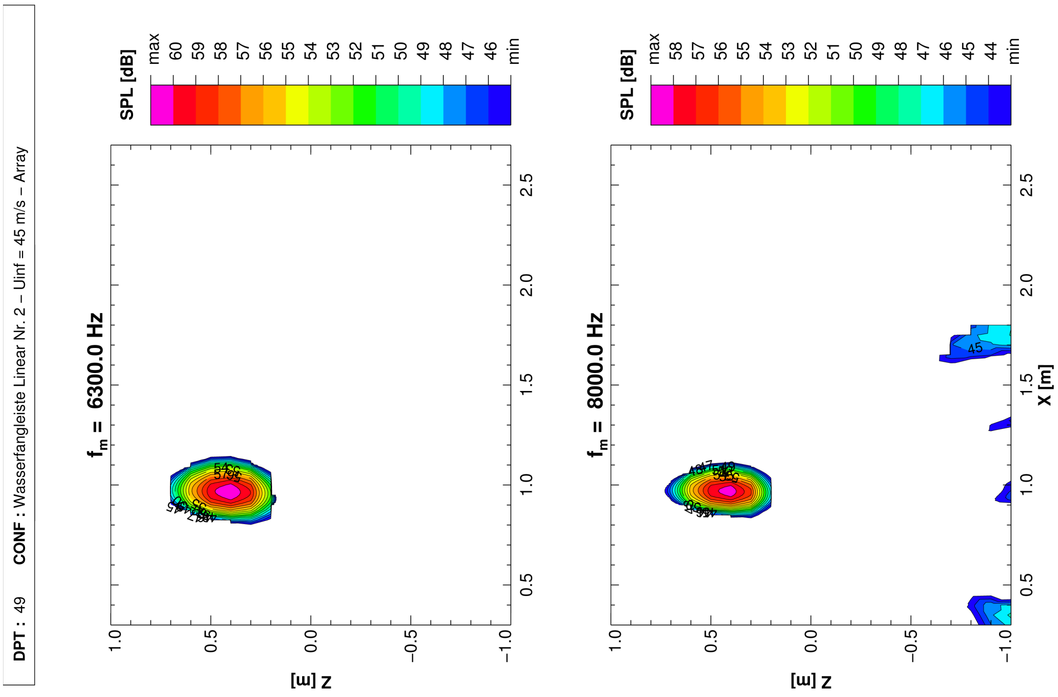

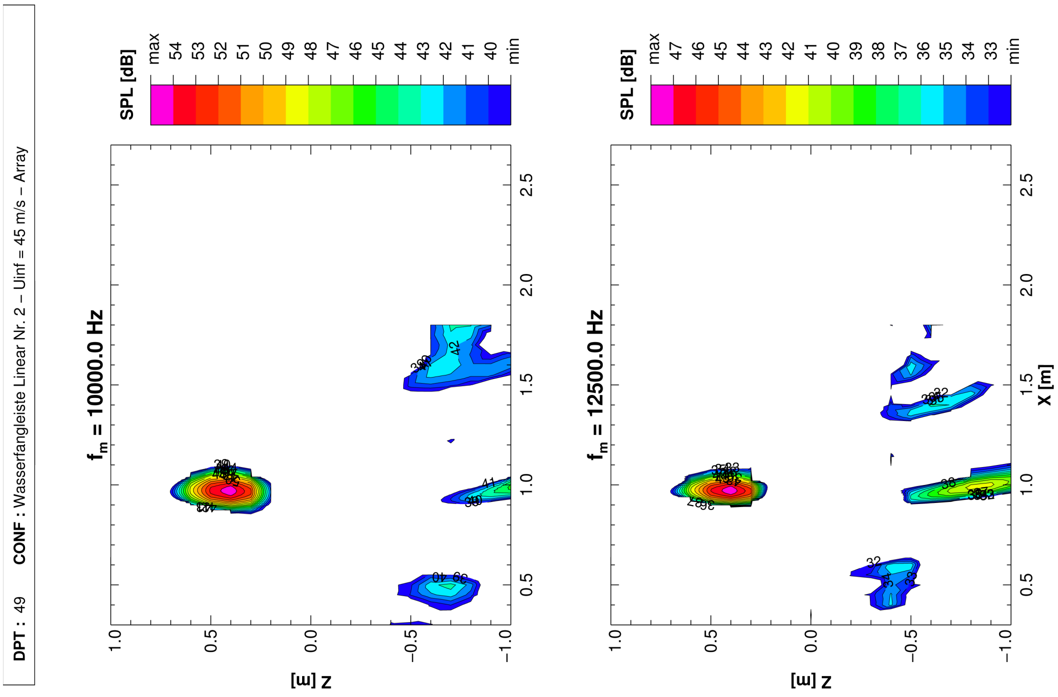

Microphone Array - Configuration B - Profile 1

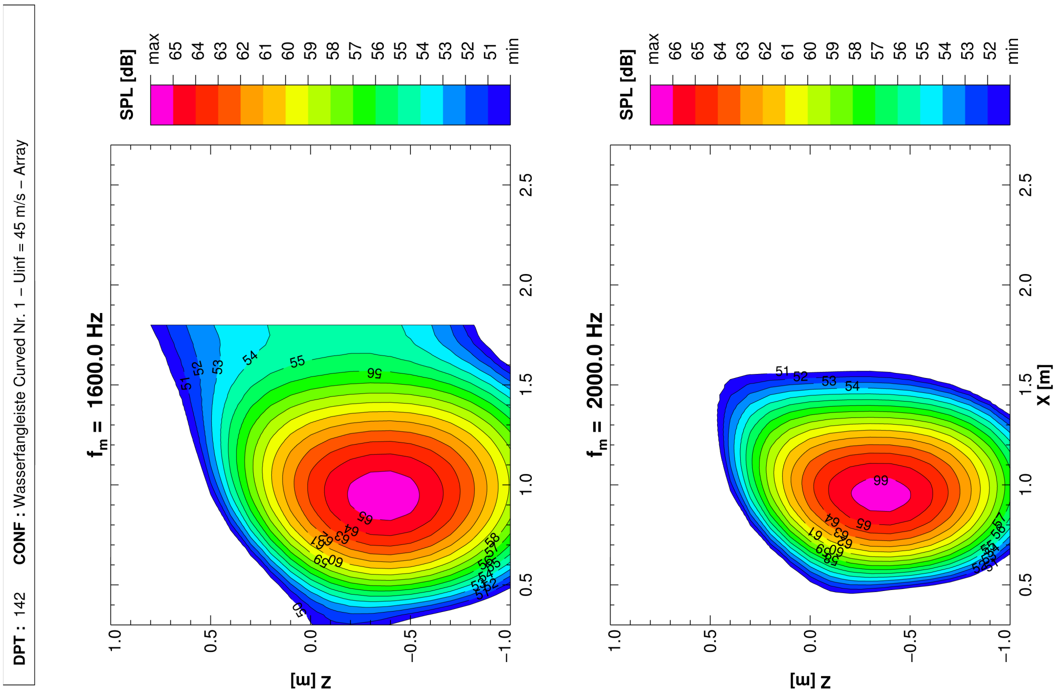

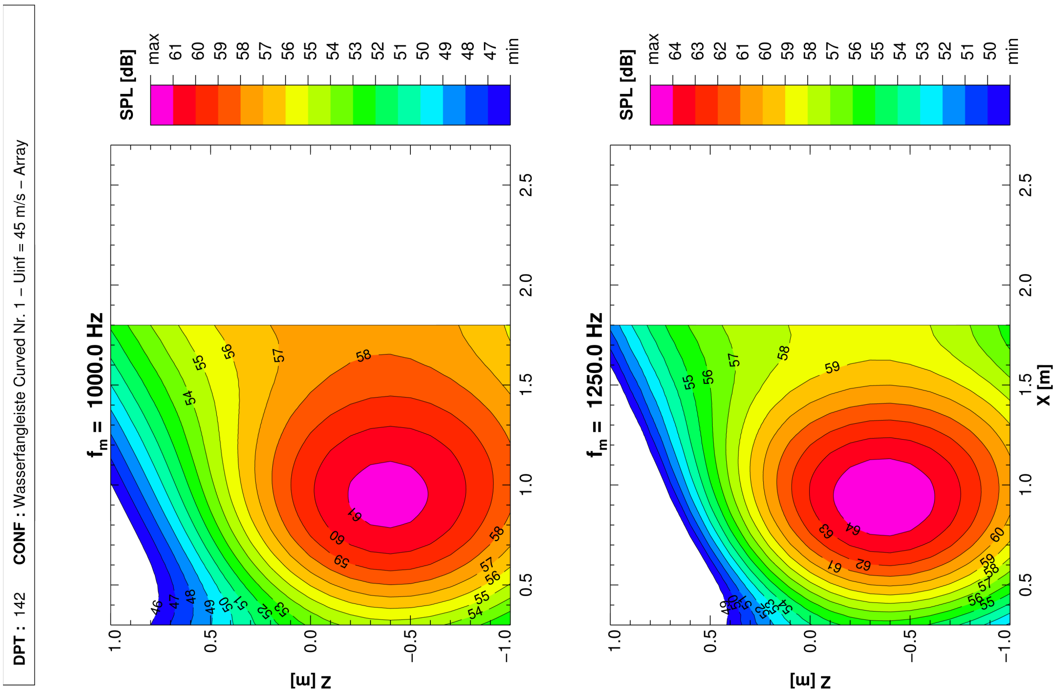

Microphone Array - Configuration B - Profile 1

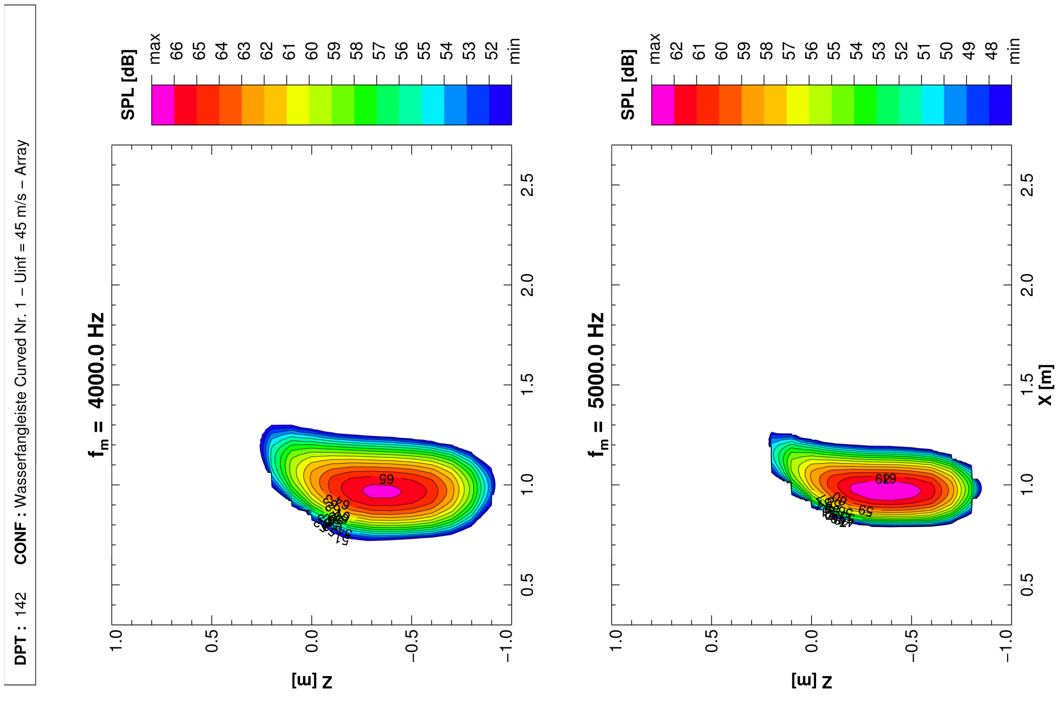

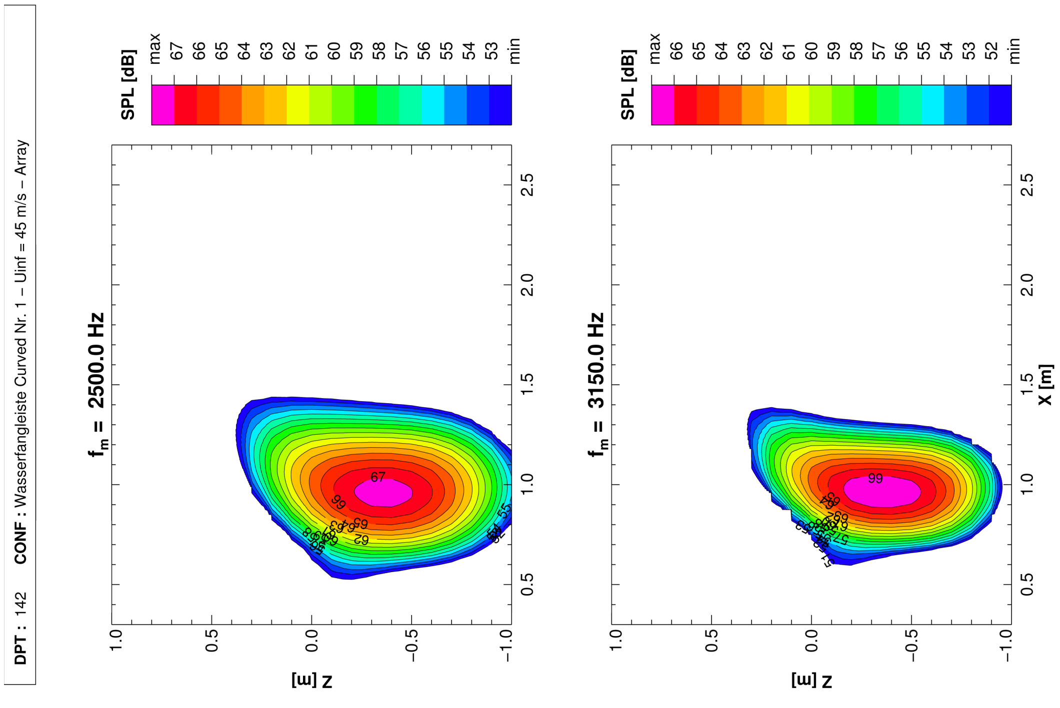

Microphone Array - Configuration B - Profile 1

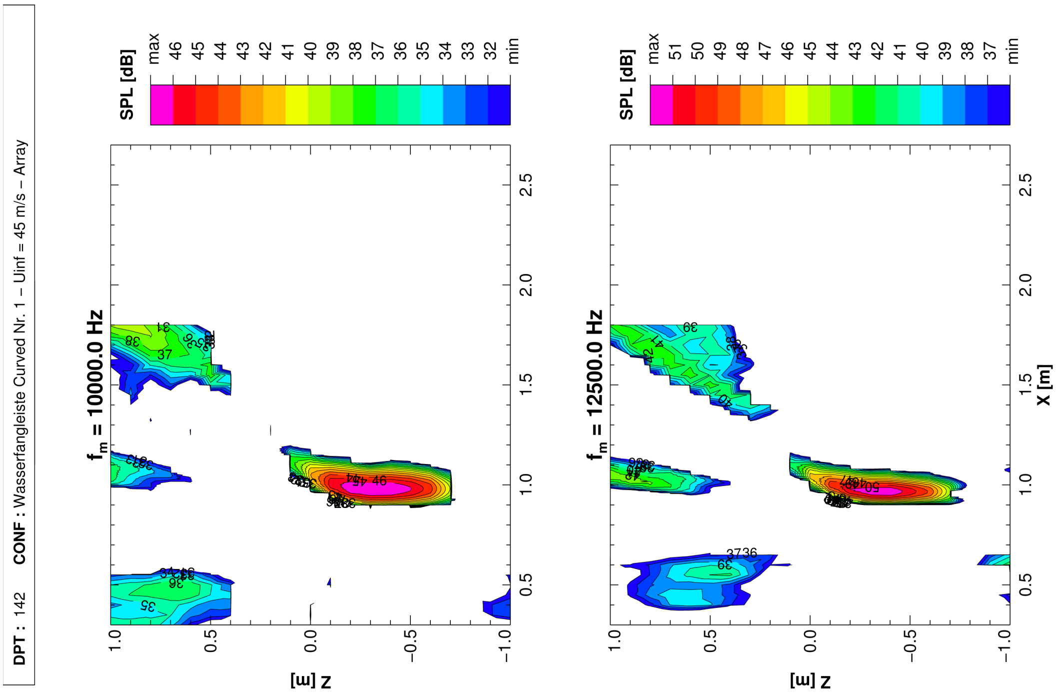

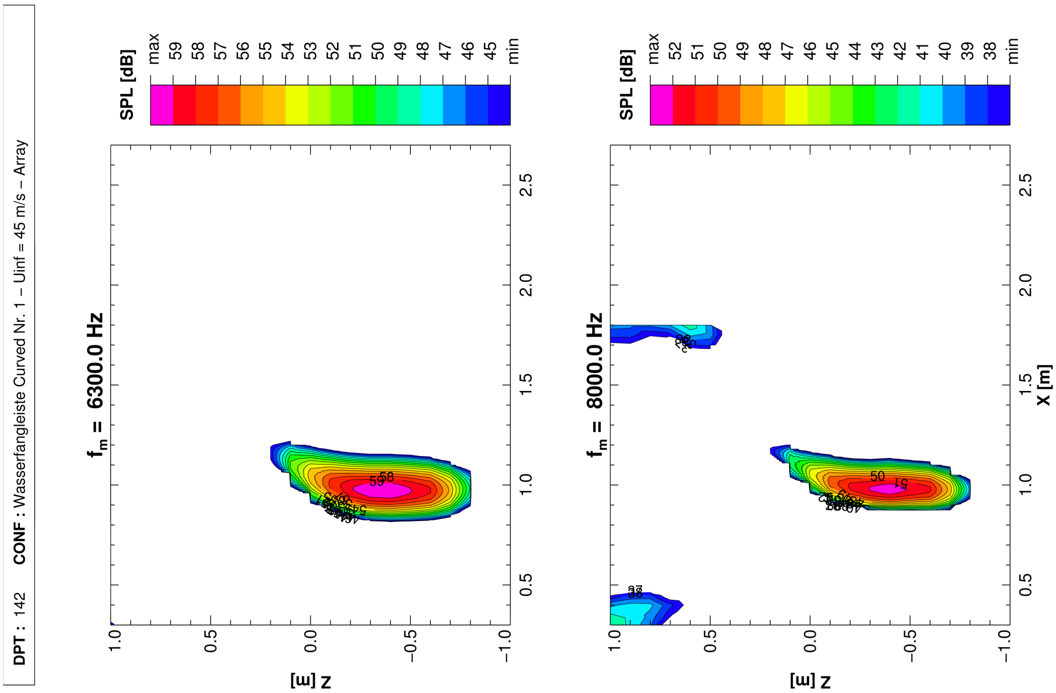

Microphone Array - Configuration B - Profile 2

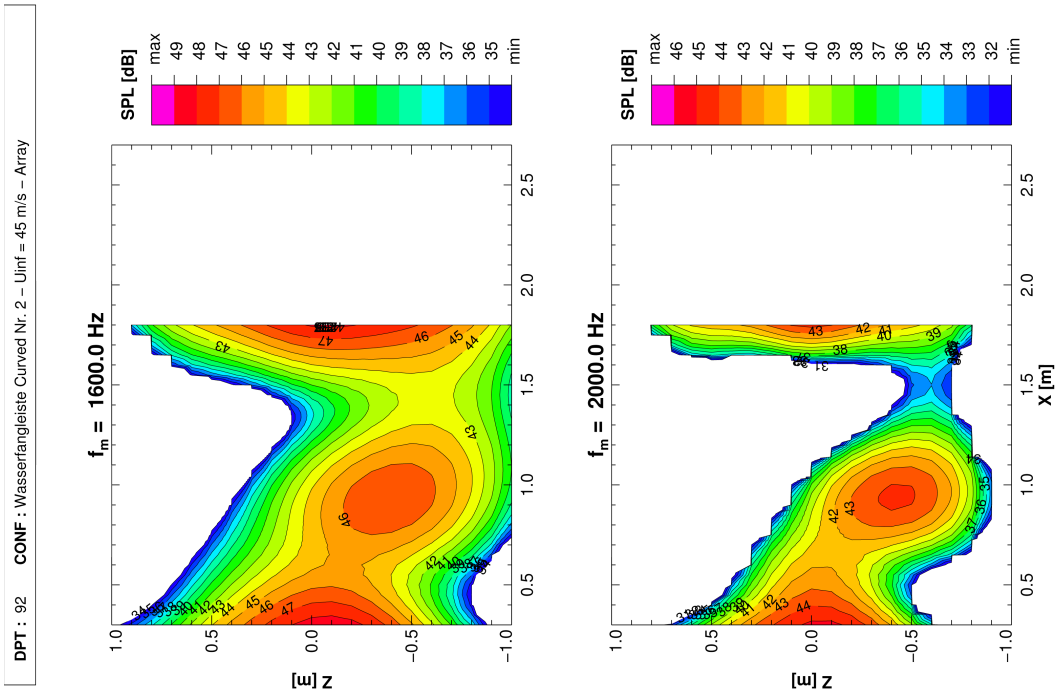

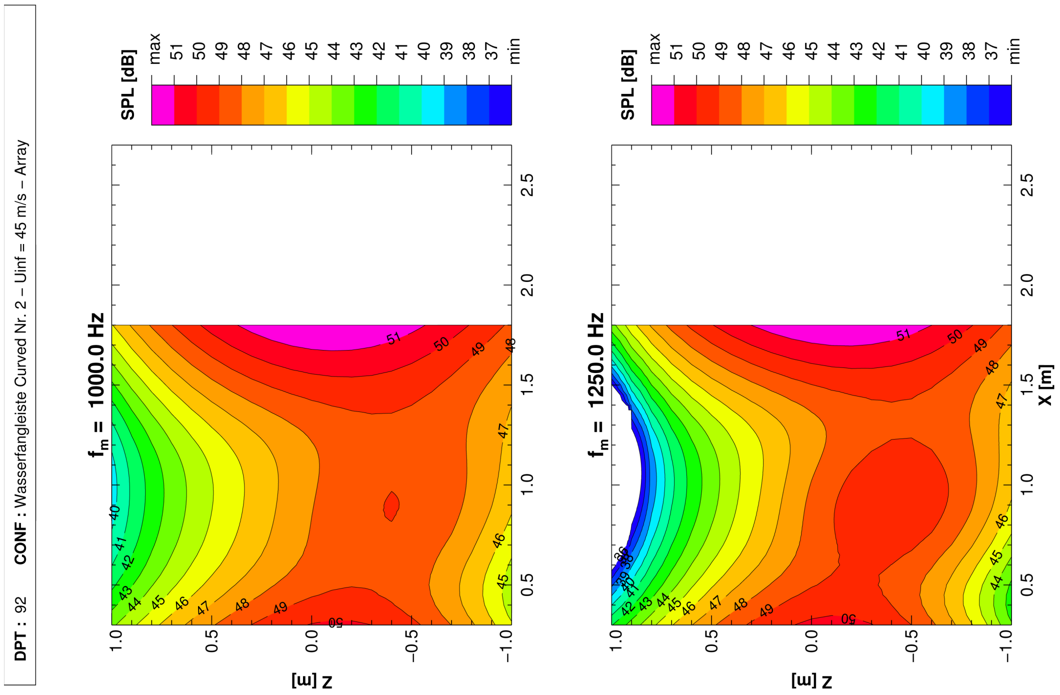

Microphone Array - Configuration B - Profile 2

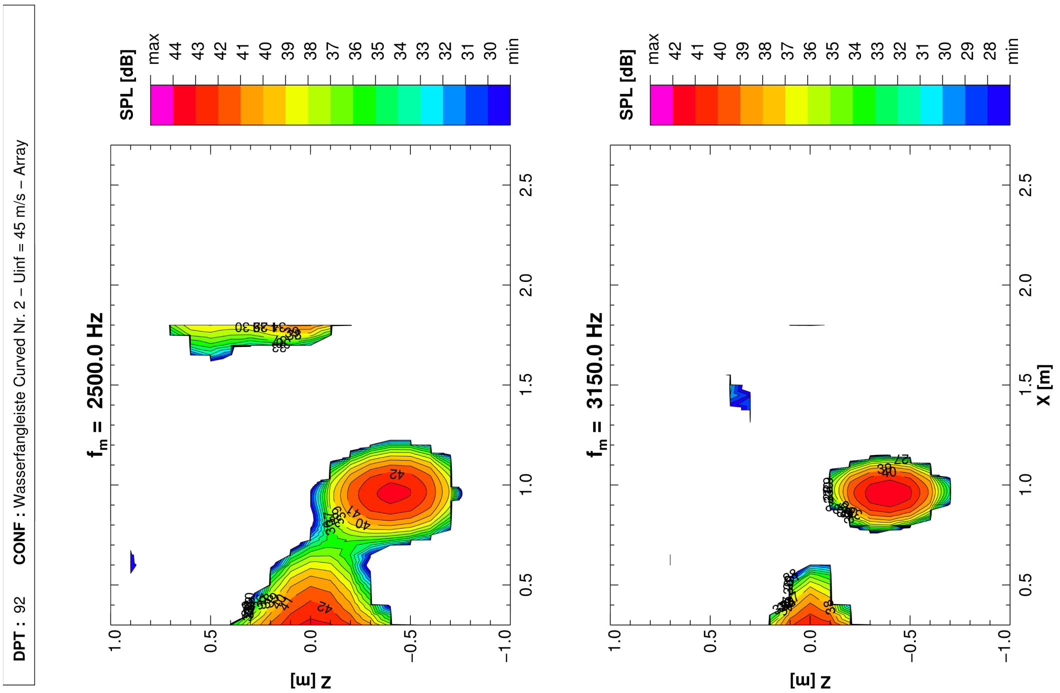

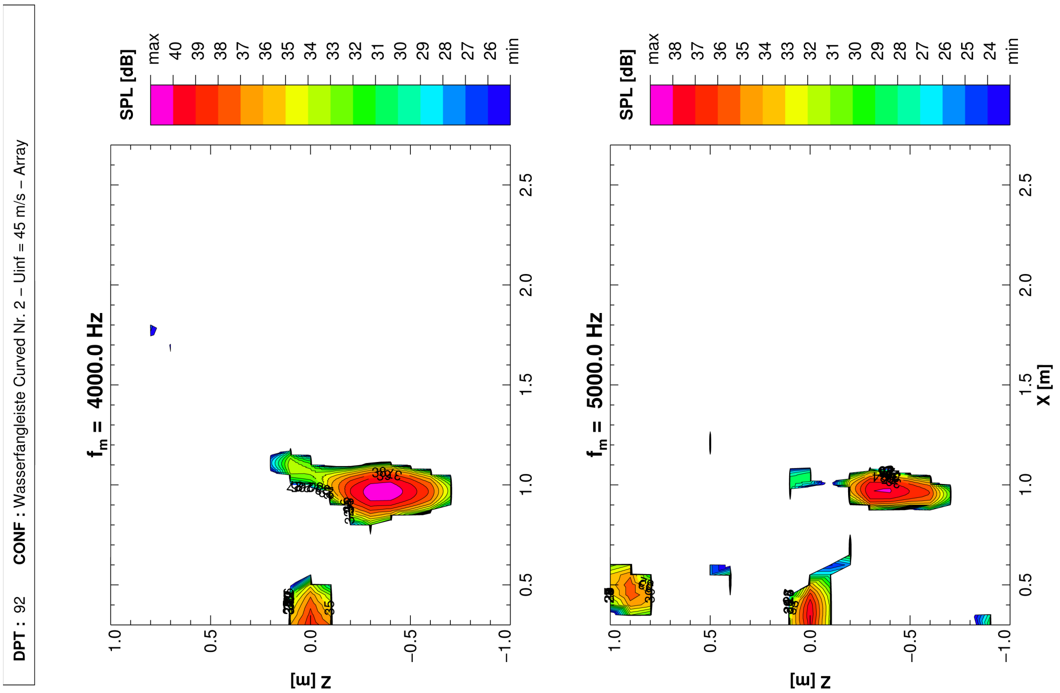

Microphone Array - Configuration B - Profile 2

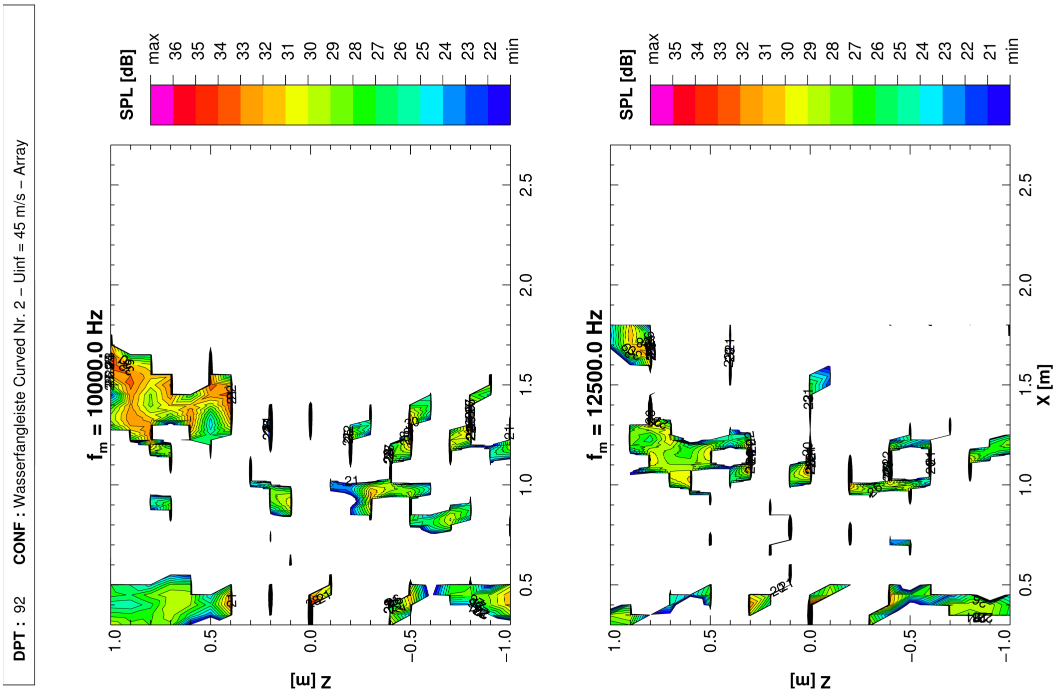

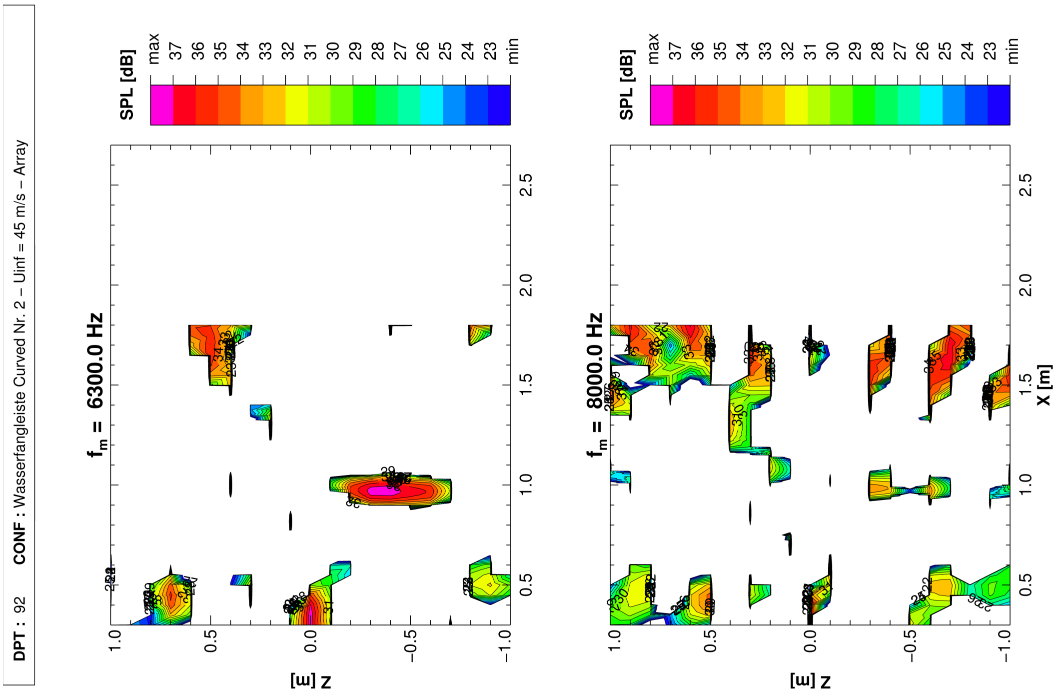

A.2 Further Experimental Coherences

Computed coherence at for the flush-mounted microphones. It illustrates the low transverse coherence for the first profile (1st row). At high frequency, the coherence of the acoustic signals between the flush-mounted microphones directly before and after the rain gutter is low for the second profile; however, the convection of the turbulent structures visible at low frequency is as for the first profile noticeable (2nd row). The next graph represents the coherence between the microphones directly before and behind the rain gutter for the configuration B / Profile 1 and confirms to the same conclusions.

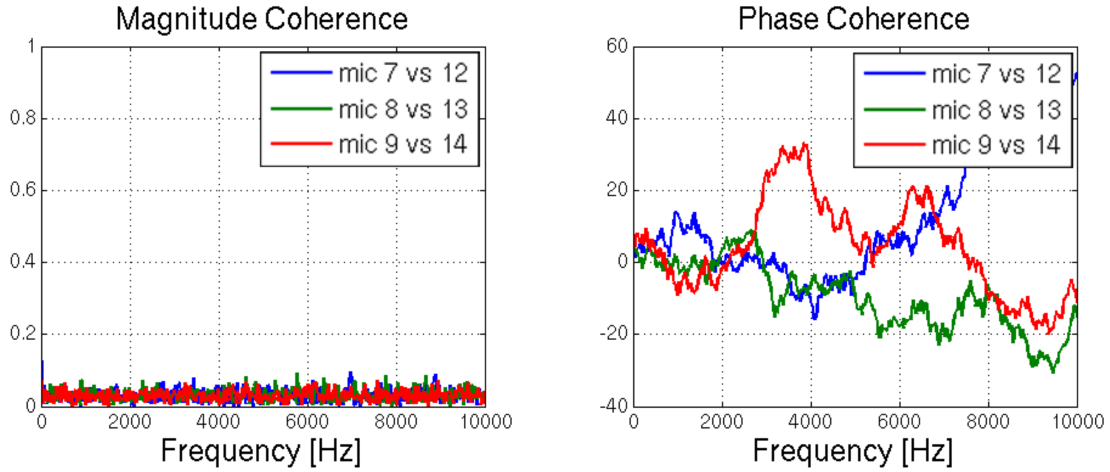

(a) Profile 1 - Configuration 1 (FMM)

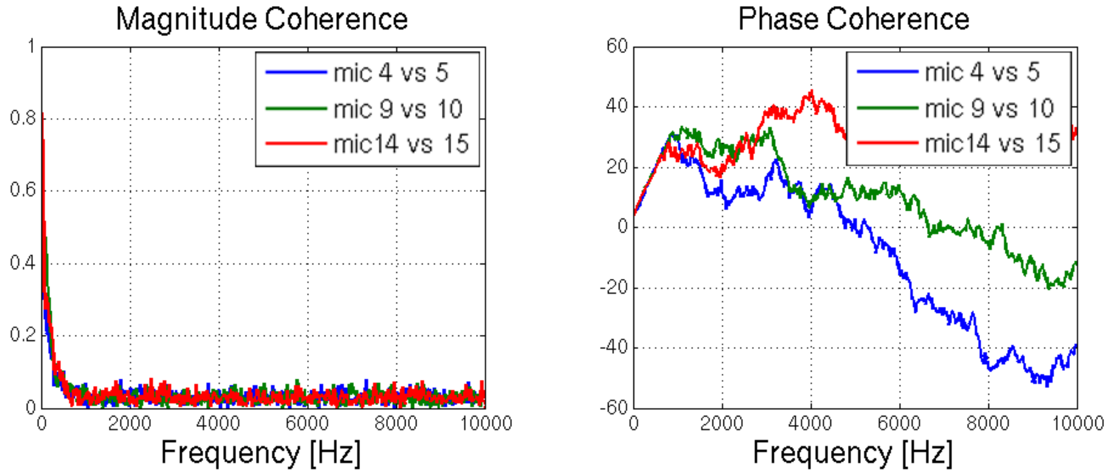

(b) Profile 2 - Configuration 1 (FMM)

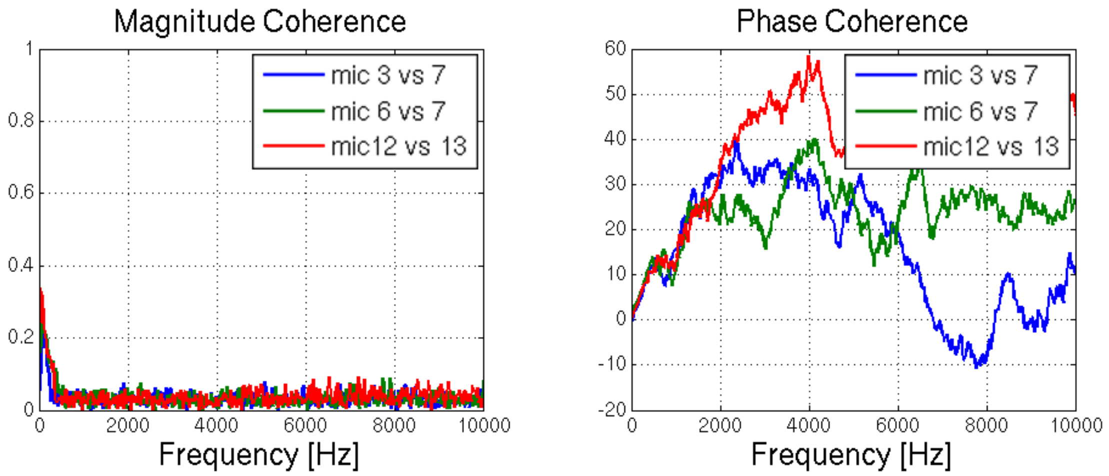

(c) Profile 1 - Configuration 2 (FMM)

Computed coherence between flush-mounted and far-field microphones:

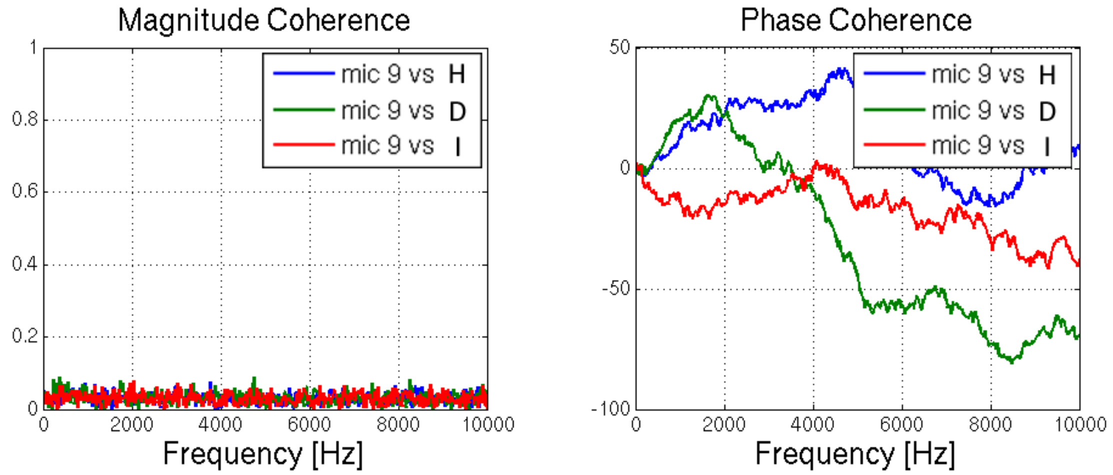

(d) Profile 1 - Configuration 1 (FFM)

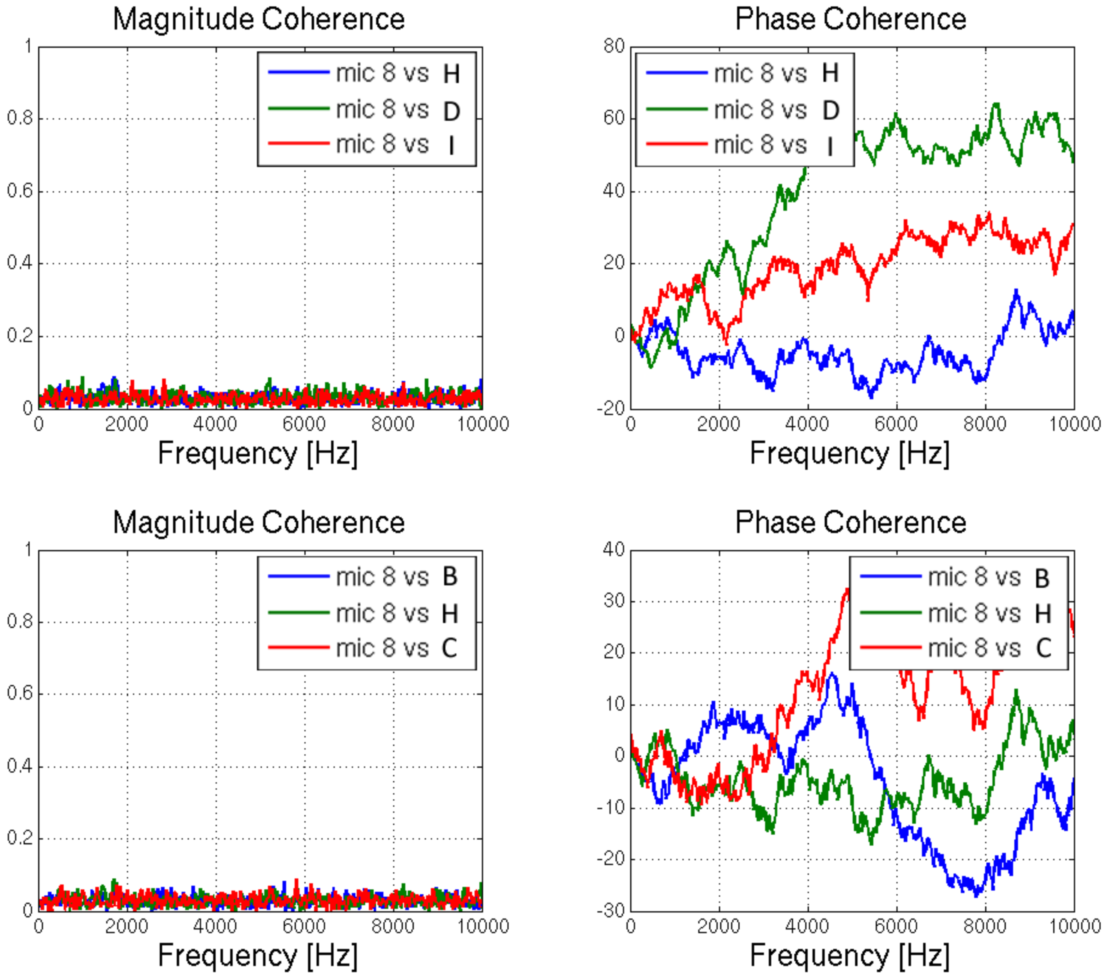

(e) Profile 2 - Configuration 1 (FFM)

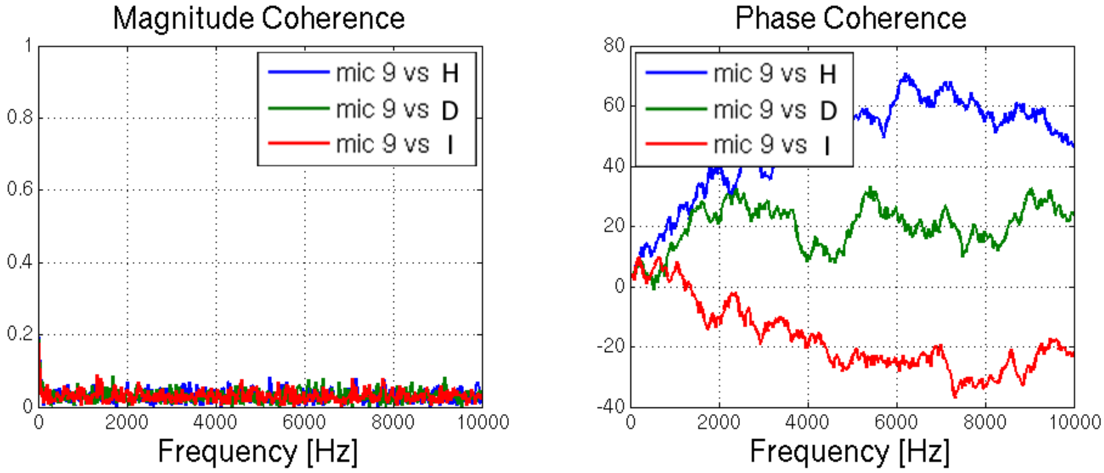

(f) Profile 2 - Configuration 1 (FFM)

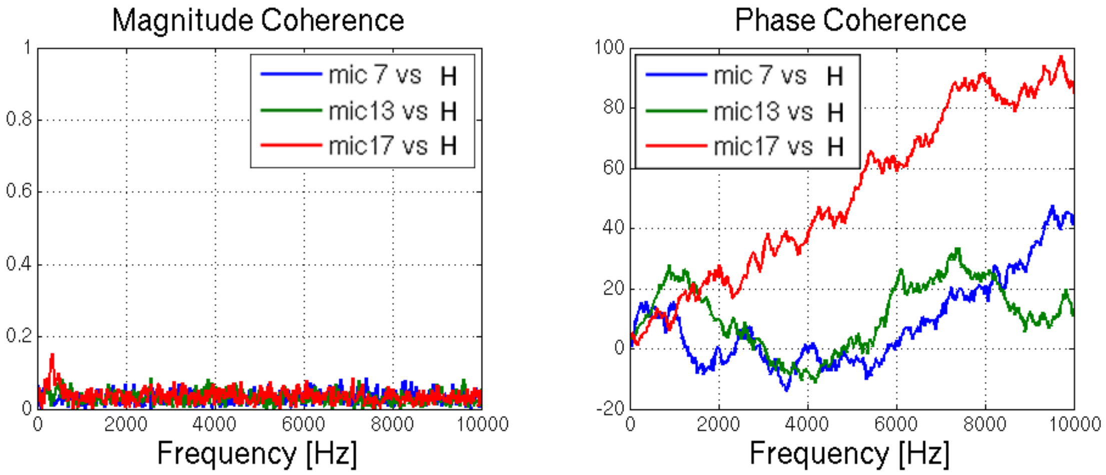

(g) Profile 1 - Configuration 2 (FFM)

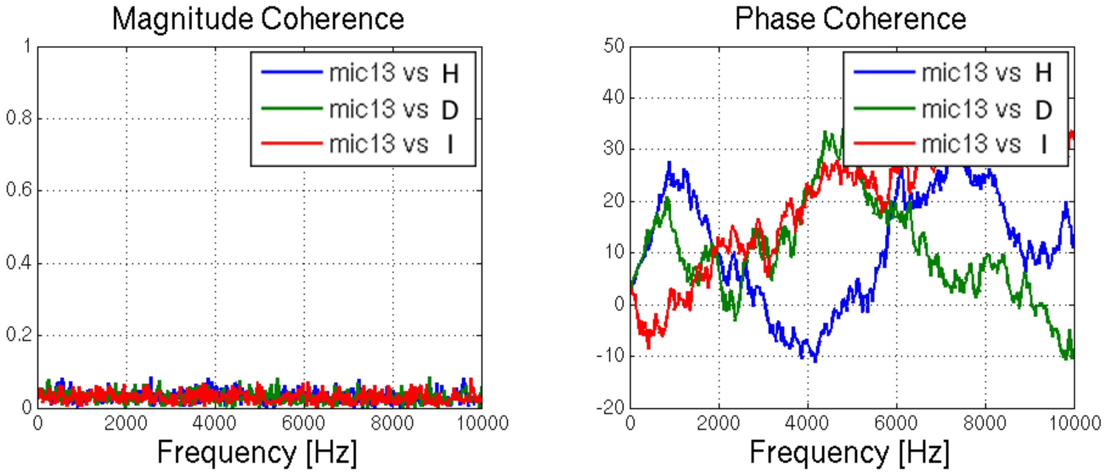

(h) Profile 1 - Configuration 2 (FFM)

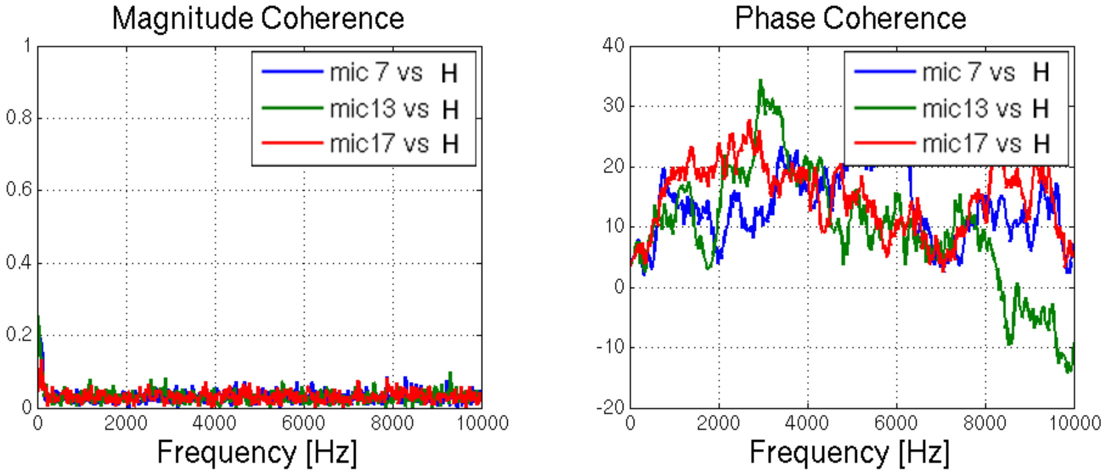

(i) Profile 2 - Configuration 2 (FFM)

A.3 Experimental length - Duration

Dispersion of the experimental spectra for a duration of 100 ms used for the simulation with DES and SAS.

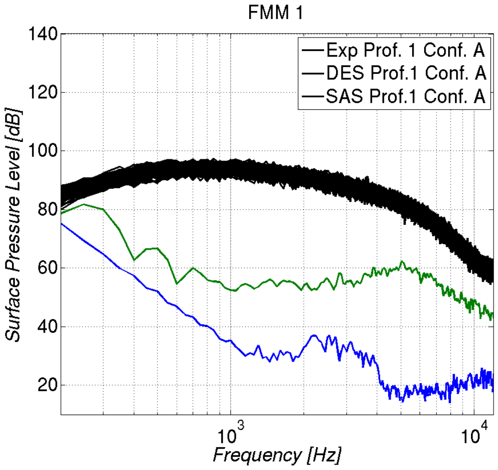

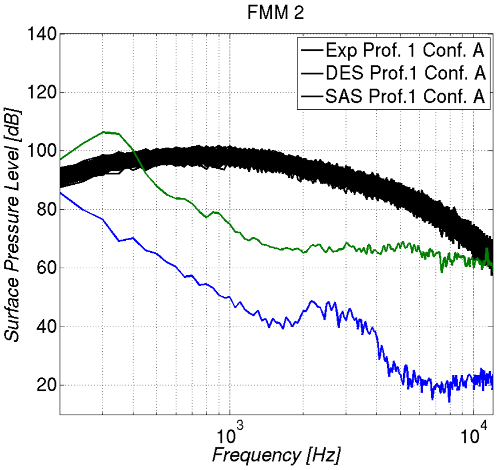

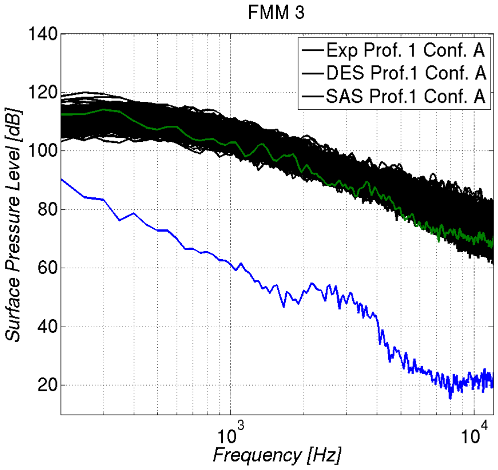

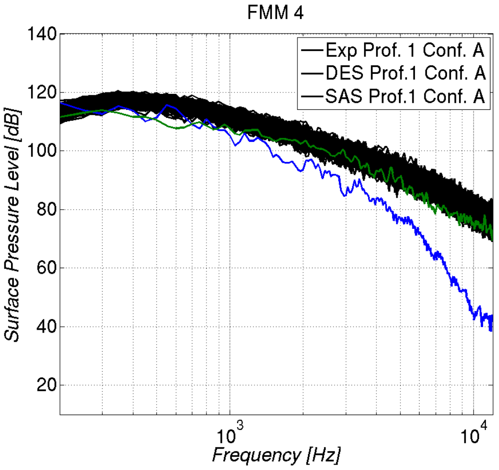

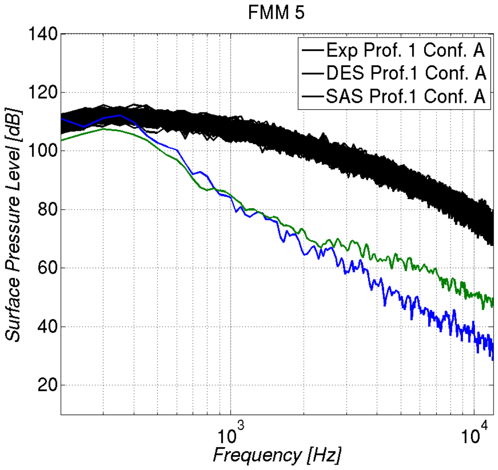

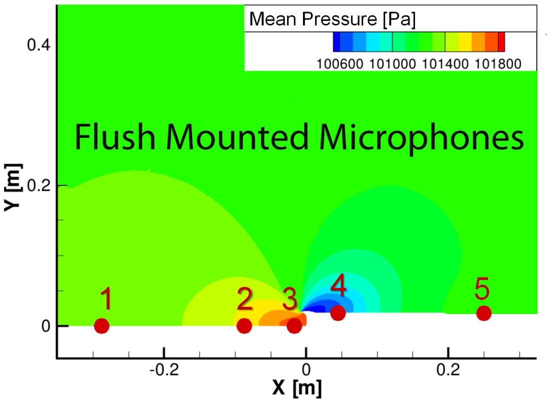

A.4 RPM Coherence (90° above RG)

Plots of the coherence computed with RPM for the microphones positioned at 90° above the rain gutter.

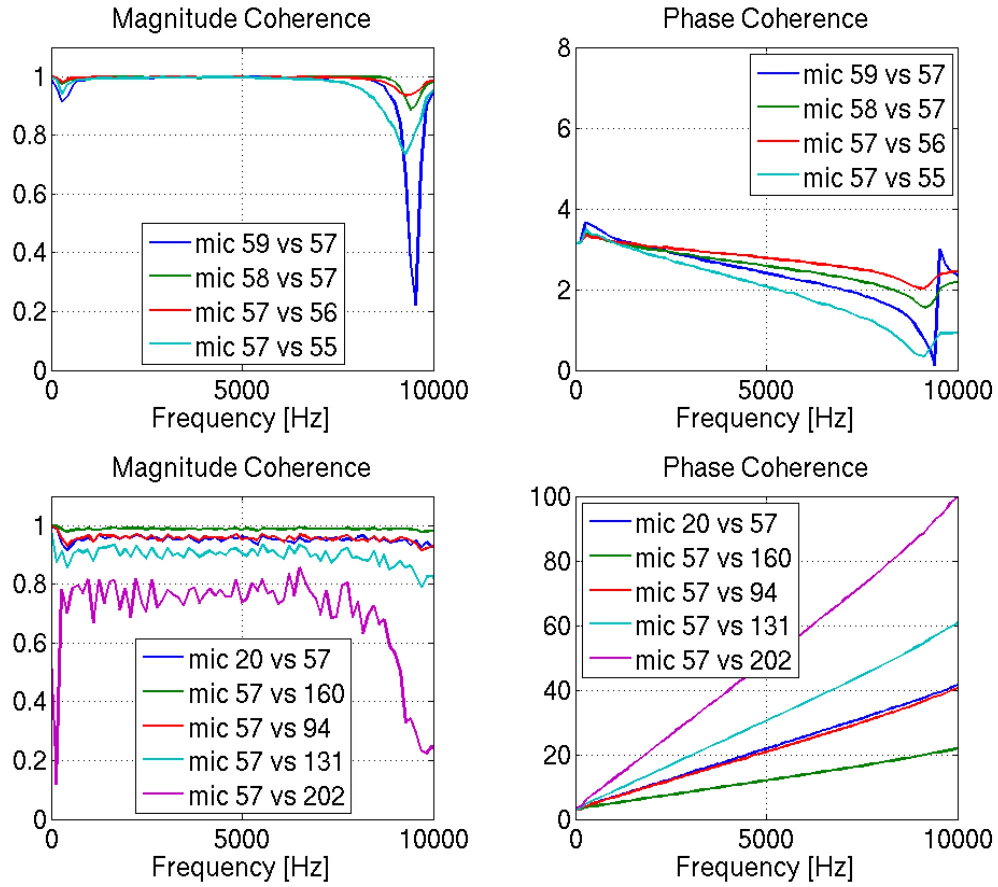

Disclaimer

Lebenslauf

Persönliche Daten

Name: Hervé Dechipre
Geburtsdatum: 23. Oktober 1980
Geburtsort: Alençon, Frankreich

Ausbildung

09/1995 - 08/1998	Lycée Alain, Alençon, Frankreich Baccalauréat S (französisches Abitur im Bereich der Naturwissenschaften) Gesamtnote: 2,0
09/1998 - 08/2001	Classes Préparatoires Scientifique, Caen, Frankreich Vorbereitungsklasse für die nationalen Aufnahmeprüfungen der „Grandes Ecoles“
09/2001 - 08/2004	ENSICA (Ecole Nationale Supérieure d´Ingenieurs de Constructions Aéronautiques), Toulouse, Frankreich Diplom der Ingenieurswissenschaften mit einer Spezialisierung in Luft- und Raumfahrt und Aerodynamik. Diplomarbeit: Windkanaluntersuchung über den Einfluss von Seitenwind an einem Automobilmodell bei PSA Peugeot Citroen.
10/2005 - 09/2006	Master Automotive Engineering (MSc), Coventry University, England Jahrgangsbester. Diplomarbeit: Verringerung des Luftwiderstandbeiwerts des Kühlsystems bei Jaguar/Land Rover in Gaydon.

Berufserfahrung

10/2004 - 09/2005	Assystem, Engineering-Dienstleister, Toulouse, Frankreich Performance Ingenieur für Aerodynamik und Anemometrie bei AIRBUS, Flugtests des A380
12/2006 - 05/2010	Volkswagen AG Konzernforschung, Fahrzeugtechnik, Wolfsburg Doktorand im Bereich Aeroakustik / CFD
08/2010 - 02/2012	RLE International, Engineering-Dienstleister, Köln Entwicklungsingenieur im Bereich Fahrzeugdurchströmung und Außeraerodynamik bei FORD-Werke GmbH
03/2012 - …	Volkswagen Motorsport CFD Ingenieur für Aerodynamik und Kühlung